Impulse maneuver design for a solar sail spacecraft in the restricted three-body problem framework

Xun Duan

Impulse maneuver design for a solar sail spacecraft in the restricted three-body problem framework

Author

Xun Duan

Thesis Advisors

Josep J. Masdemont, Gerard Gómez, Xiaokui Yue

PhD dissertation

submitted to the Universitat Politècnica de Catalunya (UPC) in
partial fulfillment of the requirements for the degree of
DOCTOR OF PHILOSOPHY

Ph.D. program on Aerospace Science and Technology
Barcelona, December 2022

Dissertation written by Xun Duan

Impulse maneuver design for a solar sail spacecraft in the restricted three-body problem framework

Ph.D. program on Aerospace Science and Technology

This work has been supported by the China Scholarship Council (Grant 201606290096), National Natural Science Foundation of China (Grant 11572248), MINECO-FEDER (Grant MTM2018-100928), Catalan government (Grant 2017SGR-1049, 2017SGR-1374) and Ministerio de Ciencia e Innovación (Grant PID2019-104851GB-I00).

ACKNOWLEDGMENTS

I would like to acknowledge all those people who have supported me over the last few years and who have helped me in the writing of the thesis with suggestions, criticisms and comments: to them goes my gratitude.

My deepest gratitude is to my respected supervisors Prof. Gerard Gómez from the Department de Matemàtiques i Informàtica at the Universitat de Barcelona (UB), Prof. Josep J. Masdemont from the Department de Matemàtiques at the Universitat Politècnica de Catalunya (UPC) and Prof. Xiaokui Yue from Northwestern Polytechnical University (NPU). It's my huge honor to have the chance of getting Gerard and Josep guidance in Barcelona. They are the best professors and friends with all the good things in this world, who have not only provided me with guidance and help in my research and life, but also made my stay in Barcelona full of fun and beautiful memories. They erudition, wisdom, tolerance, humility and sense of humor are my sole model for lifelong learning. I hope I can continue my research in this field following their footprints. Special wishes to Gerard, and hope he can have a happy life and good health in his retirement days.

Special thank for my domestic tutor Prof. Yue, his supervision, valuable insights and detailed comments make me feel the happiness of learning. He always taught me to set high goals in research and in life. His continuous encouragement and unconditional trust gave me the opportunity to study in Barcelona.

I am very grateful to all my friends, from UB, UPC and NPU. I can't image my life without them. A special thanks to Chen Gao, Jianlin Chen, Yu Cheng for sharing their knowledge and experience, Xin Wang, Lei He, Xun Pan, Zixuan Zheng, Jun Wan, Haowei Wen and so on for their kindness the continuous supports.

My gratitude is also extended to Dr. Hua Meng, Jinman Cai, Chen Li, Yutian Ye and all the colleagues from National Space Administration News and Publicity Center. Although the short internship, I am grateful for your personal and technical support. I will always be your small Dr. Duan no matter where I am.

Finally, I would like to express my deep appreciation and love to my families for their selfless and endless comparisons, supports, encouragements and love.

A tots i a cadascun de vosaltres, MOLTES GRÀCIES !!!

Abstract

A solar sail is a method of spacecraft propulsion that uses only the solar radiation pressure (SRP). It has advantages in fuel consumption, high specific impulse, high payload, and consistent small-scale of the thrust, with wide-ranging applications in deep-space exploration missions. Solar sailing was tested successfully by JAXA in 2010 with the probe IKAROS, by NASA with NanoSail-D2 in 2011, and more recently, in June 2019, by the Planetary Society with LightSail 2.

When we consider the acceleration on a solar sail spacecraft due to SRP, artificial equilibrium points appear in dynamic models of the perturbed circular restricted three-body problem (CR3BP). These are useful, for instance, for studying Sun–Earth solar sail missions. They significantly extend the dynamics in the libration point region. These new points are usually denoted by SL_1, SL_2, ..., SL_5. In addition, there are many periodic and quasi-periodic orbits around the artificial libration points. These provide good mechanical environments for relay satellites, solar observation satellites, and other applications, as we can artificially displace the equilibrium and orbits with an appropriate sail orientation. Of course, both the new equilibrium points and orbits depend on the magnitude of the SRP acceleration, which is a function of the main sail parameters, such as the sail spacecraft's area-to-mass ratio, its reflectivity, and orientation of the sail surface to the Sun-line direction.

The main research object of this thesis is a solar sail spacecraft. It proposes a strategy to accomplish impulsive maneuvers by changing the parameters of the sail. The method is applied to spacecraft mission design, including heteroclinic orbit transfers, forbidden zones for eclipse avoidance, and orbit maintenance.

The main new results of this work are the following:

1. Computation of artificial libration points as a function of the parameters of a solar sail (cone angle α, clock angle δ, and lightness number β).

   The SRP is an additional repulsive acceleration in the CR3BP. As a result, the CR3BP equilibrium points L_1, L_2, ..., L_5 are shifted from their original positions. The new points SL_1, SL_2, ..., SL_5 correspond to positions in the rotating system where the gravitational, centrifugal, and SRP forces are balanced. These points can be represented as functions of the sail parameters α, δ, and β. It's worth to note that the location of the artificial equilibrium points strongly depends on β .

2. Determination and adjustment of the solar sail parameters, computation of impulse maneuvers and their application to heteroclinic orbit transfers between Lissajous orbits plus a sensitivity analysis of the parameters of the maneuver for orbit transfers.

   The dynamics of solar sail maneuvers is conceptually different from classical control maneuvers, which rely only on impulsive changes to the velocity of a spacecraft. Solar sail orbits are continuous in both position and velocity in a varying vector field, which opens up the possibility for the existence of heteroclinic connections by changing the vector field with a sail maneuver. Based on a careful analysis of the geometry of the phase space of the linearized equations of motion around the equilibrium points, the key points are the identification of the main dynamic parameters and the representation of the solutions using the action-angle variables. The basic dynamic properties of the connecting families have been identified, presenting systematic new options for mission analysis in the libration point regime using this method for determining impulse maneuvers.

   Based on the proposed method for making impulse maneuvers, this thesis has carried out extensive research: (1) By applying a single-impulse maneuver, two spacecraft can reach the same final Lissajous orbit despite starting from different initial phases. (2) A transfer strategy is proposed that uses multi-impulse maneuvers. The initial and final solar sail parameters are fixed. (3) A spacecraft can use multi-impulse maneuvers to make back-and-forth jumps between the initial and final artificial libration point orbits.

3. Avoidance of forbidden zones considering impulsive maneuvers with the sail.

   There is a cylinder-like zone around the Sun–Earth axis where solar electromagnetic radiation is especially strong. The L_1 libration point lies on this axis and is between the two bodies. The Earth half-shadow in the L_2 region can also prevent a spacecraft from obtaining solar energy. Both problems can be modeled by placing a forbidden or exclusion zone in the YZ plane (around the libration point), which should not be crossed. To simplify and visualize the avoidance of forbidden zones, this thesis projects the 3D forbidden zones, as well as the heteroclinic transfer orbit, into the so-called effective phase plane (EPP), which has two dimensions. This helps in determining the existence of a forbidden zone and its distance relative to the spacecraft. In the proposed method of impulse maneuvers, the forbidden zones in the EPP change depending on the parameters of the solar sail. The zones can even sometimes "disappear," which means that after the impulse maneuver, the spacecraft will never cross a forbidden zone again.

4. Station-keeping of a solar sail moving along a Lissajous orbit.

   The designed station-keeping procedure periodically performs a maneuver to prevent the spacecraft to escape from a certain Lissajous orbit following its unstable manifold. The maneuver is computed so that it cancels out the unstable component of the state. Moreover, it is assumed that there is a random error in the execution of the maneuver. Considering the maneuvers performed every month, we show that the spacecraft can remain near the artificial libration points for at least 5 years, which demonstrates that station-keeping using sail reorientations to produce multiple impulses can be effective.

RESUM

Una vela solar és un procediment de propulsió de naus espacials que només utilitza la pressió de radiació solar (SRP). Té avantatges pel que fa al consum de combustible ja que proporciona un impuls específic elevat, una càrrega útil elevada i, a petita escala, una empenta constant; les veles solars tenen moltes aplicacions en missions d'exploració de l'espai profund. Les primeres veles solars van ser provades amb èxit per JAXA el 2010 amb la sonda IKAROS, per la NASA amb NanoSail-D2 el 2011 i, més recentment, el juny de 2019, per la Planetary Society amb LightSail 2.

Quan considerem l'acceleració a la qual està sotmesa una nau espacial proveïda d'una vela solar, en els models dinàmics pertorbats del problema de tres cossos restringit i circular (CR3BP) apareixen punts d'equilibri artificials degut a la SRP. Aquests models són útils, per exemple, per estudiar el moviment de les veles solars al sistema Sol-Terra, ja que enriqueixen significativament la dinàmica en la regió al voltant dels punts de libració. Aquests nous punts solen indicar-se amb els símbols SL_1, SL_2, ..., SL_5. Al voltant d'aquests punts apareixen noves òrbites periòdiques i quasi periòdiques que proporcionen bons entorns dinàmics per a, entre altres aplicacions, satèl · lits de comunicacions i satèl · lits d'observació solar, ja que es pot moure el punt d'equilibri i les òrbites al seu voltant orientant adequadament la vela. Per descomptat, tant els nous punts d'equilibri com les òrbites al seu entorn depenen de la intensitat de l'acceleració SRP que, al seu torn, és una funció dels principals paràmetres de la vela, com ara la relació àrea-massa de la nau espacial, la seva reflectivitat i l'orientació de la superfície de la vela respecte de la direcció del Sol.

El principal tema d'aquesta tesi és l'estudi del moviment d'una nau espacial proveïda d'una vela solar. Es proposa una estratègia per realitzar maniobres impulsives canviant els paràmetres de la vela. El mètode s'aplica al disseny de missions espacials, incloent-hi transferències heteroclíniques entre òrbites, estratègies per evitar regions de moviment prohibides i el manteniment en estació de la nau.

Els principals resultats nous obtinguts en aquest treball són els següents:

1. Càlcul dels punts de libració artificial en funció dels paràmetres de la vela solar (angle del con α, angle del rellotge δ i nombre de lleugeresa β).

   La SRP és una acceleració repulsiva addicional a la del CR3BP, en consequència els punts d'equilibri CR3BP (L_1, L_2, ..., L_5) es desplacen de les seves posicions

en el CR3BP. En un sistema de referència giratori, els nous punts SL_1, SL_2, ..., SL_5 corresponen a posicions on les forces gravitatòries, centrífugues i degudes a la SRP estan equilibrades. Aquests punts es poden representar com a funcions dels paràmetres de vela α, δ i β. Cal tenir en compte que la distribució dels punts de libració artificial depèn fortament del paràmetre β.

2. Determinació i ajust dels paràmetres de la vela solar per al càlcul de maniobres impulsives i la seva aplicació a transferències heteroclíniques entre òrbites de Lissajous. Anàlisi de sensibilitat dels paràmetres de les maniobres de transferència orbital.

   El procediment per a fer maniobres amb veles solars és conceptualment diferent del de les maniobres de control clàssiques, que es basen només en canvis impulsius de la velocitat. Les òrbites de les veles solars són contínues tant en posició com en velocitat en un camp vectorial variable, la qual cosa obre la possibilitat de l'existència de connexions heteroclíniques canviant el camp vectorial mitjançant una maniobra de la vela. A partir d'una anàlisi acurada de la geometria de l'espai de fases de les equacions lineals de moviment al voltant dels punts d'equilibri, els punts clau són la identificació dels principals paràmetres dinàmics i la representació de les solucions mitjançant les variables d'acció-angle. S'han identificat les propietats dinàmiques bàsiques de les famílies de connexions, presentant de forma sistemàtica noves opcions per a l'anàlisi de missió al voltant dels punts de libració i, mitjançant aquest mètode, poder determinar les maniobres adients.

   A partir del mètode proposat per fer maniobres, s'ha dut a terme un estudi exhaustiu dels següents problemes: (1) Determinació d'una maniobra d'un sol impuls tal que dues naus espacials amb diferents fases inicials arribin a la mateixa òrbita de Lissajous final. (2) Fixant els paràmetres inicials i finals de la vela solar, determinació d'una estratègia de transferència mitjançant maniobres amb multiimpuls. (3) Determinació de maniobres amb multiimpuls per fer salts d'anada i tornada entre òrbites inicials i finals fixades al voltant d'un punt de libració artificial.

3. Evitar zones prohibides mitjançant maniobres d'impuls.

   Al voltant de l'eix Sol-Terra, hi ha una zona semblant a un cilindre on la radiació electromagnètica solar és especialment forta. El punt de libració L_1 es troba sobre aquest eix i entre els dos cossos celestes. L'ombra de la Terra a la regió al voltant de L_2 també pot impedir que una nau espacial obtingui energia solar i la vela SRP. Tots dos problemes es poden modelar definint una zona prohibida, o d'exclusió, al pla YZ (al voltant del punt de libració), que no s'ha de creuar. Per simplificar, visualitzar i evitar el moviment en les zones prohibides, aquesta tesi projecta les zones prohibides, així com l'òrbita de transferència heteroclínica tridimensional, en l'anomenat pla de fases efectiu (EPP), que té dimensió dos. Això ajuda a determinar l'existència de la zona prohibida i la seva distància relativa a la nau espacial. En el mètode proposat per fer maniobres, les zones prohibides a l'EPP poden canviar variant els paràmetres finals de la vela solar. Les zones prohibides fins i tot poden "desaparèixer", el que significa que després de la maniobra d'impuls, la nau espacial mai més tornarà a creuar-les.

4. Estacionament d'una vela solar que es mou al llarg d'una òrbita de Lissajous.

El procediment de manteniment de l'estació dissenyat realitza una maniobra periòdicament per evitar que la nau espacial s'escapi d'una determinada òrbita de Lissajous seguint la seva varietat inestable. La maniobra es calcula de manera que anul · li el component inestable de l'estat. En les simulacions fetes, se suposa que hi ha un error aleatori en l'execució de la maniobra. Si es fan maniobres cada mes, mostrem que la nau pot romandre a prop dels punts de libració artificial durant, almenys, cinc anys, cosa que demostra que el manteniment de l'estació utilitzant reorientacions de veles és efectiu.

Contents

List of Figures

List of Tables

List of Acronyms

2D Two Dimensional

3D Three Dimensional

ACE Advanced Composition Explorer

ARTEMIS Acceleration, Reconnection, Turbulence and Electrodynamics of the Moon's Interaction with the Sun

AU Astronomical Unit

CNSA China National Space Administration

CR3BP Circular Restricted Three Body Problem

EM Earth–Moon System

ERTBP Elliptic Restricted Three Body Problem

EPP Effective phase plane

ESA European Space Agency

HSP Hamiltonian-structure Preserving

IKAROS Interplanetary Kite-craft Accelerated by Radiation Of the Sun

IPS InterPlanetary Superhighway

ISEE-3 International Sun-Earth Explorer 3

JAXA Japan Aerospace Exploration Agency

JWST James Webb Space Telescope

LPO Libration Point Orbit

MAP Microwave Anisotropy Probe

NASA National Aeronautics and Space Administration

NDO Nonlinear Disturbance Observer

NOAA National Oceanic and Atmospheric Administration

QBCP Quasi-Bicircular Problem

RCD Reflectivity Control Device

RTBP Restricted Three Body Problem

SE Sun–Earth System

SOHO Solar and Heliospheric Observatory

SRP Solar Radiation Pressure

SRP-RTBP solar Radiation Pressure Restricted Three-Body Problem

1

Chapter 1
Introduction

1.1 Motivation

In 1957, with the launch of the first satellite of the Soviet Sputnik program, space exploration began. For years, space exploration has been dominated by vehicles propelled either by the acceleration and expulsion of gas from a gas-dynamic nozzle, as in the case of solid or liquid propellant rockets, or by the acceleration of ionized particles, as in the case of electric propellers. Solar sailing is a revolutionary way of propelling a spacecraft through space. The idea is to utilize solar radiation pressure (SRP) to produce momentum. A solar sail spacecraft has large reflective sail that captures the momentum of light from the Sun and use that momentum to push the spacecraft forward. Light is made up of particles called photons, which do not have any mass, but as they travel through space they do have momentum. When light photons hit a sail, their momentum is transferred to the sail, giving it a small push (incident force). They also bounce off the sail, giving it another small push (reaction force), as shown in Fig. 1.1 [1]. Both pushes are very slight and much smaller than that from a "traditional" thruster. However, SRP acts continuously, allowing a spacecraft to accelerate in the vacuum of space.

Mariner 10 [5], launched in 1973, was the first spacecraft to use SRP. It demonstrated for the first time the use of solar radiation pressure only as a method for attitude control (not for propulsion). The Cosmos 1 mission [6], which was led by the Planetary Society and Cosmos Studios, aimed to test the deployment of a solar sail. Its altitude was to be increased through solar sailing, and any measurable increase in the orbit of the spacecraft would have been considered a success, however, Cosmos 1 failed because of

rocket failure [7]. In August 2008, the NanoSail-D mission [8] aimed to deploy a sail, and test the effect of atmospheric drag on the sail. This program was led by the National Aeronautics and Space Administration (NASA), however, it was lost in a launch failure.

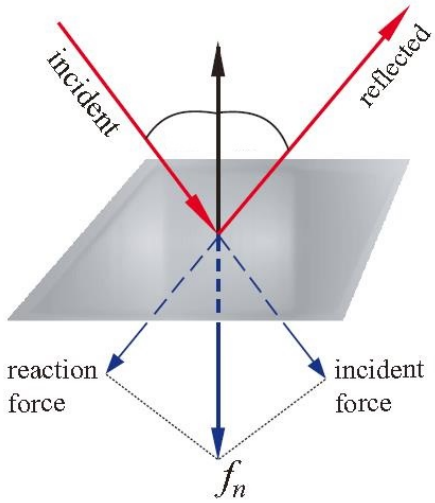

Figure 1.1: Forces exerted and produced on a perfectly reflecting surface.

Several solar sail spacecraft have already been successfully deployed. Japan Aerospace Exploration Agency (JAXA) launched on May 21, 2010, IKAROS [9, 10] that was the world's first deep-space solar sail demonstration spacecraft. IKAROS, shown in Fig. 1.2(a), is an interstellar kite-craft accelerated by SRP. The objectives of the IKAROS mission [11] were the following: deploy a solar sail in space, generate solar power with thin-film solar cells attached to the sail, verify SRP on the solar sail, and demonstrate the guidance and navigation technique for solar sailing.

NASA's NanoSail-D2 [12, 13], shown in Fig. 1.2(b), demonstrated the deployment of a small square sail in low-Earth orbit. The experiment was significant in displaying the de-orbiting capability of such a sail configuration [12, 14].

The LightSail 2 mission, see Fig. 1.2(c), is the culmination of a decade-long program, sponsored by the Planetary Society, to advance solar sailing. LightSail 2, integrated with Prox-1 carrier spacecraft, was launched on June 25, 2019, and deployed into an orbital altitude of over 720 km, a much higher low-Earth orbit than the one of LightSail 1 [15, 16]. The objective of LightSail 2 was to demonstrate controlled solar sailing in Earth orbit using a CubeSat platform. By controlling the orientation of the sail relative to the Sun after deployment, the orbit apogee and the orbital energy can be increased.

Solar sails have a wide new range of possible mission applications that cannot be achieved by conventional spacecraft [4]. First, the source of energy is unlimited, so solar sails can be used for long-term missions, like the ones for deep-space exploration [17, 18]. Within the Solar System, sunlight continuously pushes on the sail, accelerating the spacecraft

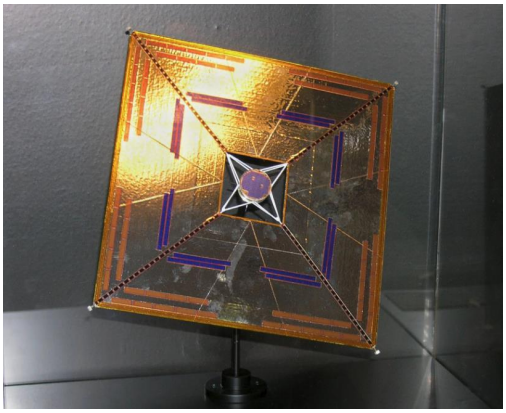

(a) IKAROS

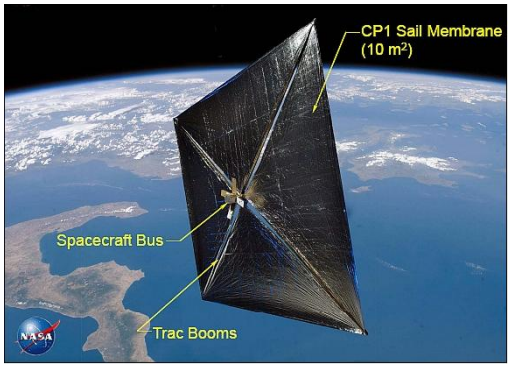

(b) NanoSail-D2

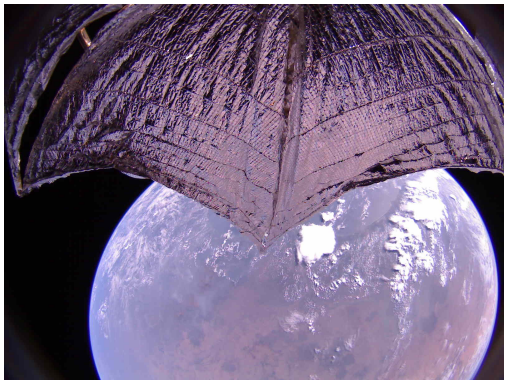

(c) LightSail 2

Figure 1.2: Demonstration solar sailing missions.

throughout its entire voyage, thus, a spacecraft could reach speeds that would be practically impossible for chemical rockets to achieve [19, 20]. This has been demonstrated in several studies [21, 22]. Second, solar sailing spacecraft can be placed in completely new orbits by using the sail acceleration as a balancing force to counteract the gravitational attraction of the Earth or any other planet [23]. For example, the Geostorm Warning Mission [24] is a National Ocean and Atmospheric Administration (NOAA) program with the objective of providing warnings of solar storms using a satellite positioned at an unnatural station that is closer to the Earth than would otherwise be possible [25].

Using the Sun–Earth system as basic reference model, this dissertation analyzes impulse maneuvers for a solar sail spacecraft in a SRP-perturbed restricted three-body problem (RTBP) model, moving in regions around the artificial libration point SL_2. The resulting analysis and results also apply to the SL_1 artificial libration point.

1.2 State of the art

1.2.1 Artificial libration points for solar sail spacecraft

The acceleration due to SRP acts on all objects exposed to it. The electromagnetic radiation impinging on a body can be absorbed, transmitted, or reflected; at one astronomical unit (1 AU), SRP is about 9.12×10^{-6} N/m^2. SRP is hardly noticeable on Earth because the force it exerts on an object is, relatively, very small [26]. However, for space missions, SRP can have a significant impact on the trajectory of the spacecraft [27].

Table 1.1 [4] summarizes the history of some of the main discoveries related to SRP. In relation with its effects on the motion of a spacecraft, Shapiro [28] and Musen [29] first observed its effects on a spacecraft moving along geocentric orbits. In a low-Earth environment, the most common effect of SRP is the long-term oscillations of the eccentricity and the orbital inclination, and, in fact, it can exceed the influence of the atmospheric drag when the orbital altitude is greater than 800 km [30, 31]. The oscillation period depends on the area-to-mass ratio of the satellite [32]. Nevertheless, SRP will cause all orbital elements to change periodically. When taking SRP into account, the traditional RTBP becomes a solar radiation pressure restricted three-body problem (SRP-RTBP).

Table 1.1: History of discoveries related to SRP.

Year	Author	Research Topics
1600		Corpuscular theory of light
1619	J. Kepler	Comet tails study
1744	L. Euler	Wave theory of light
1754	J.-J. D. de Marian and C. F. C. du Fay	Measurement of SRP
1785	C.-A. de Coulomb	Electrostatic experiments
1812	W. W. M. Olbers	Demonstration that the Sun has an electrical charge
1873	J. C. Maxwell	Theory of electromagnetism radiation
1876	A. Bartoli	Existence of SRP: second law of thermodynamics
1900	P. Lebedew	Experimentally demonstration of Maxwell's theory

Introducing in the usual RTBP differential equations a small additional acceleration, such as the one due to SRP, can produce new equilibrium points, which are usually called artificial libration points [33]. Unlike a the libration points of the RTBP, an artificial libration point is produced by an external thrust to counteract the imbalance of the gravitational attraction between the Sun and the Earth, this corresponds to a velocity increment of about 900 m/s per year [34].

The use of artificial libration points has been suggested and studied for some missions [35]. Observations of coronal mass ejections done from SL_1, which is closer to the Sun than the L_1 point, allow more time to perform safety operations of low-Earth satellites and ground equipment [36]. Cui Hutao et al. [37] built an attitude dynamics model, based

on the Lagrangian equations, for a complex multibody solar sail spacecraft located at these artificial equilibrium points. They verified its feasibility and found that it has advantages including fuel savings, a reduction in mass, and better performance. Bin et al. [38] developed a model of a solar sail and calculated its controllability at five artificial libration points in the Sun–Earth system. Artificial libration points have greatly enriched the potential of the RTBP and made actual mission designs more flexible.

In the SRP-RTBP model, the distribution of artificial libration points depends on the solar sail parameters (cone angle α, clock angle δ, and lightness number β). McInnes et al. [39] studied the family of artificial libration points in the Sun–Earth and Earth–Moon systems. They discussed the possibility of applying these points in engineering tasks [40]. Subsequently, McInnes [41] showed that the lightness number has a great influence on the feasible region for a family of artificial libration points. An analysis of the dynamic characteristics of artificial libration points found that there are (quasi-)periodic libration point orbits (LPOs) near an artificial libration point. These are similar to halo and Lissajous orbits. McInnes [42] obtained halo orbits near artificial libration points on the Sun–Earth line with a numerical method. When an artificial libration point is on the line between the Sun and the Earth, it is like there has been a change in the mass of the Sun, which is similar to the traditional Sun–Earth RTBP. Based on a Lindstedt–Poincaré perturbation analysis, Baoyin and McInnes [43] derived an approximate third-order analytical solution for a halo orbit around an artificial libration point. Taking the Sun–Earth system as an example, Waters et al. [44] constructed a high-order solution of a large-amplitude periodic orbit near an artificial libration point in the plane. They obtained a class of periodic orbits with special application. These can be used for long-term observations of the polar regions of the Earth. Gong et al. [45] studied the application of invariant manifolds near artificial libration points in the design of low-energy transfer orbits to solve the Hill problem with a solar sail.

Using dynamical system tools for the computation of the central manifold around the collinear points SL_1 and SL_2, Farrés [7] computed and described the complete phase space structure in a large neighbourhood around these two points. This study enlarged the results obtained by Howell [46], Gómez et al. [47], Andreu [48], and Aliasi [49] that systematically studied the distribution and dynamics of libration points in the Sun–Earth and Earth–Moon systems as a non-perturbed RTBP. Other contributions to the SRP-RTBP and additional perturbed RTBP models are the following: McInnes [42] computed Lissajous orbits near an artificial libration point on the Sun–Earth line; Waters et al. [44] calculated the halo orbits around artificial libration points that were not in specific regions of the Sun–Earth line; Simo et al. [50] proposed a method for approximately finding artificial libration points in the Earth–Moon RTBP; Xiao et al. [51] analyzed the advantages of using artificial libration points in the RTBP and applied the approach to deep-space exploration; Baig [52] and Ishimura [53] discussed artificial libration points for a hybrid propulsion probe; Shuang et al. [54] found an artificial libration point near an irregular asteroid; Yao et al. [55] discussed the distribution of artificial libration points for incompletely reflective solar sails; Grótte et al. [56] studied artificial libration points for RTBPs comprising the Sun, a small celestial body, and a solar sail spacecraft, but the solutions were unstable; Almeida et al. [57] identified artificial libration points under the combined action of SRP and other disturbances, and analyzed the motion of a spacecraft around

these points. In terms of practical engineering applications, Wu et al. [58] proposed, after some simulation experiments, a method for determining the orbit of an autonomous satellite around artificial libration points; Pan et al. [59,60] thoroughly studied the deployment of navigation constellations in orbits near artificial libration points; Wang et al. [61] discussed spacecraft formation flying in orbits near the artificial libration point SL_2 in the Sun–Earth system; Lazzara et al. [62] analyzed potential applications of artificial libration points in polar meteorology, environmental remote sensing, communications, and space weather monitoring.

There have been relatively few studies on orbits for spacecraft around the Sun–Earth L_3, because the Sun would hinder direct communications between the spacecraft and the Earth. In this context, and selecting an appropriate orientation and lightness number for the solar sail, Almeida [63] and Marchesin [64] improved the communications possibilities between a spacecraft and the Earth.

1.2.2 Libration point orbits and heteroclinic transfer orbits

Orbits near the libration points L_1 and L_2 open up new possibilities for future deep-space exploration and other missions [43,65,66]. Spacecraft are usually deployed in periodic and quasiperiodic orbits (LPOs) near these points [67,68] instead of at exactly the libration points. If a spacecraft wants to maintain its position at the $L_{1,2}$ libration point, it will have to consume important amounts of propellant, which increases the overall mission cost and runs against the mission goal of saving fuel. In addition, communications are complex on the Sun–Earth line [69]. An orbit near the libration point L_1 is often used for observing solar activity [70]; orbits near L_2 have wide observation angles and ideal lighting conditions, and benefit from the magnetic, thermal, and mechanical environments near this point. Furthermore, such orbits are suitable for non-cryogenic space telescopes [71], and for assembling spacecraft that can make high-resolution observations [72]. For example, the James Webb Space Telescope (JWST), launched on December 25, 2021, is deployed at the Sun–Earth L_2 point [73].

Farquhar [74] was the first to propose using the libration points of the Earth–Moon system for space missions. After the success of the ISEE-3 mission in 1978, space agencies in various countries began to research LPOs. Classical LPO missions include SOHO (which observed the outer solar corona of the Sun) [75], Gaia [which built a three-dimensional (3D) map of the galaxy] [76], LISA Pathfinder (which observed gravitational waves) [77], and JWST (which is making astronomical measurements) [78].

Orbits near a libration point can be used in multiple missions, such as spacecraft orbit transfer, i.e. Genesis, Wind, etc. Using an LPO enhances low-energy signal transmission. These orbits can also be used for accessing Solar System satellites [79]. The QueQiao relay satellite of Chang'e-4 was in an Earth–Moon periodic orbit at L_2 [80–82]. Table 1.2 [83] lists some missions in space orbit near a libration point. Most are in the Sun–Earth system (SE), and a few are in the Earth–Moon system (EM).

Table 1.2: Spacecraft missions at libration point orbits.

Mission	Agency	Launch date	Libration point	Orbit type
ISEE-3 [84]	NASA/ESA	1978	SE L_1	Halo
Wind [85]	NASA	1994	SE L_1	Quasi-Halo
SOHO [86]	ESA/NASA	1995	SE L_1	Halo
ACE [87]	NASA	1997	SE L_1	Lissajous
WMAP [88]	NASA	2001	SE L_2	Lissajous
Genesis [89]	NASA	2001	SE L_1	Quasi-Halo
ARTEMIS [90]	NASA	2007	EM L_1	Quasi-Halo
Herchel [91]	ESA/NASA	2009	SE L_2	Halo
Planck [92]	ESA	2009	SE L_2	Lissajous
Chang'e 2 [93, 94]	CNSA	2010	SE L_2	Lissajous
Gaia [95]	ESA	2013	SE L_2	Lissajous
Chang'e 5-T1 [96]	CNSA	2014	EM L_2	Lissajous
DSCOVR [97]	NASA/NOAA	2015	SE L_1	Lissajous
LISA Pathfinder [98]	ESA	2015	SE L_1	Quasi-halo
Queqiao [99]	CNSA	2018	EM L_2	Halo
Spektr-RG [100]	Roscosmos	2019	SE L_2	Lissajous
Chang'e 5 [96]	CNSA	2021	SE L_1	Lissajous

Spacecraft in LPOs lie in a highly perturbed environment due to the hyperbolic nature of the collinear equilibrium points (Section 2.2) [101, 102]. Thus, the stable and the unstable invariant manifolds associated with LPOs enhance transfer trajectories within the Solar System [103, 104].

The unstable and stable manifolds of LPOs are of great significance for transfer missions as they reduce fuel consumption. For example, in the Sun–Earth system, the invariant manifolds of the L_1 and L_2 points extend to the vicinity of the Earth, so that near-Earth spacecraft can use an invariant manifold to travel back and forth between the Earth and the LPO. In addition, invariant manifolds in different RTBPs can be spliced together to form an interstellar highway in a heliocentric system [79]. Conley [105] proved the existence of low-energy transfer orbits, which require less fuel than a traditional Hohmann transfer. Transfers between unstable orbits of the Solar System are possible due to the intersection of the invariant manifolds. These interactions are called homoclinic and heteroclinic connections [106, 107] (Fig. 1.3 [2]).

Homoclinic orbits are the result of an intersection between stable and unstable manifolds with the same libration point or periodic orbit [2, 105, 108]. Therefore, a spacecraft can start from an unstable manifold, move along a homoclinic orbit, and reach an LPO through the stable manifold [109]. A heteroclinic orbit is the intersection of a stable manifold and an unstable manifold belonging to two different LPOs [110]. For example, a spacecraft can leave the L_1 LPO through its unstable manifold and enter the L_2 LPO through its stable manifold. Heteroclinic orbit transfers are often used in deep-space exploration missions. The Artemis spacecraft used heteroclinic transfers from the Earth–Moon L_2 LPO to the

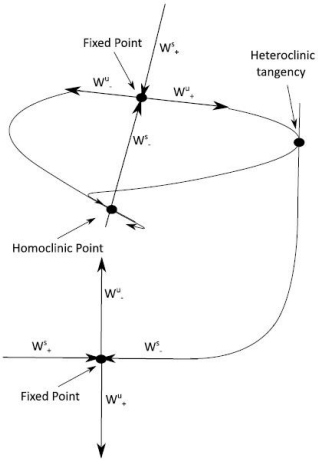

Figure 1.3: Schematic example of a homoclinic point and heteroclinic tangency.

L_1 point, as is shown in Fig. 1.4 [3].

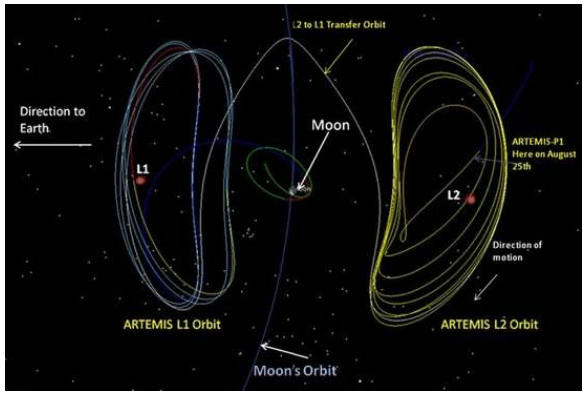

Figure 1.4: Schematic diagram of the Artemis mission orbit.

Canalias [69] designed transfer trajectories between Lissajous orbits to avoid forbidden zones due to eclise regions. This approach was combined with the introduction of the effective phase plane (EPP) concept. The designed impulsive maneuvers aimed to cancel out the unstable manifold of the target orbit by using the EPP. A similar phase plane method, that relied on SRP and J_2 around the Earth, was used by Lucking [111] and Colombo et al. [112], however, in these studies, the influence of solar sail parameters on the position of the libration point was not considered.

For transfers enhanced by SRP, Farrés and Jorba [113] proposed to use invariant manifolds to realize a transfer from libration point $SL_{1,2}$ to $SL_{4,5}$. The effect of SRP on the position of the libration point was acurately computed. Thus, a spacecraft injected into the unstable manifold of SL_1 reached the stable manifold of SL_4 when an SRP maneuver was

performed. Based on solar sail dynamics in the Sun–Earth RTBP, Sood and Howell [114] studied stable and unstable manifolds for the libration points L_1 and L_2, respectively. A spacecraft finally reached the artificial SL_5 orbit but had to use an impulse engine to accelerate. Perera et al. [115] realized a transfer from a halo orbit around a traditional libration point L_1 to a halo orbit around an artificial libration point SL_1 for a CubeSat spacecraft propelled by a solar sail. Heiligers et al. [116] proposed a complete orbit design from launch, transfer, and orbit maintenance for a solar sail spacecraft for polar observation. Pezent et al. [117] used SRP, an artificial libration point transfer, and sail maneuvers to reach areas that cannot be reached by traditional propulsion systems or require a large amount of propellant. Fernandez [118] designed a variety of algorithms that allow a solar sail spacecraft to transition from a low-Earth orbit to a Sun–Earth SL_5 regional orbit. They realized rapid transfers of between 391 and 1194 days. Farrés [119] and Soldini [120] designed transfer trajectories between Lissajous orbits using different artificial libration points SL_2 in a 2D model.There has been limited work on harnessing SRP to enhance transfer trajectories within the Sun–Earth system. In most studies, the SRP was considered to be a perturbation term. In this thesis, we investigate propellant-free transfer trajectories between LPOs around 3D collinear equilibrium points using solar sailing.

1.2.3 Station-keeping by solar sail spacecraft

Due to their instability, a spacecraft placed around the L_1 and L_2 libration points will naturally deviate from its original orbit. Thus, trajectories designed in RTBP require the spacecraft to perform maneuvers to counteract the unwanted environmental instabilities and maintain its nominal trajectory [101, 121]. SRP is the most common cause of such deviations from the original nominal orbit in the Solar System. Over time, it can have a great impact on spacecraft, especially those with a high surface-to-mass ratio and high light-pressure parameters, such as the JWST [122].

In 1993, Howell [123] used the target point technique to keep a spacecraft near its nominal trajectory with impulse maneuvers. Then, McInnes [39] and Keeter [124] considered this method and included the SRP to study how to make the spacecraft remain stable in a LPO by changing its sail orientation. Luo [125] also used the sail orientation as the control input to maintain its position. Farrés and Jorba [126–129] used Floquét modes [130, 131] to design a control law about an artificial equilibrium point. In this method, the solar sail spacecraft escapes following an unstable manifold. Then, the orientation of the solar sail is changed to bring the trajectory back to the target point [101] killing unstable components. Baoyin et al. [132] considered using SRP to offset the nonlinear part of the three-body dynamics of the solar sail. They studied the stability and maneuverability of the controlled orbit by taking the orientation and surface-to-mass ratio of the sail as control variables. These studies focused on sail orientation for fixed lightness number. However, the larger the sail surface, the more difficult it is to adjust its orientation. Moreover, frequent adjustments of the orientation can cause vibrations and reduce the service life of the solar sail.

Xu [133] were the first to use Hamiltonian-structure preserving control [134] with the SRP. The lightness number and orientation were the control parameters. Based on Hamiltonian-

structure preserving control, Soldini et al. [135] proposed a variable-structure solar sail model. The surface area of the sail was a third control variable. Bookless [136] was the first to use a linear quadratic regulator to achieve LPO control, using either the lightness number or the orientation. A linear quadratic regulator is an optimal method where the degree of control is proportional to the state error; Ceriotti [137] used a linear quadratic regulator for station-keeping of a solar sail in high-amplitude vertical Lyapunov orbits. The control vector was a function of the sail orientation and its area-to-mass ratio. Perera et al. [115] used a linear quadratic regulator for a CubeSat controlled by a solar sail. It was able to maintain its orbit despite the gravitational disturbance of Mercury, Venus, or Jupiter.

Gong et al. [138] proposed a solar sail model with variable reflectivity and designed an artificial LPO-keeping controller. In this model, part of the surface of the solar sail is covered with an electrochromic sheet, which acts as a reflective control device. The overall reflectivity of the sail can be adjusted by energizing and de-energizing different parts of the reflective control device. This is a simple and easy way to control a solar sail and is in addition to adjusting its orientation. It solves the underactuation in controlling the orbit of a solar sail, but it is difficult to apply in practice. Zhu [139] and Zhang [140] followed this model, and designed an active disturbance-rejection controller with an artificial LPO for a solar sail. For lunar exploration, it is necessary to establish continuous communication with the far side of the Moon; Tamakoshi et al. [141] designed an artificial halo orbit near the Earth–Moon L_2 artificial libration point. They used a reflective control device to achieve orbit station-keeping. To realize orbit station-keeping, Lou [142] solved the underdrive problem of traditional solar sail control in two different ways, using a light pressure model or a hybrid solar sail thrust model. For a halo orbit in the direction of the Sun sail, Qin Jianfei et al. [143] designed an orientation control strategy so that the spacecraft can successfully enter the invariant manifold of a halo orbit. For a Sun–Earth (or Moon) model, Niccolai et al. [144] studied how to stabilize an orbit near a collinear artificial libration point by properly adjusting the solar sail parameters and the thrust vector direction. In elliptical RTBP, Guzzetti et al. [145] studied orbit station-keeping near the L_4 region for a solar sail spacecraft.

Compared to continuous control techniques, impulsive ones are more mature and straightforward to apply. Therefore, all LPO missions have adopted impulsive schemes to achieve station-keeping. Moreover, the insights provided by dynamic systems theory have been very useful in increasing our understanding of the geometry of the controllers [146]. In this thesis, we propose a multi-impulse strategy to achieve station-keeping by a spacecraft. The main idea is that the spacecraft periodically performs a maneuver to prevent it from escaping from the neighborhood of a nominal Lissajous orbit along its unstable manifold. Thus, the maneuver is computed so that it cancels out the unstable component of the state. Moreover, it is assumed that there are random errors in the execution of the maneuvers.

1.3 Structure and contributions of the thesis

The main focus of the thesis is the design of impulse maneuvers for a solar sail spacecraft in the SRP-RTBP. The remaining six chapters of this dissertation are briefly described below.

- Chapter 2 studies the artificial libration points of the SRP-RTBP. The first part describes the notation and introduces the dynamic models, namely RTBP and SRP-RTBP. The second part systemically studies artificial libration points, and the influence of the solar sail parameters on the position of these points. The main solar sail parameters are the orientation (cone angle α and clock angle δ) and the lightness number (β).

- Chapter 3 investigates enhanced heteroclinic connections between Lissajous LPOs based on instantaneous impulse maneuvers using a solar sail. A careful analysis of the geometry of the phase space of the linearized equations of motion around the equilibrium points is done. The role of the main parameters is identified. Solutions are represented in terms of action-angle variables. Furthermore, a general study of all possible transfers between Lissajous orbits by changing the three main parameters (α, δ, and β) is also performed. In a SRP reorientation maneuver, the location of an artificial libration point is translated and, consequently, also the reference frame attached to it. A SRP reorientation maneuver is seen as a jump of the relative position instead of a jump in velocity. Thus, this chapter systematically analyzes the impact of a maneuver on a satellite following a libration point nominal trajectory. Using maneuvers that do not introduce unstable components in the modes of motion (which would lead to a divergence from the libration zone), we obtain enhanced heteroclinic connections between Lissajous orbits.

- Chapter 4 describes the extended research done about heteroclinic transfers of a solar sail spacecraft. The chapter has three parts: (1) With the clock angle $\delta = \pi/2$ and initial phase $\phi_1 = 0$ fixed, it is found that if two spacecraft depart from different initial phases ϕ_2, such as $\phi_2 = 0$ or $\phi_2 = \pi$, they can reach the same final Lissajous orbit with a single-impulse maneuver. This conclusion has been verified by a large number of numerical simulations. (2) This chapter proposes a transfer strategy with a multi-impulse maneuver in which the initial and final solar sail parameters are fixed. For example, if the initial and final cone angles are $\alpha_i = 0$ and $\alpha_f = \pi/4$, then during the transfer, we introduce a middle transitional cone angle $\alpha_m = \pi/8$ to prevent the solar sail angle from changing too much. (3) It has also been found that a spacecraft can use multi-impulse maneuvers to make back-and-forth jumps between the initial and final artificial LPOs.

- Chapter 5 investigates the avoidance of forbidden zones using impulse maneuvers of the sail. Solar electromagnetic radiation and the Earth half-shadow can affect communications and power generation of a spacecraft at L_1 and L_2 LPOs. Both problems can be modeled by placing a forbidden or exclusion zone in the YZ plane (around the libration point), which should not be crossed. The chapter develops a

strategy, using the EPP, for avoiding forbidden zones based on impulse maneuvers. The EPP allows a simple geometric solution, not only of the eclipse avoidance problem itself but also when planning impulse maneuvers for transfers between Lissajous orbits. This chapter projects the 3D forbidden zone and the heteroclinic transfer orbit onto a 2-dimensional EPP. The results of many simulations, with different solar sail parameters, demonstrate that the area of the forbidden zones in the EPP will change after an impulse maneuver. Sometimes, the forbidden zone even disappears.

- Chapter 6 discusses propellant-free station-keeping of a solar sail around the Sun–Earth collinear equilibrium points. Due to the instability of the L_1 and L_2 libration points, a spacecraft placed around the libration points will naturally deviate from its original orbit, so trajectories designed in the SRP-RTBP require the spacecraft to perform maneuvers to maintain its trajectory by counteracting the unwanted environmental instabilities. In this thesis, we propose a multi-impulse strategy to achieve station-keeping. The spacecraft periodically performs maneuvers to prevent it from escaping from a Lissajous orbit following its unstable manifold. Random errors in the execution of the maneuvers are also considered. The results of many simulations demonstrate that station-keeping with multiple impulses by means of sail reorientation to control the unstable manifold component is effective.

- Chapter 7 highlights some useful conclusions and briefly discusses future work.

The main contributions of this thesis are the following:

- Based on research in artificial libration points in the SRP-RTBP, this thesis proposes an impulse maneuver that allows a solar sail spacecraft to achieve enhanced heteroclinic connections between Lissajous orbits. After an SRP reorientation maneuver, the location of the artificial libration point is translated, and so is the corresponding reference frame. A SRP reorientation maneuver is seen as a jump of the relative position instead of a jump of the velocity. The solar sail spacecraft follows an unstable manifold. Then the orientation of the solar sail is changed to bring the trajectory back to the stable manifold of the target LPO. For example, a spacecraft injected into the unstable manifold of the initial SL_2 can reach the stable manifold of SL_2' with an SRP maneuver. Note that the same final orientation may require different numbers of impulse maneuvers. For example, if $\alpha_i = 0$ and $\alpha_f = -0.45$, three impulse maneuvers are used to cancel out the unstable manifold of the target orbit.

- Using the impulse maneuver design, this thesis demonstrates the following: (1) Using a single-impulse maneuver, two spacecraft can arrive at the same final Lissajous orbit after starting with different initial phases. (2) A transfer strategy is proposed with a multi-impulse maneuver in which the initial and final solar sail parameters are fixed. (3) A spacecraft can use multi-impulse maneuvers to make back-and-forth jumps between the initial and final artificial LPOs.

- The impulse maneuver strategy is combined with the EPP method to design transfer trajectories between Lissajous orbits that avoid forbidden zones. The EPP method

projects the 3D heteroclinic transfer orbit and forbidden zones onto a 2D plane, which is more convenient and intuitive.

- Using periodic impulse maneuvers, a propellant-free station-keeping strategy is designed for a solar sail traveling around Sun–Earth collinear equilibrium points. The spacecraft periodically performs a maneuver to prevent it from escaping from the neighborhood of a Lissajous orbit along its unstable manifold. Thus, the maneuver is computed such that it cancels out the unstable component of the state. Moreover, it is assumed that there is a random error in executing the maneuvers. This method has been demonstrated to be reliable by a large number of simulations.

1.4 Published Work

The contributions aforementioned have been published in the following papers:

[1] **Duan X**, Gómez G, Masdemont J J, Yue X. A Picture of Solar-Sail Heteroclinic Enhanced Connections between Lissajous Libration Point Orbits[J]. Communications in Nonlinear Science and Numerical Simulation, 2020,85(7):1152–1184.

[2] **Duan X**, Gómez G, Masdemont J J, Yue X. Solar sail propellant-free transfer maneuvers between libration point orbits around the collinear equilibrium points[C]. 69th International Astronautical Congress, IAC 2018, Bremen, 2018:1-12.

[3] **Duan X**, Gómez G, Masdemont J J, Yue X. Propellant–free station–keeping design of a solar sail around the Sun–Earth collinear equilibrium points[C]. 73th International Astronautical Congress, IAC 2022, Paris, 2022:37-50.

[4] Gao Y, **Duan X**. Chang'e-5 probe completes on-orbit sample transfer[N]. Chinese Science Journal, 2020-12-07(1).

[5] **Duan X**, Gómez G, Masdemont J J, Yue X. Research on avoid forbidden zone for solar sail spacecraft based on effective phase plane[C]. The 7th National Aerospace Dynamics and Control, Shenyang, China, 2021.

The structure of the thesis is depicted in Fig. 1.5.

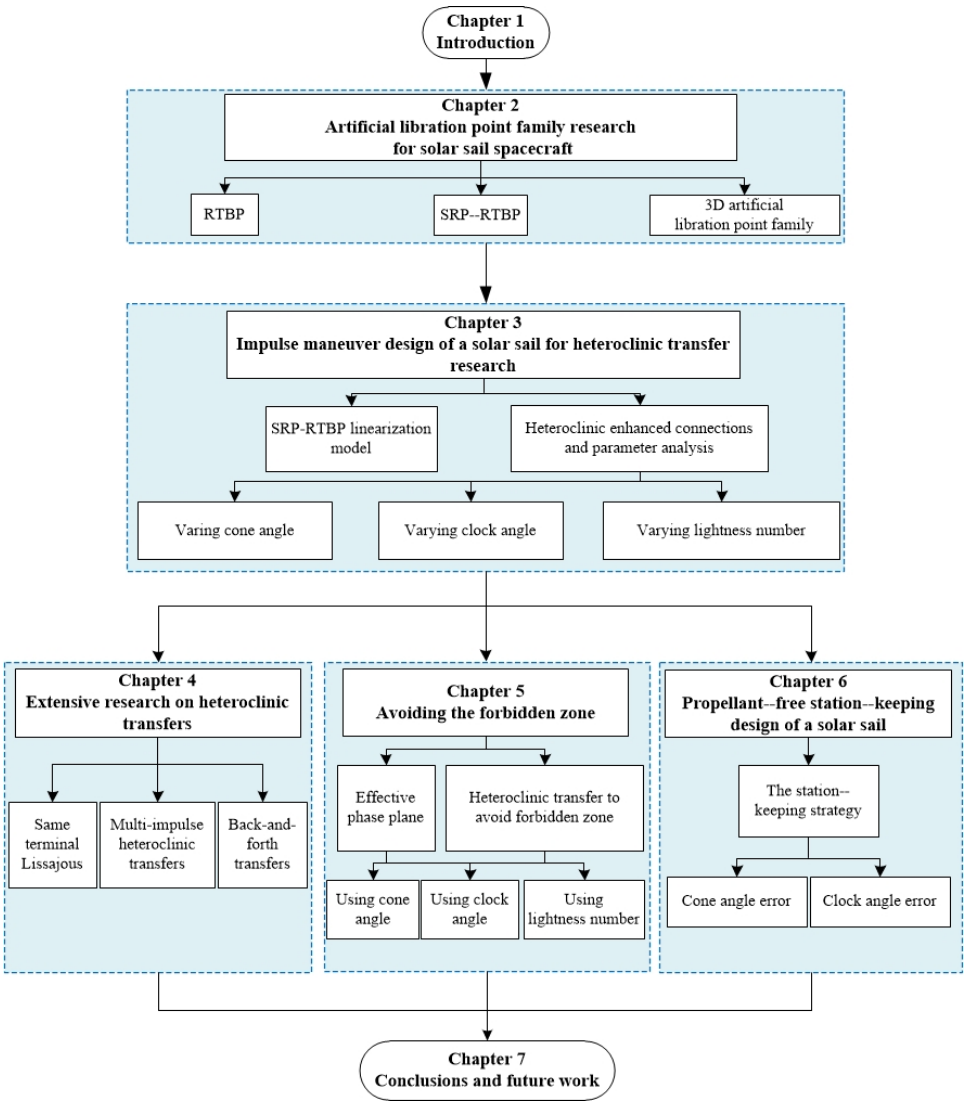

Figure 1.5: Structure of the thesis

2

Chapter 2

Artificial libration point family research for solar sail spacecraft

The application of solar sail technology is currently valued by space agencies of various countries and organizations. Although the magnitude of SRP is relatively small, when considering for instance the duration of deep–space exploration missions, its role cannot be ignored. Maxwell [147] first proposed in 1873 that the solar sail spacecraft could get solar radiation acceleration after being reflected by a solar sail surface. More than 100 years later, McInnes [42] studied the working principle of the solar sail in detail, and summarized a variety of solar sail dynamic models. In 2010, IKAROS [9] was the first pure solar sail spacecraft to complete a deep–space exploration mission. In 2019, LightSail–2 [16] used SRP to change its orbital height.

In the usual circular restricted three-body problem, there are five equilibrium points; for the SRP–RTBP model the equivalent of the libration points, also known as artificial libration points, are determined by the spatial position and the direction of the solar sail. The artificial libration points provide more flexibility for space mission applications, such as storm warning [148, 149]. A solar sail spacecraft located near the artificial Sun–Earth libration point SL_1 could provide early warnings of solar activity compared with the traditional spacecraft location, such as the one of SOHO.

In the first section of this chapter we introduce the RTBP and SRP–RTBP models. The second section is devoted to the research on the two-dimensional family of artificial

libration points. Finally, by changing the solar sail parameters (lightness number β, cone angle α, and clock angle δ), the three-dimensional artificial libration point families are computed and drawn, and the global distribution of artificial libration points under different parameters is analyzed in detail.

2.1 The Restricted Three–Body Problem

It is well known that the circular RTBP considers the motion of an infinitesimal small particle, the spacecraft, under the gravitational attraction of two bodies called primaries. The two primaries orbit around their common centre of mass in a circular way, and the gravitational attraction of the small particle on the two primaries is discarded. We consider the Sun and the Earth as the two primaries, while the small particle is a solar sail spacecraft, as shown in Fig. 2.1.

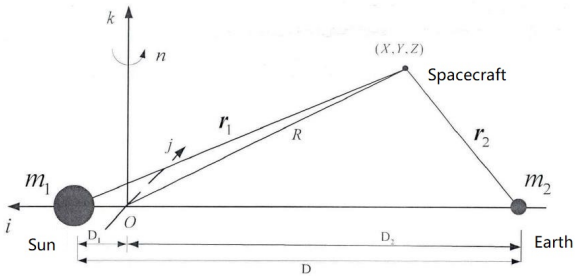

Figure 2.1: Schematic diagram of Sun–Earth RTBP reference system.

The origin O of the reference system considered is at the center of mass of the system, the i axis points in the direction from Earth to the Sun, the j axis is perpendicular to the orbital plane of the primaries, and the k axis completes the right-handed frame.

To simplify, we normalize the units of mass, distance, and time so that the total mass of the system is one, the Sun - Earth distance is one, and the period of their orbit is 2π. With these units, the gravitational constant G is also 1, this is

$$\begin{aligned} [M] &= m_1 + m_2 = 1, \\ [L] &= D = 1, \\ [T] &= \frac{1}{\sqrt{G(m_1+m_2)/D^3}} = 2\pi, \end{aligned}$$

where $[M]$, $[L]$ and $[T]$ represent the unit mass, the unit length, and the unit time, respectively, m_1 is the mass of the Sun, m_2 is the Earth mass, D is the Sun-Earth distance, and G is the gravitational constant. After normalization, the mass of the two primaries is

$$1-\mu = \frac{m_1}{m_1+m_2}, \qquad \mu = \frac{m_2}{m_1+m_2}.$$

In a rotating reference system, with the primeries fixed on the i-axis, and the above system of units, the equations of the RTBP are

$$\begin{aligned} \ddot{X} - 2\dot{Y} &= X - \frac{(1-\mu)(X+\mu)}{r_1^3} - \frac{\mu(X-1+\mu)}{r_2^3}, \\ \ddot{Y} + 2\dot{X} &= Y - \frac{(1-\mu)Y}{r_1^3} - \frac{\mu Y}{r_2^3}, \\ \ddot{Z} &= -\frac{(1-\mu)Z}{r_1^3} - \frac{\mu Z}{r_2^3}, \end{aligned} \tag{2.1}$$

where

$$r_1 = \sqrt{(X+\mu)^2 + Y^2 + Z^2}, \quad r_2 = \sqrt{(X-(1-\mu))^2 + Y^2 + Z^2},$$

Defining $\Omega(X,Y,Z) = \frac{1}{2}(X^2+Y^2) + \frac{(1-\mu)}{r_1} + \frac{\mu}{r_2} + \frac{1}{2}\mu(1-\mu)$, Eqs. (2.1) can be written as

$$\begin{aligned} \ddot{X} - 2\dot{Y} &= \frac{\partial \Omega}{\partial X}, \\ \ddot{Y} + 2\dot{X} &= \frac{\partial \Omega}{\partial Y}, \\ \ddot{Z} &= \frac{\partial \Omega}{\partial Z}. \end{aligned} \tag{2.2}$$

Equating to zero the right-hand side of the above differential equations, and solving the nonlinear system, five particular solutions can be obtained, which are called libration points or Lagrangian points. If the spacecraft stays at the libration point, where the gravitational force and centrifugal force are balanced, then

$$\begin{aligned} \dot{X} = \dot{Y} = \dot{Z} = 0, \\ \ddot{X} = \ddot{Y} = \ddot{Z} = 0. \end{aligned} \tag{2.3}$$

Combining Eqs. (2.3) and Eqs. (2.2), the five libration points (L_1,...,L_5) of the RTBP can be obtained. They are shown in Fig. 2.2 and in Table. 2.1. In the figure, L_1, L_2, and L_3 are on the Sun-Earth connection line, and they are called collinear libration points, while L_4 and L_5 are called triangular libration points. Denoting the position of a libration point L_i by (X_{Li}, Y_{Li}, Z_{Li}), and assuming that a small deviation from it is (x, y, z), we can write

$$\begin{aligned} X &= X_{Li} + x, \\ Y &= Y_{Li} + y, \\ Z &= Z_{Li} + z. \end{aligned} \tag{2.4}$$

Using Eqs. (2.4), and ignoring higher-order terms, the linearized equations around an equilibrium point can be written as

$$\begin{aligned} \ddot{x} - 2\dot{y} &= \Omega_{XX}x + \Omega_{XY}y + \Omega_{XZ}z, \\ \ddot{y} + 2\dot{x} &= \Omega_{YX}x + \Omega_{YY}y + \Omega_{YZ}z, \\ \ddot{z} &= \Omega_{ZX}x + \Omega_{ZY}y + \Omega_{ZZ}z, \end{aligned} \tag{2.5}$$

where Ω_{ij} are the second-order partial derivatives of Ω at the libration point L_i (further details are given in Appendix A).

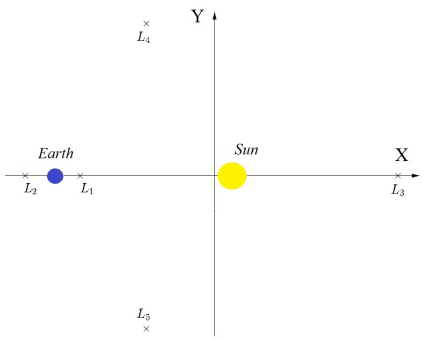

Figure 2.2: Schematic representation of the libration points in the Sun–Earth RTBP.

Table 2.1: Libration point coordinates in the RTBP.

libration point	X	Y	Z
L_1	-0.98999	0	0
L_2	-1.01008	0	0
L_3	1.00000	0	0
L_4	-0.50000	$\sqrt{3}/2$	0
L_5	-0.50000	$-\sqrt{3}/2$	0

Defining now $X{=}[x, y, z, \dot{x}, \dot{y}, \dot{z}]^T$, the linear equations Eqs. (2.5) can be written as

$$\ddot{X} = AX = \begin{bmatrix} 0_{3\times3} & I_3 \\ \Omega_{ij} & D \end{bmatrix} \begin{bmatrix} x \\ y \\ z \\ \dot{x} \\ \dot{y} \\ \dot{z} \end{bmatrix}, \tag{2.6}$$

In Eqs. (2.6), $0_{3\times3}$ denotes the zero 3×3 matrix, I_3 is the identity 3×3 matrix, and Ω_{ij} is the matrix of second partial derivatives of Ω, this is

$$\Omega_{ij} = \begin{bmatrix} \Omega_{XX} & \Omega_{XY} & \Omega_{XZ} \\ \Omega_{YX} & \Omega_{YY} & \Omega_{YZ} \\ \Omega_{ZX} & \Omega_{ZY} & \Omega_{ZZ} \end{bmatrix},$$

evaluated at the equilibrium point, while D is the matrix

$$D = \begin{bmatrix} 0 & 2 & 0 \\ -2 & 0 & 0 \\ 0 & 0 & 0 \end{bmatrix}.$$

Defining $C_0 := \dfrac{1-\mu}{r_1^3} + \dfrac{\mu}{r_2^3}$, again evaluated at the equilibrium point, it can be seen that

at the collinear libration points (L_1, L_2, L_3) we have

$$\begin{aligned} \Omega_{XX} &= 1 + 2\,C_0 > 0, \\ \Omega_{YY} &= 1 - C_0 < 0, \\ \Omega_{ZZ} &= -\,C_0 < 0. \end{aligned} \tag{2.7}$$

In the Eqs. (2.7), since $\Omega_{ZZ} < 0$, the characteristic polynomial associated to the linear differential equations has two pure imaginary roots, and since the motion in the (x, y) plane is uncoupled from the one in the z direction; note that the motion in this direction is a periodic oscillation. Then, Eqs. (2.5) reduce to

$$\begin{aligned} \ddot{x} &= \Omega_{XX}\, x + 2\dot{y}, \\ \ddot{y} &= \Omega_{YY}\, y - 2\dot{x}. \end{aligned}$$

The eigenvalues associated to this reduced system are

$$\lambda_{1,2} = \pm\sqrt{S_1}, \qquad \lambda_{3,4} = \pm\sqrt{|S_2|},$$

where

$$\begin{aligned} S_1 &= \frac{1}{2}[-(4 - \Omega_{XX} - \Omega_{YY}) + \sqrt{(4 - \Omega_{XX} - \Omega_{YY})^2 - 4\Omega_{XX}\Omega_{YY}}], \\ S_2 &= \frac{1}{2}[-(4 - \Omega_{XX} - \Omega_{YY}) - \sqrt{(4 - \Omega_{XX} - \Omega_{YY})^2 - 4\Omega_{XX}\Omega_{YY}}]. \end{aligned}$$

Thus $S_1 > 0$, $S_2 < 0$, and the six characteristic roots are

$$\lambda_{1,2} = \pm d_1, \qquad \lambda_{3,4} = \pm d_2\, i, \qquad \lambda_{5,6} = \pm d_3\, i,$$

where $i = \sqrt{-1}$, and

$$d_1 = \sqrt{\frac{\sqrt{(9{C_0}^2 - 8C_0)}}{2} - (1 - \frac{C_0}{2})}, \quad d_2 = \sqrt{\frac{\sqrt{(9{C_0}^2 - 8C_0)}}{2} + (1 - \frac{C_0}{2})} \quad d_3 = \sqrt{C_0}.$$

The diagonalized linear equations of motion about the collinear libration points are

$$\begin{aligned} \ddot{x} - 2\dot{y} + (1 + 2C_0)x &= 0, \\ \ddot{y} + 2\dot{x} - (1 - C_0)y &= 0, \\ \ddot{z} + C_0 z &= 0, \end{aligned} \tag{2.8}$$

and the solution of the Eqs. (2.8) can be written as

$$\begin{aligned} x &= A_1 e^{d_1 t} + A_2 e^{-d_1 t} + A_3 \cos(d_2 t) + A_4 \sin(d_2 t), \\ y &= k_1 A_1 e^{d_1 t} - k_1 A_2 e^{-d_1 t} - k_2 A_3 \sin(d_2 t) + k_2 A_4 \cos(d_2 t), \\ z &= A_5 \cos(d_3 t) + A_6 \sin(d_3 t). \end{aligned} \tag{2.9}$$

where the parameters k_1, k_2 are

$$k_1 = \frac{{d_1}^2 - 2C_0 - 1}{2d_1}, \qquad k_2 = \frac{{d_2}^2 + 2C_0 + 1}{2d_2}.$$

2.2 The effect of a solar sail in the RTBP

2.2.1 Solar radiation pressure

Sunlight produces a solar radiation pressure on accessible objects. The solar pressure P is usually expressed, by means of the energy flux W and the light speed c, as

$$P = \frac{W}{c}, \tag{2.10}$$

where the energy flux Wsatisfies

$$W = W_E \left(\frac{R_E}{r}\right)^2,$$

where

$$W_E = \frac{L_s}{4\pi {R_E}^2},$$

is the energy flux measured at the Earth's distance from the Sun, and its average value is $1368 J/m^2 s$, L_s is the solar luminosity, R_E=$1AU$ is the Sun–Earth distance, and and r is the distance from the sail to the Sun. Then, the solar radiation pressure at a distance of $1AU$ from the Sun is P=$4.56\times10^{-6} N/m^2$. For a fully perfectly reflecting sail, the observed pressure is theoretically twice this value.

2.2.2 The force on a Solar sail

Different SRP models have been proposed for a variety of mission applications, but the most popular is the one known as the cannonball model. This model describes how SRP would affect a cannonball like spherical object which has equally distributed optical properties. The solar sail acceleration is determined by two parameters: the area of the solar sail, and its orientation. The orientation is given by the normal direction $\mathbf{n}$ to the solar sail, as shown in Figure 2.3.

The force exerted by the incident photons, along the direction $\mathbf{r}_i$, on the sail surface is

$$\mathbf{F}_i = PA < \mathbf{r}_i, \mathbf{n} > \mathbf{r}_i,$$

where P is the solar radiation pressure, A is the area of the sail, and $< \cdot, \cdot >$ denotes the inner product. Similarly, the force produced by the reflected photons along the $-\mathbf{r}_r$ direction is

$$\mathbf{F}_r = -PA < \mathbf{r}_r, \mathbf{n} > \mathbf{r}_r.$$

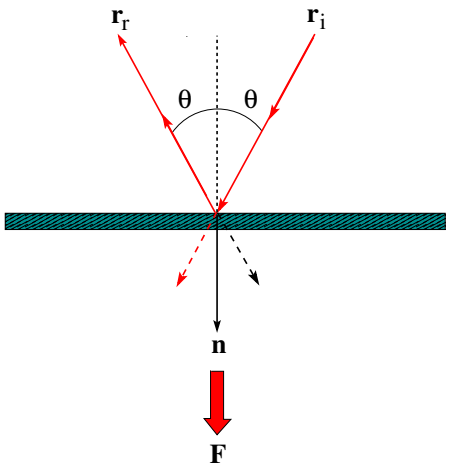

Figure 2.3: Schematic representation of the incident ($\mathbf{r}_i$) and reflected ($\mathbf{r}_r$) photons emitted by the Sun on the surface of a flat perfectly reflecting solar sail.

For a perfectly reflecting solar sail, the total force on the surface of the sail is

$$\mathbf{F}_{sail} = \mathbf{F}_i + \mathbf{F}_r = 2PA < \mathbf{r}_i, \mathbf{n} >^2 \mathbf{n}. \tag{2.11}$$

Combining Eqs. (2.10) and Eqs. (2.11), the total force can be written as

$$\mathbf{F}_{sail} = \frac{2AW_E{R_E}^2}{cr^2} PA < \mathbf{r}_i, \mathbf{n} >^2 \mathbf{n}. \tag{2.12}$$

The acceleration of the solar sail spacecraft can be written in terms of the gravitational acceleration as

$$\boldsymbol{a}^s = \beta \frac{Gm_{Sun}}{r^2} < \mathbf{r}, \mathbf{n} >^2 \mathbf{n}, \tag{2.13}$$

where G is the gravitational constant, and m_{Sun} is the mass of the Sun. The solar sail lightness number β is the ratio of the pressure acceleration generated by the solar radiation to the acceleration produced by solar gravity. If β=1, the solar radiation pressure is equal to the solar gravitational force; if $\beta > 1$, the solar radiation pressure is greater than the solar gravitational force. In practice, β is less than 1 and small. Its expression is given by

$$\beta = \frac{\sigma^*}{\sigma},$$
$$\sigma^* = \frac{L_S}{2\pi G M_S c} \approx 1.53 g/m^2,$$

where σ=m/A is known as the sail loading parameter, and is the ratio between the the spacecraft's mass m and the area of the solar sail A. The relation between the lightness number β, the sail loading parameter σ, and the acceleration a^s is given in Table 2.2.

Table 2.2: Relation between β, σ and a^s.

β	0.02	0.04	0.05	0.06	0.1	0.2
$\sigma(g/m^2)$	76.5	38.25	30.60	25.50	15.30	7.65
$a^s(mm/s^2)$	0.12	0.24	0.30	0.36	0.59	1.19

2.2.3 Solar sail orientation

The solar sail orientation is defined by the normal direction to the sail surface, which is usually represented by two angles. There are different ways to define the angles that define the attitude [150, 151], with explicit relations between them. In this thesis we have used the cone angle α and clock angle δ, that are displayed in Fig. 2.4.

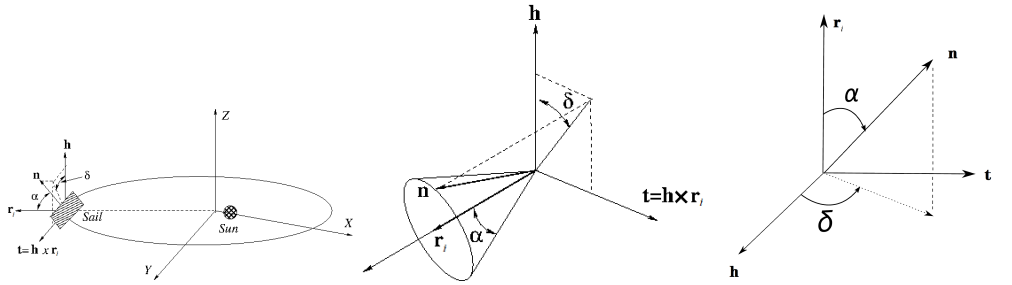

Figure 2.4: Schematic representation of the sail orientation angles $\alpha \in [-\pi/2, \pi/2]$ and $\delta \in [0, \pi]$

We consider the usual restricted three-body reference system with coordinates (X, Y, Z). Let $\mathbf{n}$ be the normal direction of the solar sail spacecraft, and ($\mathbf{r}_i$, $\mathbf{h}$, $\mathbf{t}$) the unitary vectors defining the solar sail spacecraft centered coordinate system, where $\mathbf{r}_i$ is the Sun-spacecraft direction, $\mathbf{h}$ is perpendicular to the orbital plane (so parallel to Z), and $\mathbf{t}$ completes the right-handed frame. As it has already been said, the normal direction $\mathbf{n}$ to the sail is determined by the solar sail cone angle α, and the clock angle δ. The cone angle α is the angle between the normal $\mathbf{n}$ and the incident ray $\mathbf{r}_i$, which measures the elongation of $\mathbf{n}$ with respect to the Sun. The clock angle δ is the angle between the $\mathbf{h}$ axis and the projection of $\mathbf{n}$ onto the $(\mathbf{h}, \mathbf{t})$ plane, as shown in Figure 2.4.

Because the solar sail spacecraft cannot generate acceleration towards the Sun, the α range is inside $[-\pi/2, \pi/2]$. In theory, the range of δ is $[0, 2\pi]$, but there are two different angles representing the same direction, such as $\alpha{=}\pi/4$, $\delta{=}\pi/2$ and $\alpha{=}-\pi/4$, $\delta{=}3\pi/2$. In order to avoid the same solar sail direction being represented by two different angles, we consider the α range in $[-\pi/2, \pi/2]$, and the δ range in $[0, \pi]$.

2.3 Equations of motion

Acording to the equations (2.2) of the RTBP, the equations of motion of the SRP–RTBP model are

$$\begin{aligned} \ddot{X} - 2\dot{Y} &= \Omega_X + a_X^s, \\ \ddot{Y} + 2\dot{X} &= \Omega_Y + a_Y^s, \\ \ddot{Z} &= \Omega_Z + a_Z^s, \end{aligned} \tag{2.14}$$

where a_X^s,a_Y^s,a_Z^s, are the three components of the SRP acceleration $\boldsymbol{a}^s$ which, according to [4], is given by

$$\boldsymbol{a}^s = \beta \frac{1-\mu}{r_1^2} \cos^2\alpha \, \mathbf{n}. \tag{2.15}$$

Introducing the unitary vector $\boldsymbol{z} = (0,0,1)^T$, the components of $\boldsymbol{a}^s$, in terms of α and δ, are

$$\begin{aligned} a_X^s &= \frac{\beta(1-\mu)(X-\mu)}{|\boldsymbol{r}_1|^3}\cos^3\alpha - \frac{\beta(1-\mu)(X-\mu)Z}{|\boldsymbol{r}_1|^2|(\boldsymbol{r}_1\times\boldsymbol{z})\times\boldsymbol{r}_1|}\cos^2\alpha\sin\alpha\cos\delta \\ &\quad + \frac{\beta(1-\mu)Y}{|\boldsymbol{r}_1|^2|(\boldsymbol{r}_1\times\boldsymbol{z})|}\cos^2\alpha\sin\alpha\sin\delta, \\ a_Y^s &= \frac{\beta(1-\mu)Y}{|\boldsymbol{r}_1|^3}\cos^3\alpha - \frac{\beta(1-\mu)YZ}{|\boldsymbol{r}_1|^2|(\boldsymbol{r}_1\times\boldsymbol{z})\times\boldsymbol{r}_1|}\cos^2\alpha\sin\alpha\cos\delta \\ &\quad - \frac{\beta(1-\mu)(X-\mu)}{|\boldsymbol{r}_1|^2|(\boldsymbol{r}_1\times\boldsymbol{z})|}\cos^2\alpha\sin\alpha\sin\delta, \\ a_Z^s &= \frac{\beta(1-\mu)Z}{|\boldsymbol{r}_1|^3}\cos^3\alpha + \frac{\beta(1-\mu)(Y^2+(X-\mu)^2)}{|\boldsymbol{r}_1|^2|(\boldsymbol{r}_1\times\boldsymbol{z})\times\boldsymbol{r}_1|}\cos^2\alpha\sin\alpha\cos\delta. \end{aligned} \tag{2.16}$$

Note that when the lightness number β is zero, or when $\alpha = \pm\pi/2$, we recover the RTBP equations. Moreover, when the clock angle is $\delta{=}\pi/2$, then $\mathbf{n}$ is in the plane expanded by $\boldsymbol{r}_1$ and $\boldsymbol{r}_1 \times \boldsymbol{h}$, and there is no SRP acceleration in the orthogonal direction $\mathbf{h}$.

2.4 The families of artificial libration points

Similar to the RTBP case, the artificial equilibrium points of the SRP–RTBP model are the solutions of the non-linear system of equations

$$\begin{aligned} \Omega_X + a_X^s &= 0, \\ \Omega_Y + a_Y^s &= 0, \\ \Omega_Z + a_Z^s &= 0, \end{aligned} \tag{2.17}$$

which, using Eqs. (2.15), can be written in a compact way as

$$-\nabla\boldsymbol{\Omega} = \beta\frac{\mu}{r^2}\cos^2\alpha\mathbf{n}. \tag{2.18}$$

Using Eqs. (2.16), Eq. (2.18) can be expressed as

$$\begin{aligned}
&\Omega_X + \frac{\beta(1-\mu)(X-\mu)}{|\boldsymbol{r}_1|^3}\cos^3\alpha - \frac{\beta(1-\mu)(X-\mu)Z}{|\boldsymbol{r}_1|^2|(\boldsymbol{r}_1\times\boldsymbol{z})\times\boldsymbol{r}_1|}\cos^2\alpha\sin\alpha\cos\delta \\
&+\frac{\beta(1-\mu)Y}{|\boldsymbol{r}_1|^2|(\boldsymbol{r}_1\times\boldsymbol{z})|}\cos^2\alpha\sin\alpha\sin\delta = 0, \\
&\Omega_Y + \frac{\beta(1-\mu)Y}{|\boldsymbol{r}_1|^3}\cos^3\alpha - \frac{\beta(1-\mu)YZ}{|\boldsymbol{r}_1|^2|(\boldsymbol{r}_1\times\boldsymbol{z})\times\boldsymbol{r}_1|}\cos^2\alpha\sin\alpha\cos\delta \\
&-\frac{\beta(1-\mu)(X-\mu)}{|\boldsymbol{r}_1|^2|(\boldsymbol{r}_1\times\boldsymbol{z})|}\cos^2\alpha\sin\alpha\sin\delta = 0, \\
&\Omega_Z + \frac{\beta(1-\mu)Z}{|\boldsymbol{r}_1|^3}\cos^3\alpha + \frac{\beta(1-\mu)(Y^2+(X-\mu)^2)}{|\boldsymbol{r}_1|^2|(\boldsymbol{r}_1\times\boldsymbol{z})\times\boldsymbol{r}_1|}\cos^2\alpha\sin\alpha\cos\delta = 0.
\end{aligned} \tag{2.19}$$

It is well known that the RTBP ($a_X^s = a_Y^s = a_Z^s = 0$) has five equilibrium points, usually denoted by L_1, L_2,...,L_5. When we further consider the SRP the new equilibrium points will be denoted by SL_1, SL_2,...,SL_5, as shown in the Fig. 2.5.

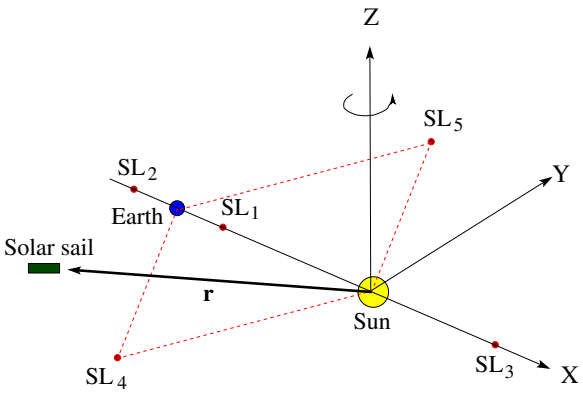

Figure 2.5: Schematic representation of SRP–RTBP and its equilibrium points.

The position of the artificial equilibrium points is constrained by the orientation of the sail, and the normal vector $\mathbf{n}$ must be parallel to $-\nabla\boldsymbol{\Omega}$, which implies

$$\mathbf{n} = \frac{-\nabla\boldsymbol{\Omega}}{|-\nabla\boldsymbol{\Omega}|}. \tag{2.20}$$

According to the definition of α, we can write

$$\cos^2\alpha = <\mathbf{r},\mathbf{n}>^2 = \left\langle \mathbf{r}, \frac{-\nabla\boldsymbol{\Omega}}{|-\nabla\boldsymbol{\Omega}|}\right\rangle^2. \tag{2.21}$$

Substituting Eq. (2.21) in Eq. (2.18), we get that the artificial libration points satisfy the flowing equation

$$\beta = \frac{r^2}{\mu}\frac{|-\nabla\boldsymbol{\Omega}|^3}{<\mathbf{r},-\nabla\boldsymbol{\Omega}>^2}. \tag{2.22}$$

It must be noted that not all the solutions of Eq. (2.22) are feasible, due to the constraint in the direction of the SRP acceleration, since it is not possible to produce acceleration in the direction towards the Sun. So, in the computations the following inequality must be taken into account

$$\langle \mathbf{r}, -\nabla \mathbf{\Omega} \rangle \geq 0.$$

2.4.1 The SL_1 family

We are particularly interested in the location of the two libration points SL_1 and SL_2 when the cone angle α, the clock angle δ, and the lightness number β vary. In this thesis, the SL_1 point will be the point between the Sun and the Earth, and SL_2 the one at the far side of the Earth with respect to the Sun. According to the results obtained, when β is small the SL_1 family of equilibrium points is a closed sphere, as shown in Fig 2.6, Fig. 2.7 and Fig. 2.8.

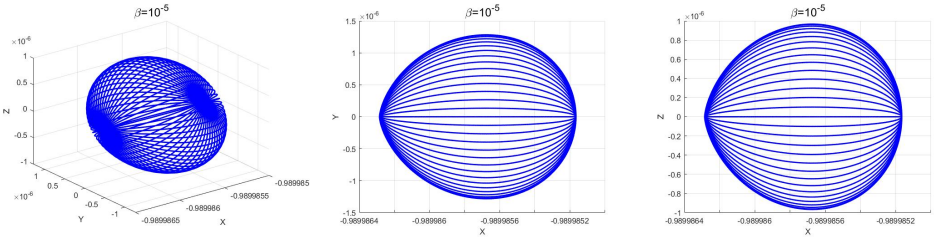

(a) 3D (b) XY plane (c) XZ plane

Figure 2.6: Family $SL_1(\alpha, \delta)$ of equilibrium points when β=10^{-5}.

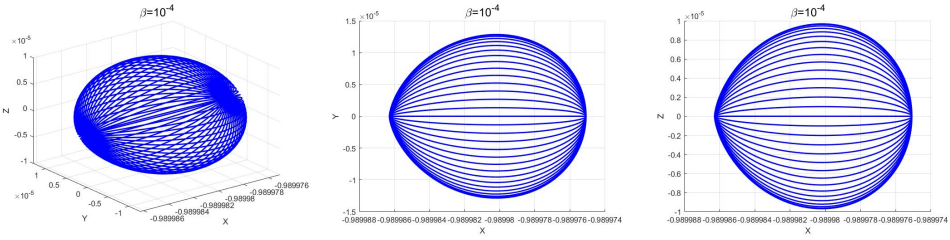

(a) 3D (b) XY plane (c) XZ plane

Figure 2.7: Family of $SL_1(\alpha, \delta)$ equilibrium points when β=10^{-4}.

In Fig. 2.6 and Fig. 2.7 we represent the $SL_1(\alpha, \delta)$ family of equilibrium points for different β values. Both families are closed spheres and the $SL_1(\alpha, \delta)$ family with $\beta = 10^{-4}$ is larger.

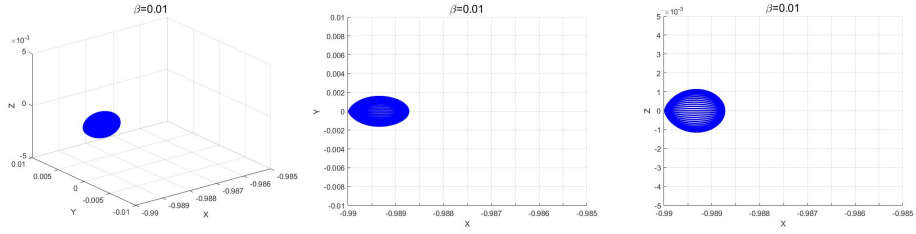

(a) β=0.01

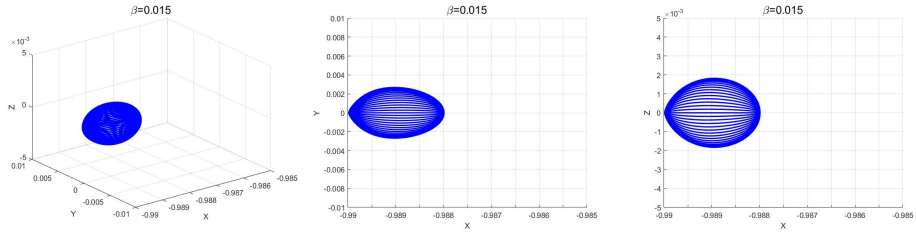

(b) β=0.015

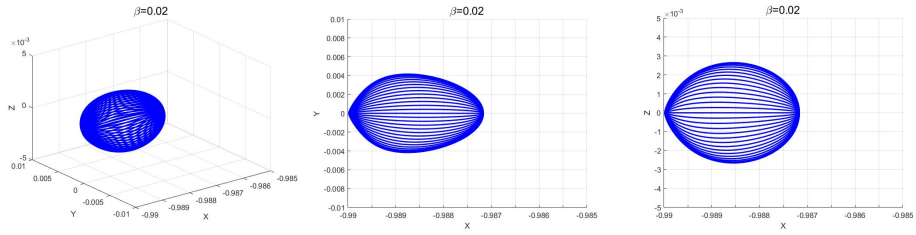

(c) β=0.02

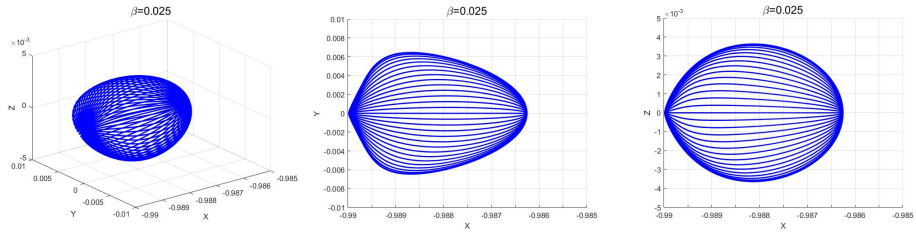

(d) β=0.025

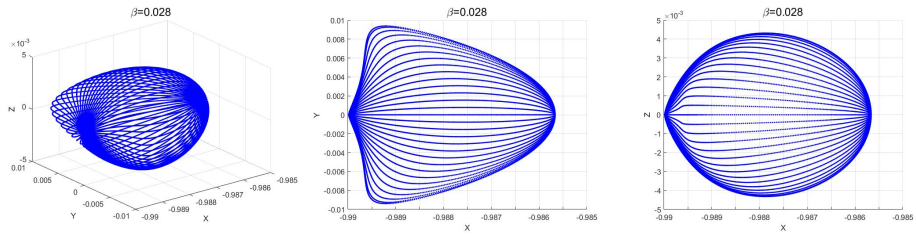

(e) β=0.028

Figure 2.8: Family $SL_1(\alpha, \delta)$ of equilibrium points for $\beta = 0.01, 0.015, 0.02, 0.025, 0.028$.

For $\beta = 0.01, 0.015, 0.02, 0.025, 0.028$ we show the corresponding $SL_1(\alpha, \delta)$ families in Fig. 2.8. The first column is the 3D representation while the second and third columns are projections on the XY and XZ planes. When $\beta < 0.029$, the $SL_1(\alpha, \delta)$ family is always a closed spherical surface. Table. 2.3 lists the $SL_1(\alpha, \delta)$ family amplitudes when $\beta < 0.029$. The minimum X amplitude is -0.98998628 and the Y and Z amplitudes vary significatively when the value of β increases.

Table 2.3: Range of the SL_1 family amplitudes when $\beta < 0.029$

β	X_{min}	X_{max}	Y_{min}	Y_{max}	Z_{min}	Z_{max}
10^{-6}	-0.99	-0.98998617	-1.28×10^{-7}	1.28×10^{-7}	-9.67×10^{-8}	9.67×10^{-8}
10^{-5}	-0.99	-0.98998517	-1.28 ×10^{-6}	1.28 ×10^{-6}	-9.67×10^{-7}	9.67×10^{-7}
10^{-4}	-0.99	-0.98997509	-1.28×10^{-5}	1.28×10^{-5}	-9.68×10^{-6}	9.68×10^{-6}
10^{-3}	-0.99	-0.98987316	-1.31×10^{-4}	1.31×10^{-4}	-9.81×10^{-5}	9.81×10^{-5}
10^{-2}	-0.99	-0.98873132	-0.00157490	0.00157490	-0.00112043	0.00112043
1.5×10^{-2}	-0.99	-0.98799090	-0.00267861	0.00267861	-0.00182248	0.00182248
2×10^{-2}	-0.99	-0.98716700	-0.00416437	0.00416437	-0.00264999	0.00264999
2.5×10^{-2}	-0.99	-0.98625546	-0.00645974	0.00645974	-0.00363520	0.00363520
2.8×10^{-2}	-0.99	-0.98566562	-0.00939128	0.00939128	-0.00431925	0.00431925

For $\beta = 0.03$, the $SL_1(\alpha, \delta)$ family is shown in Fig. 2.9 and it is no longer a closed sphere. The (b) plot gives the XY plane projection, the vertex part is disconnected and merges into the $SL_{3,4,5}$ family. The (c) plot is the SL_1 XZ plane projection.

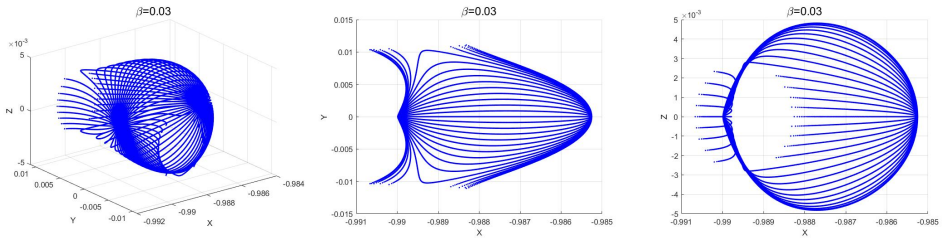

(a) 3D (b) XY plane (c) XZ plane

Figure 2.9: Family $SL_1(\alpha, \delta)$ of equilibrium points for $\beta = 0.03$.

For $\beta = 0.04, 0.05$, the $SL_1(\alpha, \delta)$ family is shown in Fig. 2.10. When compared with Fig. 2.9, we see less connected lines as β increases.

The main results obtained for the $SL_1(\alpha, \delta)$ artificial libration point family are the following:

1. When $\beta = 0$ (there is no SRP), SL_1 becomes the traditional L_1 point.
2. When $\beta \neq 0$, the $SL_1(\alpha, \delta)$ family expand from a point to a surface under the action of α and δ.

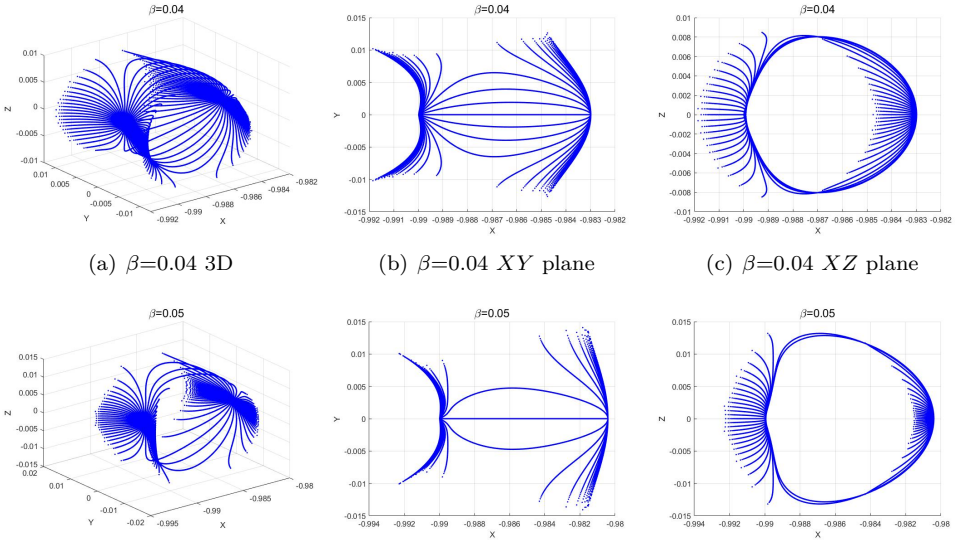

(a) β=0.04 3D (b) β=0.04 XY plane (c) β=0.04 XZ plane

(d) β=0.05 3D (e) β=0.05 XY plane (f) β=0.05 XZ plane

Figure 2.10: Family $SL_1(\alpha, \delta)$ of equilibrium points for $\beta = 0.04, 0.05$.

3. When β is close to 0.030, a part of $SL_1(\alpha, \delta)$ family merges with $SL_{3,4,5}$.
4. When $SL_1(\alpha, \delta)$ the family merges with the one of $SL_{3,4,5}$. There are only two disconnected surfaces in the system, one is $SL_{1,3,4,5}$, and the other one is SL_2.

2.4.2 The SL_2 family

When compared with the complex evolutions of the SL_1 and $SL_{3,4,5}$ families, the SL_2 family behaves more stable and intuitive. In Fig. 2.11 we show the family $SL_2(\alpha, \delta)$ for $\beta = 0.01$.

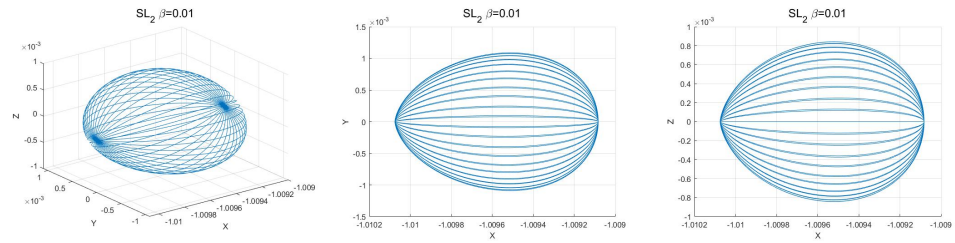

(a) 3D (b) XY plane (c) XZ plane

Figure 2.11: The family $SL_2(\alpha, \delta)$ of equilibrium points for $\beta = 0.01$

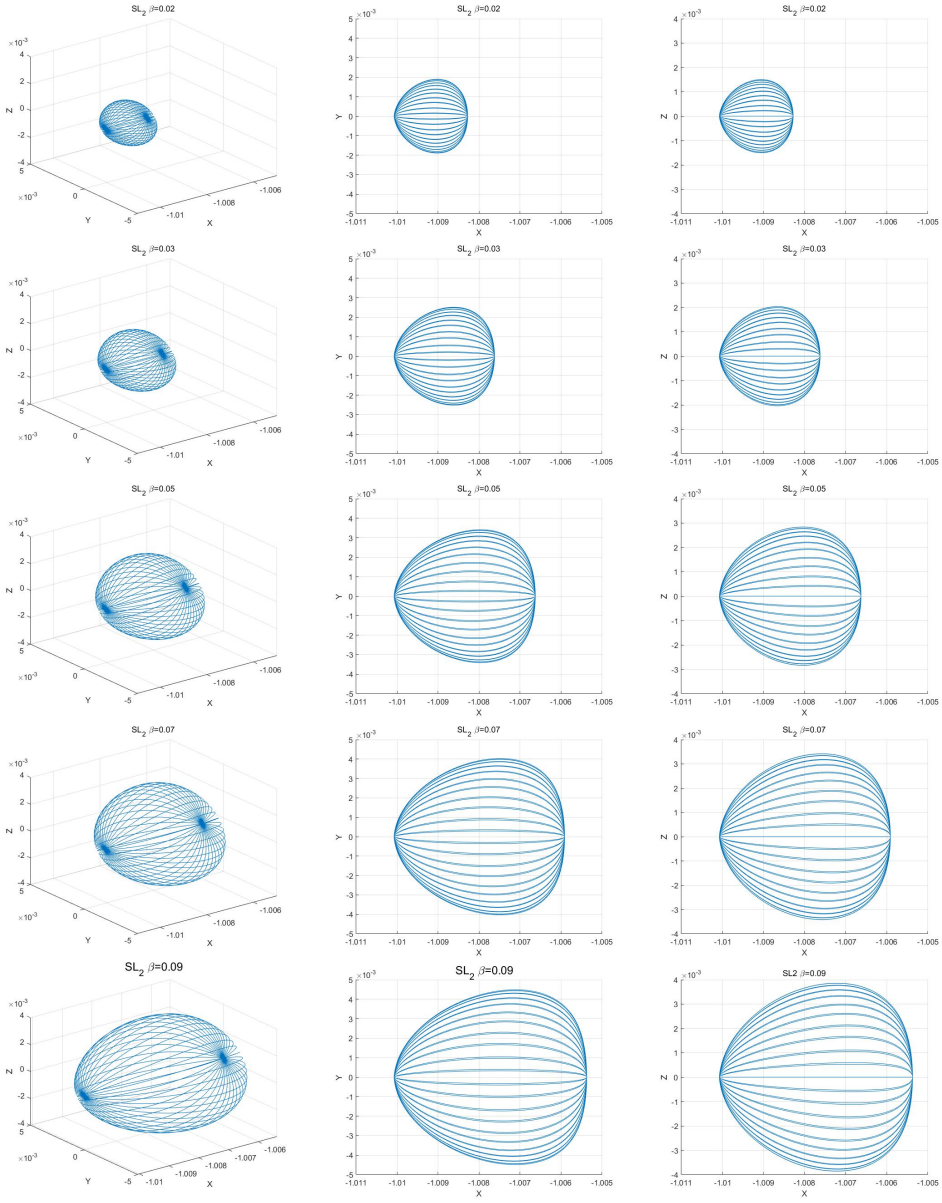

Figure 2.12: Family $SL_2(\alpha, \delta)$ of equilibrium points for $\beta = 0.02, 0.03, 0.05, 0.07, 0.09$.

For $\beta = 0.02, 0.03, 0.05, 0.07, 0.09$, the $SL_2(\alpha, \delta)$ family is shown in Fig. 2.12 and in Table. 2.4.

Table 2.4: The amplitudes of the SL_2 family for different β values.

β	X_{min}	X_{max}	Y_{min}	Y_{max}	Z_{min}	Z_{max}
0.01	-1.01007489	-1.00908220	-0.00108965	0.00108965	-0.00084222	0.00084222
0.02	-1.01007489	-1.00827950	-0.00189529	0.00189529	-0.00150443	0.00150443
0.03	-1.01007489	-1.00762435	-0.00251593	0.00251593	-0.00203741	0.00203741
0.05	-1.01007489	-1.00662946	-0.00341176	0.00341176	-0.00284115	0.00284115
0.07	-1.01007489	-1.00591423	-0.00403178	0.00403178	-0.00342009	0.00342009
0.09	-1.01007489	-1.00537556	-0.00448983	0.00448983	-0.00385957	0.00385957

Then, according to Figure. 2.12 and Table. 2.4, the main results are the following

1. For the practical values of β, the family $SL_2(\alpha, \delta)$ of equilibrium points is always a closed ellipsoid surface (a different fact with respect to other libration point families).
2. When β increases, the size of the closed ellipsoid surface also increases.

2.5 Chapter summary

This chapter is devoted to fix the notation and to introduce the dynamical models, used in this work, including the RTBP and the SRP–RTBP models. It has been followed by systematic studies of the artificial libration point families with respect to the orientation angles (cone angle α and clock angle δ) and the lightness number (β). The most relevant results obtained are the following:

- When $\alpha = \pm\pi/2$, the incident photon direction is parallel to the solar sail panel, and there is no solar pressure. In this case the model can be simplified to the traditional restricted three-body model and (SL_i=L_i).
- When $\alpha = 0$, the plane of the solar sail is perpendicular to $\mathbf{r}_i$. In this case the force due to the SRP is aligned with the gravitational attraction of the Sun, so the model can be seen as the usual RTBP with the mass of the Sun, $1 - \mu$, decreased. The position of SL_1 and SL_2 moves towards the Sun as the value of β increases.
- When $\alpha \neq 0$ and $\delta = \pi/2$, the solar sail surface is subjected to the force in the XY plane, and the artificial libration point will also correspond moving left or right but inside the plane. Similarly, if $\delta = 0$ or π, it will be subjected to a force perpendicular to the XY plane, and the artificial libration point will move up or down.

- When $\beta = 0$ there is no solar pressure force and the model is the traditional restricted three-body model. When β is small, there are five independent and disconnected libration point families in the system. When $\beta < 0.028$, the SL_3, SL_4 and SL_5 families gradually expand and merge with each other, while SL_1 and SL_2 families are independent closed ellipsoid surfaces. When $0.029 < \beta < 0.04$, part of SL_1 and $SL_{3,4,5}$ merge with each other, while SL_2 family is always an independent closed ellipsoid surface. Table. 2.5 shows the relation between libration point family and lightness number β.

Table 2.5: Topology of the artificial libration point families depending on the lightness number.

β	SL_2	SL_1	SL_3	SL_4	SL_5
β<10^{-5}	ellipsoid	ellipsoid	surface	surface	surface
10^{-5}<β<0.028	ellipsoid	ellipsoid	$SL_{3,4,5}$	$SL_{3,4,5}$	$SL_{3,4,5}$
0.029<β<0.04	ellipsoid	$SL_{1,3,4,5}$	$SL_{1,3,4,5}$	$SL_{1,3,4,5}$	$SL_{1,3,4,5}$

3

Chapter 3

Impulse maneuver design of a solar sail for enhanced heteroclinic transfer research

The orbits near the libration points L_1 and L_2 have dynamic characteristics of great significance in the field of deep space exploration [43, 66], which provide a variety of possibilities for future space missions. Libration point orbits are a kind of periodic and quasi–periodic orbits [67, 68] which are relatively inexpensive to reach from Earth, and also with easy communication with our planet. Usually, orbits around the L_1 point can be used as a platform for observing the activity of the Sun, and orbits around the L_2 point are convenient for deep space exploration observations [69].

Halo orbits are a frequent choice for libration point orbital missions, but Halo orbits are slender in the direction perpendicular to the Sun-Earth line, so they need control, not only for the orbital station-keeping, but also for the antennas to keep them pointing to the Earth [152]. Another usual option are Lissajous orbits, which are quasi–periodic orbits around the libration points that allow a greater mission flexibility [153].

The stable and unstable manifolds associated with the libration point orbits ensure the departure and approach of the spacecraft from and towards to them. The unstable manifolds can make the spacecraft to leave the libration point orbit neighbourhood in a relatively short time, (about two orbital revolutions) while the stable manifolds provide the chance for the spacecraft to come back to the libration point orbit [154]. Likewise, homoclinic and heteroclinic connections play a key role in transfer designs [105]. Heteroclinic connections

involve the intersection of stable and unstable manifolds, using two different manifolds at the same energy level. For example, in the Artemis and Wind missions, the spacecraft leaves the L_1 orbit through the unstable manifold, and then enters the L_2 orbit through the stable manifold [155].

In this chapter, an impulse maneuver method for solar sail spacecraft, based on the three-dimensional artificial libration point family, is proposed. We use the method to solve the spacecraft heteroclinic transfer problem between two different artificial libration point orbits. Firstly, the restricted three-body problem, including solar radiation pressure, is linearized, solved, and tested to check it can meet the mission requirements. Secondly, we propose the solar sail impulse maneuver method, by adjusting the solar sail parameters, to change the artificial libration point position. A detailed algorithm of the full procedure is given. Finally, we use the developed method to study impulsive heteroclinic transfers between Lissajous orbits near three-dimensional artificial libration points.

The chapter is organised as follows. The solutions of the linearized CR3BP-SRP model around the collinear equilibrium points are computed in Section 3.1. These solutions are used in Section 3.2 to determine the enhanced heteroclinics using SRP maneuvers. The detailed procedure and simulations are given in the last sections of the chapter.

3.1 SRP–RTBP linearization model

From now on, we focus our attention on the motion in the vicinity of SL_2 (the study around SL_1 is similar). For given values of α, δ and on β, let $(\gamma_1, \gamma_2, \gamma_3)$ be the position of SL_2 in the CR3BP reference frame and units. Following [120], we perform a change of scale, and set the origin of coordinates at the equilibrium point by means of the translation

$$\begin{aligned} X &= \gamma x + \gamma_1, \\ Y &= \gamma y + \gamma_2, \\ Z &= \gamma z + \gamma_3, \end{aligned} \tag{3.1}$$

where γ is a scaling factor chosen in order to normalize the Eath-equilibrium point distance. In our case, we have taken $\gamma = 0.01$, since this value is very close to the Earth-L_2 distance in the CR3BP. Therefore, in the new coordinates, the adimensional distance unit will be, approximately, 1.5×10^6 km.

Applying the above change of coordinates to the CR3BP-SRP equations we get

$$\begin{aligned} \ddot{x} - 2\dot{y} &= \frac{1}{\gamma^2}\Omega_x + \frac{1}{\gamma}a_x^s, \\ \ddot{y} + 2\dot{x} &= \frac{1}{\gamma^2}\Omega_y + \frac{1}{\gamma}a_y^s, \\ \ddot{z} &= \frac{1}{\gamma^2}\Omega_z + \frac{1}{\gamma}a_z^s, \end{aligned} \tag{3.2}$$

and the linearized equations of motion at the equilibrium point become

$$\begin{aligned} \ddot{x} - 2\dot{y} &= a_1 x + a_2 y + a_3 z, \\ \ddot{y} + 2\dot{x} &= b_1 x + b_2 y + b_3 z, \\ \ddot{z} &= c_1 x + c_2 y + c_3 z, \end{aligned} \tag{3.3}$$

where the coefficients a_i, b_i and c_i, that deppend on μ, α, δ, β, γ_1, γ_2, γ_3 and γ, are given in Appendix B.

3.1.1 Analytical solution of the linearized equations

We look for solutions of the linear system (3.3) with one of the following two patterns, that will be respectively associated to planar and vertical modes of motion

$$\text{Case 1:} \qquad x(t) = e^{\lambda t}, \quad y(t) = k e^{\lambda t}, \quad z(t) = \overline{k} e^{\lambda t}, \tag{3.4}$$

$$\text{Case 2:} \qquad x(t) = \overline{k} e^{\lambda t}, \quad y(t) = k e^{\lambda t}, \quad z(t) = e^{\lambda t}, \tag{3.5}$$

where, in both cases, the parameters k, $\overline{k}$, and the exponent λ are, in general, complex numbers to be determined independently for each case.

Inserting (3.4) into the differential equations (3.3) we get the following two systems of equations for the parameters

$$\text{Case 1:} \quad \begin{cases} \lambda^2 - 2k\lambda &= a_1 + a_2 k + a_3 \overline{k}, \\ k\lambda^2 + 2\overline{k}\lambda &= b_1 + b_2 k + b_3 \overline{k}, \\ \overline{k}\lambda^2 &= c_1 + c_2 k + c_3 \overline{k}, \end{cases}$$

$$\text{Case 2:} \quad \begin{cases} \overline{k}\lambda^2 - 2k\lambda &= a_1 \overline{k} + a_2 k + a_3, \\ k\lambda^2 + 2\overline{k}\lambda &= b_1 \overline{k} + b_2 k + b_3, \\ \lambda^2 &= c_1 \overline{k} + c_2 k + c_3. \end{cases}$$

In both cases λ is an eigenvalue of the linearized system around the equilibrium point, so it must satisfy the following equation

$$\begin{aligned} &\lambda^6 - (a_1 + b_2 + c_3 - 4)\lambda^4 + (2a_2 - 2b_1)\lambda^3 - (4c_3 - a_1 b_2 + a_2 b_1 - a_1 c_3 + a_3 c_1 \\ &- b_2 c_3 + b_3 c_2)\lambda^2 - 2(a_2 c_3 - a_3 c_2 - b_1 c_3 + b_3 c_1)\lambda \\ &- a_3 b_1 c_2 - a_2 b_3 c_1 - a_1 b_2 c_3 + a_3 b_2 c_1 + a_2 b_1 c_3 + a_1 b_3 c_2 = 0. \end{aligned} \tag{3.6}$$

For the equilibrium points SL_1 and SL_2, two roots of this polynomial, $\lambda_{1,2}$ ($\lambda_1 > 0$, $\lambda_2 < 0$), are always real, and the remaining ones are two complex conjugate pairs: $\lambda_{3,4} = \eta_1 \pm \omega_1$ and $\lambda_{5,6} = \eta_2 \pm \omega_2$. In general, $\lambda_1 \simeq -\lambda_2$, and the equality only holds when the cone angle $\alpha = 0$.

For a given value of λ, solution of Eqs. (3.6), the associated values of k and $\overline{k}$ depend on the case under consideration.

In Case 1 we get

$$k = \frac{\lambda^4 - (c_3 + a_1)\lambda^2 + a_1 c_3 - a_3 c_1}{2\lambda^3 + a_2\lambda^2 - 2c_3\lambda - a_2 c_3 + a_3 c_2}, \tag{3.7}$$

$$\overline{k} = \frac{c_2\lambda^4 + 2c_1\lambda^3 + (a_2 c_1 - c_2 c_3 - a_1 c_2)\lambda^2 - 2c_1 c_3\lambda + a_1 c_2 c_3 - a_2 c_1 c_3}{2\lambda^5 + a_2\lambda^4 - 4c_3\lambda^3 + (a_3 c_2 - 2a_2 c_3)\lambda^2 + 2c_3^2\lambda + a_2 c_3^2 - a_3 c_2 c_3}. \tag{3.8}$$

While in Case 2 the values of k and $\overline{k}$ are

$$k = \frac{\lambda^4 - (c_3 + a_1)\lambda^2 + a_1 c_3 - a_3 c_1}{c_2\lambda^2 + 2c_1\lambda - a_1 c_2 + a_2 c_1}, \qquad \overline{k} = \frac{2\lambda^3 + a_2\lambda^2 - 2c_3\lambda - a_2 c_3 + a_3 c_2}{c_2\lambda^2 + 2c_1\lambda a_1 c_2 + a_2 c_1}. \tag{3.9}$$

From the expressions given in Appendix B it follows that if $\gamma_3 = 0$ then $C_1 = C_2 = C_3 = 0$; furthermore, according to the values of c_1 and c_2

$$\begin{aligned} c_1 &= \frac{1-\mu}{\gamma^3}\frac{3A_1C_1}{D_1^5} + \frac{\mu}{\gamma^3}\frac{3A_2C_2}{D_2^5} \\ &\quad -\frac{\beta(1-\mu)\cos^2\alpha}{\gamma^3 D_1^3 D_3}\left(\frac{3A_1C_1D_3}{D_1^2}\cos\alpha - (E_3D_3^2 - 2)A_1\sin\alpha\cos\delta\right), \\ c_2 &= \frac{1-\mu}{\gamma^3}\frac{3C_1B_1}{D_1^5} + \frac{\mu}{\gamma^3}\frac{3B_2C_2}{D_2^5} \\ &\quad -\frac{\beta(1-\mu)\cos^2\alpha}{\gamma^3 D_1^3 D_3}\left(\frac{3B_1C_1D_3}{D_1^2}\cos\alpha - (E_3D_3^2 - 2)B_1\sin\alpha\cos\delta\right), \end{aligned}$$

where, if $\gamma_3 = 0$ (equilibrium points in the $Z = 0$ plane) we have that $C_1 = C_2 = C_3 = 0$. Hence, for $\alpha = 0$ and $\delta = \pi/2$ then $c_1 = c_2 = 0$, and the expresion (3.9) for k and $\overline{k}$ in Case 2 have a singularity. In other to avoid this situation, we can write k and $\overline{k}$ in terms of a_i and b_i as

$$k = \frac{b_3\lambda^2 - 2a_3\lambda - a_1 b_3 + a_3 b_1}{\lambda^4 - (a_1 + b_2 - 4)\lambda^2 + (2a_2 - 2b_1)\lambda + a_1 b_2 - a_2 b_1},$$

$$\overline{k} = \frac{a_3\lambda^2 + 2b_3\lambda + a_2 b_3 - a_3 b_2}{\lambda^4 - (a_1 + b_2 - 4)\lambda^2 + (2a_2 - 2b_1)\lambda + a_1 b_2 - a_2 b_1},$$

which are not singular for the above values of the parameters. Something similar happens in Case 1, in this case the singularity disappears using the following expressions for k and $\overline{k}$

$$\begin{aligned} k &= \frac{-2\lambda^3 + b_3\lambda^2 + 2a_1\lambda - a_1 b_3 + a_3 b_1}{(a_3 - 4)\lambda^2 + 2(b_3 - a_2)\lambda + a_2 b_3 - a_3 b_2}, \\ \overline{k} &= \frac{\lambda^4 - (a_1 + b_2)\lambda^2 - 2b_1\lambda + a_1 b_2 - b_1 a_2}{(a_3 - 4)\lambda^2 + 2(b_3 - a_2)\lambda + a_2 b_3 - a_3 b_2}. \end{aligned}$$

In Case 1, the solution of the differential equations (3.3) associated to the planar mode

can be written as

$$\begin{aligned} x(t) &= A_1 e^{\lambda_1 t} + A_2 e^{\lambda_2 t} + A_3 e^{\eta_1 t}\cos\omega_1 t + A_4 e^{\eta_1 t}\sin\omega_1 t, \\ y(t) &= A_1 k_1 e^{\lambda_1 t} + A_2 k_2 e^{\lambda_2 t} + A_3 e^{\eta_1 t}(k_3\cos\omega_1 t + k_4\sin\omega_1 t) \\ &\quad + A_4 e^{\eta_1 t}(k_3\sin\omega_1 t - k_4\cos\omega_1 t), \\ z(t) &= A_1 \overline{k}_1 e^{\lambda_1 t} + A_2 \overline{k}_2 e^{\lambda_2 t} + A_3 e^{\eta_1 t}(\overline{k}_3\cos\omega_1 t + \overline{k}_4\sin\omega_1 t) \\ &\quad + A_4 e^{\eta_1 t}(\overline{k}_3\sin\omega_1 t - \overline{k}_4\cos\omega_1 t), \end{aligned}$$

and in Case 2, associated to the vertical mode, as

$$\begin{aligned} x(t) &= A_5 e^{\eta_2 t}(\overline{k}_5\cos\omega_2 t + \overline{k}_6\ sin\omega_2 t) + A_6 e^{\eta_2 t}(\overline{k}_5\sin\omega_2 t - \overline{k}_6\cos\omega_2 t), \\ y(t) &= A_5 e^{\eta_2 t}(k_5 cos\omega_2 t + k_6\sin\omega_2 t) + A_6 e^{\eta_2 t}(k_5\sin\omega_2 t - k_6\cos\omega_2 t), \\ z(t) &= A_5 e^{\eta_2 t}\cos\omega_2 t + A_6 e^{\eta_2 t}\sin\omega_2 t. \end{aligned}$$

So, in general, the final form of the solution (3.3) containing all modes becomes

$$\begin{aligned} x(t) &= A_1 e^{\lambda_1 t} + A_2 e^{\lambda_2 t} + A_3 e^{\eta_1 t}\cos\omega_1 t + A_4 e^{\eta_1 t}\sin\omega_1 t \\ &\quad + A_5 e^{\eta_2 t}(\overline{k}_5\cos\omega_2 t + \overline{k}_6\sin\omega_2 t) + A_6 e^{\eta_2 t}(\overline{k}_5\sin\omega_2 t - \overline{k}_6\cos\omega_2 t), \\ y(t) &= A_1 k_1 e^{\lambda_1 t} + A_2 k_2 e^{\lambda_2 t} \\ &\quad + A_3 e^{\eta_1 t}(k_3\cos\omega_1 t + k_4\sin\omega_1 t) + A_4 e^{\eta_1 t}(k_3\sin\omega_1 t - k_4\cos\omega_1 t) \\ &\quad + A_5 e^{\eta_2 t}(k_5\cos\omega_2 t + k_6\sin\omega_2 t) + A_6 e^{\eta_2 t}(k_5\sin\omega_2 t - k_6\cos\omega_2 t), \\ z(t) &= A_1 \overline{k}_1 e^{\lambda_1 t} + A_2 \overline{k}_2 e^{\lambda_2 t} \\ &\quad + A_3 e^{\eta_1 t}(\overline{k}_3\cos\omega_1 t + \overline{k}_4\sin\omega_1 t) + A_4 e^{\eta_1 t}(\overline{k}_3\sin\omega_1 t - \overline{k}_4\cos\omega_1 t) \\ &\quad + A_5 e^{\eta_2 t}\cos\omega_2 t + A_6 e^{\eta_2 t}\sin\omega_2 t. \end{aligned} \tag{3.10}$$

In the above equations $A_1, ..., A_6$ are arbitrary parameters, $\lambda_{1,2}$ are the real roots of (3.6), ($\lambda_1 > 0$, $\lambda_2 < 0$), and $\lambda_{3,4} = \eta_1 \pm \omega_1 i$ and $\lambda_{5,6} = \eta_2 \pm \omega_2 i$ are the two complex conjugate pairs. The eigenvalues $\lambda_{3,4}$ are the ones associated to the planar oscillations of the solutions, and $\lambda_{5,6}$ are the ones associated to the vertical ones. The values of k_i and $\overline{k}_i$, for $i = 1, ..., 6$, are given in Appendix C.

An important property of the formulation chosen in (3.10) is that it gives a continuous global representation when crossing bifurcations varying the values α, δ, β and changing the type of equilibrium point associated. To have a general idea of the magnitude of the eigenvalues, Table 3.1 shows some values of $\lambda_{1,2}$, $\eta_{1,2}$, $\omega_{1,2}$ depending on α and δ for $\beta = 0.02$. From the first two lines, we see that if $\alpha = 0$, the eigenvalues do not change no matter what value of δ is. Lines 3 to 9 show how the variation of eigenvalues when $\delta = \pi/2$ and the value of α changes. Lines 10 to 20 show the behavior of the roots when $\alpha = \pi/6$, and the value of δ varies.

The expression (3.10) can be also written in matrix form as,

$$[x(t),\, y(t),\, z(t),\, \dot{x}(t),\, \dot{y}(t),\, \dot{z}(t)]^T = H(t)\,[A_1,\, A_2,\, A_3,\, A_4,\, A_5,\, A_6]^T\,, \tag{3.11}$$

Table 3.1: Some relevant example values of $\lambda_{1,2}$, $\eta_{1,2}$, $\omega_{1,2}$ depending on α and δ for a given $\beta = 0.02$.

No.	α	δ	λ_1	λ_2	η_1	ω_1	η_2	ω_2
1	0	$\pi/2$	3.30475	−3.30475	0	2.57190	0	2.51131
2	0	$\pi/4$	3.30475	−3.30475	0	2.57190	0	2.51131
3	$\pi/6$	$\pi/2$	3.00566	−3.00466	−0.00050	2.37048	0	2.32633
4	$\pi/4$	$\pi/2$	2.75492	−2.75382	−0.00055	2.21122	0	2.16727
5	$\pi/3$	$\pi/2$	2.57546	−2.57471	−0.00038	2.10685	0	2.04750
6	-$\pi/6$	$\pi/2$	3.00466	−3.00566	0.00050	2.37048	0	2.32633
7	-$\pi/4$	$\pi/2$	2.75382	−2.75492	0.00055	2.21122	0	2.16727
8	-$\pi/3$	$\pi/2$	2.57470	−2.57546	0.00038	2.10685	0	2.04750
9	$\pm\,\pi/2$	$\pi/2$	2.48432	−2.48432	0	2.05701	0	1.98508
10	$\pi/6$	0	3.01329	−3.01329	0	2.48569	0	2.21387
11	$\pi/6$	$\pi/6$	3.01150	−3.01100	−0.00014	2.46770	−0.00011	2.23117
12	$\pi/6$	$\pi/3$	3.00762	−3.00676	−0.00027	2.41942	−0.00016	2.27808
13	$\pi/6$	$\pi/2$	3.00566	−3.00466	−0.00050	2.37048	0	2.32633
14	$\pi/6$	$2\pi/3$	3.00762	−3.00676	−0.00027	2.41942	−0.00016	2.27808
15	$\pi/6$	$5\pi/6$	3.01150	−3.01100	−0.00014	2.46770	−0.00011	2.23117
16	$\pi/6$	π	3.01329	−3.01329	0	2.48569	0	2.21387
17	$\pi/6$	$7\pi/6$	3.01100	−3.01150	0.00014	2.46770	0.00011	2.23117
18	$\pi/6$	$2\pi/3$	3.00676	−3.00762	0.00027	2.41942	0.00016	2.27808
19	$\pi/6$	$3\pi/2$	3.00466	−3.00566	0.00050	2.37048	0	2.32633
20	$\pi/6$	$4\pi/3$	3.00676	−3.00762	0.00027	2.41942	0.00016	2.27808
21	$\pi/6$	$11\pi/6$	3.01100	−3.01150	0.00014	2.46770	0.00011	2.23117

where the components of the matrix H are given in Appendix C. Inverting the above system we get

$$[A_1,\, A_2,\, A_3,\, A_4,\, A_5,\, A_6]^T = H^{-1}(t)\,[x(t),\, y(t),\, z(t),\, \dot{x}(t),\, \dot{y}(t),\, \dot{z}(t)]^T\,, \tag{3.12}$$

that for $t = 0$ gives the values of the amplitudes as a function of the initial conditions

$$[A_1,\, A_2,\, A_3,\, A_4,\, A_5,\, A_6]^T = H^{-1}(0)\,[x_0,\, y_0,\, z_0,\, \dot{x}_0,\, \dot{y}_0,\, \dot{z}_0]^T\,. \tag{3.13}$$

Unfortunately, it is not possible to write short expressions for the components of the matrix $H^{-1}(t)$.

It is also convenient to write the oscillatory solutions (3.10) of the differential equations (3.3) using amplitudes and the associated phases. Defining the unstable and stable amplitudes, A_u and A_s, and the planar (in-plane) and vertical (out-of-plane) amplitudes, $A_x = \sqrt{A_3^2 + A_4^2}$ and $A_z = \sqrt{A_5^2 + A_6^2}$, respectively, by means of the relations

$$\begin{aligned} A_1 &= A_u, & A_2 &= A_s, \\ A_3 &= A_x \cos\phi_1, & A_4 &= -A_x \sin\phi_1, \\ A_5 &= A_z \cos\phi_2, & A_6 &= -A_z \sin\phi_2, \end{aligned} \tag{3.14}$$

we can write the general solution (3.10), as a function of $(A_u, A_s, A_x, A_z, \phi_1, \phi_2)$, as

$$\begin{aligned}
x(t) &= A_u e^{\lambda_1 t} + A_s e^{\lambda_2 t} + A_x e^{\eta_1 t}\cos(\omega_1 t + \phi_1) \\
&\quad + A_z e^{\eta_2 t}\overline{k}_5 \cos(\omega_2 t + \phi_2) + A_z e^{\eta_2 t}\overline{k}_6 \sin(\omega_2 t + \phi_2), \\
y(t) &= A_u k_1 e^{\lambda_1 t} + A_s k_2 e^{\lambda_2 t} + A_x e^{\eta_1 t} k_3 \cos(\omega_1 t + \phi_1) + A_x e^{\eta_1 t} k_4 \sin(\omega_1 t + \phi_1) \\
&\quad + A_z e^{\eta_2 t} k_5 \cos(\omega_2 t + \phi_2) + A_z e^{\eta_2 t} k_6 \sin(\omega_2 t + \phi_2), \\
z(t) &= A_u \overline{k}_1 e^{\lambda_1 t} + A_s \overline{k}_2 e^{\lambda_2 t} + A_x e^{\eta_1 t}\overline{k}_3 \cos(\omega_1 t + \phi_1) + A_x e^{\eta_1 t}\overline{k}_4 \sin(\omega_1 t + \phi_1) \\
&\quad + A_z e^{\eta_2 t}\cos(\omega_2 t + \phi_2),
\end{aligned} \tag{3.15}$$

or, in a more compact form

$$\begin{aligned}
x(t) &= A_u e^{\lambda_1 t} + A_s e^{\lambda_2 t} + A_x e^{\eta_1 t}\cos(\omega_1 t + \phi_1) + A_z e^{\eta_2 t}\overline{k}_{56}\cos(\omega_2 t + \overline{\phi}_{56}), \\
y(t) &= A_u k_1 e^{\lambda_1 t} + A_s k_2 e^{\lambda_2 t} + A_x e^{\eta_1 t} k_{34}\cos(\omega_1 t + \phi_{34}) + A_z e^{\eta_2 t} k_{56}\cos(\omega_2 t + \phi_{56}), \\
z(t) &= A_u \overline{k}_1 e^{\lambda_1 t} + A_s \overline{k}_2 e^{\lambda_2 t} + A_x e^{\eta_1 t}\overline{k}_{34}\cos(\omega_1 t + \overline{\phi}_{34}) + A_z e^{\eta_2 t}\cos(\omega_2 t + \phi_2),
\end{aligned} \tag{3.16}$$

where the relations between the values of the parameters in (3.15) and in (3.16) are

$$\begin{aligned}
k_{34}\cos\phi_{34} &= k_3\cos\phi_1 + k_4\sin\phi_1, & k_{34}\sin\phi_{34} &= k_3\sin\phi_1 - k_4\cos\phi_1, \\
\overline{k}_{34}\cos\overline{\phi}_{34} &= \overline{k}_3\cos\phi_1 + \overline{k}_4\sin\phi_1, & \overline{k}_{34}\sin\overline{\phi}_{34} &= \overline{k}_3\sin\phi_1 - \overline{k}_4\cos\phi_1. \\
k_{56}\cos\phi_{56} &= k_5\cos\phi_2 + k_6\sin\phi_2, & k_{56}\sin\phi_{56} &= k_5\sin\phi_2 - k_6\cos\phi_2, \\
\overline{k}_{56}\cos\overline{\phi}_{56} &= \overline{k}_5\cos\phi_2 + \overline{k}_6\sin\phi_2, & \overline{k}_{56}\sin\overline{\phi}_{56} &= \overline{k}_5\sin\phi_2 - \overline{k}_6\cos\phi_2.
\end{aligned} \tag{3.17}$$

Note that taking $A_u = A_s = 0$ in (3.16) produces quasi-periodic solutions, i.e. Lissajous orbits, with frequencies ω_1 and ω_2, and respective planar and vertical amplitudes equal to A_x and A_z. The values A_u and A_s are related to the unstable and stable manifold of the Lissajous orbit. For instance, the relations $A_u = 0$ and $A_s \neq 0$ define the stable manifold of the Lissajous orbit defined by A_x and A_z (in-plane and out-of-plane amplitudes); any orbit verifying this condition will tend forward in time to the Lissajous orbit, since the term in A_s goes to zero. A similar fact happens when $A_u \neq 0$ and $A_s = 0$, in this case the term with A_u increases as time increases but goes to zero backwards in time, therefore, these solutions will go away exponentially fast forward in time, and define the unstable manifold of the Lissajous orbit.

3.1.2 Accuracy of the linear approximation

Clearly the solution given by equations (3.16) does not fulfil the equations of motion (2.14). In order to test the accuracy of this solution we have computed the residual acceleration RA defined as the norm of the difference between the acceleration given by the equations of motion (2.14) $(\ddot{x}, \ddot{y}, \ddot{z})$ and the one given by the linearised equations (3.3) $(\ddot{x}_L, \ddot{y}_L, \ddot{z}_L)$, this is

$$RA = ((\ddot{x} - \ddot{x}_L)^2 + (\ddot{y} - \ddot{y}_L)^2 + (\ddot{z} - \ddot{z}_L)^2)^{1/2}. \tag{3.18}$$

The computation of the residual acceleration has been done taking points (position and velocity) along Lissajous orbits with different amplitudes, computed using (3.16), during

a certain time interval determined according to the values of the two frequencies of the Lissajous. The Lissajous orbits considered have equal X and Z amplitudes.

Fig.3.1 shows the results obtained for both the value of the residual acceleration RA and its relative value RRA, defined as

$$RRA = \frac{RA}{(\ddot{x}^2 + \ddot{y}^2 + \ddot{z}^2)^{1/2}}. \tag{3.19}$$

For each Lissajous orbit, we have computed both the maximum value of the residual acceleration along the orbit and its average value.

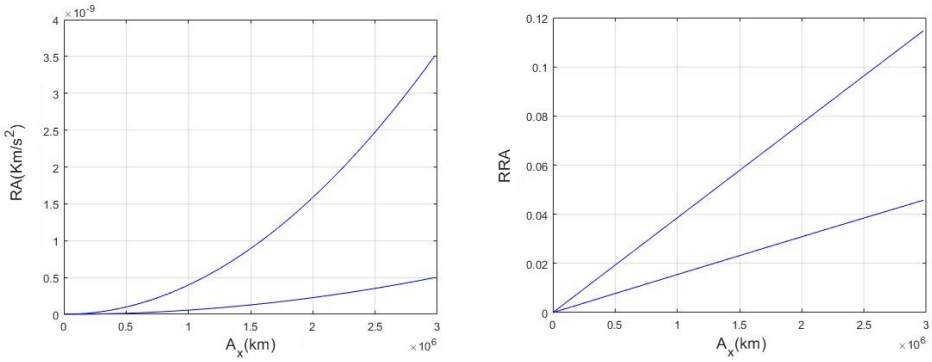

Figure 3.1: The residual acceleration RA and relative residual acceleration RRA as a function of the X-amplitude of the Lissajous orbit.

3.2 Lissajous orbital enhanced heteroclinic transfers and parameter analysis at SL_2 point

This section is devoted to introduce the SRP maneuver strategy that defines the heteroclinic enhanced connections between libration point orbits around the collinear equilibrium points. These transfers are propellant-free and are performed by means of a variation of the sail parameters: α (cone angle), δ (clock angle) or β (lightness number). The influence of the phases ϕ_1 and ϕ_2 at the departing point, as well as the amplitudes A_x and A_z of the initial orbit, will be also analyzed.

As we have seen, the stability and location of the SRP-libration points change with the sail parameters, for this reason we use three different reference systems to design a transfer. The first one is the usual CR3BP synodic frame (X, Y, Z) centered on the Sun-Earth center of mass. The second and third ones are, respectively, associated with the departure and target libration points, and we denote by (x, y, z) and (x', y', z') their

coordinates. The three reference systems are related by the change of variables

$$\begin{array}{rcccl} X & = & \gamma x + \gamma_1 & = & \gamma x' + \gamma_1', \\ Y & = & \gamma y + \gamma_2 & = & \gamma y' + \gamma_2', \\ Z & = & \gamma z + \gamma_3 & = & \gamma z' + \gamma_3', \\ \dot{X} & = & \gamma \dot{x} & = & \gamma \dot{x}', \\ \dot{Y} & = & \gamma \dot{y} & = & \gamma \dot{y}', \\ \dot{Z} & = & \gamma \dot{z} & = & \gamma \dot{z}', \end{array} \tag{3.20}$$

where $(\gamma_1, \gamma_2, \gamma_3)$ and $(\gamma_1', \gamma_2', \gamma_3')$ are the coordinates of the departure and target SRP libration points in the CR3BP reference system, and $\gamma = 0.01$, is a convenient scaling factor introduced to normalize the Earth-equilibrium point distance (using this scaling factor the distance from the Earth to the SL_2 point in the local reference frames is approximately one, corresponding to about 1.5×10^6 km in physical units). In Fig. 3.2 we schematically show the three reference systems involved when, by means of a solar-sail maneuver, we intend to connect a LPO around SL_2 with another one around $SL_2^{'}$.

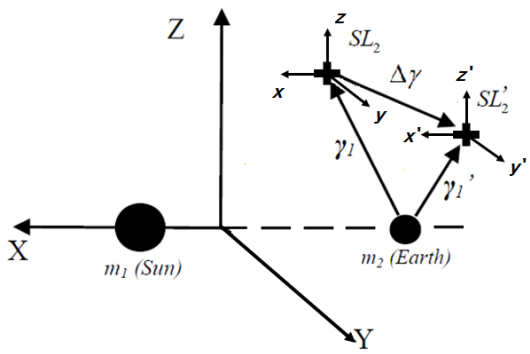

Figure 3.2: Schematic representation of the three reference systems involved in the study of solar-sail maneuvers. Due to the maneuver, the equilibrium point moves from SL_2 (position before the maneuver) to $SL_2^{'}$ (position after the maneuver).

An interesting dynamical remark on solar-sail maneuvers using always these SLi centered local reference frames is that, contrary to usual impulsive maneuvers that involve a change in velocities (known as a a Δv), the solar-sail maneuver changes the position coordinates of the artificial equilibrium point but keeps the velocity. So it can be assumed as a jump in position in the (lowercase) local frame, although in the usual CR3BP the orbit is continuous in both position and velocity. For example, assume initial and final cone angle are $\alpha_i = 0, \alpha = \pi/3$, the corresponding position and velocity change curves in the coordinate system are shown in Figure 3.3 and Figure 3.4.

In Fig. 3.3, the red star point is the starting point and the spacecraft moves along the blue curve. at some time, changes the cone angle from 0 to $\pi/3$, its position will "jump"

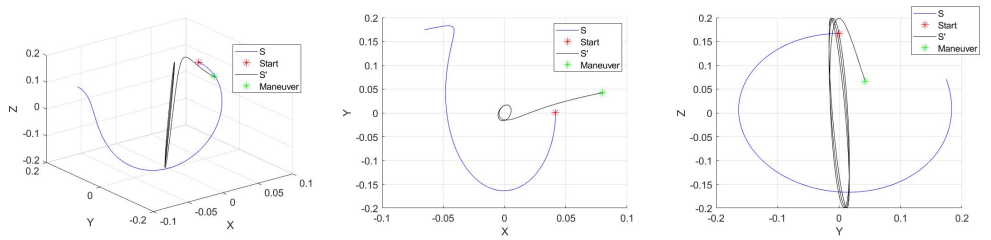

(a) 3D (b) XY plane (c) YZ plane

Figure 3.3: Position change curve of the solar sail spacecraft after changing the cone angle.

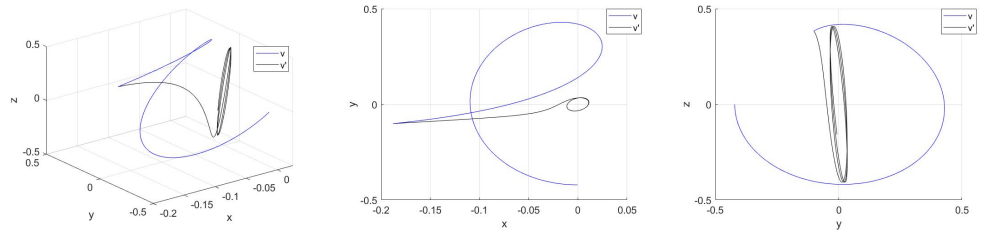

(a) 3D (b) XY plane (c) YZ plane

Figure 3.4: Velocity change curve of the solar sail spacecraft after changing the cone angle.

to the green star point in the new coordinate system and will move along the black curve. Similarly, in Fig. 3.4, the speed curve remains continuous.

Assuming that we are departing from a Lissajous orbit by means of a trajectory on its unstable manifold, we accomplish an heteroclinic enhanced connection by means of a solar-sail maneuver that injects on the stable manifold of the target one. In what follows, we study the characteristics of the these transfers considering:

- Maneuvers that change of the cone angle α of the sail.
- Maneuvers that change of the clock angle δ of the sail.
- Maneuvers that change the lightness number β of the sail.
- Dependency on the phases, ϕ_1 and ϕ_2, of the departing point.
- Dependency on the amplitudes of the departing Lissajous orbit.

3.3 Heteroclinic enhanced connections varying α

3.3.1 Heteroclinic enhanced connections when varying α for a fixed ϕ_1 and ϕ_2

We note that to obtain such connection between two Lissajous orbits, the unstable component, A_u, of the arrival one should be equal to zero after the solar-sail maneuver. In this section we explore the changes of the cone angle α that fulfill this arrival condition. For all the computations that follow we keep fixed the value of the clock angle $\delta = \pi/2$, the lightness number $\beta = 0.02$, the phases of the departing point $\phi_1 = \phi_2 = 0$, and the size of the departing orbit, given by the normalized amplitudes $A_x = 1/24$ and $A_z = 1/6$.

Since the departure of the initial Lissajous orbit is done along its unstable manifold, we must set the amplitudes $A_s = 0$ and $A_u \neq 0$; we have used $A_u = -10^{-4}$. Fixing the values of the phases ϕ_1 and ϕ_2 at $t_0 = 0$ we are selecting an orbit of the unstable manifold of the Lissajous orbit, the whole manifold of the orbit can be obtained varying the values of these phases. Along the selected orbit on the unstable manifold we consider a fixed time step of $\Delta t = 10^{-4}$ adimensional time units, for a maximum time interval of $t_{max} - t_0 = 15$ adimensional time units. At each time step we consider a potential change in the cone angle from its initial value α_i to a final one α_f. This means that the cone angle variation we consider is always equal to $\Delta\alpha = \alpha_f - \alpha_i$. Then, we compute the unstable component of the resulting trajectory associated to the new sail parameters in order to check for the condition $A'_u = 0$, that guarantees that we are on the stable manifold of a Lissajous orbit. The computations are done according to the following scheme:

1. Initialize the parameters: μ, α_i, α_f, δ, β, $\phi_1 = \phi_2 = 0$, $t_0 = 0$, Δt, t_{max}, and the amplitudes A_x and A_z (from which ones we can compute A_3, A_4, A_5 and A_6 using the Eqs. (3.14)).

2. Set $\alpha = \alpha_i$, and compute the coordinates $(\gamma_1, \gamma_2, \gamma_3)$ of the equilibrium point.

3. Using the expressions given in Appendix B, compute the coefficients of the polynomial in Eqs. (3.6), and its roots: λ_1, λ_2, $\lambda_{3,4} = \eta_1 \pm \omega_1 i$, $\lambda_{5,6} = \eta_2 \pm \omega_2 i$.

4. Using the expressions given in Appendix C, compute the matrix $H(t)$ and determine the state $(x, y, z, \dot{x}, \dot{y}, \dot{z})$ at time t.

5. Change α_i to α_f and compute the position of the new artificial equilibrium point $(\gamma'_1, \gamma'_2, \gamma'_3)$, as well as $(x', y', z', \dot{x}', \dot{y}', \dot{z}')$ by means of (3.20).

6. Since the vectorfield is autonomous, we can use (3.13) to get the values of the resulting amplitudes $A'_1 = A'_u$, $A'_2 = A'_s$, A'_3, A'_4, A'_5, A'_6 after the maneuver.

7. Store the values of t and the obtained unstable amplitude A'_u.

8. Set $t = t + \Delta t$ and, if $t < t_{max}$, go to step 5.

We have always taken an initial cone angle $\alpha_i = 0$, so the cone angle reorientation is $\Delta\alpha = \alpha_f - \alpha_i = \alpha_f$.

3.3.1.1 Evolution of the final unstable amplitude for positive and negative cone angle maneuvers

The analysis of the results is divided into two cases: $\Delta\alpha = \alpha_f > 0$ and $\Delta\alpha = \alpha_f < 0$. For both cases, Fig. 3.5 shows a typical evolution of A'_u as a function of the maneuver time (this is the time where the value of α changes from $\alpha_i = 0$ to α_f). In the plots of the figure, each line represents a different value of $\Delta\alpha = \alpha_f$. The values that have been explored are $\Delta\alpha \in (0.01, \pi/2)$ (left plot) and $\Delta\alpha \in (-0.01, -\pi/2)$ (right plot).

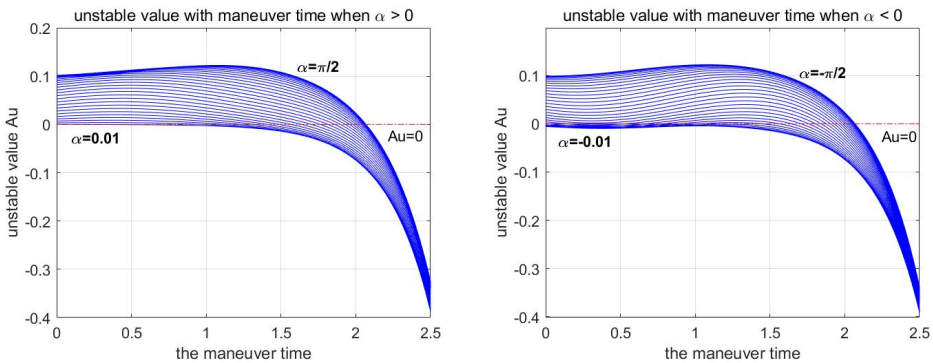

Figure 3.5: Behavior of A'_u with maneuver time for $\Delta\alpha = \alpha_f \in (0.01, \pi/2)$ (left) and for $\Delta\alpha = \alpha_f \in (-0.01, -\pi/2)$ (right).

From the left plot of the figure it follows that, for any fixed value of $\alpha_f > 0$, there is only one value of the maneuver time for which A'_u is zero. These values will be the suitable epochs (after departure) to perform the transfer maneuver by means of a change of the cone angle.

As an example, Fig. 3.6 shows the transfer connection associated to $\Delta\alpha = \pi/4$. The solar-sail reorientation is performed after 1.9 adimensional time units after the departure from the initial Lissajous orbit (in blue). The red star indicates the departing point along the unstable manifold of the initial orbit, and the green star the location of the reorientation maneuver, from this point on the orbit follows an orbit on the stable manifold of the arrival Lissajous orbit (in black). The explanation of the color symbols in Fig. 3.6 is shown in Table. 3.2, and the comparison of various parameters before and after the solar sail impulse maneuver is shown in Table. 3.3.

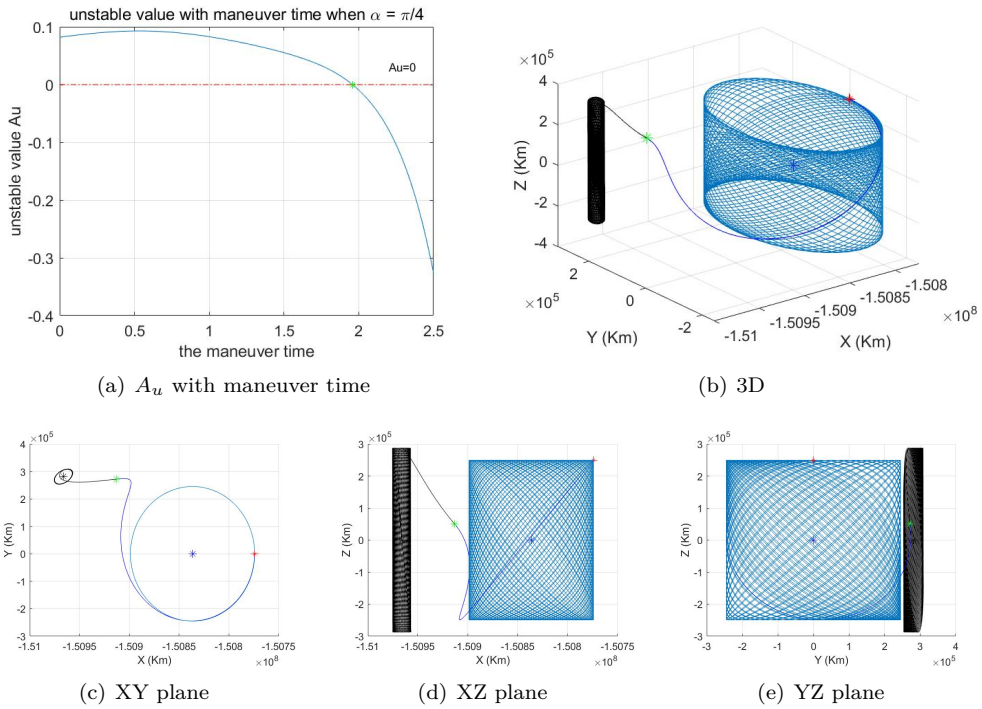

(a) A_u with maneuver time (b) 3D

(c) XY plane (d) XZ plane (e) YZ plane

Figure 3.6: Evolution of the final unstable amplitude A_u for $\alpha_f = \pi/4$ (top left), 3D representation and coordinate projections of the initial (in blue) and final (in black) Lissajous orbits. The orbit plots are in the (X, Y, Z) CR3BP reference frame, but using physical units (km).

Table 3.2: Explanation of the symbols used in Fig. 3.6.

Symbol	Explanation
blue cylinder	initial Lissajous orbit
black cylinder	final Lissajous orbit
blue orbit	unstable manifold
*	initial SL_2 artificial libration point
*	final SL_2 artificial libration point
+	starting point of the unstable manifold
*	impulse maneuver moment for the solar sail

Table 3.3: Variation of sail and orbit parameters before and after the solar sail impulse maneuver when $\alpha_f = \pi/4$.

Initial parameter	Initial parameter value	Final parameter	Final parameter value
α_i	0	α_f	$\pi/4$
δ_i	$\pi/2$	δ_f	$\pi/2$
β_i	0.02	β_f	0.02
γ_1	-1.00828	γ_{1f}	-1.00915
γ_2	0	γ_{2f}	0.00188
γ_3	0	γ_{3f}	0
A_x	0.0417	A_{xf}	0.0062
A_z	0.1667	A_{zf}	0.1921

From the right panel of Fig. 3.5 we find that, when $\Delta\alpha = \alpha_f < 0$, there are four different behaviors, according to the number of crossings with the $A'_u = 0$ axis of the lines associated to different α_f values. The curves $A'_u(\alpha_f)$ displayed in the figure have zero crossings with $A'_u = 0$ when $\alpha_f \in (-0.22, -0.01)$, one crossing when $\alpha_f \in (-\pi/2, -0.51)$, two crossings when $\alpha_f \in (-0.40, -0.23)$ and three crossings when $\alpha_f \in (-0.50, -0.41)$. In Fig. 3.7 we show one example of each case and in Fig. 3.8 we show the resulting connections obtained for each case (3D (X, Y, Z) CR3BP representation and XY-projections using physical units in km) of the initial (in blue) and final (in black, green and pink) Lissajous orbits associated to the transfers determined for $\alpha_f = -\pi/4$ (one $A'_u = 0$ crossing), $\alpha_f = -0.35$ (two $A'_u = 0$ crossings), and $\alpha_f = -0.45$ (three $A'_u = 0$ crossings). Fig. 3.8 shows also the projection of the transfer orbit onto the X-Y plane; clearly, if the value of α changes then the final Lissajous also does, and the corresponding impulse maneuver moments and the terminal Lissajous amplitudes are shown in the Table. 3.4.

Table 3.4: Impluse maneuver epochs for A_{xf} and A_{zf}, and $\alpha_f = -\pi/4, -0.35, -0.45$.

Final cone angle α_f	Maneuver epoch (days)	A_{xf} (10^6 km)	A_{zf} (10^6 km)
–$\pi/4$	113.42	15.25	28.76
–0.35	47.62	4.48	25.66
–0.35	94.12	12.15	25.52
–0.45	4.77	7.51	25.00
–0.45	34.71	1.57	26.42
–0.45	101.06	14.00	26.26

In the following we give some details about the behavior of the transitions between these three different situations.

1. When α_f varies between -0.52 and -0.50, the number of connections goes from 1 to 3, since in this interval the curve $A'_u(\alpha_f)$ goes through a tangency with the $A'_u = 0$ line for $\alpha_f \approx -0.51$. Fig. 3.9 shows the behavior of A'_u as a function of the

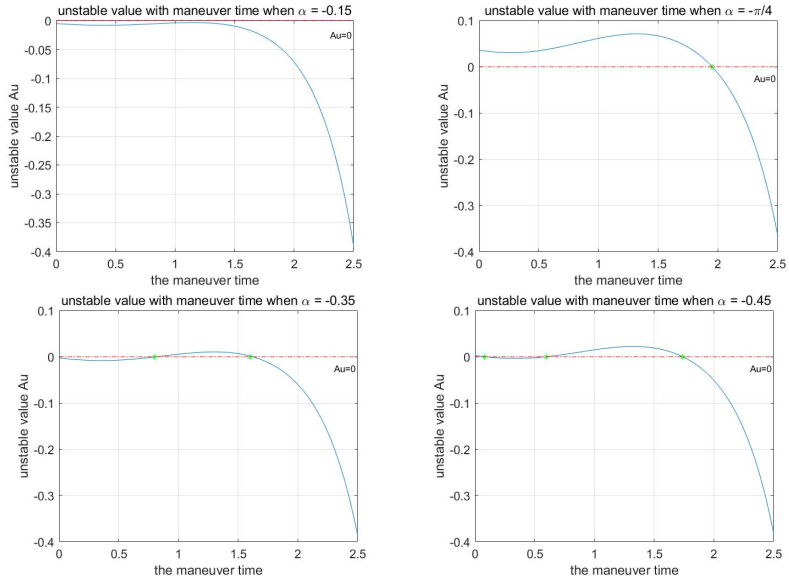

Figure 3.7: Behaviour of A_u with time for $\alpha = -0.15$ (zero crossings with $A_u = 0$), $\alpha_f = -\pi/4$ (one $A_u = 0$ crossing), $\alpha_f = -0.35$ (two $A_u = 0$ crossings), $\alpha_f = -0.45$ (three $A_u = 0$ crossings).

reorientation maneuver time for two α values: -0.50 and -0.51. For $\alpha = -0.50$ there are three connections, and for $\alpha = -0.51$ just one.

2. When α_f varies between -0.42 and -0.40, the number of connections goes from 3 to 2, since in this interval the curve $A_u(\alpha_f)$ goes through a tangency with the $A_u = 0$ line for $\alpha_f \approx -0.41$. The two top rows of Fig. 3.10 correspond to $\alpha = -0.40$ (with two connections), and $\alpha = -0.41$ (with three connections).

3. When α_f varies, approximately, between -0.23 and -0.20, the number of connections goes from 2 to 0, since in this interval the curve $A'_u(\alpha_f)$ goes through a tangency with the $A'_u = 0$ line for $\alpha_f \approx -0.20$. The bottom row of Fig. 3.10 shows the unique connection for $\alpha_f = -0.23$.

Table 3.5 gives the values of the reorientation maneuver time and amplitudes of the Lissajous final orbits in physical units, and Fig. 3.9 shows the departing and final Lissajous orbits together with the transfer path that follows the unstable manifold of the departing orbit, until the reorientation maneuver time, and the stable manifold of the final one.

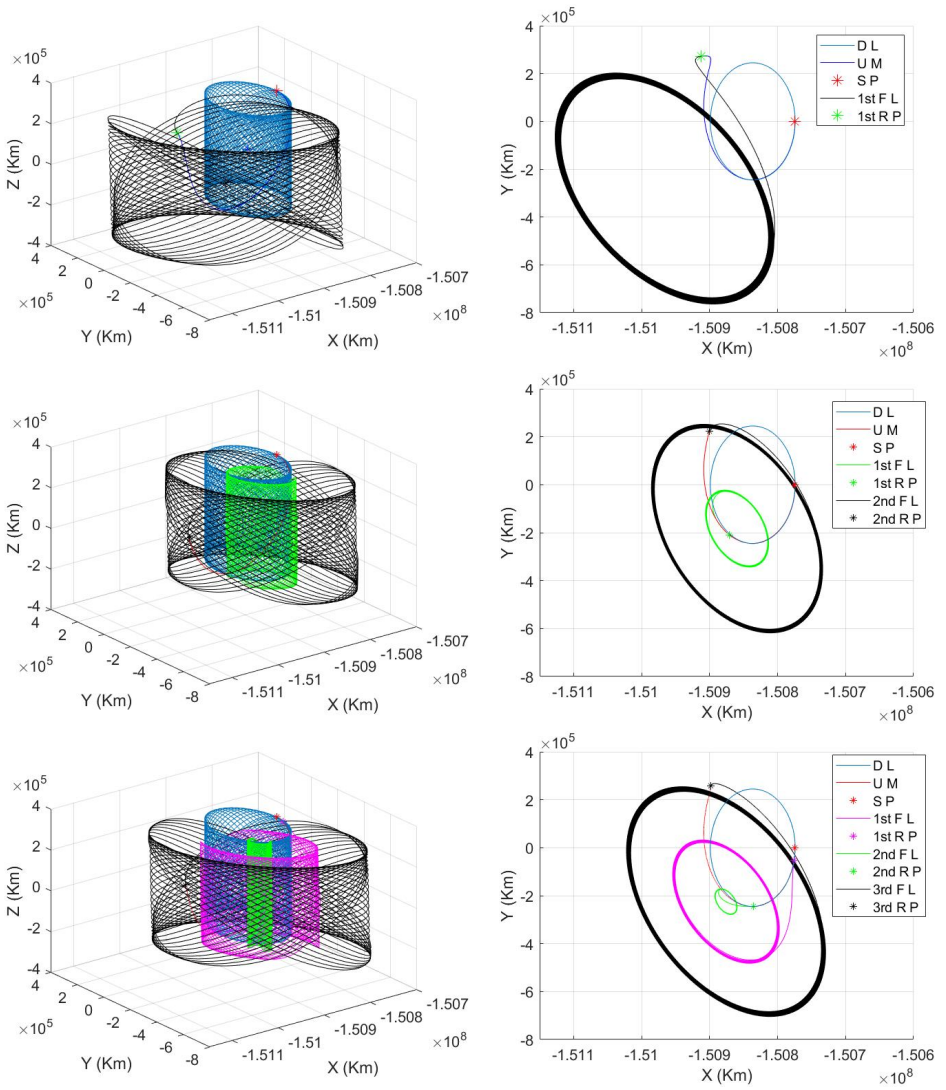

Figure 3.8: 3D representation and XY-coordinate projection for the three different cases with existing connections of Fig 3.7. In both representations, the departure Lissajous is blue and the final orbit black, green and magenta. The red star is the staring point from the departure orbit, and the black, green and pink ones the points where the reorientation maneuvers are done. The corresponding values of α, from top to bottom, are $-\pi/4$, -0.35 and -0.45, respectively. The codding of the abbreviations used in this figure and the following ones is: `DL` = Departing Lissajous, `FL` = Final Lissajous, `SP` = Starting Point, `RP` = Maneuver Reorientation Point, and `UM` = Unstable Manifold.

Table 3.5: Maneuver time and Lissajous final amplitudes of the connections close to the tangencies with $A'_u = 0$ for negative cone angle maneuvers.

α_f	Maneuver time (days)	Final X–amplitude A'_x (10^6 km)	Final Z–amplitude A'_z (10^6 km)
–0.51	104.2	14.8	26.78
–0.50	15.06	5.1	25.58
–0.50	23.08	2.8	26.18
–0.50	103.7	14.7	26.63
–0.41	0.39	8.15	24.94
–0.41	40.20	2.82	26.15
–0.41	98.66	13.35	25.96
–0.40	41.46	3.13	26.07
–0.40	98.00	13.17	25.88
–0.23	68.06	7.48	24.95
–0.23	75.12	8.42	24.94

3.3.1.2 Evolution of the planar and vertical amplitudes of the final Lissajous orbits for cone angle reorientation

We have seen how to perform a transfer from a given Lissajous orbit changing the cone angle parameter of the sail and keeping fixed the remaining sail parameters. Next we show how the X and Z amplitudes, A'_x and A'_z respectively, of the reached Lissajous orbit, as well as the epoch of the maneuver, depend on $\Delta\alpha$. The results obtained are given in Fig. 3.11. As it has already been said, for $\alpha \in (-0.22, -0.01)$ there is a gap associated to the fact that for these values of α the unstable amplitude A'_u does not intersect the $A'_u = 0$ line. In the top plots we show the amplitudes, A'_x,A'_z of the final Lissajous orbit as a function of the cone angle maneuver $\Delta\alpha$. The bottom plot shows the value of the epoch of the maneuver after the departure also as a function of the cone angle maneuver $\Delta\alpha$. When $\Delta\alpha = \alpha_f \in (-0.22, -0.01)$, there are no connections since for these values $A'_u \neq 0$.

3.3.1.3 Evolution of the reorientation maneuver time when $\alpha_i \neq 0$

In the previous computations we have set equal to zero the value of the cone angle before the maneuver ($\alpha_i = 0$); when this angle changes the maneuver time also does. Next we show how this time changes when α_i varies within its range, $(-\pi/2,\ \pi/2)$, keeping fixed the values of the remaining parameters: $\delta = \pi/2$, $A_s = 0$, $A_u = -10^{-4}$, $A_x = 1/24$, $A_z = 1/6$, and $\phi_1 = \phi_2 = 0$.

Figs. 3.12 and 3.13 show the results obtained when $\alpha_i \in (0,\ \pi/2)$. Note that in the plots of both figures $\alpha_f \in (0,\ \pi)$ instead of $\alpha_f \in (-\pi/2,\ \pi/2)$, so the results for $\alpha_f \in (\pi/2,\ \pi)$ are, in fact, the ones for $\alpha_f \in (-\pi/2,\ 0)$. This is because the maneuver time for $\alpha_f = -\pi/2$ coincides with the one for $\alpha_f = \pi/2$.

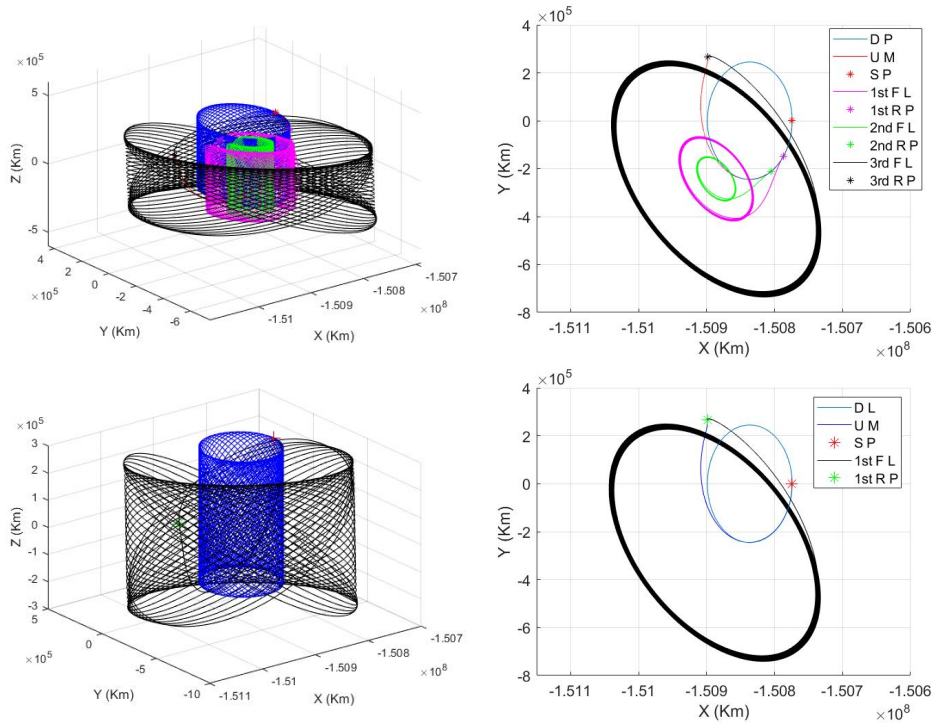

Figure 3.9: Departing (blue) and final Lissajous orbits (black, green, and magenta), together with the connecting path in the unstable manifold of the departing orbit (before the reorientation maneuver), and in the stable manifold of the final one (after the maneuver). The results correspond to $\alpha_f = -0.50$ (top) and $\alpha_f = -0.51$ (bottom). The color and label codes are the same as in Fig 3.8.

As in the case $\alpha_i = 0$, we have also that, depending on the value of $\Delta\alpha = \alpha_f - \alpha_i$, there are 0, 1 2 or 3 possible transfer times, giving $A'_u = 0$ after the the maneuver. For all possible values of α_i we get values of the solar-sail time maneuver very close to zero, which means that we can perform a transfer without using the unstable orbit of the departing Lissajous orbit. When $\alpha_i > 1.087$ it appears a gap in the possible values of the transfer time around $t_{trans} = 0.7$. The size of the gap increases, and for $\alpha_i \in (1.186,\ 1.189)$ there are no possible transfers. Transfer possibilities appear again for $\alpha_i = 1.189$. From this value on, the corresponding maximum maneuver time increases until the α_i equals to $\pi/2$. Note that the range of the possible maneuver values $\Delta\alpha = \alpha_f - \alpha_i$ also varies with α_i.

Finally, Fig. 3.14 shows the maneuver times and the final X and Z amplitudes, when both the initial and final cone angles α_i and α_f vary in $(-\pi/2, \pi/2)$. The right bottom plot of this figure is the projection on the $\alpha_i - \alpha_f$ plane of the three above plots. Note that this projection has three unconnected regions: the smaller region on the right is related to the gap already mentioned for $\alpha_i > 1.087$, the other two regions correspond to $\alpha_f < \alpha_i$ (lower region), and $\alpha_f > \alpha_i$ (upper region).

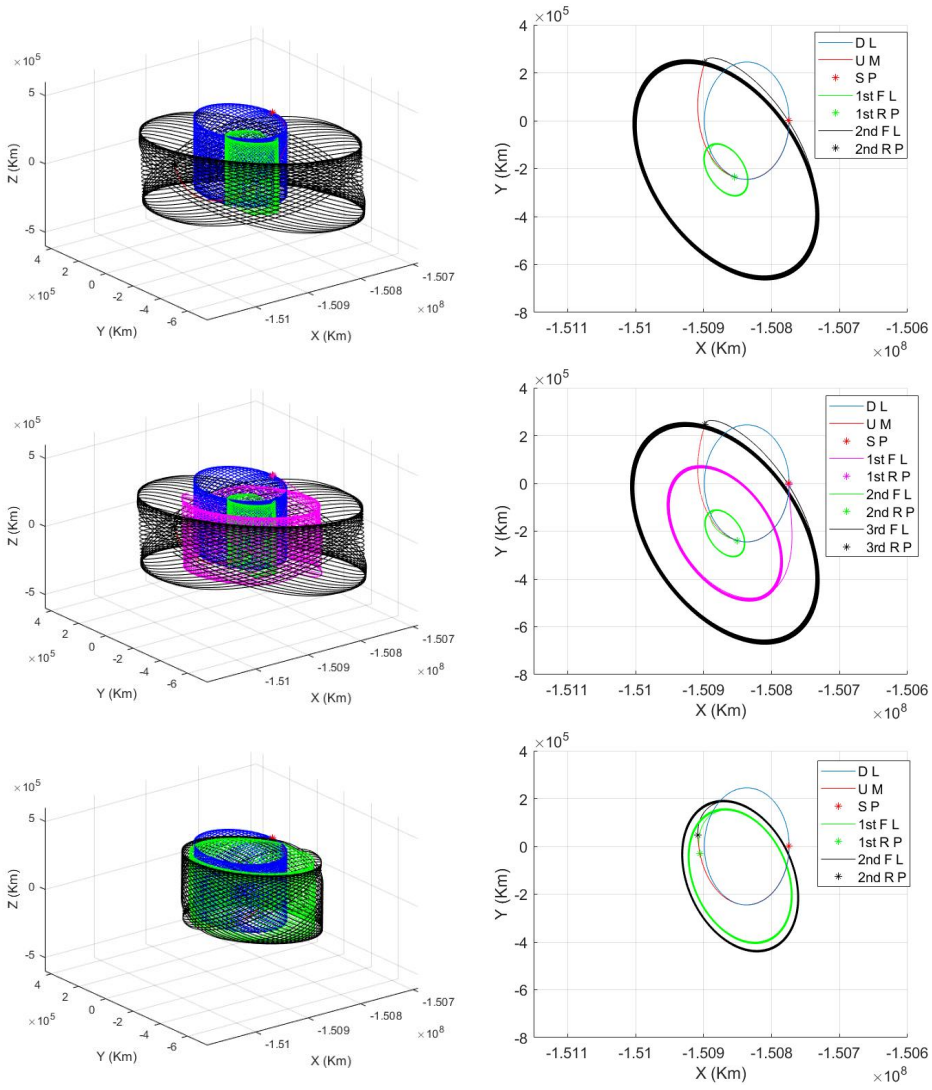

Figure 3.10: Same as Fig. 3.9 but for $\alpha_f \in (-0.41, -0.40)$ (first two rows) and $\alpha_f = -0.23$ (bottom row).

3.3.2 Heteroclinic enhanced connections varying α, ϕ_1 and ϕ_2

In the previous section we studied connections associated to changes of the cone angle for initial phases $\phi_1 = \phi_2 = 0$, which means that only one orbit of the unstable manifold of the departing Lissajous orbit is considered. Next we allow variations in both phases in order to explore the full unstable manifold of the Lissajous orbit, enlarging this way the transfer possibilities.

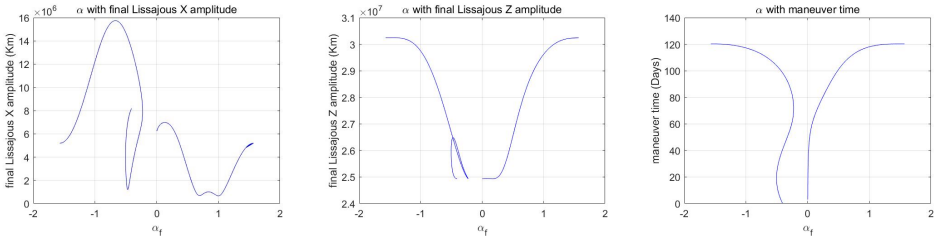

Figure 3.11: Final cone angle with X,Z Amplitudes and maneuver time.

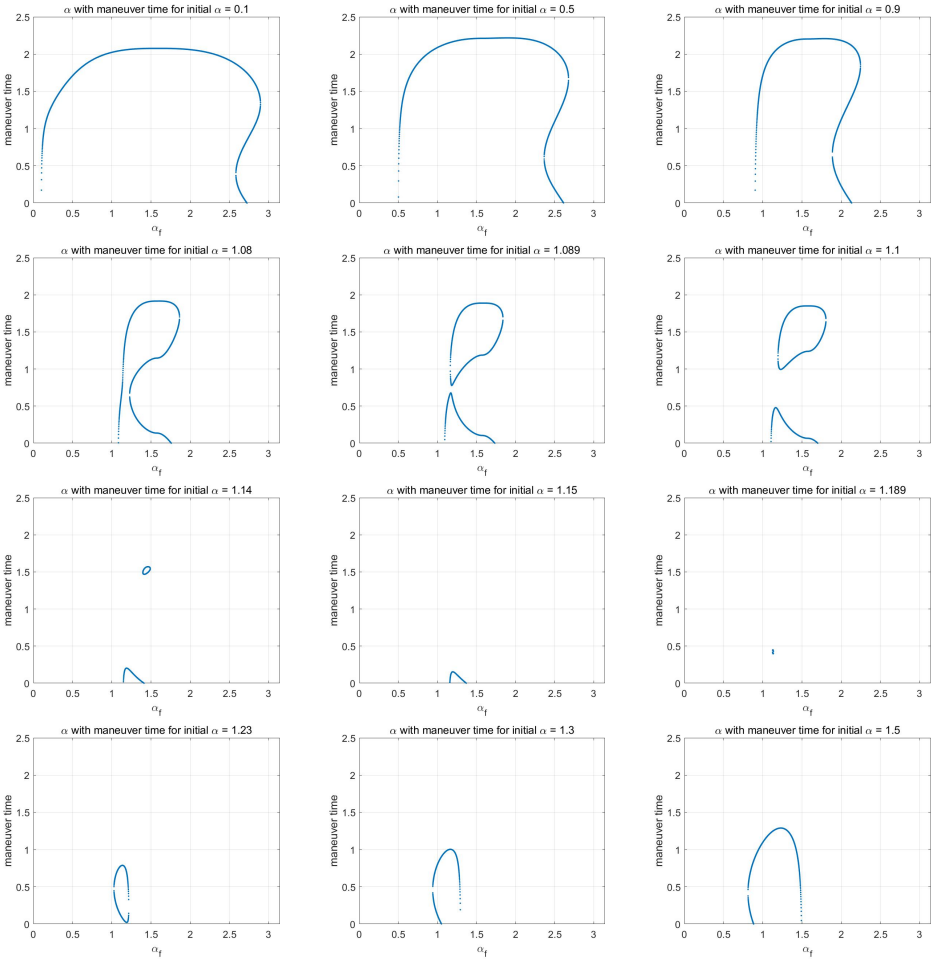

Figure 3.12: Reorientation maneuver time as a function of α_f, for different initial cone angles $\alpha_i \in (0,\ \pi/2)$. The applied reorientation maneuver is $\Delta\alpha = \alpha_f - \alpha_i$.

As in the preceding section, for all the explorations that follow we fix the initial and final values of the clock angle $\delta = \pi/2$, as well as the size of the departing orbit, given by the

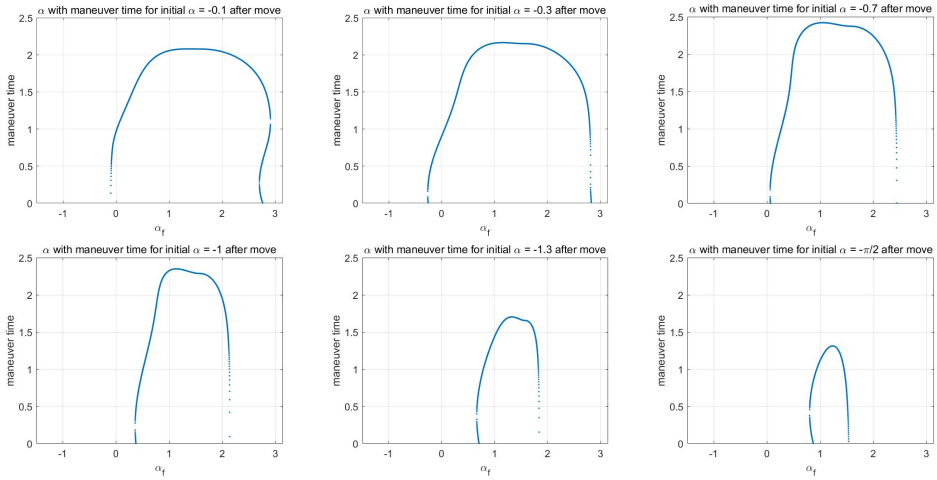

Figure 3.13: Reorientation maneuver time as a function of α_f, for different initial cone angles $\alpha_i \in (-\pi/2,\ 0)$.

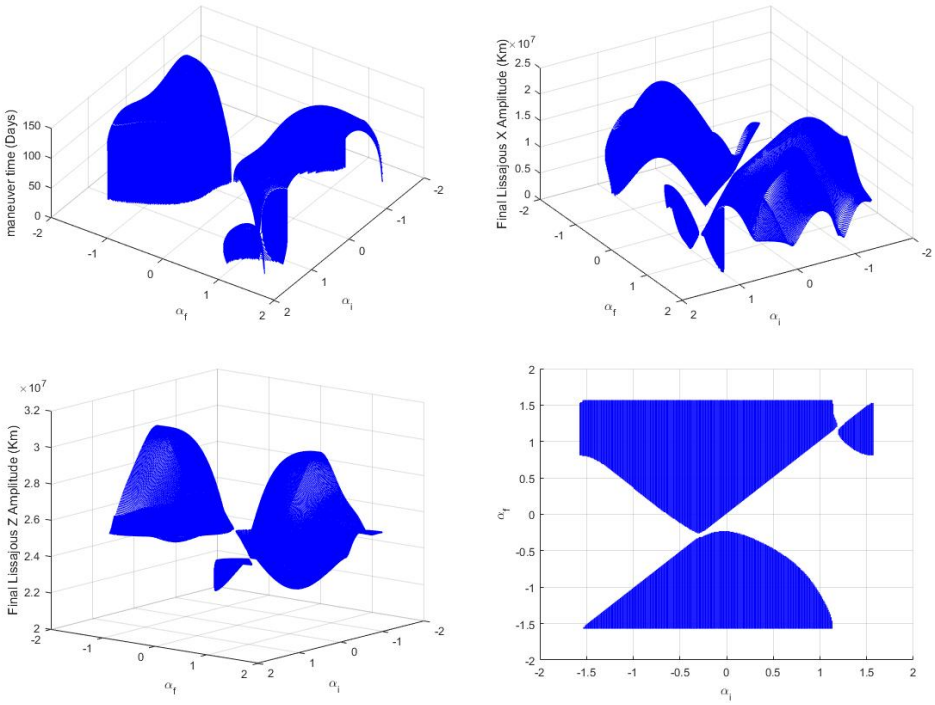

Figure 3.14: Reorientation maneuver times, and final X and Z amplitudes as a function of the initial and final cone angles α_i and α_f. The right bottom plot is the projection on the $\alpha_i - \alpha_f$ plane of the above three plots.

amplitudes $A_x = 1/24$ and $A_z = 1/6$ in normalized units.

With the above mentioned parameters, together with $\alpha_i = 0$, $\alpha_f = \pi/4$, keeping fixed $\phi_2 = 0$, and varying $\phi_1 \in (-\pi/2, 3\pi/2)$, for each value of ϕ_1 there is only one possible connection. Fig. 3.15 shows the values of the maneuver time as well as the X and Z amplitudes of the final Lissajous orbit reached with the solar-sail maneuver.

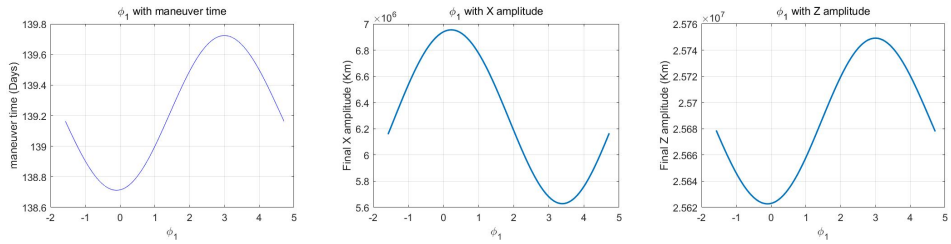

Figure 3.15: Maneuver times and final X and Z amplitudes, when $\phi_1 \in (-\pi/2, 3\pi/2)$ and $\phi_2 = 0$.

If instead of keeping fixed $\phi_2 = 0$ we fix $\phi_1 = 0$ and vary $\phi_2 \in (-\pi/2, 3\pi/2)$, for each value of ϕ_2 there is only one possible connection when, as before, $\alpha_i = 0$ and $\alpha_f = \pi/4$. Fig 3.16 shows the maneuver times as well as the X and Z amplitudes of the final Lissajous orbit reached with the solar-sail maneuver. Clearly in this case, the variation of ϕ_2 does not affect the maneuver time and the final $X-$amplitude; only the $Z-$amplitude of the final Lissajous orbits varies.

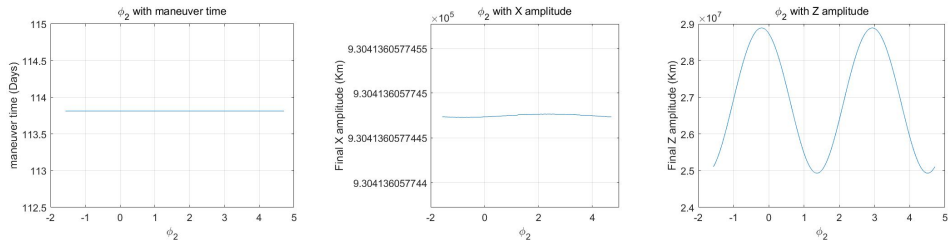

Figure 3.16: Maneuver times and final X and Z amplitudes, when $\phi_1 = 0$ and $\phi_2 \in (-\pi/2, 3\pi/2)$.

When the condition $\alpha_f = \pi/4$ is removed, allowing α_f to vary in $(-\pi/2, \pi/2)$, Figs. 3.17 and 3.18 show the values of the maneuver time, as well as the X and Z amplitudes of the final Lissajous orbit, for $\phi_1 \in (-\pi/2, 3\pi/2)$, $\phi_2 = 0$ and $\phi_1 = 0$, $\phi_2 \in (-\pi/2, 3\pi/2)$, respectively. Each transfer corresponds to different values of (α_f, ϕ_1) in the first figure, and of (α_f, ϕ_2) in the second one. Fig. 3.18 shows that the variations of ϕ_2 only modify the final Z amplitude, not affecting the maneuver time and the final X amplitude.

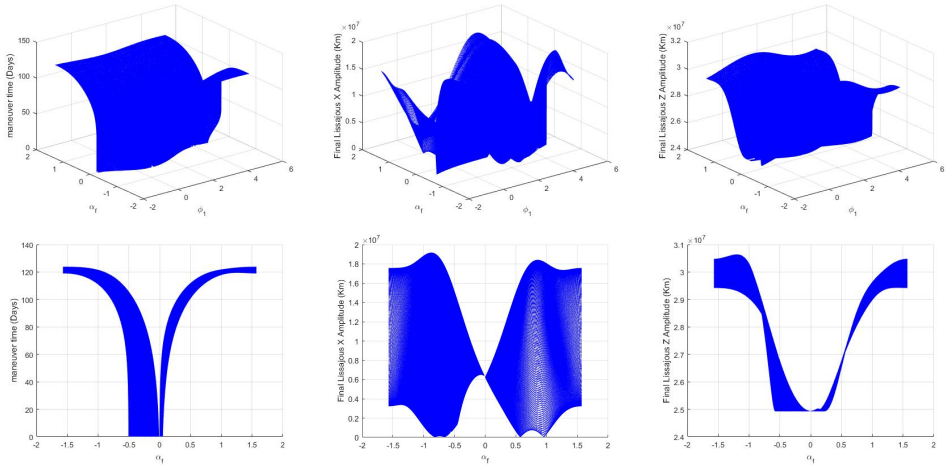

Figure 3.17: Reorientation maneuver times (left) and final X (middle) and Z (right) amplitudes , when $\phi_1 \in (-\pi/2,\, 3\pi/2)$, $\phi_2 = 0$ and $\alpha_f \in (-\pi/2,\, \pi/2)$.

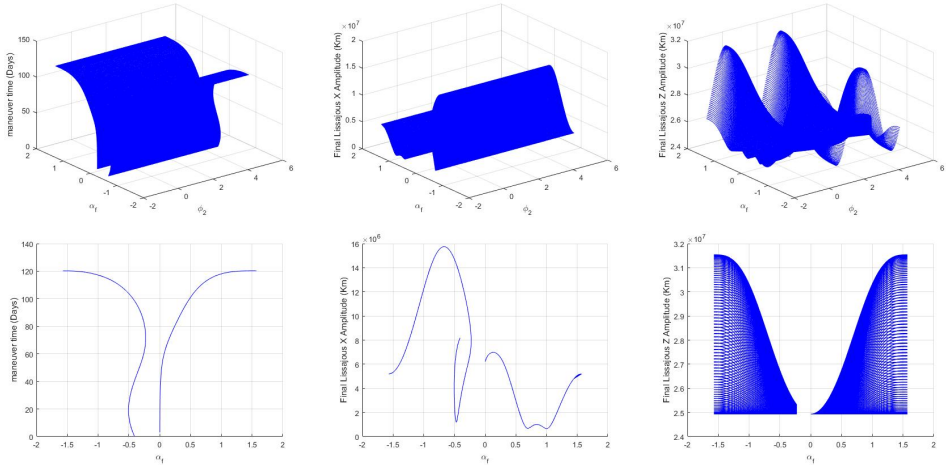

Figure 3.18: Reorientation maneuver times (left) and final X (middle) and Z (right) amplitudes , when $\phi_1 = 0$, $\phi_2 \in (-\pi/2,\, 3\pi/2)$, and $\alpha_f \in (-\pi/2,\, \pi/2)$.

3.4 Heteroclinic enhanced connections varying δ

3.4.1 Heteroclinic enhanced connections when varying δ for a fixed ϕ_1 and ϕ_2

In this section we study connections between Lissajous orbits by means of changing the clock angle δ for different fixed values of α_i. As in the preceding section, we keep fixed

the value of the lightness number $\beta = 0.02$, and the size of the departing orbit, given by the amplitudes $A_x = 1/24$, and $A_z = 1/6$ in adimensional units.

Again, during the adimensional time interval $[0,\ 15]$ we explore the leg of the unstable manifold of the departing orbit taking $A_u = -10^{-4}$, $A_s = 0$, and starting phases at $t = 0$: $\phi_1 = \phi_2 = 0$. Along the states of this orbit we consider a potential change of the initial clock angle $\delta_i = \pi/2$ into a fixed final value $\delta_f \in (0, \pi)$, so the maneuver is given by $\Delta\delta = \delta_f - \delta_i \in (-\pi,\ \pi)$. Then we compute the unstable component of the resulting state, associated to the new sail parameters, looking for the connection condition $A'_u = 0$. The resulting unstable amplitude curves $A'_u(t)$ depend on the value of α_i, and for $\alpha_i = -0.45,\ -0.78,\ +0.78$ are given in Fig. 3.19.

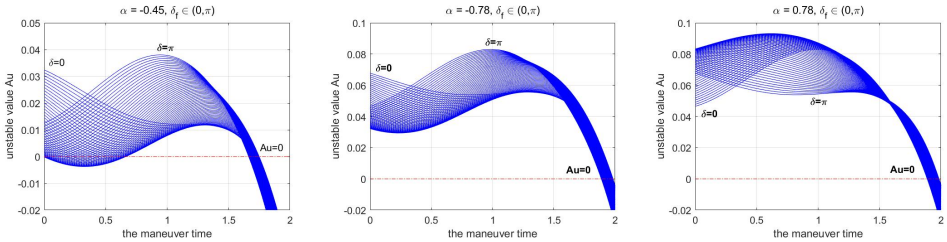

Figure 3.19: Behavior of A'_u vs maneuver time for $\alpha_f = -0.45, -0.78$ and 0.78, and $\delta_f \in (0, \pi)$.

Each curve in Fig. 3.19 corresponds to a different value of $\delta_f \in (0, \pi)$. It follows that if $\alpha_i = -0.45$, there are three different behaviors, according to the number of crossings of the $A'_u = 0$ axis of the lines associated to different δ_f values. This number can be one if $\delta_f \in (2.33, \pi)$, two when $\delta_f \in (1.94, 2.19)$, or three when $\delta_f \in (0.92, 1.93)$ and $\delta_f \in (2.20, 2.34)$. For the other two values of α_i, there are no transfer possibilities, since there are no crossings with the $A'_u = 0$ line. Fig. 3.20 shows the three amplitude curves $A'_u(t)$ for $\delta_f = 0$ (only one $A'_u = 0$ crossing), $\delta_f = 1.6$ (three $A'_u = 0$ crossings), and $\delta_f = 2$ (two $A'_u = 0$ crossings), and Fig. 3.21 shows the initial, transfer and final orbits obtained for each case.

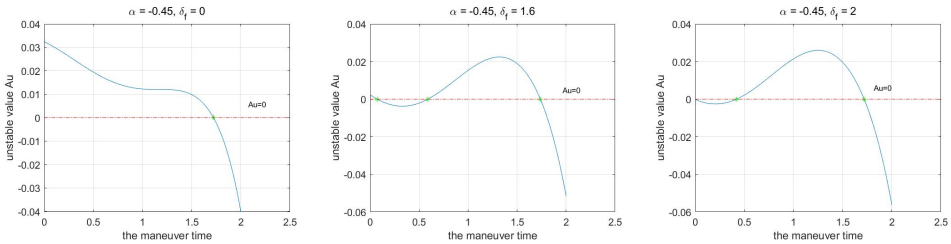

Figure 3.20: Behavior of the unstable amplitude curves $A'_u(t)$ for $\alpha_i = -0.45$, $\delta_i = \pi/2$, and different $\Delta\delta = \delta_f - \delta_i$ maneuvers.

Next we explore four different cases, according to the value of α_i, that, as we have seen can produce one, two, or three different connections. Fig. 3.22 shows the results obtained for $\alpha_i = \pi/4,\ -0.35,\ -0.45$, and $-\pi/4 = -0.7854$ (with $\Delta\alpha = \alpha_f - \alpha_i = 0$). For all the

computations $\delta_i = \pi/2$ is fixed, and δ_f varies in $(0, \pi)$.

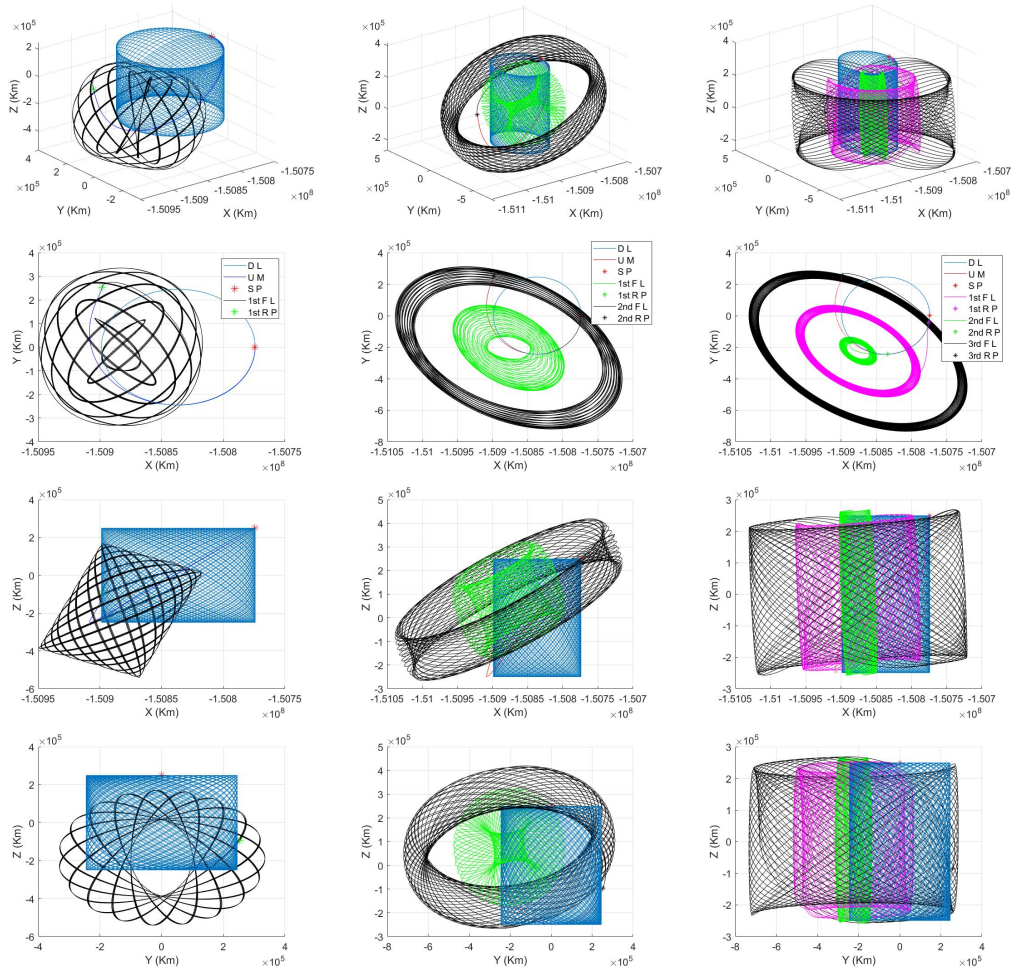

Figure 3.21: The left, central, and right columns correspond to $\delta_f = 0$ (one $A'_u = 0$ crossing), $\delta_f = 2$ (two $A'_u = 0$ crossings), and $\delta_f = 1.6$ (three $A'_u = 0$ crossings), respectively.

From the plots in the top and bottom rows of Fig. 3.22, corresponding to $\alpha_i = \pi/4$ and $\alpha_i = -\pi/4$, we can conclude that changing the δ_f value does not affect the number of crossing with the $A'_u = 0$ axis. The two middle rows, corresponding to $\alpha_i = -0.35$, and $\alpha_i = -0.45$, correspond to parameter values for which there are one, two or three transfer possibilities when $\delta_f \in (0, \pi)$. Next we give some detailed results about these transitions when $\alpha_i = -0.45$, which are summarized in Table 3.6. This table shows the the values

of the maneuver time and amplitudes of the Lissajous final orbits before and after the tangency.

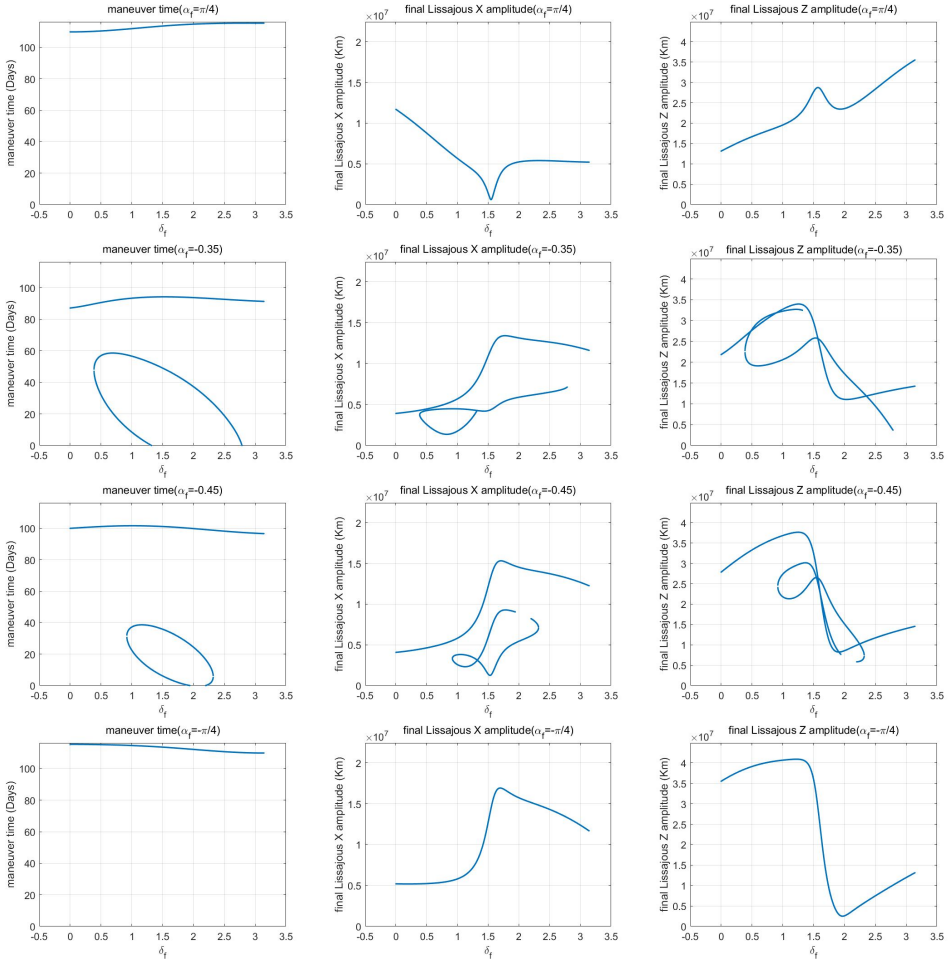

Figure 3.22: Behavior of the maneuver time, the A'_x, A'_z amplitudes as a function of δ maneuvers. The results correspond to $\alpha_f = \pi/4$, -0.35, -0.45 and $-\pi/4$.

1. When δ_f varies between 0.91 and 0.92, the number of transfers goes from 1 to 3, since in this interval the curve $A'_u(\delta_f)$ goes through a tangency with the $A'_u = 0$ line for $\delta_f \approx 0.905$. The trajectory is shown in the first row of Fig. 3.23.

2. When δ_f varies between 1.94 and 1.95, the number of transfers goes from 3 to 2, since in this interval the curve $A'_u(\delta_f)$ goes through a tangency with the $A'_u = 0$ line for $\delta_f \approx 1.94$. The trajectory is shown in the second row of Fig. 3.23.

3. When δ_f varies between 2.19 and 2.20, the number of transfers goes from 2 to 3, since in this interval the curve $A'_u(\delta_f)$ goes through a tangency with the $A'_u = 0$ line for $\delta_f \approx 2.20$. The trajectory is shown in the third row of Fig. 3.23.

4. When δ_f varies between 2.31 and 2.32, the number of transfers goes from 3 to 1, since in this interval the curve $A'_u(\alpha_f)$ goes through a tangency with the $A'_u = 0$ line for $\delta_f \approx 2.32$. The trajectory is shown in the fourth row of Fig. 3.23.

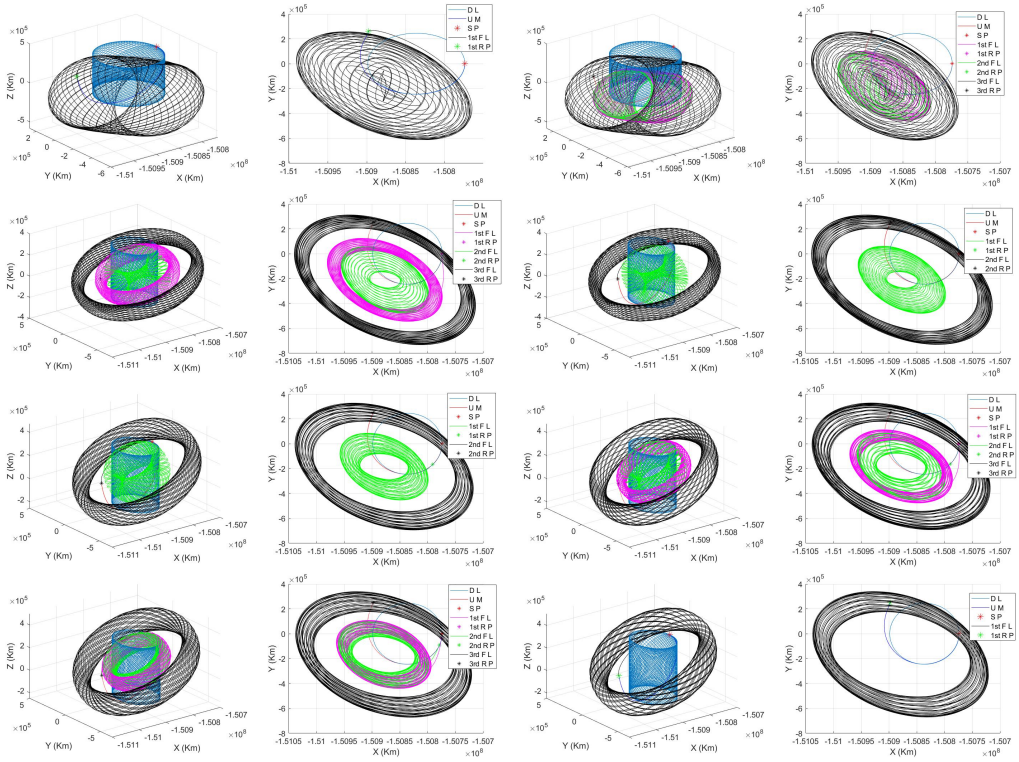

Figure 3.23: Transfers between the same departing Lissajou orbit (blue) to different final ones (black, green, and magenta), associated to different values of δ_f. The color and label codes are the same as in Fig 3.8.

Fig. 3.23 shows the departing (blue) and final Lissajous (green, magenta, and black) orbits, together with the transfer path that follows the unstable manifold of the departing orbit, until the maneuver time, and the stable manifold of the final one. The first row corresponds to the transition $\delta_f \in (0.91, 0.92)$, the second row corresponds to the transition $\delta_f \in (1.94, 1.95)$, the third row corresponds to the transition $\delta_f \in (2.19, 2.20)$, and fourth row corresponds to the transition $\delta_f \in (2.31, 2.32)$.

If we allow α_f to vary in $(-\pi/2, \pi/2)$ and $\delta_f \in (0, \pi)$ while keeping $\delta_i = \pi/2$ and $\phi_1 = \phi_2 = 0$, Fig. 3.24 shows the values of the maneuver time and the X and Z amplitudes, when $\alpha_f \in (-\pi/2, \pi/2)$, $\delta_f \in (0, \pi)$, and $\phi_1 = \phi_2 = 0$ in the top line. The bottom line shows the projection of the three surfaces on a coordinate plane: α_f-maneuver time, $\alpha_f - X$ amplitude, and $\alpha_f - Z$ amplitude.

In the preceding computations we have always set the value of the clock angle before the

Table 3.6: Maneuver time and Lissajous final amplitudes of the transfers close to the tangencies with $A_u = 0$ for clock angle maneuvers.

Tangency transition	δ_f	Maneuver time (days)	Final X–amplitude A_x (10^6 km)	Final Z–amplitude A_z (10^6 km)
$1 \to 3$	0.91	101.7	5.42	36.37
	0.92	30.2	3.22	24.85
	0.92	32.5	3.43	23.92
	0.92	101.7	5.54	36.41
$3 \to 2$	1.94	0.0009	9.05	7.67
	1.94	26.3	5.22	16.37
	1.94	100.1	14.68	8.29
	1.95	26.0	5.27	16.16
	1.95	100.0	14.65	8.32
$2 \to 3$	2.19	68.1	7.48	24.95
	2.19	75.1	8.42	24.94
	2.20	0.003	8.21	5.83
	2.20	16.4	6.12	11.20
	2.20	99.2	14.17	9.92
$3 \to 1$	2.31	3.59	7.41	6.69
	2.31	8.4	6.81	8.20
	2.31	98.8	14.02	10.62
	2.32	98.8	14.00	10.68

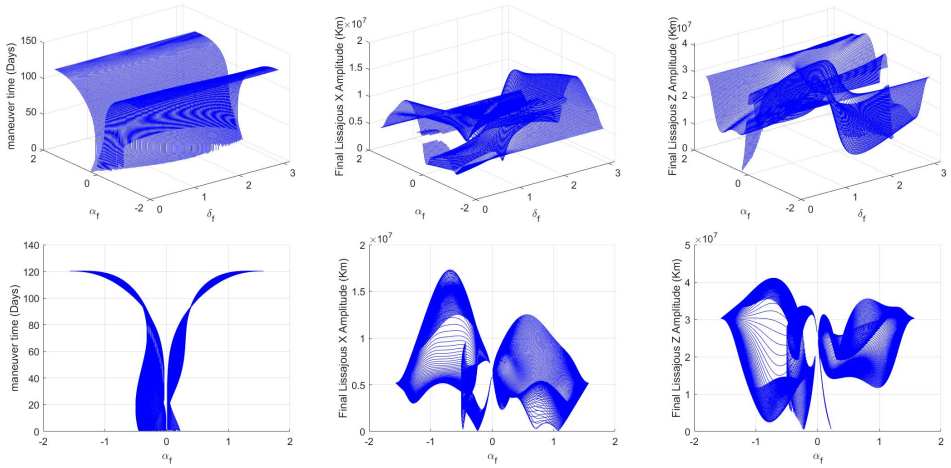

Figure 3.24: The values of the maneuver time and the X and Z amplitudes, when $\alpha_f \in (-\pi/2, \pi/2)$, $\delta_f \in (0, \pi)$, and $\phi_1 = \phi_2 = 0$.

maneuver, δ_i, equal to $\pi/2$. When this angle changes the maneuver time also does.

Fig. 3.25 shows the values of the maneuver time and the X and Z amplitudes, when

both the initial δ_i and final δ_f vary in $\in (0, \pi)$, keeping fixed the values of the remaining parameters: $\alpha_i = 0$, $\alpha_f = -0.45$, $A_u = -10^{-4}$, $A_x = 1/24$, $A_z = 1/6$, and $\phi_1 = \phi_2 = 0$. The bottom line the figure shows the projection of the three surfaces on a coordinate plane: δ_f-maneuver time, δ_f-X amplitude, and δ_f-Z amplitude. Comparing the bottom line in Fig. 3.25 and Fig. 3.22, we can conclude that δ_i does not affect the maneuver time and the final X and Z amplitudes.

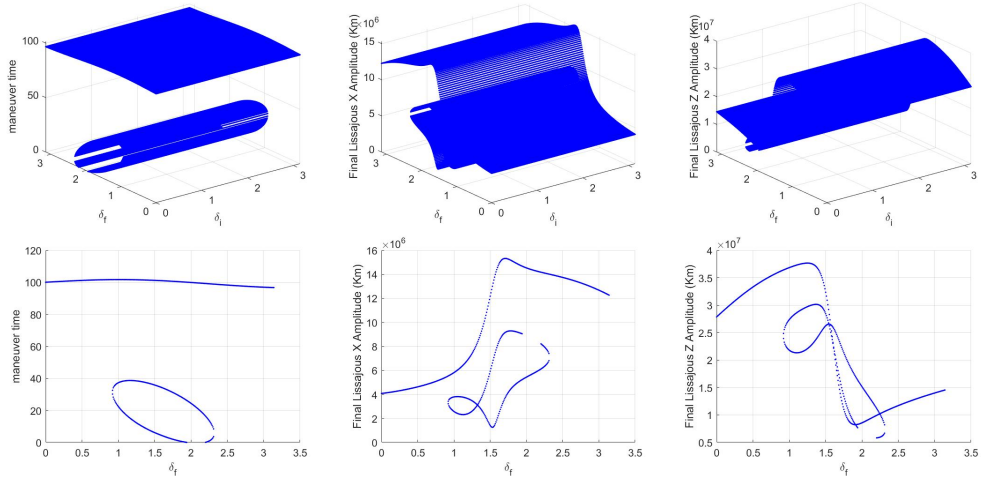

Figure 3.25: Maneuver times and final X and Z amplitudes, when α_f= -0.45, $\delta_i \in (0, \pi)$ and $\delta_f \in (0, \pi)$.

3.4.2 Heteroclinic enhanced connections when varying δ, ϕ_1 and ϕ_2

In the previous section we studied transfers associated to changes of the clock angle δ_f for fixed phases $\phi_1 = \phi_2 = 0$. Now we allow variations in both phases, which means that we consider different orbits of the unstable manifold of the departing Lissajous orbits.

As in the preceding section, for all the explorations that follow, we fix the initial and final values of the cone angle $\alpha_i = 0$, $\alpha_f = \pi/4$, as well as the size of the departing orbit, given by the amplitudes $A_x = 1/24$ and $A_z = 1/6$.

For the Fig. 3.26, In the first and third lines, values of the maneuver time and the X and Z amplitudes, when $\phi_1 \in (-\pi/2, 3\pi/2)$, $\phi_2 = 0$ (first line), and $\phi_1 = 0$, $\phi_2 \in (-\pi/2, 3\pi/2)$ (third line). In both cases $\delta_f \in (0, \pi)$. The second and forth lines show the projection of the surfaces on the coordinate planes: δ_f-maneuver time, δ_f-X amplitude, and δ_f-Z amplitude, respectively.

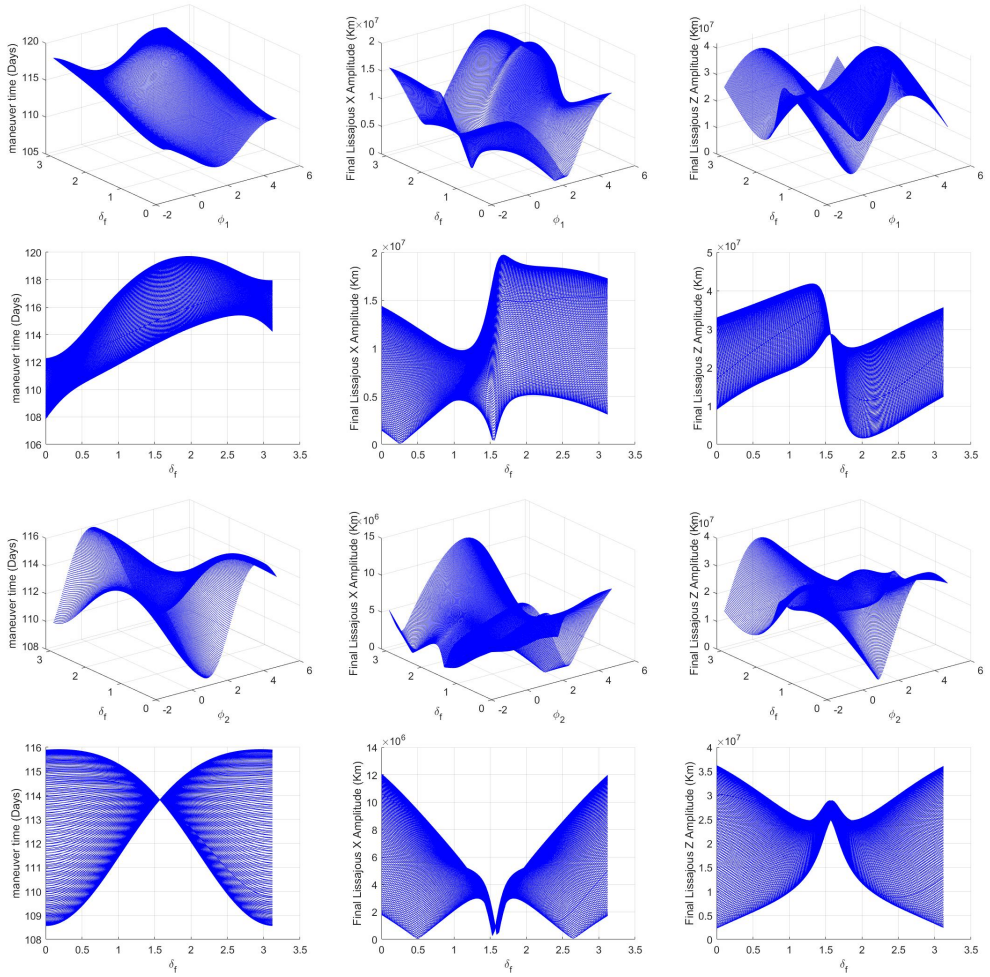

Figure 3.26: Values of the maneuver time and the final X and Z amplitudes, as function of ϕ_1, ϕ_2 and δ_f.

3.5 Heteroclinic enhanced connections when varying β

In this section, we consider the influence of variations of the β parameter when it varies in $(0.01, 0.1)$. The initial and final cone and clock angles are: $\alpha_i = 0$, $\alpha_f = \pi/4$, $\delta_i = \delta_f = \pi/2$. As in the preceding sections, the amplitudes of the Lissajous orbit are: $A_x = 1/24$ and $A_z = 1/6$.

Fig. 3.27 shows the values of the maneuver time and the X and Z amplitudes, when $\beta_i = 0$ and $\beta_f \in (0.01, 0.1)$. The top row correspond to use as transfer orbit the one of the unsta-

ble manifold departing from $\phi_1 = \phi_2 = 0$, and the bottom row when $\phi_1 \in (-\pi/2, 3\pi/2)$, $\phi_2 \in (-\pi/2, 3\pi/2)$. Fig. 3.28 displays 3D representation and XY coordinate projection of two transfers performed changing the cone angle from $\alpha_i = 0$ to $\alpha_f = \pi/4$, for two different values of the β parameter. Both departing Lissajous orbits have the same amplitudes $A_u = -10^{-4}, A_s = 0, A_x = 1/24, A_z = 1/4, \beta_i = 0.02$, but for $\beta_f = 0.01, 0.02, 0.03$.

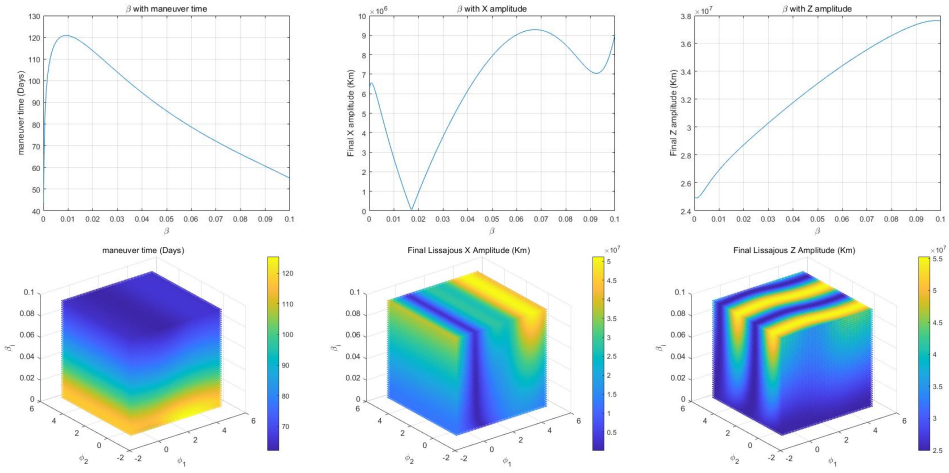

Figure 3.27: Maneuver times and final X and Z amplitudes, when $\beta_i = 0$, $\beta_f \in (0.01, 0.1)$ and $\phi_1, \phi_2 \in (-\pi/2, 3\pi/2)$.

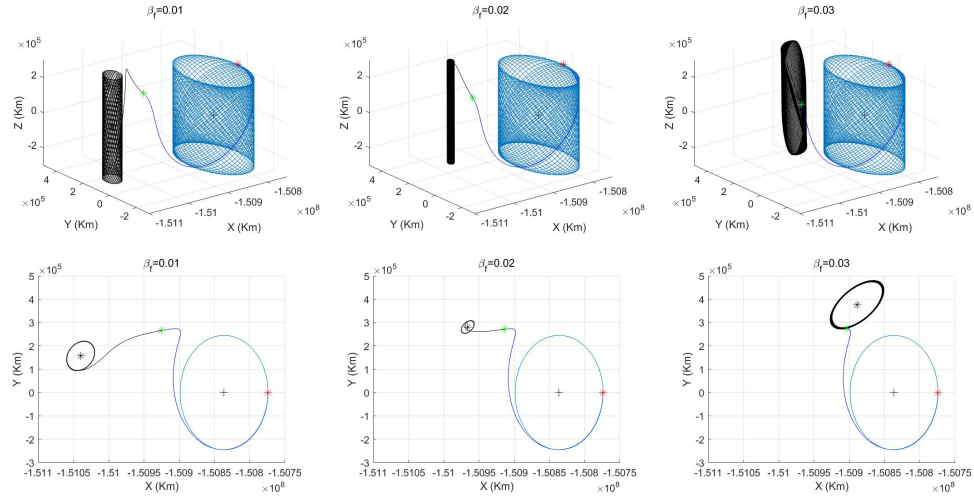

(a) $\beta_f = 0.01$ (b) $\beta_f = 0.02$ (c) $\beta_f = 0.03$

Figure 3.28: The heteroclinic enhanced connection transfer orbits when $\beta_i = 0.02$, $\beta_f = 0.01, 0.02, 0.03$

3.6 Chapter summary

This chapter investigates heteroclinic enhanced connections between libration point orbits using solar sailing impulse maneuver. They can be seen as transfer trajectories continuous in both position and velocity in a instantaneous changing vectorfield, with many potential applications including libration point exclusion avoidance. The dynamical model considered is the CR3BP including the solar radiation pressure, and the key point for the analysis is the representation of the solutions of the linearized system about the artificial equilibrium points, that change position according to the sail attitude and its reflective properties.

The invariant manifolds of libration point orbits are used for the design of transfer trajectories between Lissajous orbits in the Sun-Earth system, and the transfer maneuvers are performed by changing the angular parameters; the so called cone and clock angles, that determine the orientation of the sail with respect to the Sun, as well as phases, reflectivity parameter and initial amplitudes.

The connections considered correspond to:

1. Select one orbit of the unstable manifold of the departing Lissajous orbit, and explore the different transfer possibilities associated to transfer maneuvers done by means of cone and clock angle variations and, for a fixed cone (or clock) angle variation, to different epochs at which the solar-sail maneuver is performed.
2. Consider all the orbits of the unstable manifold of the departing Lissajous orbit, and to explore the different connection possibilities associated to the cone and clock angles solar-sail maneuvers departing from a fixed cone angle value.
3. Apart from the above parameters, the paper considers the reflectivity parameter β and initial X and Z amplitudes (A_{xi}, A_{zi}) that impact the solar-sail maneuvers and final Lissajous orbits amplitude.

In all cases the results obtained include a description of the size of the final Lissajous orbit together with the epoch at which the solar-sail maneuver has to be performed (i.e. the transfer time).

4

Chapter 4

Further explorations on enhanced heteroclinic transfers

In this chapter, three types of enhanced heteroclinic transfers between Lissajous orbits using the proposed impulse maneuver strategy are extensively studied. Due to the symmetry of the solutions with respect to the $z = 0$ plane, the same final Lissajous orbit can be reached when departing from two different points of the initial orbit. This is achieved by changing only the value of the phase from ϕ_2 to $\phi_2 + \pi$. Taking into account the constraints on the ranges of the solar sail parameters, a strategy for determining the multi-impulse maneuvers by a spacecraft is proposed. To make a double-impulse maneuver, the parameters of the solar sail are gradually changed. The transition from the initial orbit to the terminal one is accomplished using a transitional Lissajous orbit. Finally, back-and-forth transfers between two artificial libration point regions of a Lissajous orbit are realized using the proposed method.

4.1 Arriving at the same terminal Lissajous orbit

Using the impulse maneuver method described in Chapter 3, wich consists in an instantaneous change of the attitude of the sail, this section studies how two spacecraft starting from different positions in an initial Lissajous orbit can transfer to the same terminal orbit. Eqs. (3.11) and (3.16) indicate that the state vector, orbital amplitude, and pa-

rameter amplitude of a Lissajous orbit can be transformed into each other, as shown in Fig. 4.1.

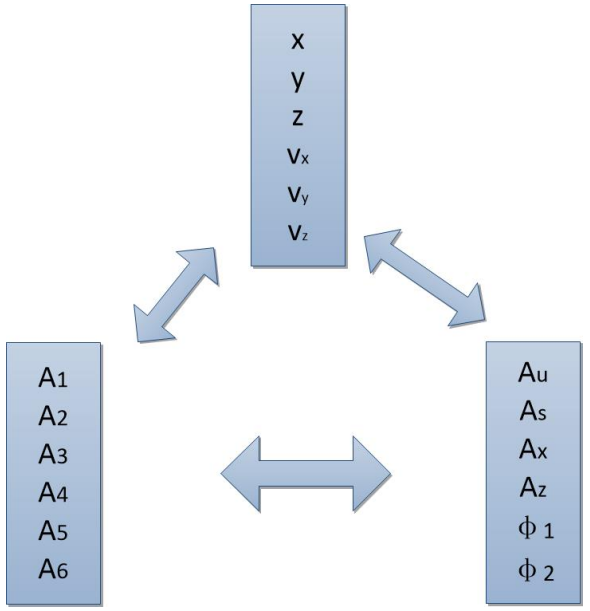

Figure 4.1: Relation between state vector, orbital amplitude, and parameter amplitude.

We assume that the two spacecraft transfer from the same initial Lissajous orbit to the same final orbit given by $A_u = 0$, $A_s = 0$, with A_x, A_z and the solar sail parameters α, δ, β being fixed. From Fig. 4.1, we can see that only the initial phase angles ϕ_1 and ϕ_2 can change. Chapter 3 showed that ϕ_1 can affect the maneuver amplitudes A_{xf} and A_{zf}, whereas ϕ_2 only periodically affects A_{zf}. So, if $\delta_{i,f} = \pi/2$, then two solar sail spacecraft can start from different positions and both will arrive at the same terminal Lissajous orbit if the difference in the values of ϕ_2 is π.

4.1.1 Arriving at the same final Lissajous orbit for different α

Fig. 4.2 shows the two connections obtained when departing from a Lissajous orbit with $A_x = 1/24$, $A_z = 1/6$, $\phi_1 = 0$, and $\phi_2 = 0$ or π. For both connections, we keep $\delta = \pi/2$. The spacecraft maneuver from $\alpha = 0$ to $\pi/4$ after, approximately, 1.9 non-dimensional time units. The departing Lissajous orbit is in blue, and the two final Lissajous orbits, which are, in fact, the same orbit, are in black and pink. The yellow line represents the orbit departing from the Lissajous orbit at the initial phases $\phi_1 = \phi_2 = 0$, and the pink line the one corresponding to $\phi_1 = 0$ and $\phi_2 = \pi$. The asterisks indicate the reorientation maneuver points along the two departure orbits. The parameter values are listed in Table 4.1.

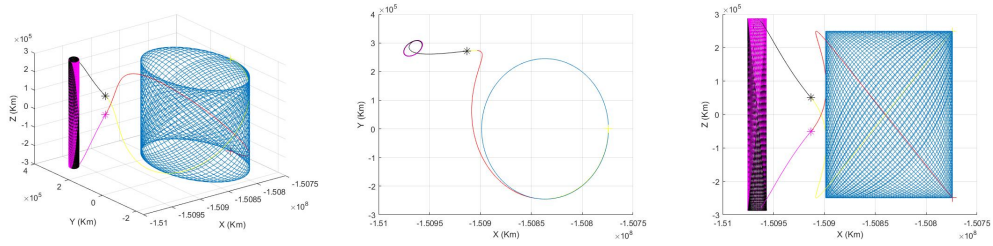

(a) 3D (b) XY plane (c) XZ plane

Figure 4.2: Transfers from the Lissajous orbit (blue) toward the same final orbit (black and pink). The initial phases at the departure orbit are $\phi_1 = \phi_2 = 0$ (yellow) and $\phi_1 = 0$ and $\phi_2 = \pi$ (pink). The asterisks denote the maneuver points.

Table 4.1 shows that, when two spacecraft have the same final artificial libration point $(\gamma_{1f}, \gamma_{2f}, \gamma_{3f})$, the same final amplitude (A_s, A_x, A_z), the same reorientation maneuver opportunity, and even the same terminal phase angle ϕ_{1f}, the terminal phase angles ϕ_{2f} are different but the difference is π. Here, (X_c, Y_c, Z_c) is the impulse maneuver position. The values of X_c and Y_c are the same. Although the values of Z_c are not the same, they have the same absolute value. In summary, two solar sail spacecraft starting from different positions, $\phi_2 = 0$ or π, but experiencing the impulse maneuver at the same time with the same terminal solar sail parameters will finally reach the same terminal Lissajous orbit.

Table 4.1: Parameters for the enhanced heteroclinic transfer orbits for $\phi_2 = 0$ or π when $\alpha_i = 0$ and $\alpha_f = \pi/4$.

$\phi_2 = 0$		$\phi_2 = \pi$	
Parameter	Value	Parameter	Value
γ_{1f}	-1.0091	γ_{1f}	-1.0091
γ_{2f}	0.00188	γ_{2f}	0.00188
γ_{3f}	0	γ_{3f}	0
A_s	0.035602	A_s	0.035602
A_X	0.00622	A_X	0.00622
A_Z	0.19210	A_Z	0.19210
Time	1.95791	Time	1.95791
ϕ_{1f}	1.61016	ϕ_{1f}	1.61016
ϕ_{2f}	-1.39367	ϕ_{2f}	1.74792
X_c	-1.00879	X_c	-1.00879
Y_c	0.001817	Y_c	0.001817
Z_c	0.000338	Z_c	-0.000338

When there are two transfer opportunities along an unstable manifold, the two solar sail spacecraft will also arrive at the same final Lissajous orbit after starting from different positions ($\phi_2 = 0$ or π), as shown in Fig. 4.3, where the solar sail parameters are chosen to be $\alpha_i = 0$, $\alpha_f = -0.35$, and $\beta_{i,f} = 0.02$.

Fig. 4.3(a) shows both enhanced heteroclinic orbits, and Table 4.2 lists the values of the parameters. Fig. 4.3(b) shows the enhanced heteroclinic transfer orbits for the first impulse maneuver. After the two spacecraft have moved along the two unstable manifolds for about 47.6 days, they perform an impulse maneuver. They then enter the same terminal Lissajous orbit (blue and yellow cylinders). Fig. 4.3(c) shows the enhanced heteroclinic transfer orbits at the time of the second impulse maneuver. After spending about 94.1 days performing the impulse maneuver, they finally reach the same terminal orbit (purple and black cylinders). Similarly, when there are three transfer opportunities along the unstable manifold, the enhanced heteroclinic transfers to the same final Lissajous orbit are shown in Fig. 4.4. Table 4.3 lists the parameters. The solar sail parameters are $\alpha_i = 0$, $\alpha_f = -0.45$, and $\beta_{i,f} = 0.02$.

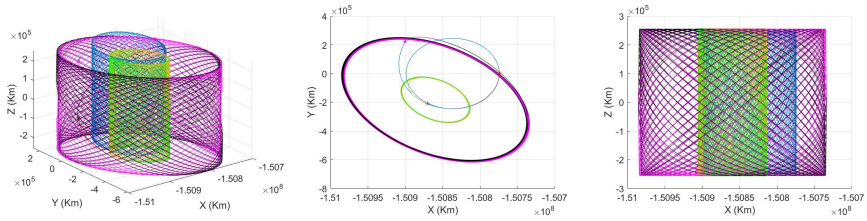

(a) Enhanced heteroclinic transfer orbits with two impulse maneuvers.

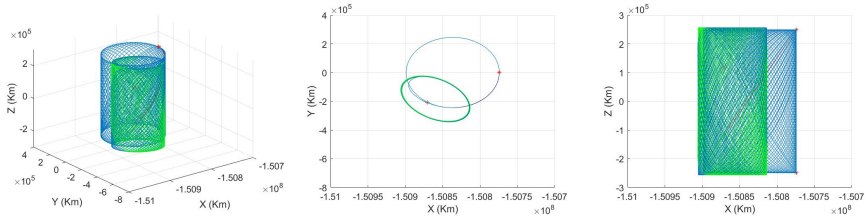

(b) Enhanced heteroclinic transfer orbits for the first impulse maneuver.

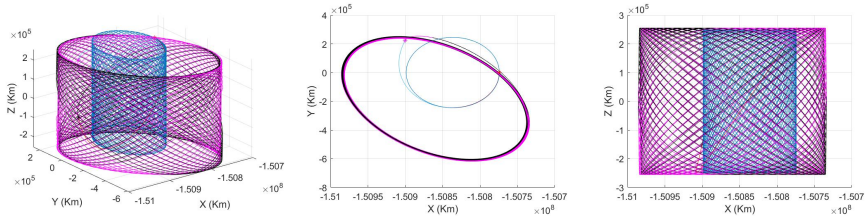

(c) Enhanced heteroclinic transfer orbits for the second impulse maneuver.

Figure 4.3: Enhanced heteroclinic transfer orbits toward the same final Lissajous orbit when $\alpha_i = 0$ and $\alpha_f = -0.35$.

Table 4.2: Parameters for the enhanced heteroclinic transfer orbits when $\alpha_i = 0$ and $\alpha_f = -0.35$, for the first and second maneuver.

	$\phi_2 = 0$			$\phi_2 = \pi$	
Parameter	First	Second	Parameter	First	Second
γ_{1f}	−1.00843	−1.00843	γ_{1f}	−1.00843	−1.00843
γ_{2f}	−0.00122	−0.00122	γ_{2f}	−0.00122	−0.00122
γ_{3f}	0	0	γ_{3f}	0	0
A_s	0.01622	0.03440	A_s	0.01622	0.03440
A_X	0.02997	0.08123	A_X	0.02997	0.08123
A_Z	0.17149	0.170616	A_Z	0.17149	0.170616
Time	0.81925	1.61920	Time	0.81925	1.61920
$\phi 1_f$	−2.434306	−2.434306	$\phi 1_f$	−2.434306	−2.434306
$\phi 2_f$	−2.199525	−2.199525	$\phi 2_f$	0.942068	0.942068
X_{c1}	−1.008507	−1.008707	X_{c1}	−1.008507	−1.008707
Y_{c1}	−0.001402	0.001484	Y_{c1}	−0.001402	0.001484
Z_{c1}	−0.000779	−0.001003	Z_{c1}	0.000779	0.001003

Table 4.3: Parameters for enhanced heteroclinic transfer orbits for $\phi_2 = 0$ or π when $\alpha_i = 0$ and $\alpha_f = -0.45$, for the three maneuvers.

	$\phi_2 = 0$			$\phi_2 = \pi$			
Param.	First	Second	Third	Param.	First	Second	Third
γ_{1f}	−1.00843	−1.00843	−1.00843	γ_{1f}	−1.00843	−1.00843	−1.00843
γ_{2f}	−0.00122	−0.00122	−0.00122	γ_{2f}	−0.00122	−0.00122	−0.00122
γ_{3f}	0	0	0	γ_{3f}	0	0	0
A_s	0.04142	0.02739	0.05157	A_s	0.04142	0.02739	0.05157
A_X	0.05020	0.01046	0.09361	A_X	0.05020	0.01046	0.09361
A_Z	0.16710	0.17660	0.17553	A_Z	0.16710	0.17660	0.17553
Time	0.08207	0.59717	1.73857	Time	0.08207	0.59717	1.73857
$\phi 1_f$	−2.36023	−2.36023	−2.36023	$\phi 1_f$	−2.36023	−2.36023	−2.36023
$\phi 2_f$	−1.89893	−1.89893	−1.89893	$\phi 2_f$	1.24266	1.24266	1.24266
X_{c1}	−1.00787	−1.00827	−1.00869	X_{c1}	−1.00787	−1.00827	−1.00869
Y_{c1}	0.00034	−0.00163	0.00172	Y_{c1}	0.00034	−0.00163	0.00172
Z_{c1}	0.00163	0.00012	−0.00057	Z_{c1}	-0.00163	-0.00012	0.00057

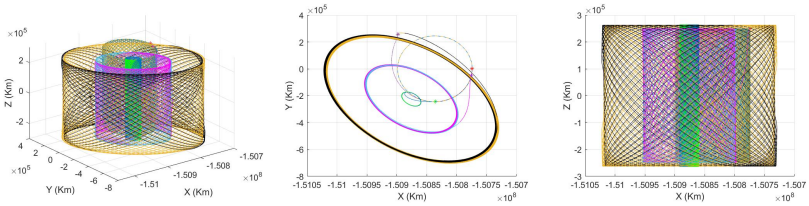

(a) Enhanced heteroclinic transfer orbits with three impulse maneuvers.

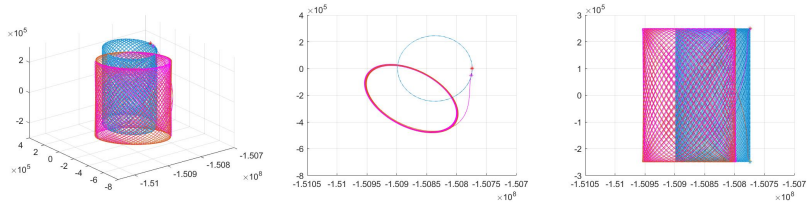

(b) Enhanced heteroclinic transfer orbits for the first impulse maneuver.

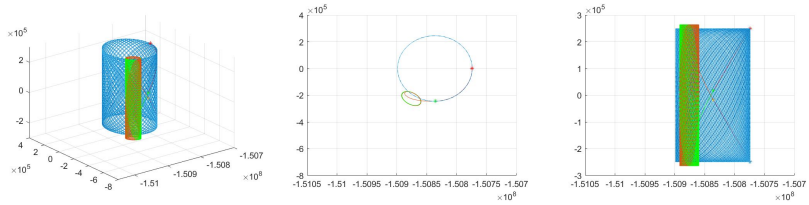

(c) Enhanced heteroclinic transfer orbits for the second impulse maneuver.

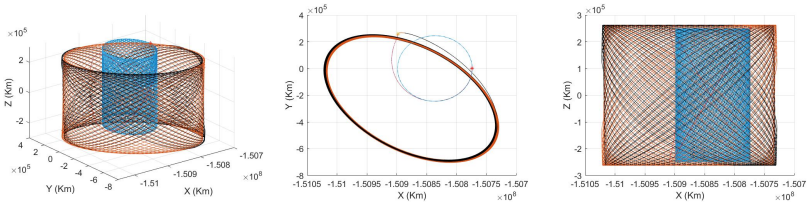

(d) Enhanced heteroclinic transfer orbits for the third impulse maneuver.

Figure 4.4: Enhanced heteroclinic transfer orbits toward the same final Lissajous orbit for $\alpha_i = 0$ and $\alpha_f = -0.45$.

4.1.2 Arriving at the same final Lissajous orbit for different β and α_f

When using both α_f and β_f, Fig. 4.5 shows the two enhanced heteroclinic transfer orbits when departing from the same Lissajous orbit ($\phi_2 = 0$ or π). In this particular example, the solar sail parameters are $\alpha_i = 0$, $\alpha_f = \pi/4$, $\beta_i = 0.02$, and $\beta_f = 0.03$. The time taken for the reorientation impulse maneuver is about 110 days. The parameters are listed in Table 4.4.

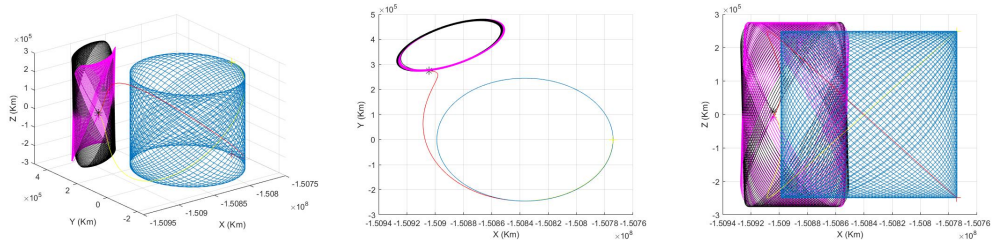

(a) 3D (b) XY plane (c) XZ plane

Figure 4.5: Enhanced heteroclinic transfer orbits toward the same final Lissajous orbit when $\alpha_i = 0$, $\alpha_f = \pi/4$, $\beta_i = 0.02$, and $\beta_f = 0.03$.

Table 4.4: Parameters for enhanced heteroclinic transfer orbits for $\phi_2 = 0$ or π when $\alpha_i = 0$, $\alpha_f = \pi/4$, $\beta_i = 0.02$, and $\beta_f = 0.03$.

$\phi_2 = 0$		$\phi_2 = \pi$	
Parameter	Value	Parameter	Value
γ_{1f}	-1.00863	γ_{1f}	-1.00863
γ_{2f}	0.00252	γ_{2f}	0.00252
γ_{3f}	0	γ_{3f}	0
A_s	0.00659	A_s	0.00659
A_X	0.02563	A_X	0.02563
A_Z	0.18453	A_Z	0.18453
Time	1.88822	Time	1.88822
ϕ_{1f}	2.28307	ϕ_{1f}	2.28307
ϕ_{2f}	-1.54414	ϕ_{2f}	1.59745
X_c	-1.00873	X_c	-1.00873
Y_c	0.00183	Y_c	0.00183
Z_c	0.000005	Z_c	-0.000005

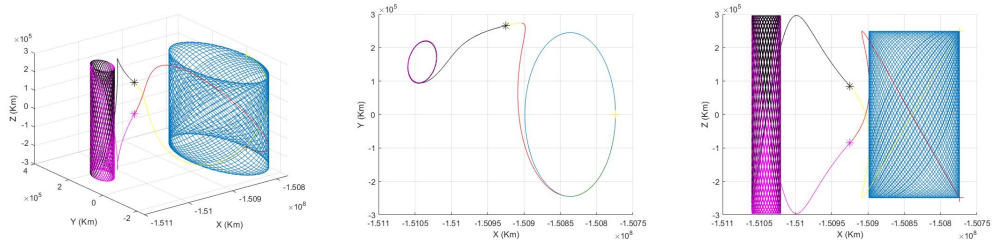

(a) 3D (b) XY plane (c) XZ plane

Figure 4.6: Enhanced heteroclinic transfer orbits with $\phi_2 = 0$ or π, when $\alpha_i = 0$, $\alpha_f = \pi/4$, $\beta_i = 0.02$, and $\beta_f = 0.01$

Enhanced heteroclinic transfer orbits to the same final Lissajous orbit are shown in Fig. 4.6 when $\beta_f < \beta_i$. The parameters are listed in Table 4.5. After performing an impulse maneuver for about 117 days, $\alpha_f = \pi/4$ and $\beta_f = 0.01$. The two spacecraft then finally reach the same terminal Lissajous orbit.

Table 4.5: Parameters for enhanced heteroclinic transfer orbits for $\phi_2 = 0$ or π when $\alpha_i = 0$, $\alpha_f = \pi/4$, $\beta_i = 0.02$, and $\beta_f = 0.01$

$\phi_2 = 0$		$\phi_2 = \pi$	
Parameter	Value	Parameter	Value
γ_{1f}	-1.00964	γ_{1f}	-1.00964
γ_{2f}	0.00105	γ_{2f}	0.00105
γ_{3f}	0	γ_{3f}	0
A_s	0.07250	A_s	0.07250
A_X	0.01341	A_X	0.01341
A_Z	0.19806	A_Z	0.19806
Time	2.01564	Time	2.01564
ϕ_{1f}	-1.24175	ϕ_{1f}	-1.24175
ϕ_{2f}	-1.27850	ϕ_{2f}	1.86310
Z_c	0.00057	Z_c	-0.00057

4.2 Multi-impulse enhanced heteroclinic transfers

The enhanced heteroclinic transfers described above use a single-impulse maneuver to inject the spacecraft in the stable manifold of the target orbit. Since a solar sail panel cannot move through a large angle in a short time, the terminal Lissajous orbital amplitudes were chosen small in those examples. In this section, the spacecraft performs two impulse maneuvers using a middle transitional cone angle α_m, clock angle δ_m, and lightness number β_m.

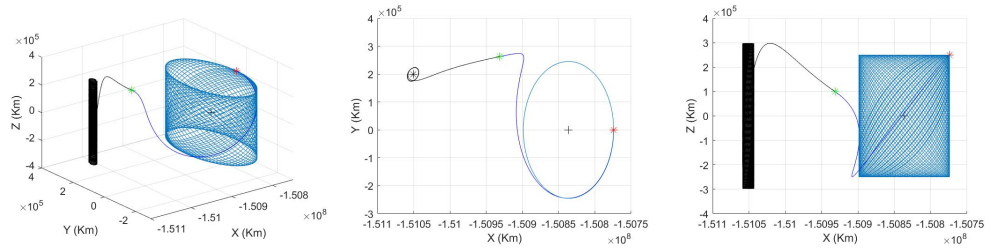

Figure 4.7: Enhanced heteroclinic transfer orbits for initial $\alpha_i = 0$, $\delta_i = \pi/2$ and final $\alpha_f = \pi/3$, $\delta_f = \pi/2$.

Suppose the solar sail spacecraft escapes from the Lissajous orbit near the artificial libration point SL_2 ($\alpha_i = 0$, $\delta_i = \pi/2$, and $\beta_i = 0.02$) after a single-impulse maneuver and it reaches the Lissajous orbit near the artificial libration point SL_2' ($\alpha_f = \pi/3$, $\delta_f = \pi/2$,

and $\beta_f = 0.02$). The transfer orbit is shown in Fig. 4.7, and the parameters are listed in Table 4.6. However, A_{xf} is small, which is not conducive for a long-term mission. Therefore, it is necessary to apply two or more impulse maneuvers. In this section we will analyze the effects of using a transitional cone angle α_m, clock angle δ_m, and lightness number β_m.

Table 4.6: Parameters for the enhanced heteroclinic transfer orbits for initial $\alpha_i = 0$, $\delta_i = \pi/2$ and final $\alpha_f = \pi/3$, $\delta_f = \pi/2$.

Parameter	Value
γ_{1f}	-1.00971
γ_{2f}	0.00133
γ_{3f}	0
A_{xf}	0.00536
A_{zf}	0.19887

4.2.1 Middle transitional cone angle α_m

Assume that the solar sail spacecraft escapes from the initial artificial libration point SL_2 of a Lissajous orbit ($\alpha_i = 0$, $\delta_i = \pi/2$, and $\beta_i = 0.02$). Fig. 4.8(a) shows the 3D representation of the transfer orbits with two impulse maneuvers. The spacecraft starts from the initial Lissajous orbit (blue cylinder) and enters the transitional Lissajous orbit (black cylinder) after the first impulse maneuver ($\alpha_m = \pi/4$, $\delta_m = \pi/2$, and $\beta_m = 0.02$). It performs the first impulse maneuver by changing the solar sail to the middle transitional cone angle $\alpha_m = \pi/4$. Finally, it performs the second impulse maneuver to reach the target Lissajous orbit (purple cylinder) near the artificial libration point SL_2' ($\alpha_f = \pi/3$, $\delta_f = \pi/2$, and $\beta_f = 0.02$). Figs. 4.8(b) and 4.8(c) are the projections onto the XY and XZ planes, respectively. The orbital parameters are listed in Table 4.7.

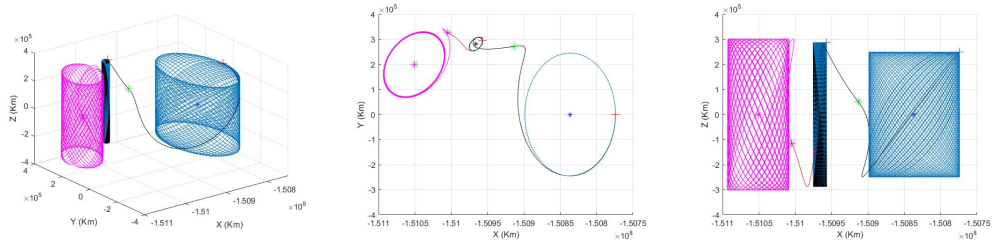

(a) 3D (b) XY plane (c) XZ plane

Figure 4.8: Enhanced heteroclinic transfer orbits using as middle transitional cone angle $\alpha_m = \pi/4$.

Comparing Tables 4.6 and 4.7 we note that for the same initial and terminal solar sail parameters, using a transitional cone angle α_m we have a greater impact on the terminal

Table 4.7: Parameters for the enhanced heteroclinic transfer orbits using as middle transitional cone angle $\alpha_m = \pi/4$.

$\alpha_m = \pi/4$, $\delta_m = \pi/2$, $\beta_m = 0.02$		$\alpha_f = \pi/3$, $\delta_f = \pi/2$, $\beta_f = 0.02$	
Parameter	Value	Parameter	Value
γ_{1m}	-1.00915	γ_{1f}	-1.00971
γ_{2m}	0.00188	γ_{2f}	0.00133
γ_{3m}	0	γ_{3f}	0
A_{xm}	0.00622	A_{xf}	0.02856
A_{zm}	0.19210	A_{zf}	0.20160

A_{xf}. For a single-impulse maneuver, the terminal Lissajous orbital amplitude $A_{xf} = 0.00536$, whereas with the transitional cone angle α_m, $A_{xf} = 0.02856$, which is more suitable for a mission. Moreover, it solves the problem that a solar sail panel cannot rotate through a large angle in a short time.

This approach can overcome the problem when the terminal Lissajous orbital amplitude is small. However, with the transitional cone angle $\alpha_m = \pi/4$, the transitional Lissajous orbital amplitude is also small $A_{xm} = 0.0062$. Thus, we set the transitional cone angle $\alpha_m = \pi/6$. The transitional orbits are shown in Fig. 4.9, and the parameters are listed in Table 4.8. Comparing with Fig. 4.8, this demonstrates that using a different transitional cone angle α_m we can change the transitional and terminal Lissajous orbital amplitudes. In conclusion, the transitional cone angle α_m can be adjusted according to the actual needs of the mission.

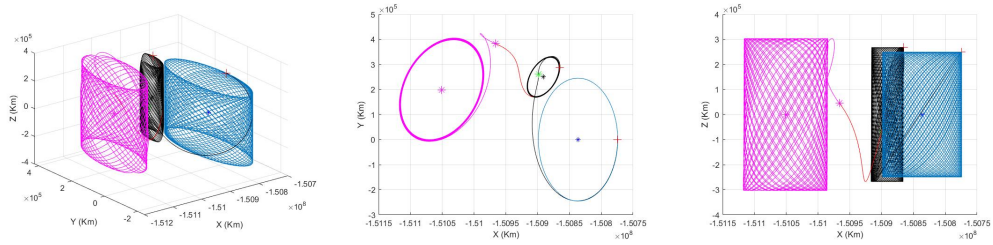

(a) 3D (b) XY plane (c) XZ plane

Figure 4.9: Enhanced heteroclinic transfer orbits using as middle transitional cone angle $\alpha_m = \pi/6$.

4.2.2 Middle transitional clock angle δ_m

We illustrate the procedure taking the solar sail spacecraft starting from the initial artificial libration point SL_2 of a Lissajous orbit ($\alpha_i = 0$, $\delta_i = \pi/2$, and $\beta_i = 0.02$). Then it performs the first impulse maneuver by changing the solar sail to the middle transitional

Table 4.8: Parameters for the enhanced heteroclinic transfer orbits using as middle transitional cone angle $\alpha_m = \pi/6$.

$\alpha_m = \pi/6$, $\delta_m = \pi/2$, $\beta_m = 0.02$		$\alpha_f = \pi/3$, $\delta_f = \pi/2$, $\beta_f = 0.02$	
Parameter	Value	Parameter	Value
γ_{1m}	-1.00864	γ_{1f}	-1.00971
γ_{2m}	0.00167	γ_{2f}	0.00133
γ_{3m}	0	γ_{3f}	0
A_{xm}	0.01720	A_{xf}	0.04461
A_{zm}	0.17890	A_{zf}	0.20261
Transfer days	102.46	Transfer days	121.97

angles $\alpha_m = \pi/3$ and $\delta_m = \pi/4$ and entering a transitional Lissajous orbit. Finally, the spacecraft makes another impulse maneuver to reach the target Lissajous orbit about the artificial libration point SL_2' ($\alpha_f = \pi/3$, $\delta_f = \pi/2$, and $\beta_f = 0.02$). The enhanced heteroclinic transfer orbits are shown in Fig. 4.10. The black cylinder is the transitional Lissajous orbit after the first impulse maneuver ($\alpha_m = \pi/3$, $\delta_m = \pi/4$, and $\beta_m = 0.02$). The orbital parameters are listed in Table 4.9.

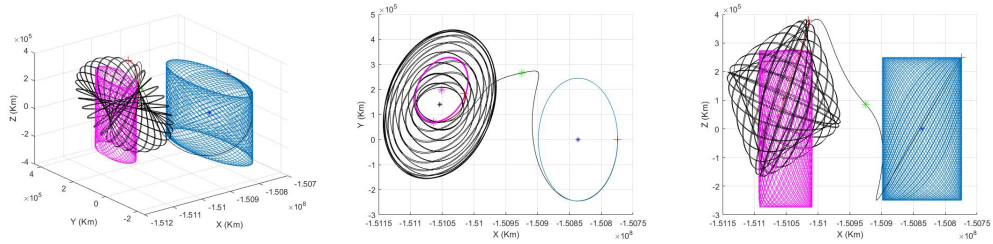

(a) 3D (b) XY plane (c) XZ plane

Figure 4.10: Enhanced heteroclinic transfer orbits using as middle transitional clock angle $\delta_m = \pi/4$.

Figs. 4.7, 4.8, and 4.10 show that applying a double-impulse maneuver with different values of the middle transitional clock angle δ_m could solve the problem when the middle transitional orbital amplitude A_{xm} and final target Lissajous orbital amplitude A_{xf} are small.

Since there are many possibilities for the middle transitional sail-attitude angle, it is necessary to study the effect of different α_m and δ_m on the transitional orbit and the target Lissajous orbit. As an exmaple, when the transitional solar sail parameters are $\alpha_m = \pi/6$ and $\delta_m = \pi/4$, the double-impulse enhanced heteroclinic transfer orbits are shown in Fig. 4.11 and the parameters are listed in Table 4.10. As we can see, when comparing with Table 4.9, the choice of the transitional attitude angle affects the target Lissajous orbital amplitudes A_{xf} and A_{zf}.

Table 4.9: Parameters for the enhanced heteroclinic transfer orbits using as middle transitional clock angle $\delta_m = \pi/4$.

$\alpha_m = \pi/3$, $\delta_m = \pi/4$, $\beta_m = 0.02$		$\alpha_f = \pi/3$, $\delta_f = \pi/2$, $\beta_f = 0.02$	
Parameter	Value	Parameter	Value
γ_{1m}	-1.00973	γ_{1f}	-1.00971
γ_{2m}	0.00094	γ_{2f}	0.00133
γ_{3m}	0.00072	γ_{3f}	0
A_{xm}	0.04207	A_{xf}	0.02829
A_{zm}	0.12221	A_{zf}	0.18280
Transfer days	117.20	Transfer days	53.61

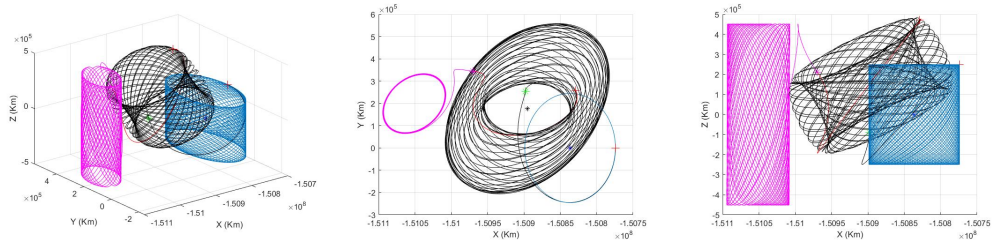

(a) 3D (b) XY plane (c) XZ plane

Figure 4.11: Enhanced heteroclinic transfer orbits when $\alpha_m = \pi/6$ and $\delta_m = \pi/4$.

Table 4.10: Parameters of the enhanced heteroclinic transfer orbits when $\alpha_m = \pi/6$ and $\delta_m = \pi/4$.

$\alpha_m = \pi/6$, $\delta_m = \pi/4$, $\beta_m = 0.02$		$\alpha_f = \pi/3$, $\delta_f = \pi/2$, $\beta_f = 0.02$	
Parameter	Value	Parameter	Value
γ_{1m}	-1.00867	γ_{1f}	-1.00971
γ_{2m}	0.00118	γ_{2f}	0.00133
γ_{3m}	0.00096	γ_{3f}	0
A_{xm}	0.05801	A_{xf}	0.029137
A_{zm}	0.11751	A_{zf}	0.30196
Transfer days	100.46	Transfer days	125.76

4.2.3 Middle transitional lightness number β_m

Sections 4.2.1 and 4.2.2 displayed the influence of transitional cone angle α_m and transitional clock angle δ_m. This section will illustrate some facts on the influence of the middle transitional lightness number β_m on the target Lissajous orbital amplitudes A_{xf} and A_{zf}.

We assume the solar sail spacecraft starts from the initial artificial libration point SL_2 of a Lissajous orbit ($\alpha_i = 0$, $\delta_i = \pi/2$, and $\beta_i = 0.02$), and we consider the transitional

solar sail parameters $\alpha_m = \pi/3$, $\delta_m = \pi/2$, and $\beta_m = 0.03$ for the first impulse maneuver. So the spacecraft enters in a transitional Lissajous orbit, and then it performs another impulse maneuver to reach the terminal Lissajous orbit about the artificial libration point SL_2' ($\alpha_f = \pi/3$, $\delta_f = \pi/2$, and $\beta_f = 0.02$). The outcome is shown in Fig. 4.12. The black cylinder is the transitional orbit after the first impulse maneuver and the orbital parameters are listed in Table 4.11.

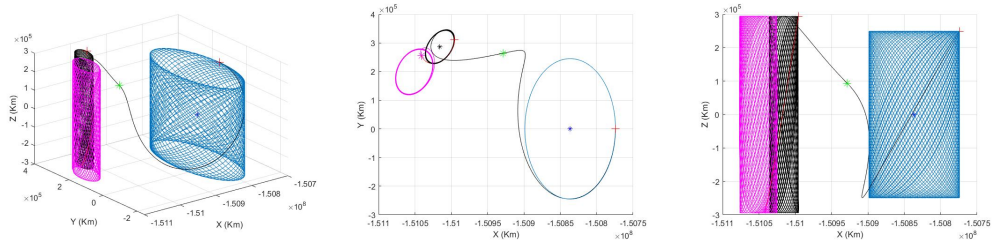

(a) 3D (b) XY plane (c) XZ plane

Figure 4.12: Enhanced heteroclinic transfer orbit under $\beta_m = 0.03$.

Table 4.11: Parameters for enhanced heteroclinic transfer orbits when $\beta_m = 0.03$.

$\alpha_m = \pi/3$, $\delta_m = \pi/2$, $\beta_m = 0.03$		$\alpha_f = \pi/3$, $\delta_f = \pi/2$, $\beta_f = 0.02$	
Parameter	Value	Parameter	Value
γ_{1m}	-1.00948	γ_{1f}	-1.00971
γ_{2m}	0.00192	γ_{2f}	0.00133
γ_{3m}	0	γ_{3f}	0
A_{xm}	0.01360	A_{xf}	0.01744
A_{zm}	0.19670	A_{zf}	0.19692
Transfer days	117.98	Transfer days	80.38

Comparing Tables 4.6 and 4.11 we see that A_{xf} becomes larger. So, again the possibility to increase the amplitude with this technique still exist, however we also considered the transitional lightness number $\beta_m = 0.015$ and there was no enhanced heteroclinic transfer orbit.

When the transitional solar sail parameters $\alpha_m = \pi/6$ and $\beta_m = 0.03$, the double-impulse enhanced heteroclinic transfer orbits are shown in Fig. 4.13. The parameters are listed in Table 4.12. As it can be seen, the terminal Lissajous orbital amplitude A_{xf} is larger.

These different examples demonstrate that the selection of the transitional solar sail parameters is very important, especially when considering a transitional lightness number β_m, which has a great influence on the terminal Lissajous orbital amplitudes A_{xf} and A_{zf}. In the former example, when $\beta_m = 0.015$, there is no transfer orbit, but when $\beta_m = 0.03$, the combined action of β_m and α_m produced an interesting increase in the final A_{xf} with respect to the one obtained by the direct transfer procedure.

In summary, if the spacecraft can make two or more impulse maneuvers, it is worth to study the impact of middle transitional parameters α_m and δ_m.

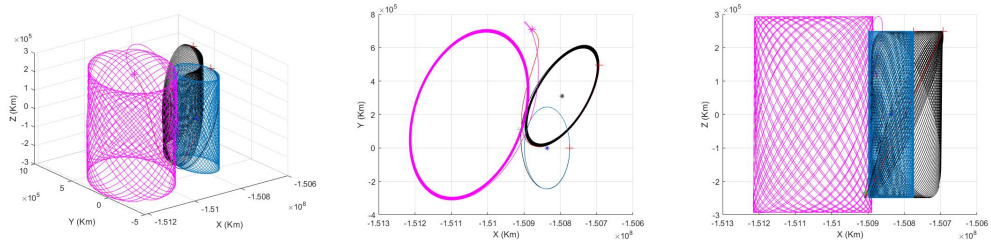

(a) 3D (b) XY plane (c) XZ plane

Figure 4.13: Enhanced heteroclinic transfer orbits when $\beta_m = 0.03$ and $\alpha_m = \pi/6$.

Table 4.12: Parameters of the enhanced heteroclinic transfer orbits for $\beta_m = 0.03$ and $\alpha_m = \pi/6$.

$\alpha_m = \pi/6$, $\delta_m = \pi/2$, $\beta_m = 0.03$		$\alpha_f = \pi/3$, $\delta_f = \pi/2$, $\beta_f = 0.02$	
Parameter	Value	Parameter	Value
γ_{1m}	-1.00800	γ_{1f}	-1.00971
γ_{2m}	0.00208	γ_{2f}	0.00133
γ_{3m}	0	γ_{3f}	0
A_{xm}	0.06841	A_{xf}	0.11052
A_{zm}	0.16664	A_{zf}	0.19608
Transfer days	80.87	Transfer days	120.86

4.3 Back-and-forth transfers

Using impulse maneuvers by means of instantaneous changes in the attitude of the sail, we showed that a spacecraft can realize a enhanced heteroclinic transfer from an initial SL_2 Lissajous orbit to another one about SL_2'. In an actual mission, the enhanced heteroclinic transfer to another Lissajous orbit may only be a temporary docking maneuver (such as for avoiding a forbidden zone), while the optimal mission requirement still is in the initial SL_2 Lissajous orbit. Related with this fact, in this section we consider back-and-forth transfers between two artificial libration point regions. We also consider the potential reversibility of the maneuvers we discussed in Section 4.2.

4.3.1 Back-and-forth transfers using α

For a Sun-pointing spacecraft, we consider the cone angle α switching from 0 to $\pi/4$ and then switching back to 0. In the case example shown in Fig. 4.14, we perform three loops by switching α between these values. The other parameters are $\delta_{i,f} = \pi/2$ and $\beta_{i,f} = 0.02$.

For the first impulse maneuver, α is changed from 0 to $\pi/4$, and the spacecraft reaches the SL_2' Lissajous orbit. For the second impulse maneuver, α_f is changed back from $\pi/4$ to 0, and it returns to the initial SL_2 Lissajous orbit. The parameters considered are listed in Table 4.13.

Fig. 4.14(a) shows the back-and-forth transfers due to all three impulse maneuvers. Figs. 4.14(b) to 4.14(d) show the corresponding enhanced heteroclinic transfer orbits for the first, second, and third impulse maneuvers, respectively. In Fig. 4.14(b), the solar sail spacecraft starts from the initial Lissajous orbit (blue cylinder) near SL_2. The cone angle is $\alpha_i = 0$. Then the spacecraft escapes along the unstable manifold (black curve) and reaches the black asterisk, where the cone angle is changed to $\alpha_f = \pi/4$. It then arrives at the target Lissajous orbit near SL_2' (black cylinder) along the stable manifold. In Fig. 4.14(c), the spacecraft escapes along the purple curve. For the second impulse maneuver, the cone angle becomes $\alpha_f = 0$, and the spacecraft returns to the Lissajous orbit near SL_2 (purple cylinder). In Fig. 4.14(d), the spacecraft escapes along the yellow curve. For the third impulse maneuver, the cone angle is $\alpha_f = \pi/4$. The spacecraft reaches the SL_2' Lissajous orbit (yellow cylinder). Table 4.13 shows that the enhanced heteroclinic transfers for the three impulse maneuvers are all around the two artificial libration points. The amplitudes of the Lissajous orbits also change during the process.

Table 4.13: Parameters for back-and-forth transfers when $\alpha = 0$ or $\pi/4$.

Parameter	$\alpha_i = 0$	$\alpha_f = \pi/4$	$\alpha_f = 0$	$\alpha_f = \pi/4$
γ_1	-1.00828	-1.00915	-1.00828	-1.00915
γ_2	0	0.00188	0	0.00188
γ_3	0	0	0	0
A_x	0.04167	0.00622	0.04639	0.00431
A_z	0.16667	0.19210	0.17128	0.19758

Fig. 4.15 shows the back-and-forth transfer orbits for different phase angles. The orbital parameters are given in Table 4.14. A comparison of Figs. 4.14 and 4.15 indicates that when the spacecraft starts from different initial phase angles, the amplitudes of the terminal Lissajous orbit are also different.

Table 4.14: Parameters for back-and-forth transfers for $\alpha = 0$ or $\pi/4$ with different initial phase angles.

Parameter	$\alpha_i = 0$	$\alpha_f = \pi/4$	$\alpha_f = 0$	$\alpha_f = \pi/4$
γ_1	-1.00828	-1.00915	-1.00828	-1.00915
γ_2	0	0.00188	0	0.00188
γ_3	0	0	0	0
A_x	0.04167	0.00622	0.03776	0.02264
A_z	0.16667	0.19210	0.17212	0.19350

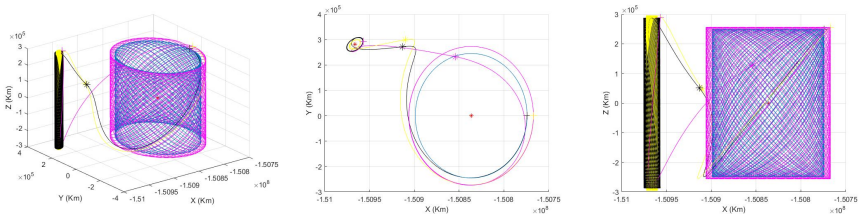

(a) Enhanced heteroclinic transfer with all three impulse maneuvers.

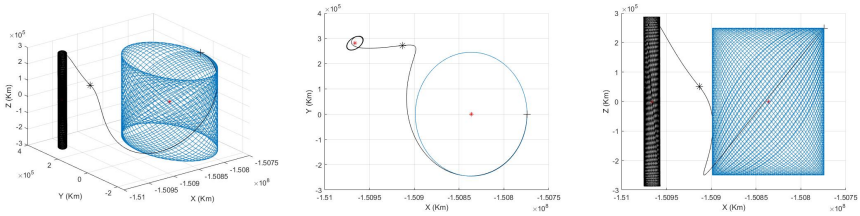

(b) First impulse maneuver: α from 0 to $\pi/4$.

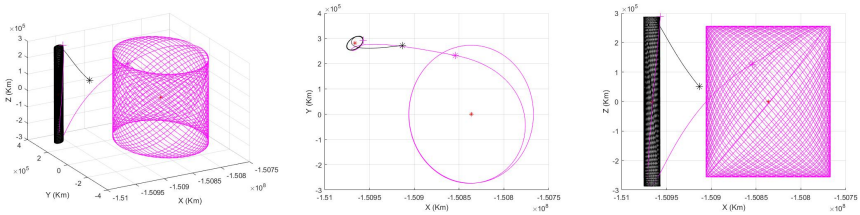

(c) Second impulse maneuver: α from $\pi/4$ to 0.

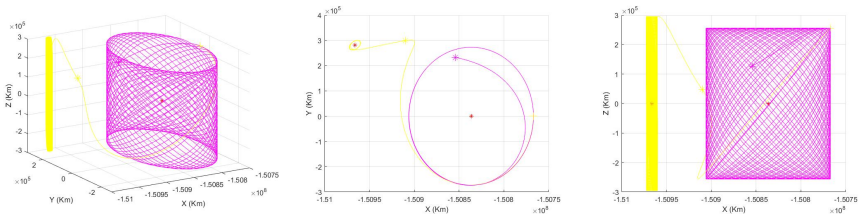

(d) Third impulse maneuver: α from 0 to $\pi/4$.

Figure 4.14: Back-and-forth transfers for $\alpha = 0$ or $\pi/4$.

4.3.2 Back-and-forth transfers using α and δ

In Section 4.3.1 we considered some examples of back-and-forth transfers based on varying the cone angle α between 0 and $\pi/4$. In this section, we will see the influence of different clock angles δ. If $\alpha = 0$, it would be futile changing δ, so this section assumes that α changes from $\pi/6$ to $\pi/3$ and that δ changes from $\pi/2$ to $\pi/4$. Also, $\phi_1 = \phi_2 = 0$. Back-and-forth transfer orbits are shown in Fig. 4.16. The parameters are listed in Table 4.15.

The results show that the enhanced heteroclinic back-and-forth transfers are all around the two artificial libration points. Again, the Lissajous orbital amplitudes also change in the process.

Table 4.15: Parameters for back-and-forth transfers for α from $\pi/6$ to $\pi/3$ and for δ from $\pi/4$ to $\pi/2$.

Parameter	$\alpha_i = \pi/6$ $\delta_i = \pi/2$	$\alpha_f = \pi/3$ $\delta_f = \pi/4$	$\alpha_f = \pi/6$ $\delta_f = \pi/2$	$\alpha_f = \pi/3$ $\delta_f = \pi/4$
γ_1	−1.00864	−1.00973	−1.00864	−1.00973
γ_2	0.00167	0.00094	0.00167	0.00094
γ_3	0	0.00072	0	0.00072
A_x	0.04167	0.08825	0.05259	0.10147
A_z	0.16667	0.06904	0.19940	0.08648

4.3.3 Back-and-forth transfers using α and β

In this section we show that back-and-forth transfers are also possible by changing β. In the example we assume that α changes between $\pi/6$ and $\pi/3$, β between 0.02 and 0.03, while $\phi_1 = \phi_2 = 0$. The back-and-forth transfer orbits are shown in Fig. 4.17, and the parameters are listed in Table 4.16. Similarly, we changed the lightness number β between 0.02 and 0.01. The back-and-forth transfer orbits are shown in Fig. 4.18. In this example, we see that the amplitudes A_{xf} and A_{zf} become larger after each transfer. Procedures like this could be used to increase or decrease the sice of an artificial libration orbit.

Table 4.16: Parameters for back-and-forth transfers for α from $\pi/6$ to $\pi/3$ and for β from 0.02 to 0.03.

Parameter	$\alpha_i = \pi/6$ $\beta_i = 0.02$	$\alpha_f = \pi/3$ $\beta_f = 0.03$	$\alpha_f = \pi/6$ $\beta_f = 0.02$	$\alpha_f = \pi/3$ $\beta_f = 0.03$
γ_1	−1.00864	−1.00948	−1.00864	−1.00948
γ_2	0.00167	0.00192	0.00167	0.00192
γ_3	0	0	0	0
A_x	0.04167	0.05480	0.06204	0.07526
A_z	0.16667	0.18624	0.18589	0.20767

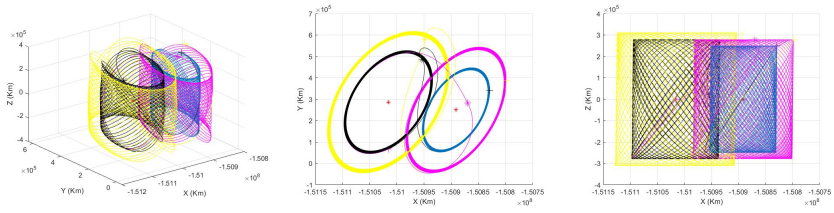

(a) Enhanced heteroclinic transfer with all three impulse maneuvers

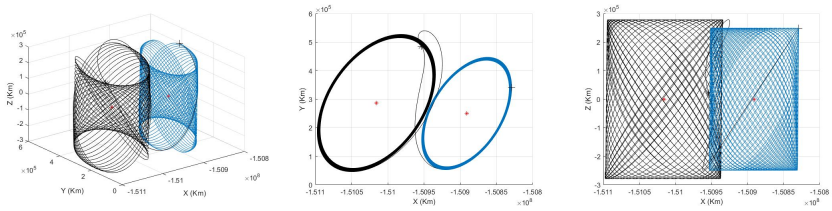

(b) First impulse maneuver: α from $\pi/6$ to $\pi/3$ and β from 0.02 to 0.03.

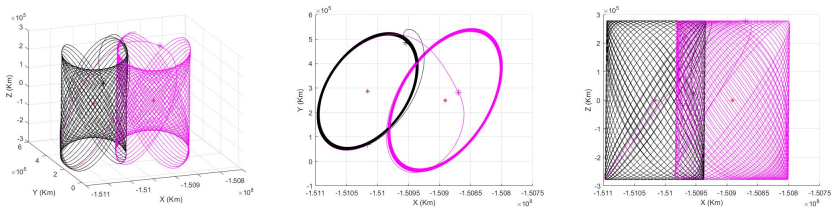

(c) Second impulse maneuver: α from $\pi/3$ to $\pi/6$ and β from 0.03 to 0.02.

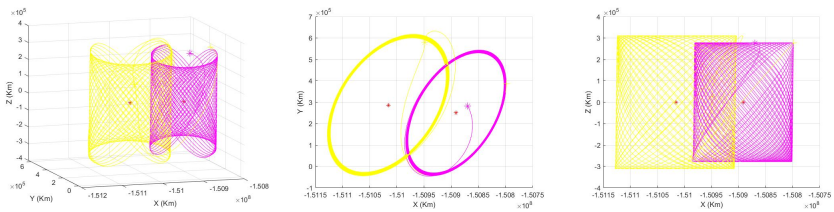

(d) Third impulse maneuver: α from $\pi/6$ to $\pi/3$ and β from 0.02 to 0.03.

Figure 4.17: Back-and-forth transfers for α from $\pi/6$ to $\pi/3$ and for β from 0.02 to 0.03.

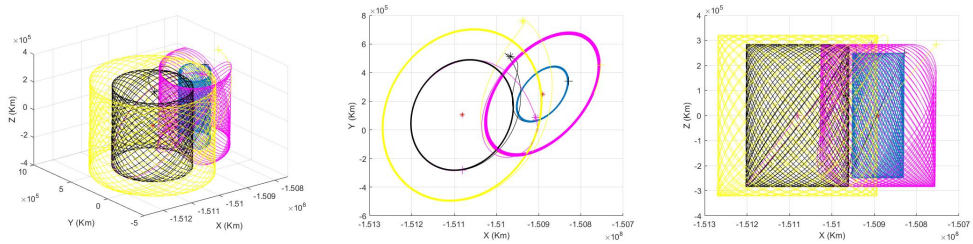

Figure 4.18: Back-and-forth transfers for α from $\pi/6$ to $\pi/3$ and for β from 0.02 to 0.01

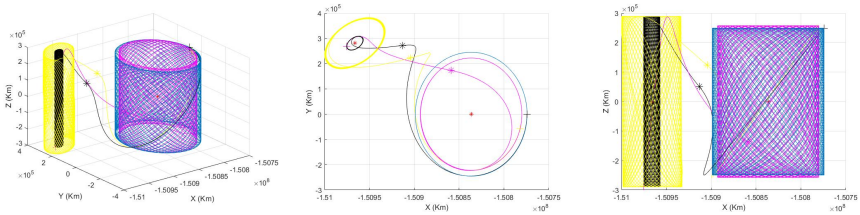

(a) Enhanced heteroclinic transfer with all three impulse maneuvers.

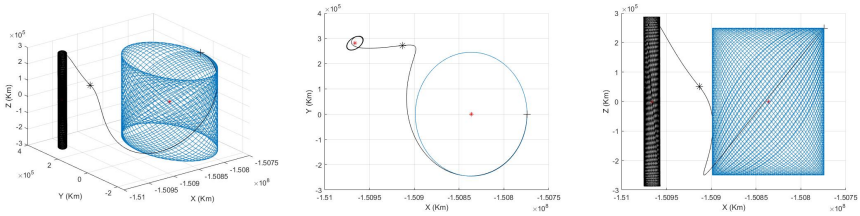

(b) First impulse maneuver with $\phi_1 = \phi_2 = 0$.

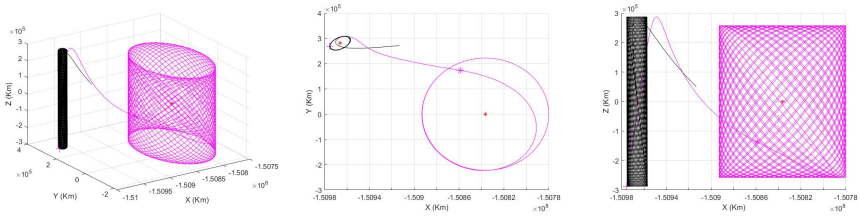

(c) Second impulse maneuver with $\phi_1 = \phi_2 = \pi/4$.

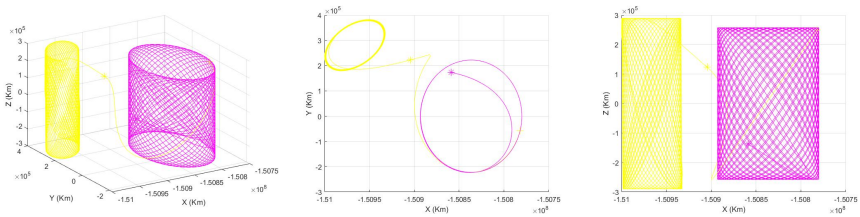

(d) Third impulse maneuver with $\phi_1 = \phi_2 = \pi/12$.

Figure 4.15: Back-and-forth transfers for $\alpha = 0$ or $\pi/4$ with different initial phase angles.

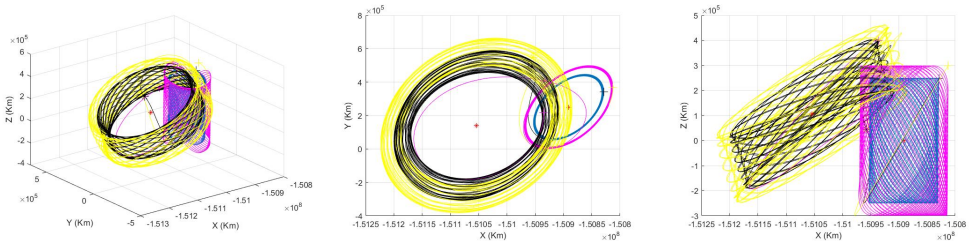

(a) Enhanced heteroclinic transfers with all three impulse maneuvers.

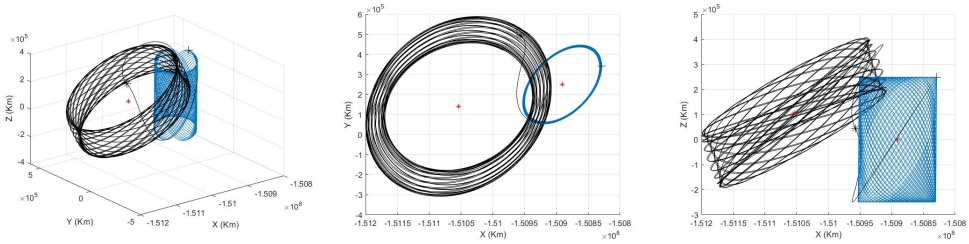

(b) First impulse maneuver: α from $\pi/6$ to $\pi/3$ and δ from $\pi/2$ to $\pi/4$.

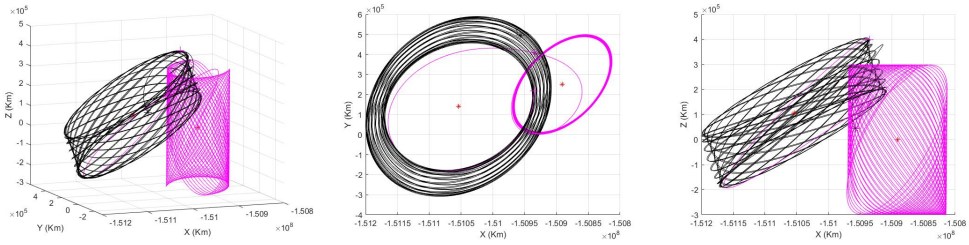

(c) Second impulse maneuver: α from $\pi/3$ to $\pi/6$ and δ from $\pi/4$ to $\pi/2$.

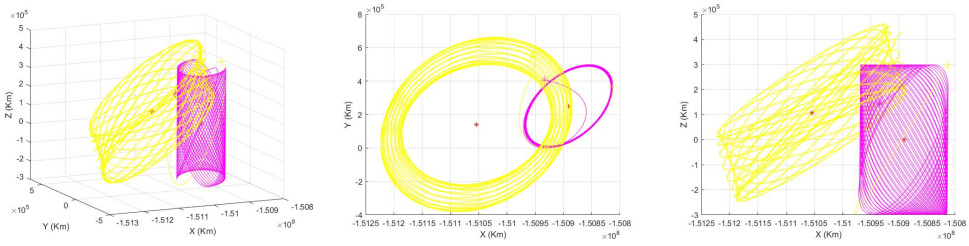

(d) Third impulse maneuver: α from $\pi/6$ to $\pi/3$ and δ from $\pi/2$ to $\pi/4$.

Figure 4.16: Back-and-forth transfers for α from $\pi/6$ to $\pi/3$ and for δ from $\pi/4$ to $\pi/2$.

4.4 Chapter summary

This chapter describes an extensive research on three applications of the proposed impulse maneuver method: (1) a transfer to the same terminal Lissajous orbit, (2) multi-impulse maneuvers to achieve an enhanced heteroclinic transfer, and (3) back-and-forth transfers. The specific work and conclusions are the following:

1. Spacecraft in different positions on the initial Lissajous orbit can transfer to the same terminal Lissajous orbit. However, the spacecraft may miss the transfer window. We found that when the initial and final clock angles are $\delta_{i,f} = \pi/2$, and when the difference in the initial phase angles ϕ_2 is π, then the solar sail spacecraft can transfer to the same terminal Lissajous orbit through an impulse maneuver. This has been verified by the simulations done together with Fig. 3.17.

2. A solar sail panel cannot perform large angular variations in a short time interval. Thus, we propose a multi-impulse maneuver method to achieve Lissajous orbital enhanced heteroclinic transfers. As a result, the terminal Lissajous orbital amplitude is larger. We investigated the effects of different values of α_m, δ_m, and β_m on the middle transitional and terminal Lissajous orbital amplitudes. Considering that β_m has a great influence on the amplitude, and that is difficult to modify β in an actual mission, it is more reasonable to use α_m and δ_m as the middle transitional parameters.

3. In some solar sail missions, the spacecraft may need to return to its original Lissajous orbit near an initial artificial libration point. Thus, we analyzed back-and-forth transfers between two different artificial libration points. We first assessed back-and-forth transfers by changing the cone angle α and compared transfers for different phase angles. Second, we studied changing the clock angle δ and the lightness number β to achieve back-and-forth transfers. During the transfer process, the Lissajous orbital amplitudes will change. We found that A_{xf} and A_{zf} became larger after each transfer.

5

Chapter 5
Avoiding the forbidden zone

In the Solar System, the solar wind, solar eclipses, and the Earth shadow all have a great impact on the safety and work of a spacecraft. For example, in January 2017, India's Mars orbiter made a special orbit adjustment to avoid a solar eclipse. Sun-Earth L_1 libration point missions, like the SOHO spacecraft, have to avoid an exclusion zone of six degrees about the apparent solar disc in order to communicate with the Earth, and space telescopes orbiting near Sun-Earth L_2 must avoid the Earth shadow for the solar panels.

In the restricted three-body problem framework, there is a cylindrical region near the Sun–Earth axis where the Sun's electromagnetic radiation is particularly strong. If a Sun-Earth L_1 satellite passes through this cylinder, the communication link between the satellite and the Earth will be disrupted or interrupted. On the other hand, inside the cylinder at the libration point L_2, the Earth is in front of the Sun, so that a spacecraft will be temporarily unable to generate solar energy. These two regions around the libration points are collectively referred as the forbidden or exclusion zone in the YZ plane, as they should not be spanned by a spacecraft.

Traditionally, big halo orbits, which do not cross the exclusion zone, have been used as nominal paths to avoid this problem [156]. The main disadvantage of this kind of periodic motion is that the in-plane and out-of-plane amplitudes of a halo orbit have to satisfy a fixed relation. Such orbits may not always be optimal for a mission, as they increase the complexity and the cost of some of the hardware parts for a satellite. In contrast, Lissajous LPOs are quasi-periodic motions that provide a high degree of freedom when choosing their amplitudes. However, Lissajous orbits cross the exclusion zone if no maneuvers are

applied. This is the motivation for the work presented in this chapter.

Combining impulsive maneuvers by a solar sail, together with the effective phases plane (EPP) method, this chapter presents a strategy for eclipse avoidance based on solar sail maneuvers that do not introduce unstable terms into the dynamics about a Lissajous orbit. Moreover, we study the influence of the sail attitude and the lightness number on the area of the forbidden zone inside the EPP.

5.1 Effective phase plane

From Eqs. 3.16 it follows that if a satellite is on a Lissajous orbit, then the trajectory satisifes

$$\begin{aligned} x(t) &= A_x e^{\eta_1 t}\cos(\omega_1 t+\phi_1) + A_z e^{\eta_2 t}\overline{k}_{56}\cos(\omega_2 t+\overline{\phi}_{56}), \\ y(t) &= A_x e^{\eta_1 t}k_{34}\cos(\omega_1 t+\phi_{34}) + A_z e^{\eta_2 t}k_{56}\cos(\omega_2 t+\phi_{56}), \\ z(t) &= A_x e^{\eta_1 t}\overline{k}_{34}\cos(\omega_1 t+\overline{\phi}_{34}) + A_z e^{\eta_2 t}\cos(\omega_2 t+\phi_2), \end{aligned} \tag{5.1}$$

for selected values of the in-plane and out of plane amplitudes A_x and A_z, and phases ϕ_1 and ϕ_2. We recall that the phases $\phi_{34}, \overline{\phi}_{34}, \phi_{56}$ and $\overline{\phi}_{56}$ are a function of ϕ_1 and ϕ_2, according to Eqs. 3.17. Moreover, the values of η_1 and η_2, as shown in Table. 3.1, are close to zero, and for the time intervals considered we can assume $e^{\eta_1 t} \approx 1$ and $e^{\eta_2 t} \approx 1$[1].

Taking the time derivative of Eqs. (5.1) we get the state of the spacecraft at time t, and for a given state $(x(t), y(t), z(t), \dot{x}(t), \dot{y}(t), \dot{z}(t))$ on a Lissajous orbit we can assign amplitudes A_x, A_z and phases ϕ_1 and ϕ_2. In the other way round, given these amplitudes, phases, and time t we can compute the state of the spacecraft at this epoch t. Moreover, at any value of $t = t_0$ along the trajectory we can reset time to zero, from this value on the expression of the trajectory is again given by Eqs. (5.1), where the amplitudes A_x and A_z remain the same (in fact change into $A_x e^{\eta_1 t_0}$ and $A_z e^{\eta_2 t_0}$), and the phases ϕ_1 and ϕ_2 experience a "jump" of $\omega_1 t_0$ and $\omega_2 t_0$ units, respectively (i.e. $\phi_i \to \phi_i + \omega_i t_0$).

We define the effective phase Φ (resp. Ψ) as all the epochs t and all the phases ϕ_1 (resp. ϕ_2) such that

$$\Phi(t, \phi_1) = \omega_1 t + \phi_1 \ (\mathrm{mod}, 2\pi), \qquad \Psi(t, \phi_2) = \omega_2 t + \phi_2 \ (\mathrm{mod}, 2\pi). \tag{5.2}$$

Even though from this definition the effective phases are a function of time and the initial phase, it is more convenient to identify them by numbers Φ and Ψ in $[0,\ 2\pi]$.

Considering again Eqs. 5.1, and taking also into account the velocities, we note that there is a biunivocal correspondence between a pair of effective phases (Φ, Ψ) and a

[1] This means that, for the discussion thta follows, we can consider in-plane and out-of-plane constant amplitudes but, even for very long time intervals, the slight variation in $A_x e^{\eta_1 t}$ and $A_z e^{\eta_2 t}$ can be easily taken into account, and implemented in practice, just considering a slightly bigger exclusion zone than the one required by the nominal one.

state $(x, y, z, \dot{x}, \dot{y}, \dot{z})$ on a Lissajous orbit of given amplitudes A_x and A_z. In fact, from a dynamical systems point of view, this is a consequence that Lissajous orbits are 2D tori. Therefore, we are just using the well known action-angle variables of the torus [157, 158]. The time evolution of the effective phase angles $\Phi(t)$ and $\Psi(t)$ are shown in Fig. 5.1 when the solar sail parameters are $\alpha_i = 0$, $\delta_i = \pi/2$, and $\beta_i = 0.02$. The solid line is the effective phase angle Φ over time, and the dotted line is Ψ over time.

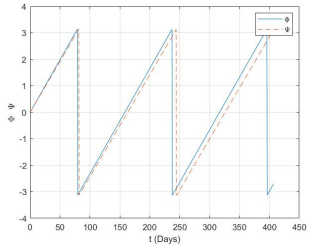

Figure 5.1: Time evolution of $\Phi(t)$ and $\Psi(t)$ when $\alpha_i = 0$, $\delta_i = \pi/2$, $\beta_i = 0.02$, and $\phi_{1,2} = 0$. The slopes are $\omega_1 = 2.5719$ and $\omega_2 = 2.5113$. Note that $\omega_2/\omega_1 \simeq 1$.

Similarly, Figs. 5.2 to 5.4 show the time evolution of $(\Phi(t), \Psi(t))$ with different initial values of ϕ_1, ϕ_2, α_i, or β_i. Except where indicated, the values of the other solar sail parameters are $\alpha_i = 0$, $\delta_i = \pi/2$, $\beta_i = 0.02$, and $\phi_1 = \phi_2 = 0$.

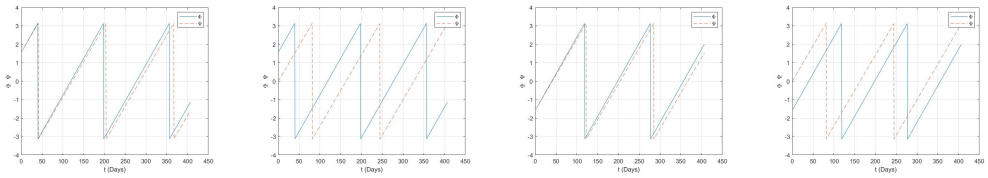

(a) (b) (c) (d)

Figure 5.2: Time evolution of $\Phi(t)$ and $\Psi(t)$ with different values of ϕ_1 and ϕ_2: (a) $\phi_1 = \pi/2$, $\phi_2 = \pi/2$; (b) $\phi_1 = \pi/2$, $\phi_2 = 0$; (c) $\phi_1 = -\pi/2$, $\phi_2 = -\pi/2$; (d) $\phi_1 = -\pi/2$, $\phi_2 = 0$. In all the cases $\omega_1 = 2.5719$ and $\omega_2 = 2.5113$.

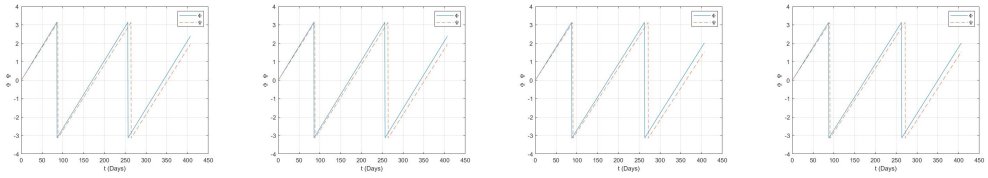

(a) (b) (c) (d)

Figure 5.3: Time evolution of $\Phi(t)$ and $\Psi(t)$ with different values of α_i: (a) $\alpha_i = \pi/4$, $\omega_1 = 2.2112$, $\omega_2 = 2.1673$; (b) $\alpha_i = -\pi/4$, $\omega_1 = 2.2112$, $\omega_2 = 2.1673$; (c) $\alpha_i = \pi/3$, $\omega_1 = 2.1068$, $\omega_2 = 2.0475$; (d) $\alpha_i = -\pi/3$, $\omega_1 = 2.1068$, $\omega_2 = 2.0475$.

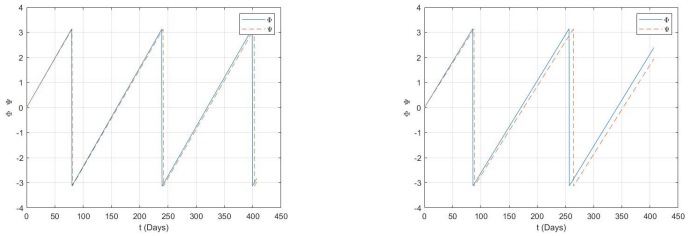

(a) (b)

Figure 5.4: Time evolution of $\Phi(t)$ and $\Psi(t)$ with different values of β_i: (a) $\beta_i = 0.03$, $\omega_1 = 2.2884$, $\omega_2 = 2.2681$; (b) $\beta_i = 0.01$, $\omega_1 = 2.1362$, $\omega_2 = 2.0734$.

In the EPP, $(\Phi(t), \Psi(t)) \in [0,\ 2\pi] \times [0,\ 2\pi]$, an orbit departs from the point (ϕ_1, ϕ_2) at $t = 0$, and travels with constant velocity components ω_1 and ω_2. Using this representation, the 2D tori defined by Lissajous orbits become straight lines with slope $\omega_2/\omega_1 \simeq 1$, as we can check in Figs. 5.1–5.4. Note that each point (Φ, Ψ) of the EPP corresponds to a position on a Lissajous orbit. Although the size of the orbit, given by the constant values A_x and A_z, is not represented, the EPP is a direct way to represent the states of the spacecraft on a Lissajous orbit. Fig. 5.5 shows the correspondence between the EPP and the Lissajous.

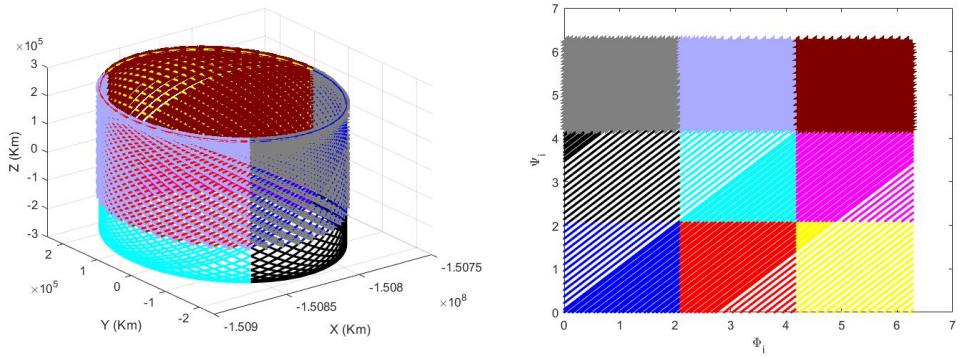

(a) Initial Lissajous (b) EPP of Initial Lissajous

Figure 5.5: Correspondence between the EPP and the Lissajous states. Different colors in the Lissajous orbit correspond to different colors in the EPP.

Fig. 5.6 is an example of a transfer between two Lissajous orbits. Fig. 5.6(a) shows the departure orbit (blue) and arrival orbit (black) in the configuration space. Fig. 5.6(b) is the EPP representation of the departure orbit, and Fig. 5.6(c) the arrival orbit. The red cross in the departure orbit indicates the starting position, whereas the red cross in the arrival orbit indicates the maneuver insertion in the stable manifold of the arrival orbit.

More applications will be shown in the following sections.

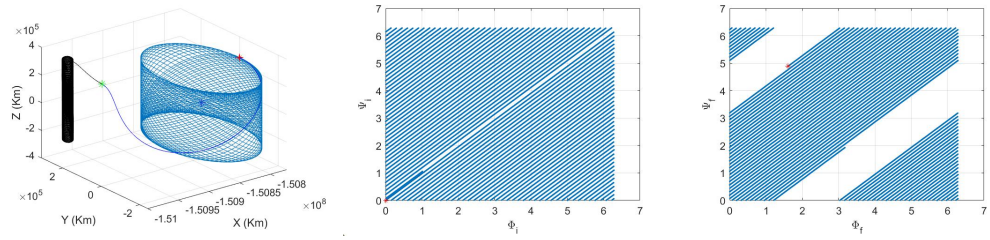

(a) Configuration space (b) EPP of departure orbit (c) EPP of arrival orbit

Figure 5.6: Transfer between two Lissajous orbits in the configuration space and in the EPP.

Table 5.1: Parameters corresponding to the transfer trajectory shown in Fig. 5.6.

Parameter	Value before maneuver	Parameter	Value after maneuver
α_i	0	α_f	$\pi/4$
δ_i	$\pi/2$	δ_f	$\pi/2$
β_i	0.02	β_f	0.02
ϕ_{1i}	0	ϕ_{1f}	1.6102
ϕ_{2i}	0	ϕ_{2f}	4.8895
ω_{1i}	2.5719	ω_{1f}	2.2112
ω_{2i}	2.5113	ω_{2f}	2.1673
ω_{2i}/ω_{1i}	0.9764	ω_{2f}/ω_{1f}	0.9801

5.2 Enhanced heteroclinic transfers to avoid the forbidden zone

For orbits around L_1 in the Sun–Earth system, there is a region around the solar disk, as seen from the Earth, that has to be avoided to ensure that any data sent from a spacecraft are not hidden by the electromagnetic radiation from the Sun. This exclusion zone extends for approximately 3° about the solar disk as seen from the Earth. Similarly, for orbits around the L_2 point of the same system, a spacecraft must avoid the regions eclipsed by the Earth, as well as some bright regions of the sky. The exclusion zone can be considered as a disk in the YZ plane centered at (0,0) (actually a cylinder about the x-axis). So, in the configuration space, is defined by

$$y^2 + z^2 < R^2, \tag{5.3}$$

with $R = 90\,000$ km (see [69] and references therein).

Considering, for instance, $A_x = A_z$ (square Lissajous) that as, it was already mentioned, implies $A_x e^{\eta_1 t} \approx A_x$ and $A_z e^{\eta_2 t} \approx A_z$, and using Eqs. (5.3), we get

$$\begin{aligned}[k_{34}\cos(\Phi - \phi_1 + \phi_{34}) + k_{56}\cos(\Psi - \phi_2 + \phi_{56})]^2 + \\ +[\overline{k}_{34}\cos(\Phi - \phi_1 + \overline{\phi}_{34}) + \cos(\Psi)]^2 < R^2/A_x^2,\end{aligned} \tag{5.4}$$

which is a suitable formula to represent the exclusion zones in the EPP in terms of the size R/A_x.

In general, exclusion zones, similar to ellipses, appear in the EPP. For instance, if we set $A_x = A_z$=1/8, then the initial Lissajous and the exclusion zones are shown in the Fig 5.7.

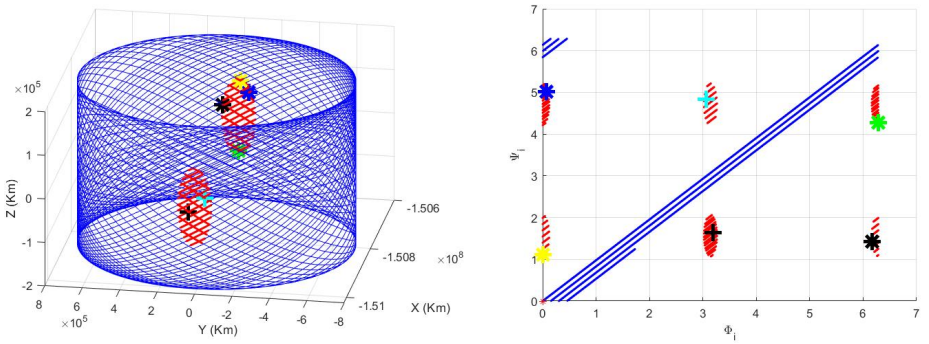

(a) 3D

(b) EPP with a forbidden zone

Figure 5.7: Correspondence between the exclusion zones in the Lissajous orbit and in the EPP.

In Fig. 5.7(a) we represent a 3D Lissajous orbit with the forbidden zone. The red areas denote the places when the orbit is in the forbidden zone. A spacecraft following this Lissajous orbit will certainly cross though the forbidden zones over time, which may hinder the mission.

An initial trajectory on the Lissajous represented in the EPP is shown in Fig. 5.7(b). The blue lines represent the effective phase angle of the spacecraft along the Lissajous orbit and the areas in red are the forbidden areas. Over time, the blue line, with slope slightly less than one, descends at each passage, and it will eventually touch a red area. In the same Fig. 5.7 we also mark different pairs (Φ, Ψ) inside the exclusion zone Eqs. (5.4) and their associated points in the Lissajous orbit.

Taking $A_x = 1/24$, and $A_z = 1/6$, the corresponding Lissajous and the exclusion zones are shown in the Fig.5.8, in which the same comments as for Fig. 5.7 apply to the subplots (a) and (b). In Fig. 5.8(c) we show a time contour map. It indicates the time it would take for the spacecraft to hit the exclusion zone if initially is inserted in the corresponding

point of the EPP. The points in yellow require more time than the ones in blue to reach the exclusion zone. For example, if the spacecraft starts at the red point ($\Phi = \Psi = 0$), it will reach the exclusion zone after 843.6 days, and if it starts at the blue and green points, it will cross the red zone after 654.8 days and 523.9 days, respectively.

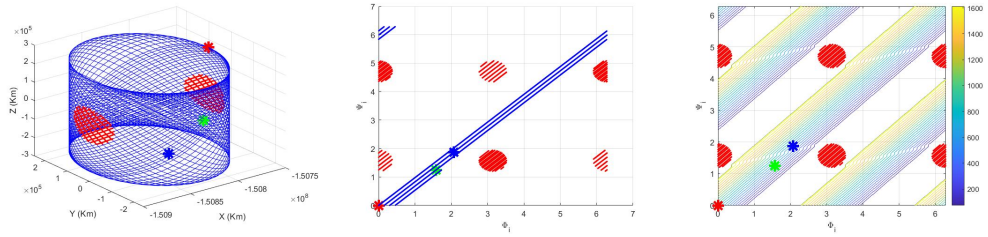

(a) 3D (b) EPP with a forbidden zone (c) Time contour map for crossing the forbidden zone

Figure 5.8: Correspondence between the exclusion zones in the Lissajous and in the EPP and time contour map.

5.2.1 Avoiding the forbidden zone using α_f

In this section, we will show the results of the study done to avoid the forbissen zone combining the impulse maneuver strategy with the EPP method. We will project the 3D forbidden zone, as well as the enhanced heteroclinic transfer orbit, onto a 2D EPP.

For the solar sail parameters $\alpha_i = 0$, $\alpha_f = -\pi/3$, and $\beta_{i,f} = 0.02$, the enhanced heteroclinic transfer orbit and corresponding EPP are shown in Fig. 5.9. Fig. 5.9(a) indicates that the spacecraft escapes from the initial Lissajous orbit (blue cylinder) and reaches the target Lissajous orbit (black cylinder) through impulse maneuvers. The red areas are the forbidden zones, and Figs. 5.9(c) to 5.9(e) are the projections of the enhanced heteroclinic transfer orbits onto the XY, XZ, and YZ planes, respectively. Fig. 5.9(b) is the projection of Fig. 5.9(a) onto the EPP, and it shows the enhanced heteroclinic transfer orbit, Lissajous orbits, and the forbidden zone. The blue straight line corresponds to the initial Lissajous orbit and unstable manifold. The straight black lines are the stable manifold and the terminal Lissajous orbit. The blue ellipses are in the forbidden zone of the initial Lissajous orbit. The black ellipses are in the forbidden zone of the terminal Lissajous orbit. The dotted line represents the change in the effective phase angle before and after the impulse maneuver.

Therefore, the whole enhanced heteroclinic transfer process in Fig. 5.9(a) is represented in Fig. 5.9(b). The spacecraft starts from the red asterisk at the origin, moves along the straight blue line, and performs an impulse maneuver by changing to $\alpha_f = -\pi/3$. The effective phase angle jumps to the black straight line on the left and continues to move along it. Note that the blue ellipse becomes a black ellipse after the impulse maneuver. Since there is always a black ellipse, the straight black line will eventually touch the

forbidden zone.

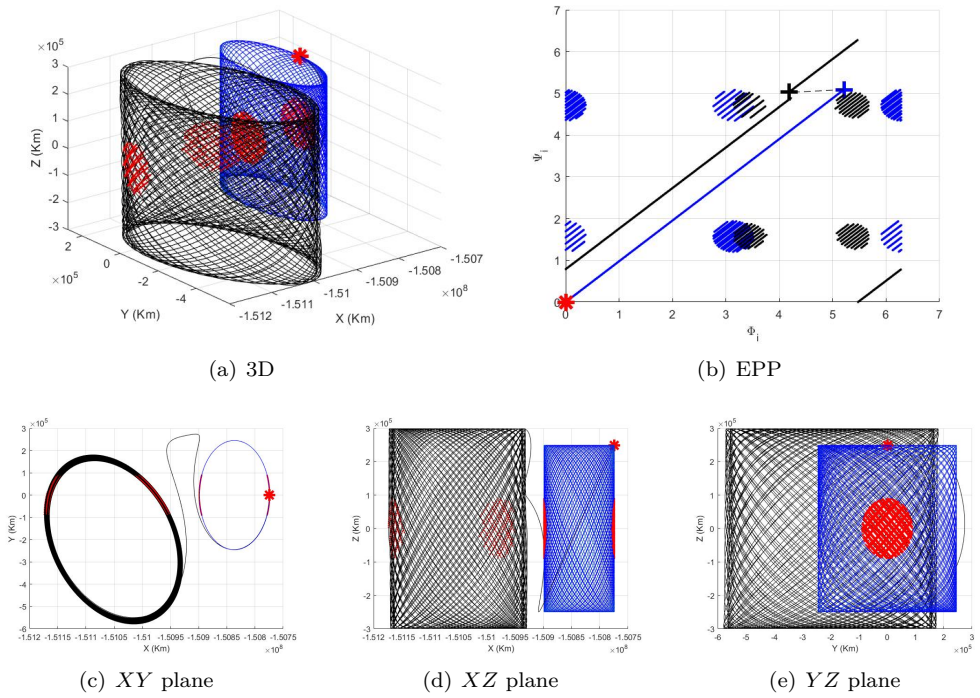

(a) 3D (b) EPP

(c) XY plane (d) XZ plane (e) YZ plane

Figure 5.9: Enhanced heteroclinic transfer orbits and EPPs when $\alpha_i = 0$, $\alpha_f = -\pi/3$, and $\beta_{i,f} = 0.02$.

Fig. 5.10 shows the enhanced heteroclinic transfer orbit and EPP when the solar sail parameters $\alpha_i = 0$, $\alpha_f = \pi/3$, and $\beta_{i,f} = 0.02$. Note that, unlike Fig. 5.9(b), the black ellipse in the EPP has disappeared in Fig. 5.10(b), which means that the spacecraft will not enter the forbidden zone after the impulse maneuver. Fig. 5.10(a) shows the 3D enhanced heteroclinic transfer orbits, and Figs. 5.10(c) to 5.10(e) are their projections onto each plane. The red forbidden zone is in only the initial Lissajous orbit (blue cylinder) and not in the terminal Lissajous orbit (black cylinder). In summary, when the final cone angle $\alpha_f = \pi/3$, the solar sail spacecraft can avoid the forbidden zone through an impulse maneuver. A comparison of Figs. 5.10(a) and 5.10(b) shows that it is more intuitive and clear to identify the change to the forbidden zone on the EPP than with the traditional representation.

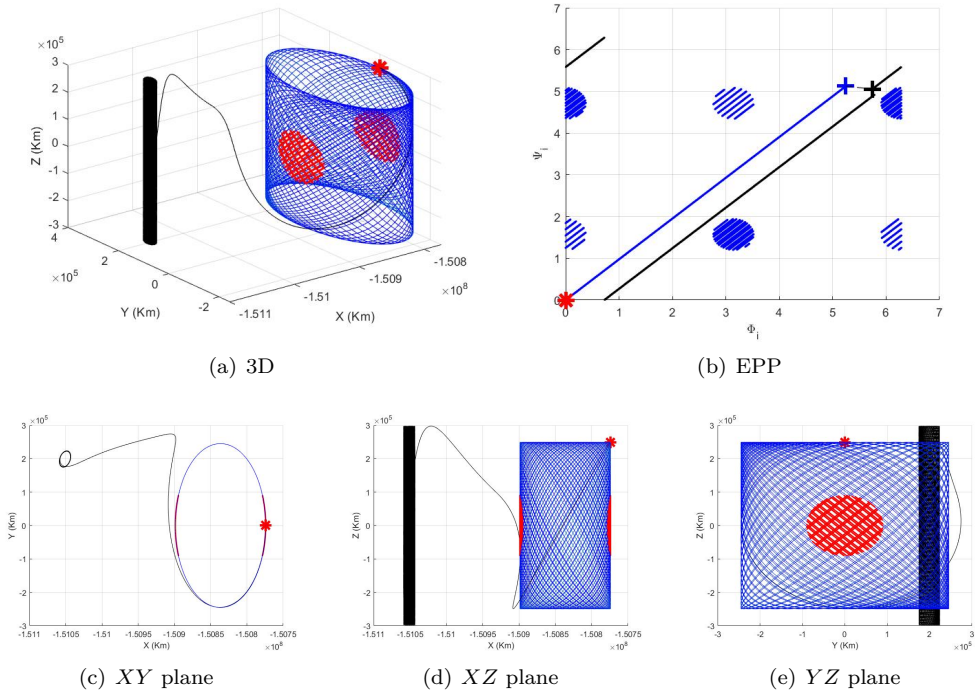

(a) 3D (b) EPP

(c) XY plane (d) XZ plane (e) YZ plane

Figure 5.10: Enhanced heteroclinic transfer orbits and EPPs when $\alpha_i = 0$, $\alpha_f = \pi/3$, and $\beta_{i,f} = 0.02$.

Fig. 5.11 shows the enhanced heteroclinic transfer orbits and EPPs when $\alpha_i = 0$, $\beta_{i,f} = 0.02$, and $\alpha_f \in (0, \pi/2)$. When $\alpha_f = \pi/12$ or $5\pi/12$, the spacecraft will enter the forbidden zone after the impulse maneuver, and when $\alpha_f = \pi/6$ or 1.15, the spacecraft will not enter it. Further simulations show that when $\alpha_f \in (0.045, 1.15)$, the spacecraft will not enter the forbidden zone after the impulse maneuver.

Fig. 5.12 is for the same parameter values as Fig. 5.9 but with an initial phase angle of $\phi_1 = 3\pi/4$. Fig. 5.12(a) shows the 3D orbit enhanced heteroclinic transfer, and Figs. 5.12(c) to 5.12(e) are the projections onto each plane. After the impulse maneuver, there is no red region on the terminal Lissajous orbit, so the spacecraft does not enter the forbidden zone, as shown in Fig. 5.12(e). Fig. 5.12(b) shows the EPP corresponding to the enhanced heteroclinic transfer orbit. The blue ellipses are in the forbidden zone of the initial Lissajous orbit. The solar sail spacecraft starts from $(3\pi/4, 0)$ (red asterisk) and moves along the blue solid line with slope ω_2/ω_1. After the impulse maneuver, the effective phase angle jumps to the black solid line along the dotted line. Again, unlike Fig. 5.9(b), there are no black ellipses, which means that as the spacecraft moves along the black solid line it will never enter the forbidden zone. The corresponding orbital parameters are given in Table 5.2.

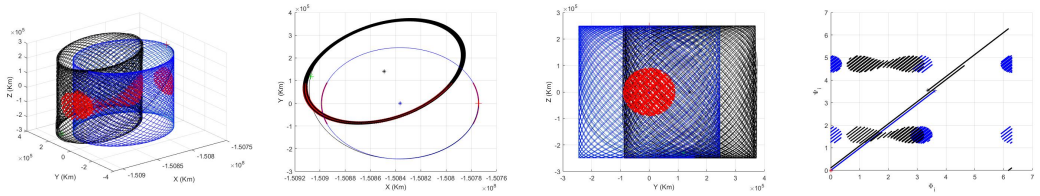

(a) $\alpha_f = \pi/12$

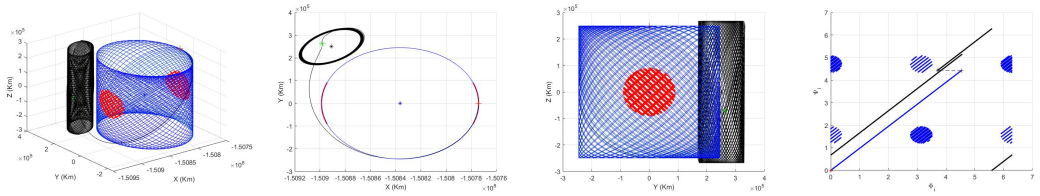

(b) $\alpha_f = \pi/6$

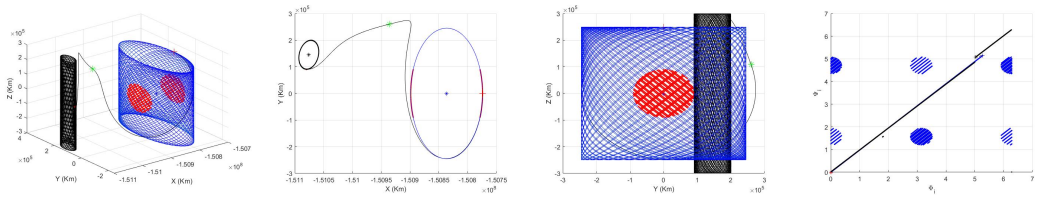

(c) $\alpha_f = 1.15$

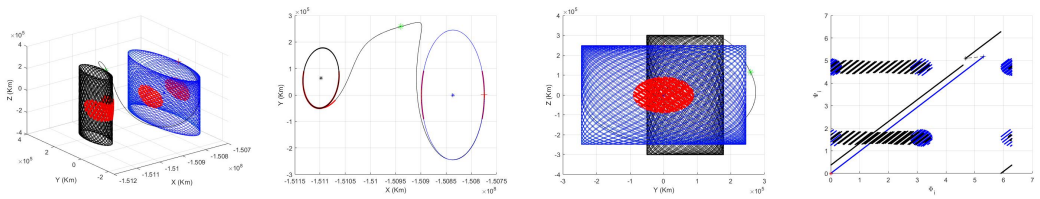

(d) $\alpha_f = 5\pi/12$

Figure 5.11: Enhanced heteroclinic transfer orbits and EPPs when $\alpha_i = 0$, $\beta_{i,f} = 0.02$, and $\alpha_f \in (0, \pi/2)$.

Table 5.2: Parameters for enhanced heteroclinic transfer orbits when $\alpha_i = 0$, $\alpha_f = -\pi/3$, and $\phi_1 = 3\pi/4$.

	α	δ	β	γ_1	γ_2	γ_3	ϕ_1	ϕ_2
Initial	0	$\pi/2$	0.02	-1.0083	0	0	$3\pi/4$	0
Terminal	$-\pi/3$	$\pi/2$	0.02	-1.0097	-0.0013	0	1.8484	-1.4023

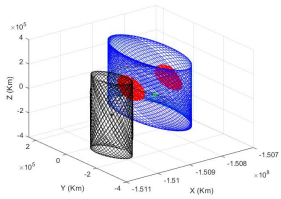

(a) 3D

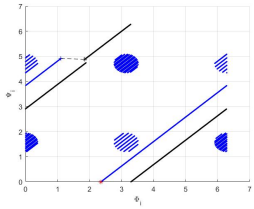

(b) EPP

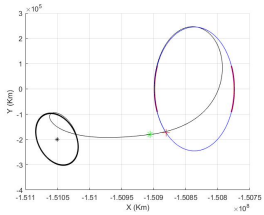

(c) XY plane

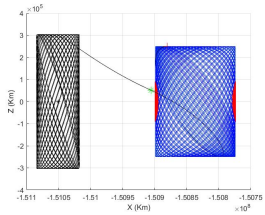

(d) XZ plane

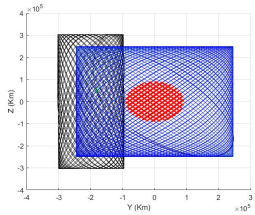

(e) YZ plane

Figure 5.12: Enhanced heteroclinic transfer orbits and EPPs when $\alpha_i = 0$, $\alpha_f = -\pi/3$, and $\phi_1 = 3\pi/4$.

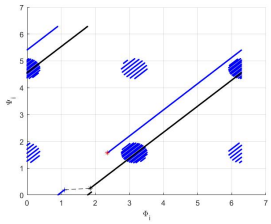

(a) $\phi_1 = 3\pi/4$, $\phi_2 = \pi/2$

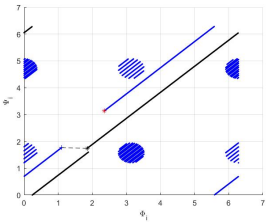

(b) $\phi_1 = 3\pi/4$, $\phi_2 = \pi$

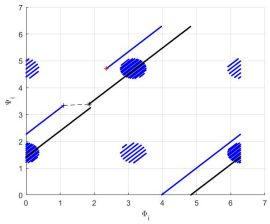

(c) $\phi_1 = 3\pi/4$, $\phi_2 = 3\pi/2$

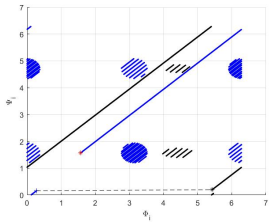

(d) $\phi_1 = \pi/2$, $\phi_2 = \pi/2$

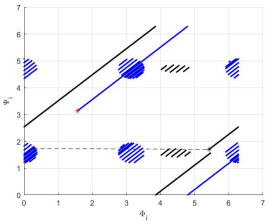

(e) $\phi_1 = \pi/2$, $\phi_2 = \pi$

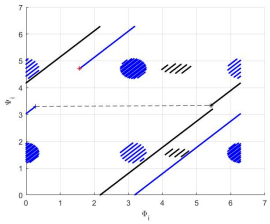

(f) $\phi_1 = \pi/2$, $\phi_2 = 3\pi/2$

Figure 5.13: EPPs with different initial phase angles when $\alpha_i = 0$, $\alpha_f = -\pi/3$, $\delta_{i,f} = \pi/2$, and $\beta_{i,f} = 0.02$.

Fig. 5.13 shows the enhanced heteroclinic transfer orbit for different initial phase angles ϕ_1 and ϕ_2 when $\alpha_i = 0$, $\alpha_f = -\pi/3$, $\delta_{i,f} = \pi/2$, and $\beta_{i,f} = 0.02$. Figs. 5.13(a) to 5.13(c) are the EPPs corresponding to $\phi_1 = 3\pi/4$ and $\phi_2 = \pi/2$, π, or $3\pi/2$, respectively. There

is no forbidden zone after the impulse maneuver. Figs. 5.13(d) to 5.13(f) are the EPPs corresponding to $\phi_1 = \pi/2$ and $\phi_2 = \pi/2$, π, or $3\pi/2$, respectively. There is still a black ellipse after the reorientation by the impulse maneuver. Further calculations show that when the initial phase angle $\phi_1 \in (1.689, 2.356)$, the solar sail spacecraft will not enter a forbidden zone after an impulse maneuver. Fig. 5.10 shows the enhanced heteroclinic transfer orbit and EPP when the initial phase angle $\phi_{1,2} = 0$. Although the spacecraft avoids the forbidden zone after the impulse maneuver, the terminal amplitude is too narrow. Fig. 5.14 presents EPPs with the same solar sail parameters but for different initial phase angles.

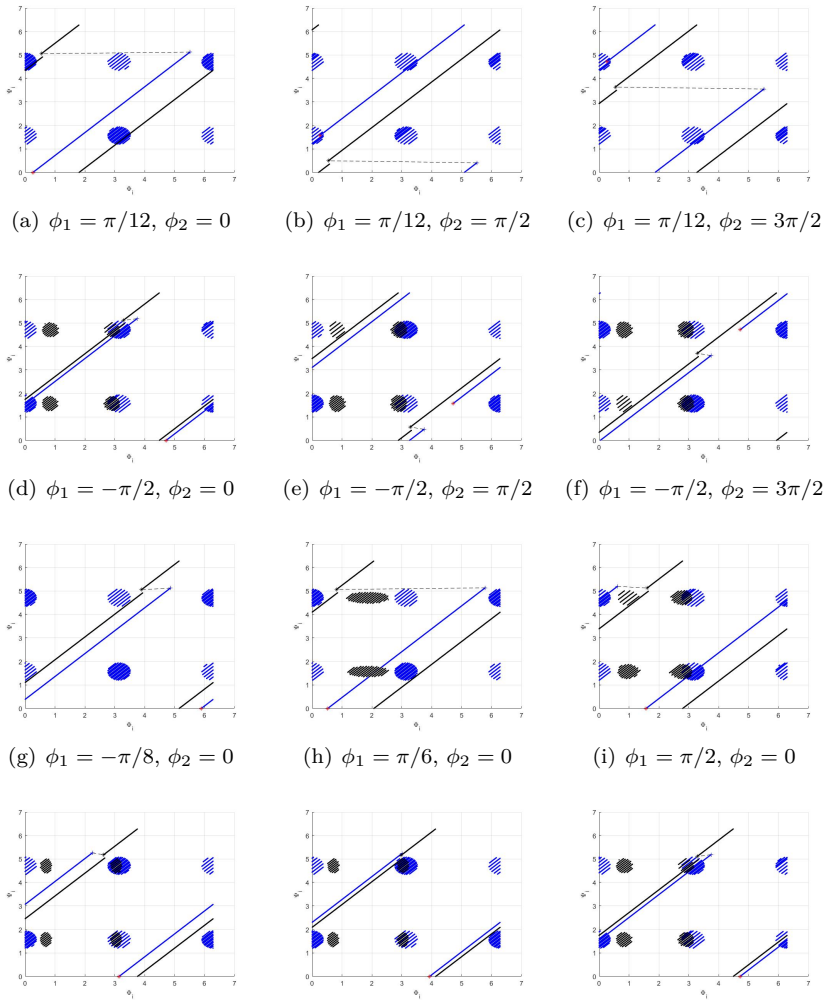

(a) $\phi_1 = \pi/12$, $\phi_2 = 0$ (b) $\phi_1 = \pi/12$, $\phi_2 = \pi/2$ (c) $\phi_1 = \pi/12$, $\phi_2 = 3\pi/2$

(d) $\phi_1 = -\pi/2$, $\phi_2 = 0$ (e) $\phi_1 = -\pi/2$, $\phi_2 = \pi/2$ (f) $\phi_1 = -\pi/2$, $\phi_2 = 3\pi/2$

(g) $\phi_1 = -\pi/8$, $\phi_2 = 0$ (h) $\phi_1 = \pi/6$, $\phi_2 = 0$ (i) $\phi_1 = \pi/2$, $\phi_2 = 0$

(j) $\phi_1 = \pi$, $\phi_2 = 0$ (k) $\phi_1 = 5\pi/4$, $\phi_2 = 0$ (l) $\phi_1 = 3\pi/2$, $\phi_2 = 0$

Figure 5.14: EPPs with different initial phase angles when $\alpha_i = 0$, $\alpha_f = \pi/3$, $\delta_{i,f} = \pi/2$, and $\beta_{i,f} = 0.02$.

When the initial phase angle $\phi_1 \in (-0.39, 0.27)$, the solar sail spacecraft will not enter the forbidden after the impulse maneuver. Figs. 5.14(d) to 5.14(f) suggest that the initial phase angle ϕ_2 has little impact on the forbidden zone in the EPP.

We next consider a enhanced heteroclinic transfer with two reorientation impulse maneuvers. Here, $\alpha_i = 0$, $\alpha_f = -0.35$, $\delta_{i,f} = \pi/2$, and $\beta_{i,f} = 0.02$. The two enhanced heteroclinic transfer orbits and EPPs are shown in Fig. 5.15. The solar sail spacecraft starts from the initial Lissajous orbit (blue cylinder) and changes to the final cone angle $\alpha_f = -0.35$ for the first impulse maneuver. The spacecraft then enters the black terminal Lissajous orbit. After the second impulse maneuver, the spacecraft enters the green Lissajous orbit. Figs. 5.15(d) and 5.15(e) are the EPPs for the two impulse maneuvers. In Fig. 5.15(d), the blue and black ellipses are in the forbidden zones before and after the first maneuver. Fig. 5.15(e) shows the EPP with the second impulse maneuver. The red ellipses, which are after the second maneuver, are smaller than the initial blue ellipses. However, in general, two maneuvers do not always allow the spacecraft to completely avoid the forbidden zone, so that it will eventually touch it.

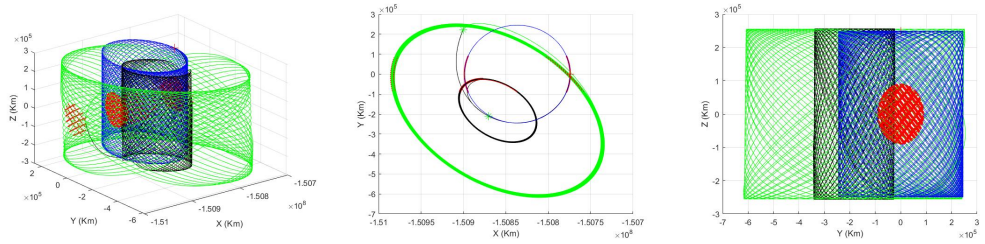

(a) 3D (b) XY plane (c) YZ plane

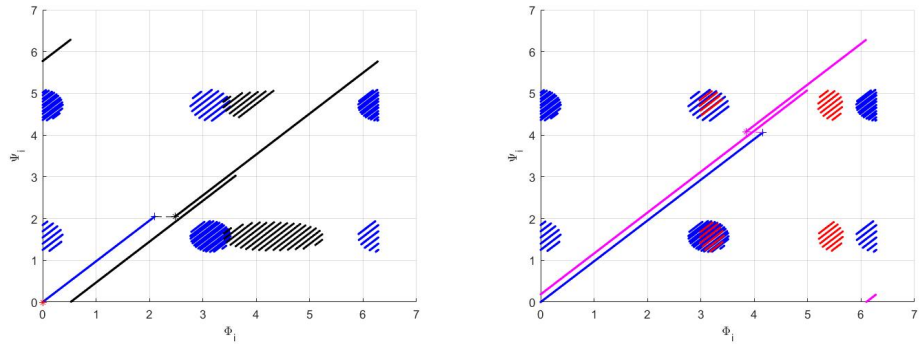

(d) EPP 1st impulse maneuver (e) EPP 2nd impulse maneuver

Figure 5.15: Enhanced heteroclinic transfer orbits and EPP representations when $\alpha_i = 0$ and $\alpha_f = -0.35$.

Finally, we consider a enhanced heteroclinic transfer with three impulse maneuvers. Here, $\alpha_i = 0$, $\alpha_f = -0.45$, $\delta_{i,f} = \pi/2$, and $\beta_{i,f} = 0.02$. The three enhanced heteroclinic transfer

orbits and EPPs are shown in Fig. 5.16.

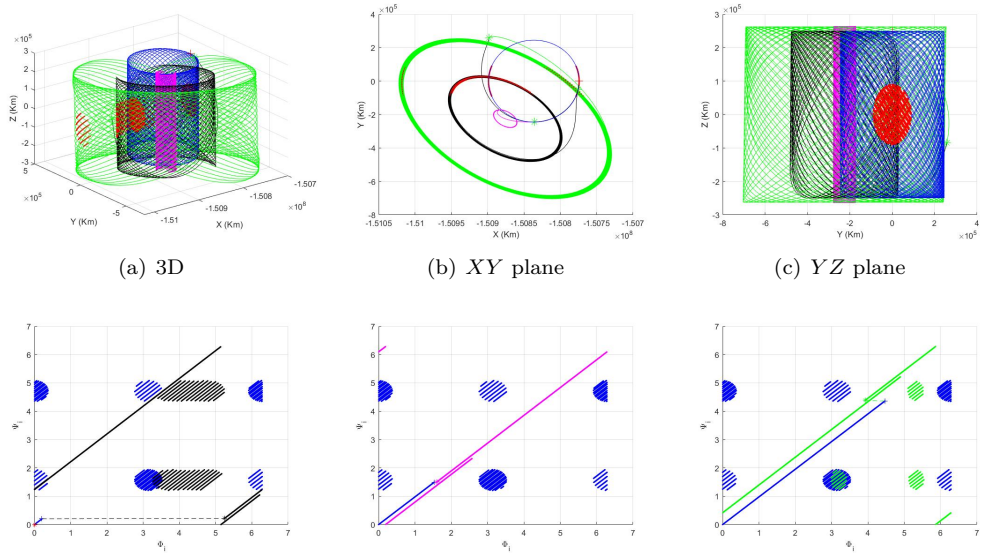

(a) 3D (b) XY plane (c) YZ plane

(d) EPP 1st impulse maneuver (e) EPP 2nd impulse maneuver (f) EPP 3rd impulse maneuver

Figure 5.16: Enhanced heteroclinic transfer orbits and EPP representations when $\alpha_i = 0$ and $\alpha_f = -0.45$.

5.2.2 Avoiding the forbidden zone using δ_f

Section 5.2.1 mainly studied how to avoid the forbidden zone using the cone angle and phase angle; this section will consider using α_f and δ_f to avoid it.

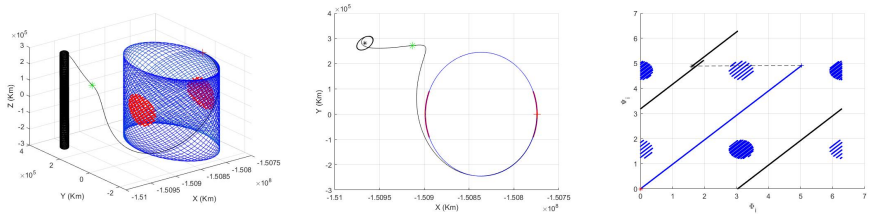

(a) 3D (b) XY plane (c) EPP

Figure 5.17: Enhanced heteroclinic transfer orbits and EPPs when $\alpha_i = 0$ and $\alpha_f = \pi/4$.

Fig. 5.17 shows the enhanced heteroclinic transfer orbit and the EPP representation when $\delta_{i,f} = \pi/2$, $\alpha_i = 0$, and $\alpha_f = \pi/4$. After the impulse maneuver, the spacecraft will not enter the forbidden zone, however, the amplitude A_{xf} is too small, which is not suitable

for many missions. Thus, we changed δ_f and observed the influence on the final Lissajous orbital amplitude and the forbidden area. Fig. 5.18 shows the enhanced heteroclinic transfer orbits and EPPs when $\delta_f = 1.45$, 1.68, and 2. The colors in the figure are similar to those used in previous ones. Note that the dotted line, which represents the jump, is no longer parallel to the X-axis. This figure shows that changing δ_f not only can change the terminal amplitude but also avoids the forbidden zone. The parameters of this example are listed in Table 5.3. From further calculations when $\delta_f \in (1.45, 1.68)$, it has been found that there is no forbidden zone after the impulse maneuver.

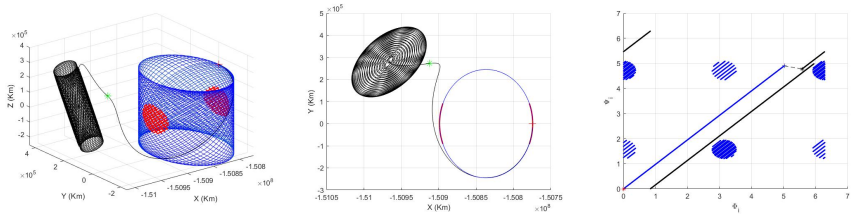

(a) $\delta_f = 1.45$

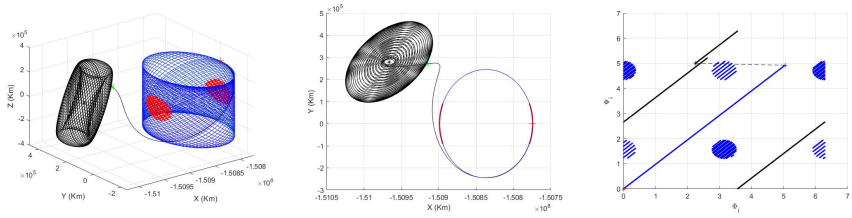

(b) $\delta_f = 1.68$

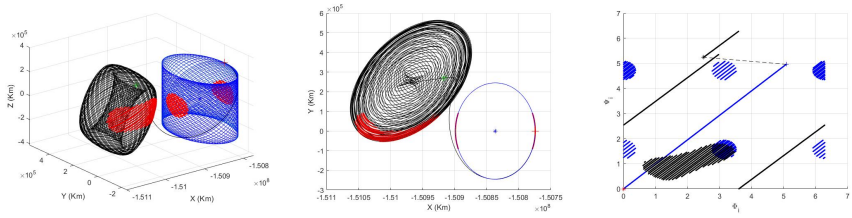

(c) $\delta_f = 2$

Figure 5.18: Enhanced heteroclinic transfer orbits and EPPs when $\alpha_i = 0$, $\alpha_f = \pi/4$, and $\delta_f = 1.45$, 1.68, or 2.

Table 5.3: Parameters for enhanced heteroclinic transfer orbits and EPP when $\alpha_i = 0$, $\alpha_f = \pi/4$, and $\delta_f = 1.45$, 1.68, or 2.

α_f	δ_f	β_f	γ_1	γ_2	γ_3	ϕ_1	ϕ_2
$\pi/4$	2	0.02	−1.00915	0.00187	0	0	0
$\pi/4$	1.45	0.02	−1.00915	0.00186	0.00018	0	0
$\pi/4$	1.68	0.02	−1.00915	0.00187	0.00016	0	0

For $\alpha_f = -\pi/3$ and $\delta_f = 0, \pi/6, \ldots, \pi$, the enhanced heteroclinic transfer orbits and EPPs are shown in Fig. 5.19. As it can be seen, when $\alpha_f = -\pi/3$, regardless of the value of δ_f, the terminal Lissajous orbit will enter the forbidden zone.

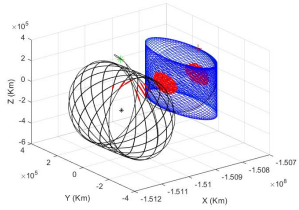

(a) 3D: $\alpha_f = -\pi/3$, $\delta_f = 0$

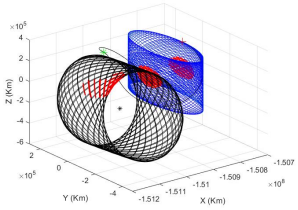

(b) 3D: $\alpha_f = -\pi/3$, $\delta_f = \pi/6$

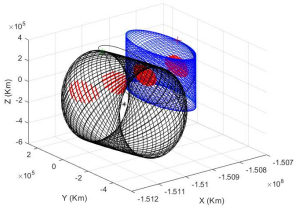

(c) 3D: $\alpha_f = -\pi/3$, $\delta_f = \pi/3$

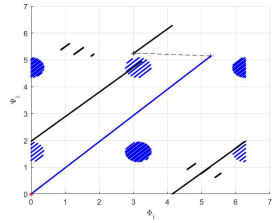

(d) EPP: $\alpha_f = -\pi/3$, $\delta_f = 0$

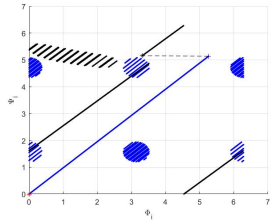

(e) EPP: $\alpha_f = -\pi/3$, $\delta_f = \pi/6$

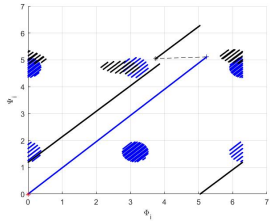

(f) EPP: $\alpha_f = -\pi/3$, $\delta_f = \pi/3$

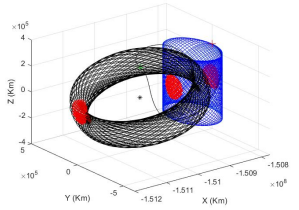

(g) 3D: $\alpha_f = -\pi/3$, $\delta_f = 2\pi/3$

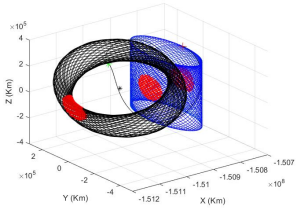

(h) 3D: $\alpha_f = -\pi/3$, $\delta_f = 5\pi/6$

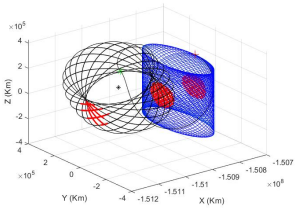

(i) 3D: $\alpha_f = -\pi/3$, $\delta_f = \pi$

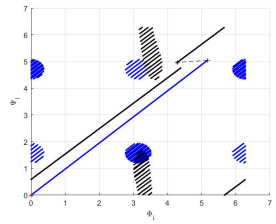

(j) EPP: $\alpha_f = -\pi/3$, $\delta_f = 2\pi/3$

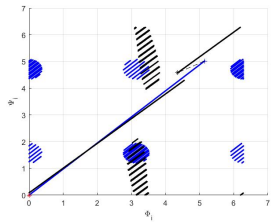

(k) EPP: $\alpha_f = -\pi/3$, $\delta_f = 5\pi/6$

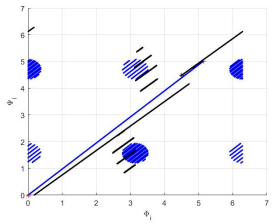

(l) EPP: $\alpha_f = -\pi/3$, $\delta_f = \pi$

Figure 5.19: Enhanced heteroclinic transfer orbits and EPPs when $\alpha_f = -\pi/3$ and $\delta_f = 0, \pi/6, 2\pi/6, \ldots, \pi$.

The above situations have only one transfer opportunity. However, there are two transfer opportunities when $\alpha_i = 0$, $\alpha_f = -0.45$, and $\delta_f = 2$. The enhanced heteroclinic transfer orbits and EPPs are shown in Fig. 5.20. Note that the forbidden zone is relatively small, and that the black forbidden zone is larger than the blue one for before the impulse maneuver. Fig. 5.20(d) is the EPP with the first impulse maneuver. Fig. 5.20(e) is the EPP corresponding to the second impulse maneuver. When $\alpha_i = 0$, $\alpha_f = -0.45$, and $\delta_f = 1.6$, there are three transfer opportunities. The enhanced heteroclinic transfer orbits and EPPs are shown in Fig. 5.21.

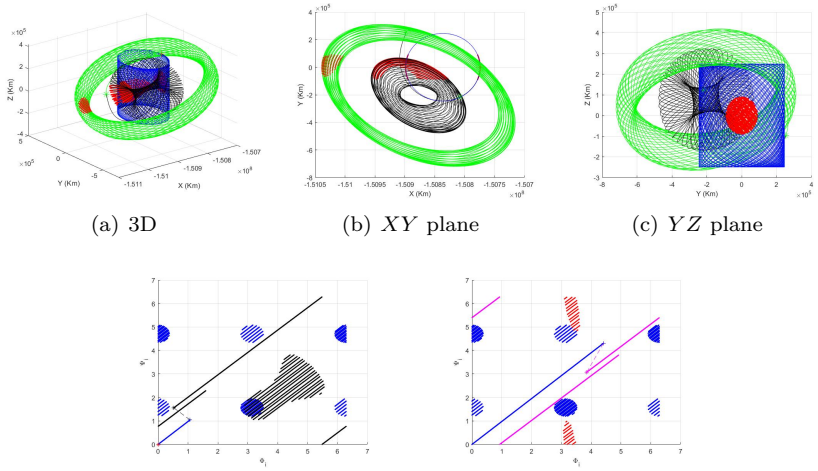

(a) 3D (b) XY plane (c) YZ plane

(d) EPP with the first impulse maneuver (e) EPP with the second impulse maneuver

Figure 5.20: Enhanced heteroclinic transfer orbits and EPPs when $\alpha_i = 0$, $\alpha_f = -0.45$, and $\delta_f = 2$.

Compared with Fig. 5.16, when $\delta_f = 1.6$, the forbidden zones after the impulse maneuvers depicted in Figs. 5.21(d)–5.21(f) are larger. The spacecraft successfully avoids the forbidden zone after the second impulse maneuver. Moreover, the terminal amplitude is larger, as shown in Fig. 5.21(f).

5.2.3 Avoiding the forbidden zone using β

5.2.3.1 Avoiding the forbidden zone using β only

The enhanced heteroclinic transfer orbits and EPPs with $\beta_f = 0.01$ or 0.04 are shown in Fig. 5.22 when the solar sail parameters $\alpha_{i,f} = 0$, $\delta_{i,f} = \pi/2$, and $\beta_i = 0.02$. Since $\alpha = 0$, the artificial libration point can move only along the Sun–Earth line. As a result, the forbidden zone does not change, so changing β alone cannot avoid it.

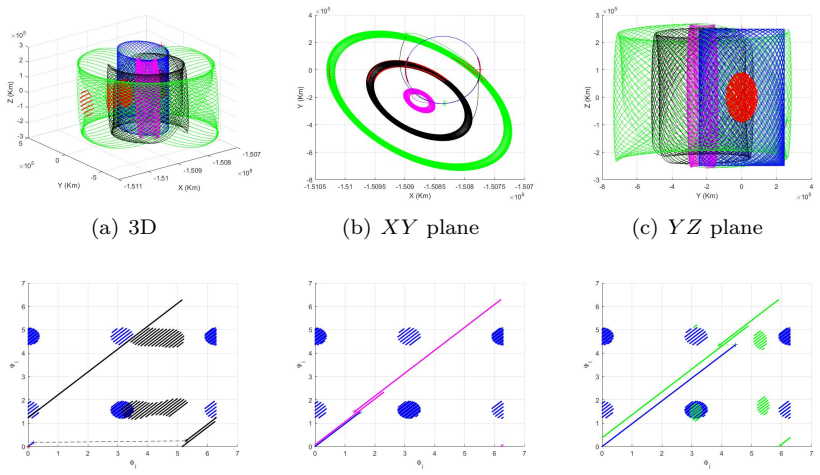

(a) 3D (b) XY plane (c) YZ plane

(d) EPP with the first impulse maneuver (e) EPP with the second impulse maneuver (f) EPP with the third impulse maneuver

Figure 5.21: Enhanced heteroclinic transfer orbits and EPPs when $\alpha_i = 0$, $\alpha_f = -0.45$, and $\delta_f = 1.6$.

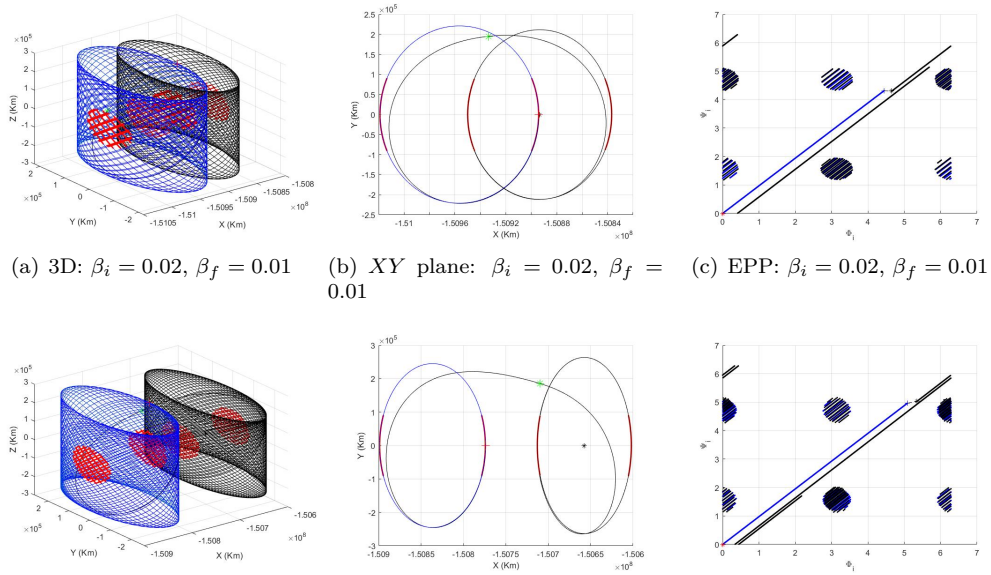

(a) 3D: $\beta_i = 0.02$, $\beta_f = 0.01$ (b) XY plane: $\beta_i = 0.02$, $\beta_f = 0.01$ (c) EPP: $\beta_i = 0.02$, $\beta_f = 0.01$

(d) 3D: $\beta_i = 0.02$, $\beta_f = 0.04$ (e) XY plane: $\beta_i = 0.02$, $\beta_f = 0.04$ (f) EPP: $\beta_i = 0.02$, $\beta_f = 0.04$

Figure 5.22: Enhanced heteroclinic transfer orbits and EPPs when $\beta_i = 0.02$ and $\beta_f = 0.01$ or 0.04.

5.2.3.2 Avoiding the forbidden zone using β and α_f

The enhanced heteroclinic transfer orbits and EPPs are shown in Fig. 5.23 when the solar sail parameters $\alpha_i = 0$, $\beta_i = 0.01$, $\beta_f = 0.02$, and $\alpha_f = \pi/6$, $\pi/4$, or $\pi/3$. When α_f is small, the terminal Lissajous orbit will pass through the forbidden zone, as shown in Fig. 5.23(a), because the artificial libration point is closer to the forbidden zone. When $\alpha_f = \pi/4$ or $\pi/3$, the terminal Lissajous orbits do not pass through the forbidden zone. Further calculations show that when the solar sail parameters $\alpha_f > 0.7$, $\beta_i = 0.01$, and $\beta_f = 0.02$, the enhanced heteroclinic transfer orbit and EPP can avoid the forbidden zone.

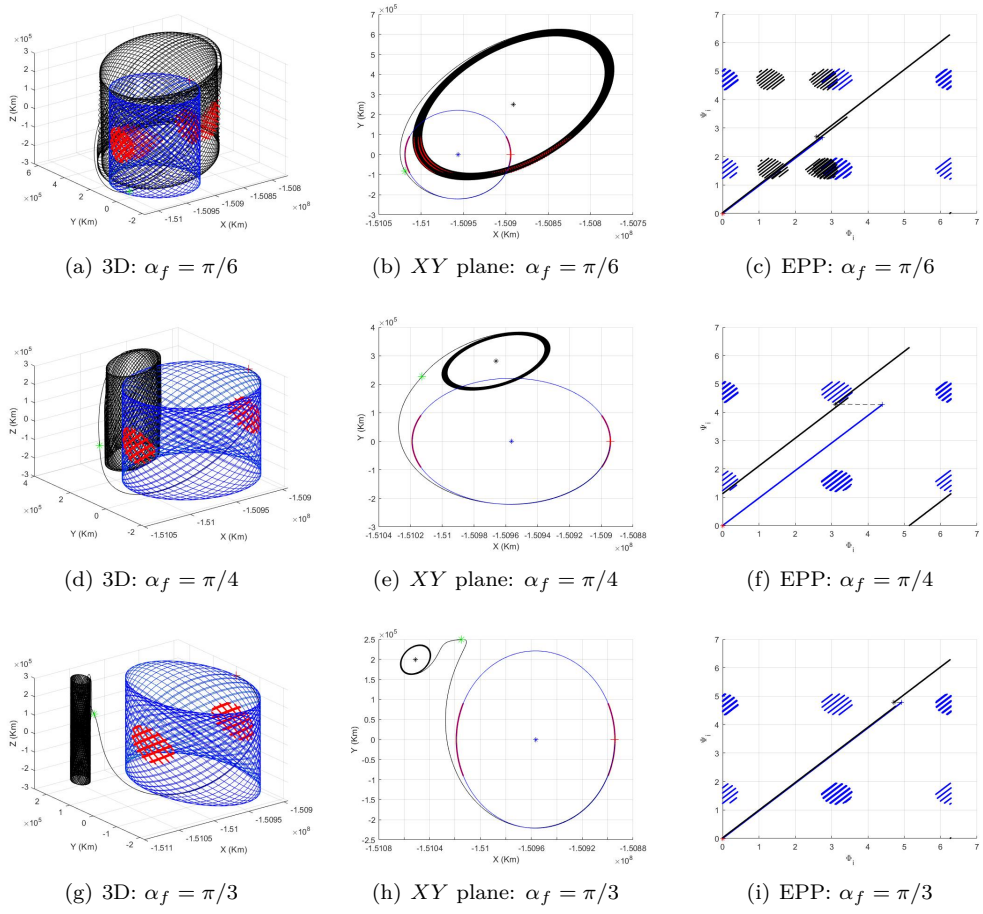

(a) 3D: $\alpha_f = \pi/6$ (b) XY plane: $\alpha_f = \pi/6$ (c) EPP: $\alpha_f = \pi/6$

(d) 3D: $\alpha_f = \pi/4$ (e) XY plane: $\alpha_f = \pi/4$ (f) EPP: $\alpha_f = \pi/4$

(g) 3D: $\alpha_f = \pi/3$ (h) XY plane: $\alpha_f = \pi/3$ (i) EPP: $\alpha_f = \pi/3$

Figure 5.23: Enhanced heteroclinic transfer orbits and EPPs when $\alpha_i = \pi/2$, $\beta_i = 0.01$, $\beta_f = 0.02$, and $\alpha_f = \pi/6$, $\pi/4$, or $\pi/3$.

The enhanced heteroclinic transfer orbits and EPPs for $\alpha_f < 0$ are shown in Fig. 5.24

when the solar sail parameters $\alpha_i = 0$, $\beta_i = 0.01$, and $\beta_f = 0.02$. When $\alpha_f = -\pi/4$, the forbidden zone cannot be avoided after the maneuver and becomes larger, as shown in Fig. 5.24(c). Figs. 5.24(f) and 5.24(i) are the EPPs corresponding to $\alpha_f = -\pi/3$ and $-\pi/2$, respectively. The forbidden zone becomes smaller after the maneuver but still exists. In summary, when $\alpha_f < 0$, $\beta_i = 0.01$, and $\beta_f = 0.02$, the terminal Lissajous orbit will always pass through the forbidden zone after an impulse maneuver.

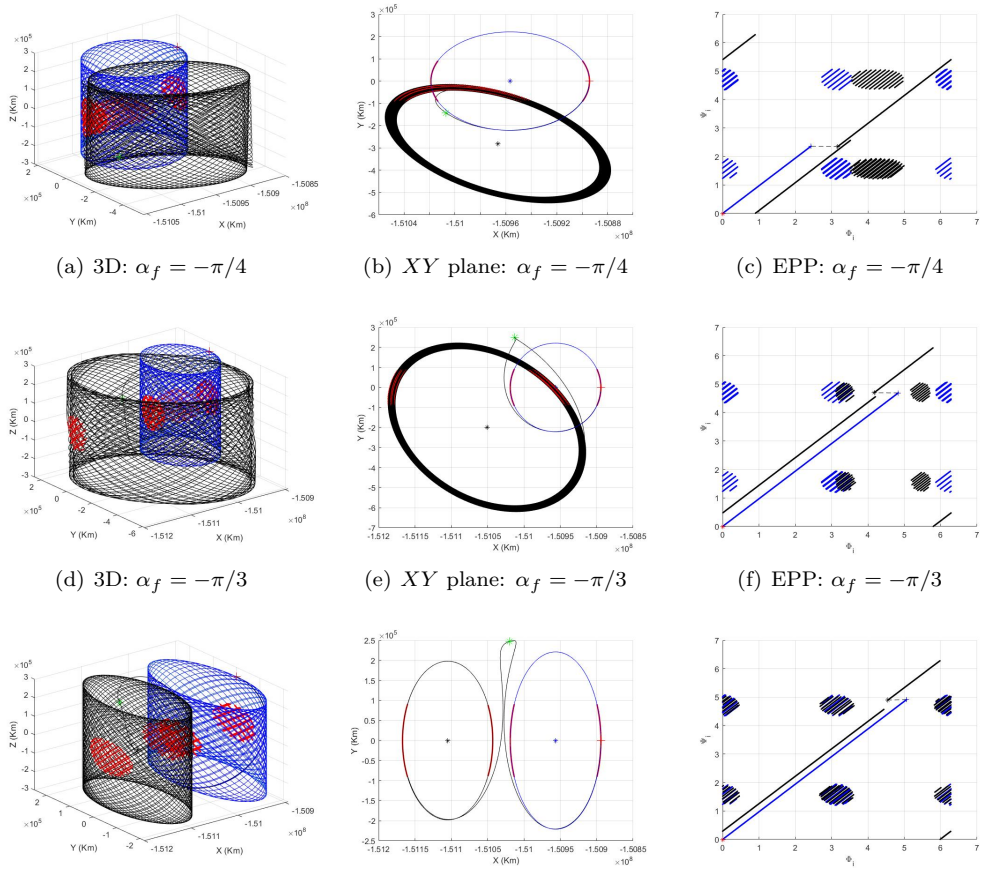

(a) 3D: $\alpha_f = -\pi/4$ (b) XY plane: $\alpha_f = -\pi/4$ (c) EPP: $\alpha_f = -\pi/4$

(d) 3D: $\alpha_f = -\pi/3$ (e) XY plane: $\alpha_f = -\pi/3$ (f) EPP: $\alpha_f = -\pi/3$

(g) 3D: $\alpha_f = -\pi/2$ (h) XY plane: $\alpha_f = -\pi/2$ (i) EPP: $\alpha_f = -\pi/2$

Figure 5.24: Enhanced heteroclinic transfer orbits and EPPs for different α_f when $\alpha_i = 0$, $\beta_i = 0.01$, and $\beta_f = 0.02$.

5.2.3.3 Avoiding the forbidden zone using α_f, δ_f, and β

The enhanced heteroclinic transfer orbits and EPPs corresponding to different terminal clock angles δ_f are shown in Fig. 5.25 when the solar sail parameters $\alpha_i = 0$, $\alpha_f = \pi/3$, $\delta_i = \pi/2$, $\beta_i = 0.01$, and $\beta_f = 0.02$.

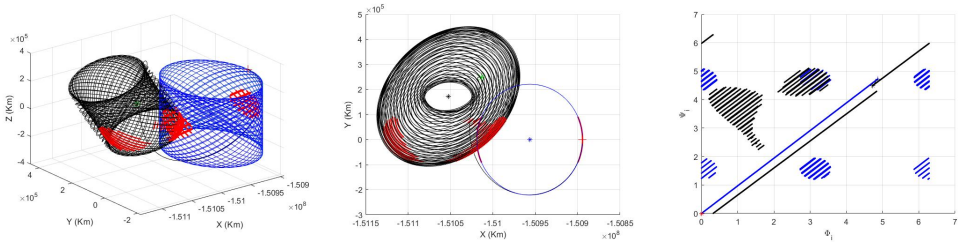

(a) $\delta_f = \pi/3$

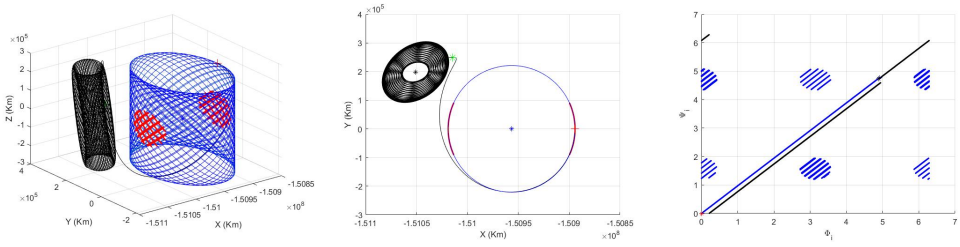

(b) $\delta_f = 1.48$

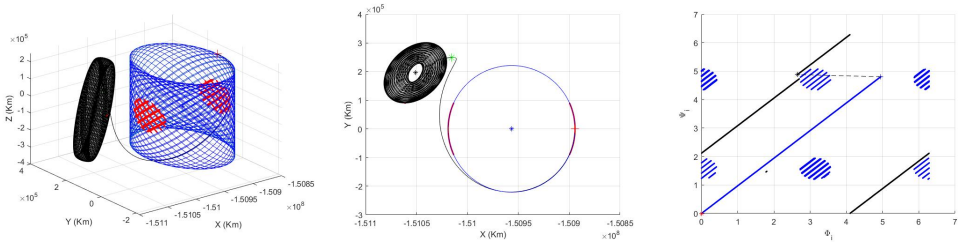

(c) $\delta_f = 1.75$

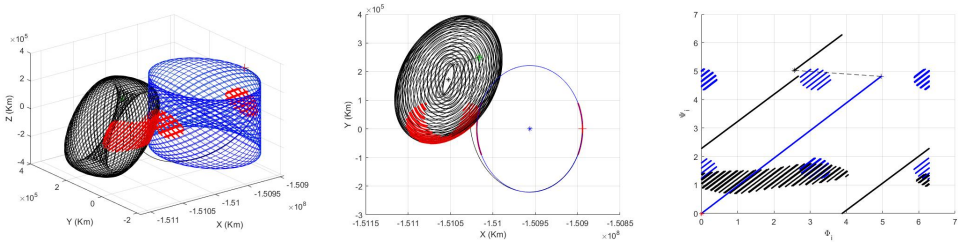

(d) $\delta_f = 2\pi/3$

Figure 5.25: Enhanced heteroclinic transfer orbits and EPPs for different δ_f when $\alpha_i = 0$, $\alpha_f = \pi/3$, $\delta_i = \pi/2$, $\beta_i = 0.01$, and $\beta_f = 0.02$.

Figs. 5.25(a) and 5.25(d) are the enhanced heteroclinic transfer orbits and EPPs when $\delta_f = \pi/3$ and $2\pi/3$, respectively. They show that the spacecraft cannot avoid the forbidden zone with an impulse maneuver. In Figs. 5.25(b) and 5.25(c), the spacecraft

avoids the forbidden zone after the maneuver. Compared with Fig. 5.23(g), the amplitude of the terminal Lissajous orbit A_{xf} is larger. Further calculations show that when $\delta_f \in (1.48, 1.75)$, the spacecraft can avoid the forbidden zone after an impulse maneuver. Thus, it is important to select the appropriate terminal solar sail parameters according to the mission needs.

5.3 Chapter summary

This chapter uses the impulse maneuver method combined with the EPP method to visually present enhanced heteroclinic transfer orbits that allow a spacecraft to avoid the forbidden zone completely, or to avoid it for a long time interval. The specific work and conclusions are the following:

1. The EPP method is introduced . To simplify and visualize the problem, we use the EPP method to project the 3D forbidden zone and enhanced heteroclinic transfer orbits onto the EPP. This approach gives an intuitive indication of whether the solar sail spacecraft will enter the forbidden zone or not. We also analyze the influence of different solar sail parameters on the effective phase angle. Finally, we plot a time contour map to show that the spacecraft reaches the forbidden zone at different positions in the Lissajous orbit.

2. The use of the cone angle has been introduced to avoid the forbidden zone. When the final cone angle $\alpha_f = \pi/3$, the forbidden zone becomes smaller. Theoretically, the spacecraft can operate for a longer time, but it will always enter the forbidden zone. Changing the initial phase angle ϕ_1, the forbidden zone can disappear in the EPP, so that the spacecraft can avoid it. When there are two or three transfer opportunities, the forbidden zone in the EPP will change after each maneuver, and there may be no forbidden zone.

3. The use of the clock angle has been introduced to avoid the forbidden zone. Although changing the cone angle alone can make the forbidden zone to disappear in the EPP, the terminal Lissajous orbit may be too narrow and the amplitude too small, which is not suitable for many missions. Changing both the cone angle and the clock angle not only solves the small amplitude problem but also allows the mission to avoid the forbidden zone.

4. The use of the lightness number has been introduced to avoid the forbidden zone. When the cone angle $\alpha_{i,f} = 0$, regardless of the value of the lightness number, since the artificial libration point is on the Sun–Earth line, the spacecraft cannot avoid the forbidden zone. However, the forbidden zone will change in the EPP. Under the combined action of cone angle, clock angle, and lightness number, the spacecraft can avoid the forbidden zone after a maneuver. For example, when $\beta_i = 0.01$, $\beta_f = 0.02$, and $\alpha_f > 0.7$, the forbidden zone in the EPP will disappear after the maneuver.

6

Chapter 6

Propellant–free station–keeping design of a solar sail around the Sun–Earth collinear equilibrium points

The IKAROS [159], NanoSail-D2 [160] and LightSail–2 [161] missions have validated the solar sail technology, showing that is possible to achieve interplanetary transfers and to change the spacecraft's orbit. However, still many other things need to be addressed, like the feasibility of station–keeping around a LPO using the solar sail technology.

NASA has proposed the Geostorm warning [126, 162] mission, which aims to obtaining solar storm data from a solar sail spacecraft positioned at an artificial equilibrium point SL_1, which is closer than the traditional Lagrangian point L_1. This will enable to alert of geo-magnetic storms at least 30 minutes earlier than the spacecraft placed in a halo orbit around L_1 [25].

In this chapter, we focus on the propellant–free station-keeping design of a solar sail spacecraft around the unstable Sun–Earth collinear equilibrium point L_2. In the libration zone, the solar sail maneuvers performed by means of changing the values of the sail parameters, can be understood as "jumps" in position instead of in velocity inside the phase space. This chapter uses this fact to systematically analyze the impact of a maneu-

ver (an instantaneous sail reorientation) on a spacecraft moving along a libration point Lissajous orbit. The station–keeping strategy periodically performs maneuvers to prevent the spacecraft to escape from a certain Lissajous orbit following its unstable manifold. Random errors in the execution of the maneuvers are also considered.

6.1 The station–keeping strategy

Previous works, like the ones of McInnes [39], Lawrence [150], Bookless [136], Biggs [44], Soldini [135] and Bianchi [163] have mainly focused on using feedback and optimal controllers that change the attitude angles and the reflectivity coefficient. Based on dynamical systems theory, only the work of Farrés [128, 129] studied the maintenance about an artificial equilibrium point.

When compared to the continuous control techniques, the impulsive ones are more mature and straightforward. Therefore, so far, all the LPOs missions adopted impulsive schemes to achieve station–keeping. Moreover the insight provided by the dynamical systems theory has been proved very useful to understand the geometry of the controllers [146]. In this section, we propose a multiple impulse strategy to achieve the spacecraft's station–keeping. The main idea is to periodically perform a maneuver to prevent the spacecraft to escape from the neighborhood of a certain Lissajous orbit along its unstable manifold. The maneuver is computed in order to cancel the unstable component of the state, moreover it is assumed that there is a random error in its execution.

We are going to assume that maneuvers that change the spacecraft cone angle α are always executed with an error α_{err} normally distributed with 3σ equal to 0.5°, and the solar sail spacecraft actively performs impulse maneuver controls to change α every Δt adimensional time units (about 30 days if $\Delta t = 0.5$). The basic loop of the procedure is done according to the following scheme:

1. Initialize the sail parameters μ, α_i, δ, β, the Lissajous orbit phases and amplitudes $\phi_1 = \phi_2 = 0$, A_x, A_z, the time step $\Delta t = 0.5$, and the maximum simulation time t_{max}. Set $t_f = 0$.
2. Using the Lissajous orbit and sail parameters, compute the coordinates of the equilibrium point $(\gamma_1, \gamma_2, \gamma_3)$, the components of the matrix $H(t_f)$ and, using equation (3.12), the departing state $(x, y, z, \dot{x}, \dot{y}, \dot{z})$.
3. Using equation (3.10), propagate the departing state up to $t_f = t_f + \Delta t$.
4. At this point, compute the curve of unstable amplitudes $A_u(\alpha)$ varying $\alpha \in [-\pi/2, \pi/2]$ with step $\Delta\alpha = \pi/32$. It must be noted that, as α varies, the coordinates of the equilibrium point $(\gamma_1', \gamma_2', \gamma_3')$ also change, as well as the matrix $H(t)$. Since system (3.3) is autonomous, for the computation of H time can always be set equal to zero and use $H(0)$.

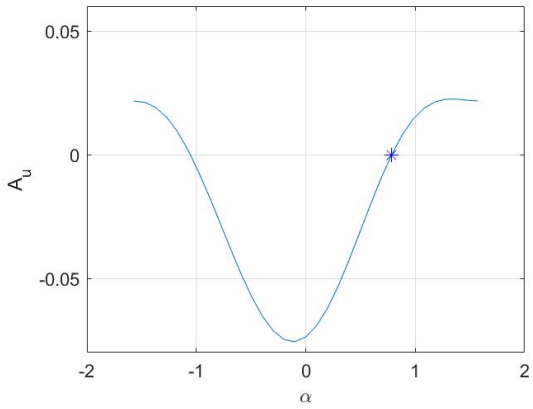

5. According to the behavior of $A_u(\alpha)$, determine the maneuver cone angle α_m such that $A_u(\alpha_m) = 0$, and is closer to the current α_i value (the blue star point in the above figure) so the new artificial libration point will be also closer to the original one. In this case $A_u(\alpha)$ crosses the $A_u = 0$ line twice, which means that there are two possible values of α such that $A_u = 0$.

6. The performed maneuver, which gives the new value of the cone angle, is $\alpha_i = \alpha_m + \alpha_{err}$, where the maneuver error α_{err} is normally distributed with 3σ equal to $0.5°$.

7. With this new value of α the procedure is repeated from step 2, until the the maximum time t_{max} is reached.

As an example, the results of the first six iterations of the above procedure are shown in Fig. 6.1.

In the Fig. 6.1, the initial parameters are $\alpha_i = \pi/12$, $\delta_i = \pi/2$, $\beta_i = 0.02$, $A_u = A_s = 0$, $A_x = 1/24$, $A_z = 1/6$, and $\Delta t = 0.5$. In this figure, for each $\Delta t = 0.5$ propagation, the left-hand side plot displays the orbit, and the right-hand side one the behavior of the final unstable amplitude A_u as a function of the cone angle α at different epochs. Fig. 6.1 (a) displays the results for $t \in (0, 1)$. During the first part of the time-interval $t \in (0, 0.5)$, the spacecraft departs from the blue asterisk point and moves along the blue curve. The blue plus sign point shows the current libration point. At $t = 0.5$, we do a maneuver affected by an error and the cone angle α_i is changed into $\alpha_i + \alpha_{err}$ (the maneuver point is marked by the black asterisk). During next $\Delta t = 0.5$ time units, the sail moves along the black curve, and the new libration point is the black plus sign point. Due to the error α_{err}, the new $A_u \neq 0$, and the spacecraft will escape as time increases. So, at $t = 1$, we apply the new maneuver to cancel again the unstable amplitude A_u.

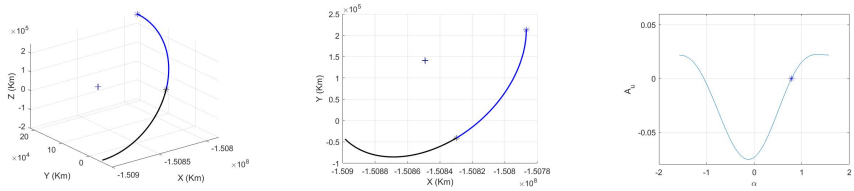

(a) First maneuver at t=0.5. $0 \leq t \leq 1$

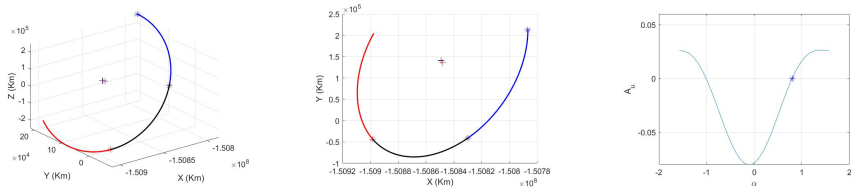

(b) Second maneuver at t=1.0. $0 \leq t \leq 1.5$

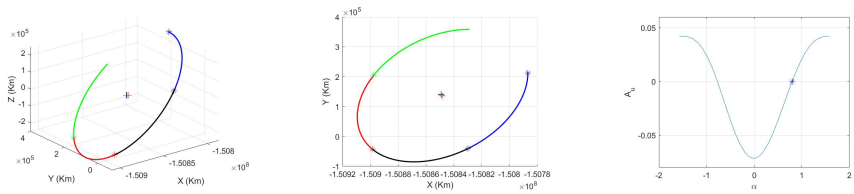

(c) Third maneuver at t=1.5. $0 \leq t \leq 2$

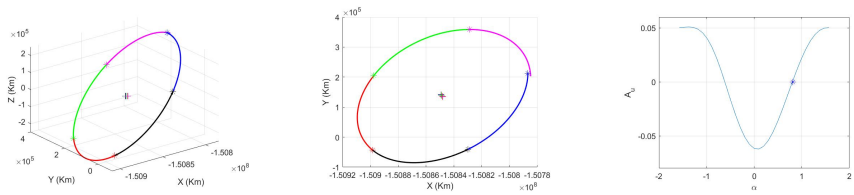

(d) Fourth maneuver at t=2.0. $0 \leq t \leq 2.5$

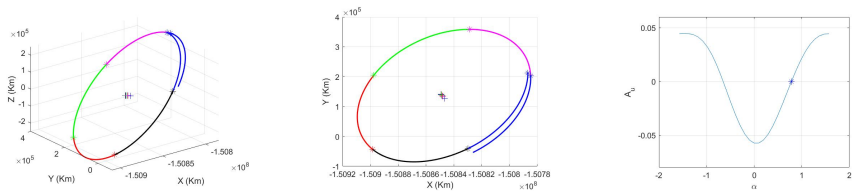

(e) Fifth maneuver at t=2.5. $0 \leq t \leq 3.0$

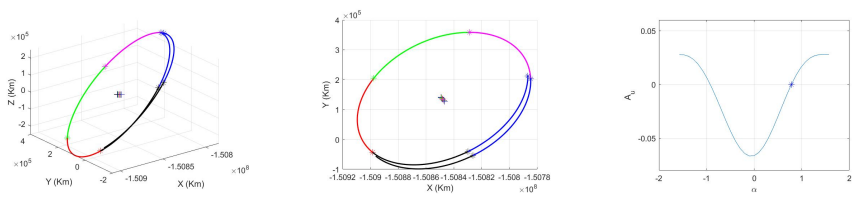

(f) Sixth maneuver at t=3. $0 \leq t \leq 3.5$

Figure 6.1: Evolution of the controlled orbit after six station–keeping impulsive solar-sail maneuvers.

The right-hand side column of the figure shows the behavior of A_u as a function of α at $t = 0.5$. As it can be clearly seen, the function crosses the $A_u = 0$ line twice, which means that there are two possible values of α such that $A_u = 0$. The value of α selected is the one that requires the smaller change of α_i; in this way, the new artificial libration point will be also closer to the original one.

The remaining lines in Fig. 6.1 show the subsequent five maneuvers determined according to the above iterative procedure. The color sequence used for the propagated orbit is: blue–black–red–green–pink–blue–black... It can be seen that after six impulsive maneuvers, the spacecraft still remains close to the Lissajous orbit around the artificial libration point SL_2 without escaping.

6.2 Numerical results

According to the results shown in Fig. 6.1, the solar sail has achieved a half year station–keeping by means of six station-keeping maneuvers. Using the orbit and the same strategy, Fig. 6.2 shows the controlled orbit for a five-year time interval.

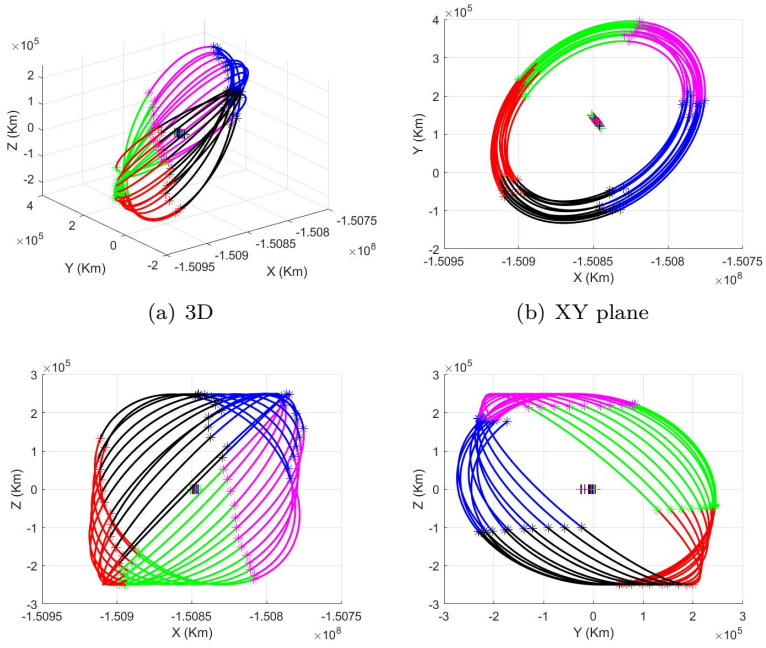

(a) 3D (b) XY plane

(c) XZ plane (d) YZ plane

Figure 6.2: 3D representation and coordinate projections of the controlled orbit during five years.

From this figure it follows that, despite the existence of the errors α_{err} in the execution of the control maneuvers, the described station-keeping control performs well using a time interval $\Delta t = 0.5$, and the solar sail spacecraft follows the Lissajous orbit near the artificial libration point SL_2.

Fig. 6.3 shows the behavior of the unstable amplitudes A_u, as a function of α, at maneuver epochs $t = 2k\Delta t$, with $k = 1, 2, ..., 6$. Since at each epoch, the associated curve $A_u(\alpha)$ always crosses twice the line $A_u = 0$, the blue asterisks (close to $\pi/4$) show the positive selected values of α that define the control maneuver, according to step 8 of the previously described iterative procedure.

Similarly, the station–keeping under different α_i are shown in Fig. 6.5. In this figure, the spacecraft also achieves long-term orbit station–keeping, which verifies the effectiveness of the method.

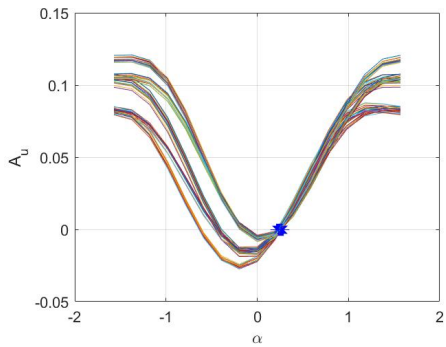

Figure 6.3: Behavior of the curves $A_u(\alpha)$ at different maneuver epochs. Note that each curve crosses twice the line $A_u = 0$. The blue asterisks indicate the selected values of α used to determine the control maneuver.

For this simulation, the evolution of α_f, A_u, A_x, A_z as a function of time along the five years is shown in Fig. 6.4.

As it follows from this figure, because when computing the maneuver an error is introduced in the computed cone angle α, the resulting unstable amplitude A_u is not zero, although it is always very small.

Since all the maneuvers are performed in such a way that the resulting cone angle is as close as possible to the initial one, the new artificial libration points are also close to the initial one $(\gamma_1, \gamma_2, \gamma_3)$. Furthermore, the size of the Lissajous orbit defined by the

amplitudes A_x and A_z remains almost constant.

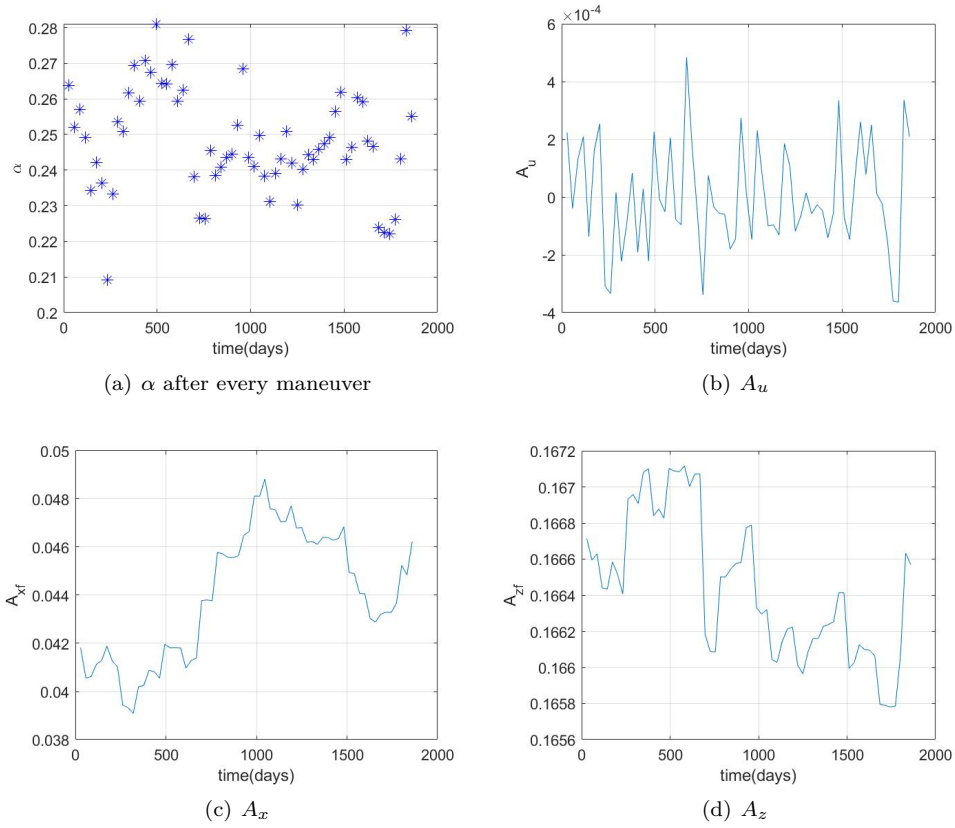

(a) α after every maneuver

(b) A_u

(c) A_x

(d) A_z

Figure 6.4: Behaviour of α, A_u, A_x, A_z as a function of time for the five-year controlled orbit displayed in Fig. 6.2.

6.2.1 Changing the cone angle α and the maneuver error α_{err}

Similar good station–keeping results are obtained for the same Lissajous orbit, but with different initial cone angles.

For different initial cone angle α_i, the results obtained for the controlled orbit and the α after each maneuver are displayed in Fig. 6.5; note that the values of α after the maneuvers remain close to their initial values.

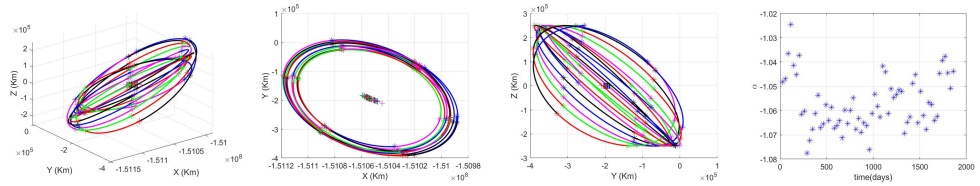

(a) $\alpha_i = -\pi/3$

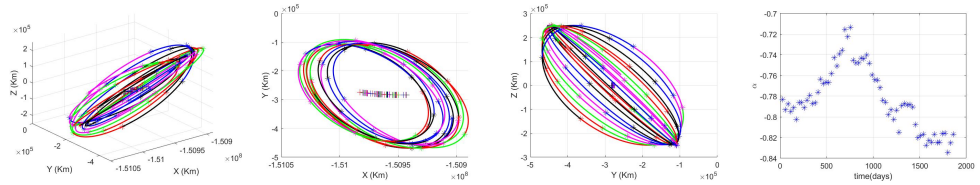

(b) $\alpha_i = -\pi/4$

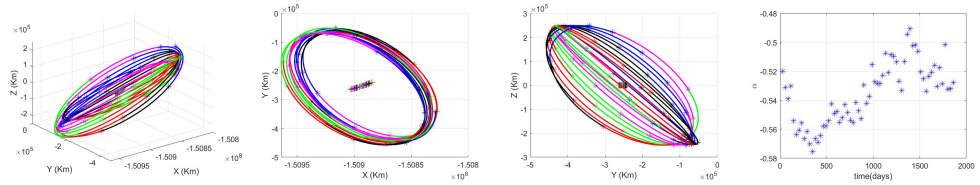

(c) $\alpha_i = -\pi/6$

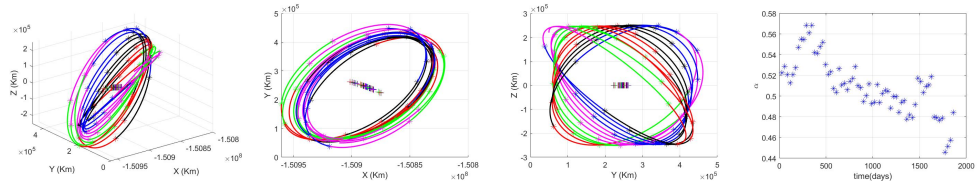

(d) $\alpha_i = \pi/6$

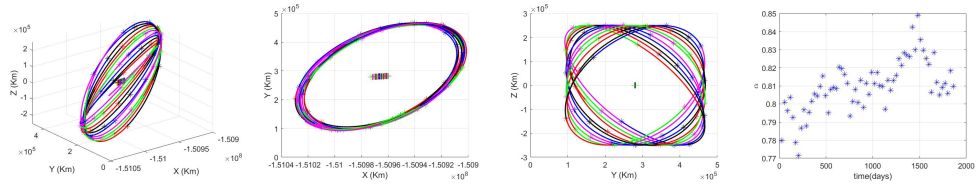

(e) $\alpha_i = \pi/4$

Figure 6.5: Behavior of the orbits for five-year station–keeping control for the same Lissajous orbit of figure 6.2, but with two different values of the cone angle α_i.

The results obtained using values of the error parameter α_{error} inside other ranges are shown in Fig. 6.6. We notice that when the size of the error range in α_{err} increases, the dispersion of the artificial libration point also does, as well as the size of the amplitudes A_x and A_z of the controlled Lissajous orbit. Even the procedure exhibits a robust behavior,

for larger errors than the ones mentioned, the controllability can be compromised.

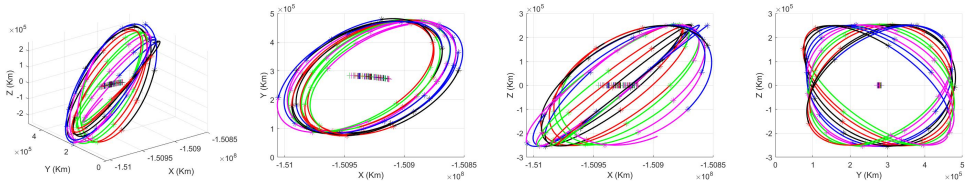

(a) 3σ α_{err} of 1 °

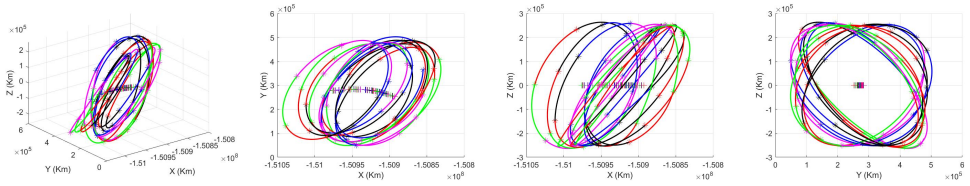

(b) 3σ α_{err} of 2 °

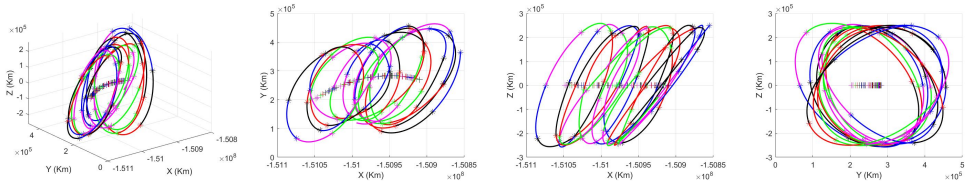

(c) 3σ α_{err} of 3 °

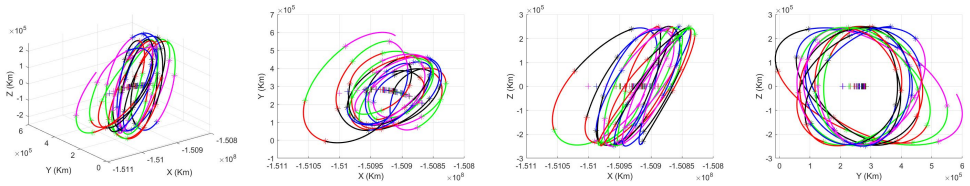

(d) 3σ α_{err} of 4 °

Figure 6.6: Behavior of the orbits for five-year station–keeping control for the same Lissajous orbit in figure 6.2, but with values of α_{err} in different ranges.

6.2.2 Changing the lightness number β and the clock angle δ

When the reflectivity of the sail is changed, the artificial libration point also changes accordingly. The station keeping also performs well when the lightness number is large (for instance $\beta = 0.04$), but in this case the sensitivity is higher. This is observed in Figs. 6.7 (b) and 6.7 (c) where we can see that big values of β increase the excursions of

the artificial libration points making the controlled orbit to oscillate in a wider range.

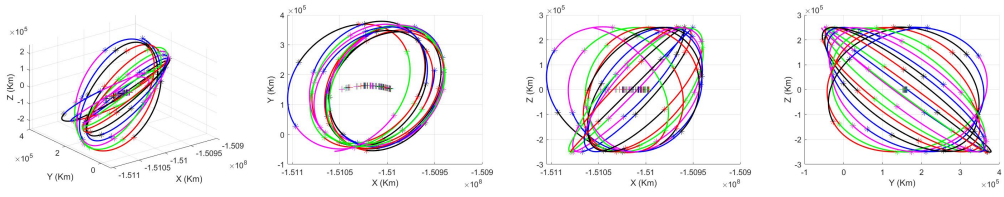

(a) $\beta = 0.01$

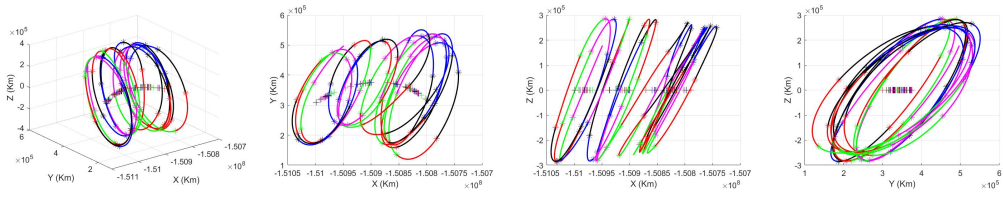

(b) $\beta = 0.03$

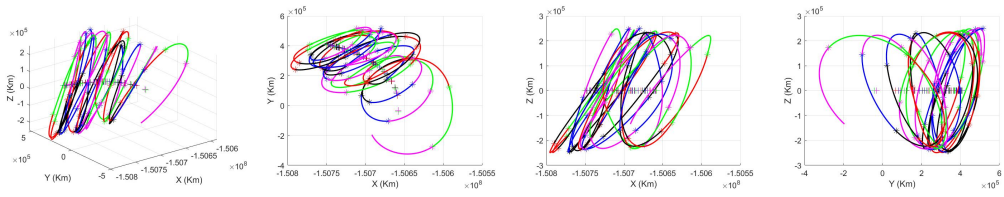

(c) $\beta = 0.04$

Figure 6.7: Five-year evolution of the controlled orbits for different values of the lightness number $\beta = 0.01, 0.03, 0.04$. In this simulations $\alpha = \pi/6$, $\delta{=}\pi/2$ and 3σ α_{err} of 2°.

As it follows from Fig. 6.8 for different values of the clock angle δ one can also achieve controllability. The five-year simulation of the three plots represented in the figure have been done using a relatively small constant value of the reflectivity $\beta_{i,f} = 0.02$ and an initial value of the cone angle $\alpha_i = \pi/12$.

Fig. 6.9 shows the results obtained, with three different values of $\Delta t = 0.75$, 1, and 1.25 for five-year control simulations. The values of the remaining parameters for these three simulations are: $\beta_{i,f} = 0.02$, $\alpha_i = -\pi/4$, $\delta_{i,f} = \pi/2$, and 3σ α_{err} of 0.5°. We note that in all cases the controllability is achieved.

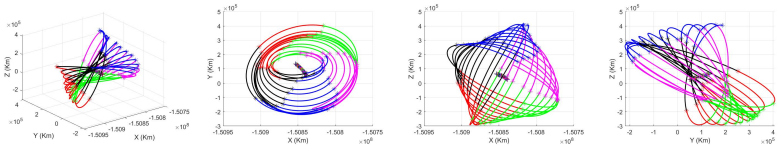

(a) $\delta_{i,f} = \pi/3$

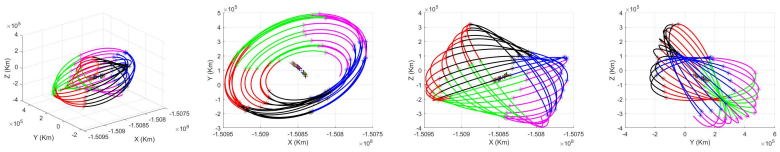

(b) $\delta_{i,f} = 2\pi/3$

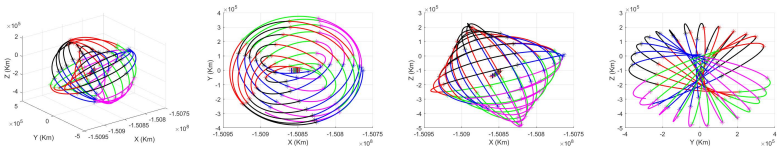

(c) $\delta_{i,f} = \pi$

Figure 6.8: Five-year station-keeping simulation for $\delta_{i,f} = \pi/3, 2\pi/3, \pi$, and $\alpha_i = \pi/12$, $\beta = 0.02$.

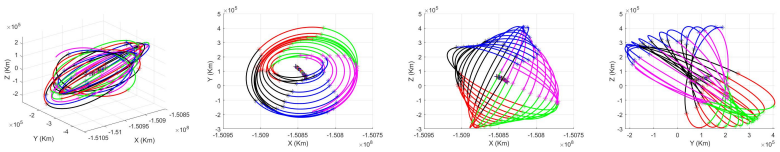

(a) $\Delta t = 0.75$

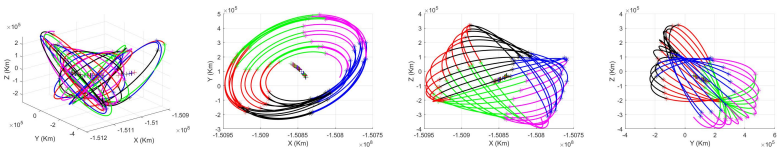

(b) $\Delta t = 1$

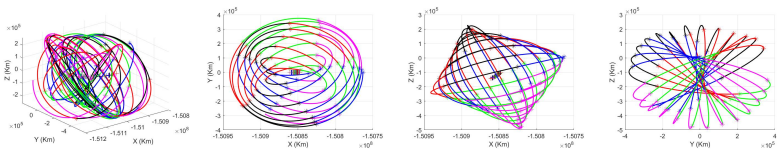

(c) $\Delta t = 1.25$

Figure 6.9: Five-year station-keeping simulation for $\Delta t = 0.75, 1, 1.25$, and $\alpha_i = -\pi/4$, $\delta = \pi/2$, $\beta = 0.02$.

According to the results obtained, some of them displayed in the last figures (from Fig. 6.5 to Fig. 6.9), it follows that, using the cone angle α as control parameter, the station–keeping is achieved, for different initial sail attitude parameters $(\alpha_i, \delta_i, \beta_i)$ and under maneuvering errors α_{err}.

It is worth to note that, when α_{err} and Δt increase, the spacecraft still moves around the libration point SL_2, although the excursions about this point are larger.

6.2.3 Introducing an error δ_{err} in the clock angle of the maneuvers

The results of the preceding section show that performing multiple impulsive maneuvers using the cone angle α, affected by an error α_{err}, the station–keeping is achieved for long time intervals. The same results hold when the cancellation of the unstable amplitude of the target Lissajous orbit is performed using the clock angle δ.

The selection of the value of δ that cancels the unstable amplitude is done according to the number of intersections of the $A_u(\delta)$ curve at each epoch (see Fig. 6.11 (d)).

1. If the $A_u(\delta)$ curve crosses twice the $A_u = 0$ line, the value selected is the one that produces the smallest variation of the angle δ;

2. if there is only one crossing, of course, the value of δ at the intersection is the one selected;

3. if there is no crossing, then the chosen value of δ is the one associated to the minimum value of A_u, which is the best option to reduce the unstable amplitude at the next maneuver.

As an example of the results obtained, Fig. 6.10 shows a five-year simulation for a solar sail with the following parameters: $\alpha_i = \pi/12$, $\delta_i = \pi/2$, $\beta_i = 0.02$, and 3σ δ_{err} of $0.5°$. Associated with this simulation, the behavior of the amplitudes of the controlled Lissajous orbit, as well as the value of the clock angle after each maneuver are displayed in Fig. 6.11.

According to this figure, both the A_{xf} and the A_{zf} amplitudes remain close to the initial amplitude of the Lissajous orbit. Figs. 6.11 (c) and (d) show the behavior of the unstable component, as a function of time (note that due to the existence of δ_{err}, the unstable amplitude is not exactly zero). In the subplot (d) the blue asterisk mark corresponds to the required impulsive maneuver in the clock angle δ that sets $A_u = 0$.

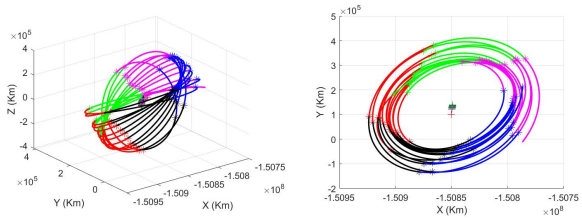

(a) 3D (b) XY plane

(c) XZ plane (d) YZ plane

Figure 6.10: Five-year station–keeping keeping simulation using clock angle δ maneuvers affected by a 3σ error δ_{err} of 0.5°.

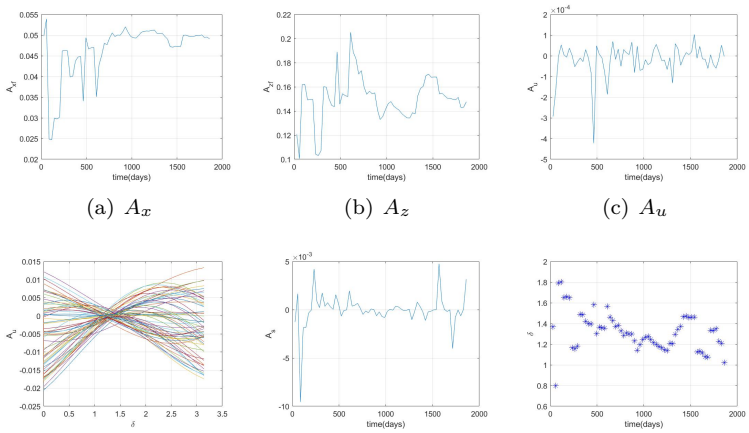

(a) A_x (b) A_z (c) A_u

(d) A_u with δ_f (e) A_s (f) Value of δ after each maneuver

Figure 6.11: Associated with Fig. 6.10, Lissajous amplitudes after each δ maneuver.

Fig. 6.12 and Fig. 6.13 show the station–keeping of the solar sail spacecraft under the multi-impulse maneuver with different initial cone α_i, and clock δ_i angles. The other initial sail parameters are $\beta_i = 0.02$, $A_u = A_s = 0$, $A_x = 1/24$, $A_z = 1/6$, and $\Delta t = 0.5$. The first six plots in Fig. 6.12, have the same initial $\alpha_i = \pi/12$ and different values of δ_i. These results show that for $\alpha_i = \pi/12$ and any $\delta_i \in (0, \pi)$ station–keeping is achieved, and the controlled orbit is of Lissajous type. The last four plots of the same figure have the same initial $\delta_i = \pi/2$ and different α_i, although the shape of the orbit changes, the

spacecraft still moves around the artificial libration point SL_2.

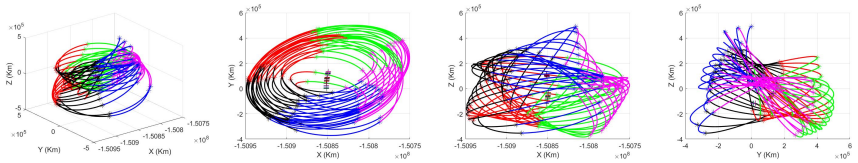

(a) $\alpha_i = \pi/12$, $\delta_i = 0$

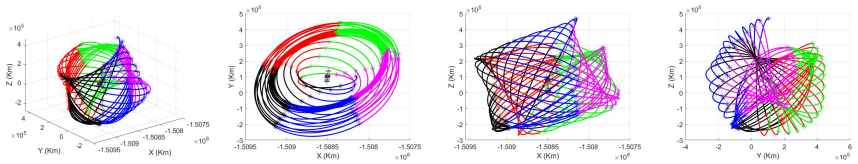

(b) $\alpha_i = \pi/12$, $\delta_i = \pi/6$

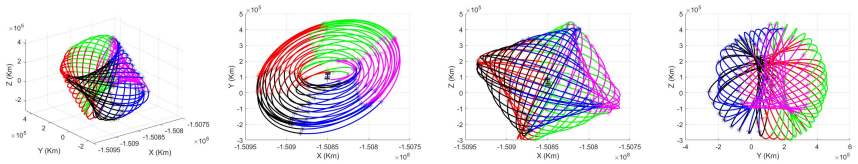

(c) $\alpha_i = \pi/12$, $\delta_i = \pi/3$

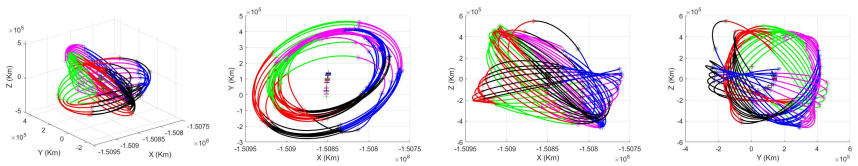

(d) $\alpha_i = \pi/12$, $\delta_i = 2\pi/3$

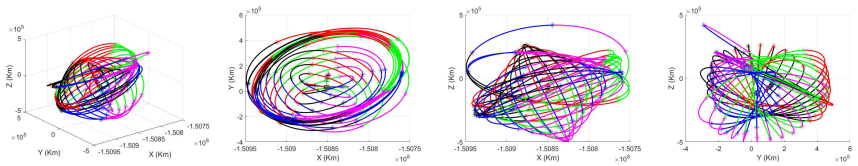

(e) $\alpha_i = \pi/12$, $\delta_i = 3\pi/4$

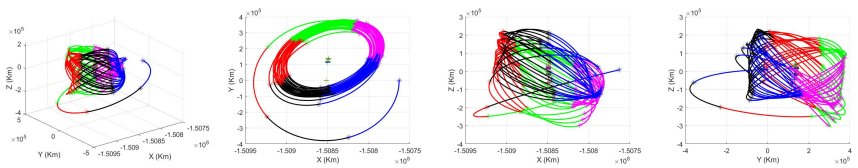

(f) $\alpha_i = \pi/12$, $\delta_i = \pi$

Figure 6.12: Five-year station–keeping simulations with different values of δ_i and fixed value of $\alpha_i = \pi/12$, and $\beta_i = 0.02$, $A_u = A_s = 0$, $A_x = 1/24$, $A_z = 1/6$, $\Delta t = 0.5$.

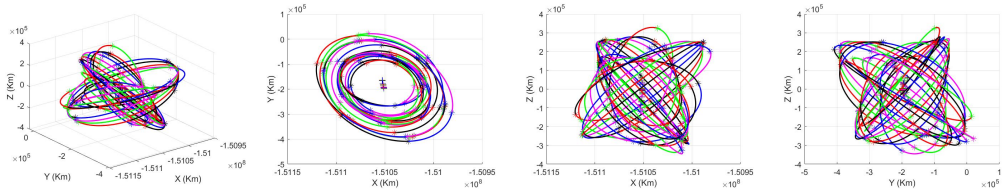

(a) $\alpha_i = -\pi/3$, $\delta_i = \pi/2$

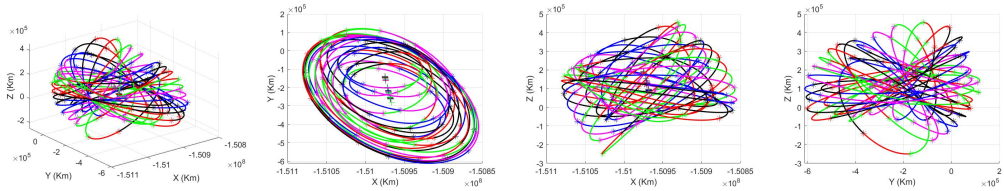

(b) $\alpha_i = -\pi/4$, $\delta_i = \pi/2$

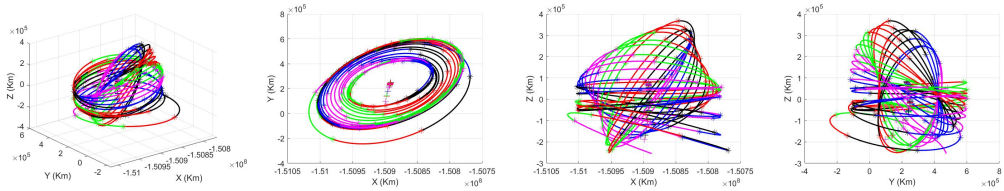

(c) $\alpha_i = \pi/6$, $\delta_i = \pi/2$

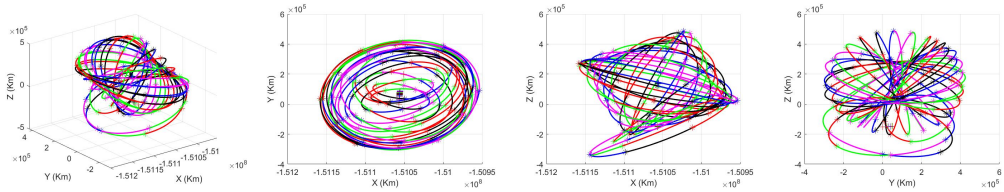

(d) $\alpha_i = \pi/3$, $\delta_i = \pi/2$

Figure 6.13: Five-year station–keeping simulations with different values of α_i and fixed value of $\delta_i = \pi/2$, and $\beta_i = 0.02$, $A_u = A_s = 0$, $A_x = 1/24$, $A_z = 1/6$, $\Delta t = 0.5$.

Fig. 6.14 shows five-year station–keeping simulations with different values of β_i. When the solar sail angles are fixed to $\alpha_i = -\pi/4, \delta_i = \pi/3$, then for larger values of β_i, the changes in the shape of the controlled Lissajous orbit are also larger.

Finally, Figs. 6.15 and 6.16 show five-year station–keeping simulations with different values of δ_{err} or Δt. From both figures, it is worth noting that when again, δ_{err} and Δt are large the spacecraft is still evolving around the artificial libration point SL_2, although the excursions are larger.

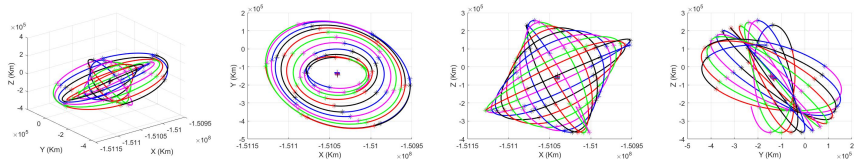

(a) $\alpha_i = -\pi/4$, $\delta_i = \pi/3$, $\beta_i = 0.01$

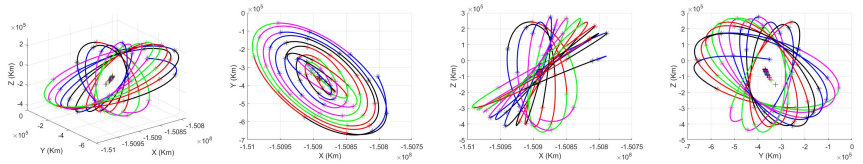

(b) $\alpha_i = -\pi/4$, $\delta_i = \pi/3$, $\beta_i = 0.03$

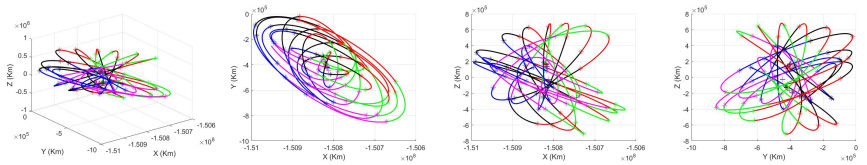

(c) $\alpha_i = -\pi/4$, $\delta_i = \pi/3$, $\beta_i = 0.04$

Figure 6.14: Five-year station–keeping simulations with different values of β_i

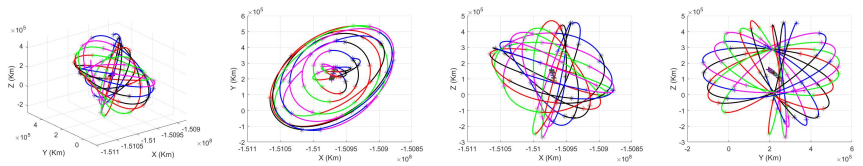

(a) 3σ δ_{err} of 1 °

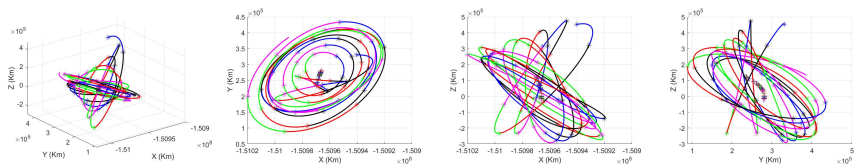

(b) 3σ δ_{err} of 1.5 °

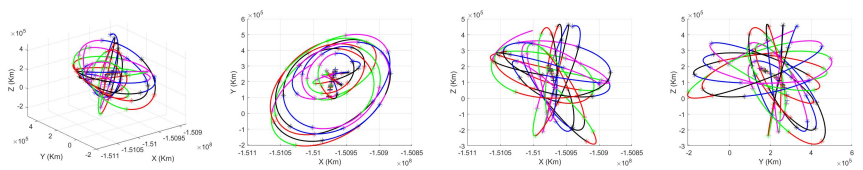

(c) 3σ δ_{err} of 2 °

Figure 6.15: Five-year station–keeping simulations with different values of δ_{err}. The sail parametres are $\alpha_i = \pi/4$, $\delta_i = \pi/3$, $\beta_i = 0.02$

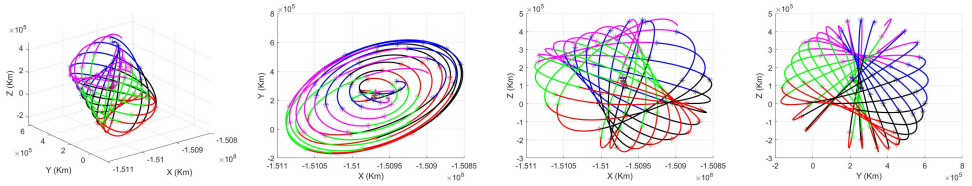

(a) $\Delta t = 0.60$

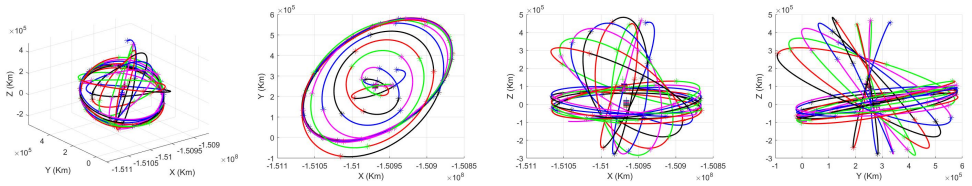

(b) $\Delta t = 0.75$

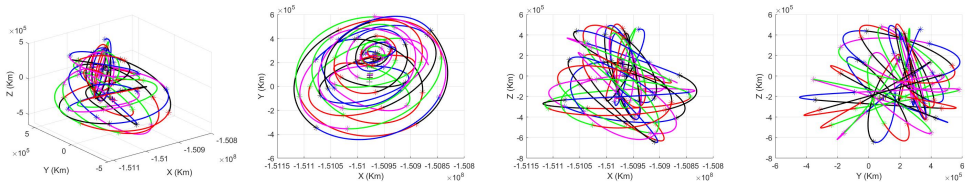

(c) $\Delta t = 0.85$

Figure 6.16: Five-year station–keeping simulations with different values of Δt. The sail parametres are $\alpha_i = \pi/4$, $\delta_i = \pi/3$, $\beta_i = 0.02$

6.3 Chapter summary

This chapter investigates a propellant-free station–keeping design for a solar sail moving around the Sun–Earth collinear equilibrium points. The dynamical model used corresponds to the linearized equations of motion around the equilibrium points of the circular restricted three body problem, including the solar radiation pressure.

The invariant manifolds of the orbits are used in the station-keeping design for Lissajous orbits in the Sun-Earth system. The sequence of maneuvers are performed changing the orientation parameters of the sail (cone and clock angles) that determine its attitude with respect to the Sun.

Considering that there could be errors in the attitude angles of the sail, all the numerical simulations have been carried out introducing random errors in the attitude angles when performing the maneuvers that cancel the unstable amplitude component of the controlled Lissajous orbit.

One of the goals of the study has been to analyze the role of the cone angle errors in the station–keeping design. For 3σ errors of 0.5 deg, and performing station-keeping maneuvers every month, the spacecraft can remain near the artificial libration points easily, even under different initial values of the cone angle as shown in Figs. 6.2 and 6.5. In this situation, the trajectory is close to the initial Lissajous orbit. When the cone angle error becomes larger, the proposed method also keeps the spacecraft near an artificial libration point, but it undergoes a large deviation with respect to the initial one. The effects of the other two sail parameters, the clock angle and the reflectivity parameter, are also studied. The change of the cone angle has little effect on the station–keeping, while the change of the reflectivity parameter has a stronger influence on the results: for reflectivities 0.01, 0.02, the station–keeping is clearly achieved, but when it is 0.03, 0.04, large deviations of the artificial libration point appear.

Another goal has been to analyze the role of the clock angle error in the station–keeping design. In this case the spacecraft can also remain near the artificial libration orbit, consideting different initial cone and clock angles, as shown in Fig. 6.12.

As final summary, the multiple impulse design of the station–keeping control by means of sail reorientation controlling the unstable manifold component is shown to be effective.

7

Chapter 7
Conclusions and future work

7.1 Conclusions

With the successful implementation of many in-orbit verification missions of solar sail spacecraft, solar sail propulsion will play an increasingly important role in future space missions. considering the SRP-RTBP model we first studied the influence of the solar sail parameters on the distribution of artificial libration points inside their families. We then proposed an impulsive maneuver technique that accomplished enhanced heteroclinic transfers between SL_2 Lissajous orbits. We also used the proposed method to avoid the forbidden zone, for station-keeping, and for general transfers. The main work and research results of this thesis are the following:

1. Based on the SRP-RTBP model, the families of artificial libration points were researched for solar sail spacecraft. First, we described the Sun–Earth RTBP and basic theory for solar sail spacecraft. Then, we established the SRP–RTBP model. Finally, we studied the influence of solar sail parameters (cone angle α, clock angle δ, and lightness number β) on the distribution of artificial libration points in families, especially SL_1 and SL_2. In addition to the traditional five independent libration points, there exist families of 3D artificial libration points, which arise in different situations with different solar sail parameters.

2. We proposed an impulse maneuver method and studied enhanced heteroclinic transfers between SL_2 Lissajous orbits. For this purpose, the SRP-RTBP model was linearized and solved. Furthermore, an analysis showed that the errors of the linear

model are very small for Sun-Earth libration points. Then, we considered changes to the families of artificial libration points. Three coordinate systems are widely used in the thesis. An impulse maneuver method for solar sail spacecraft was proposed based on adjusting the solar sail parameters. An algorithm for the method was described. Note that traditional spacecraft use impulse engines to apply sudden velocity increments, although their position changes continuously. Finally, using the proposed impulse maneuver method, we studied how to accomplish enhanced heteroclinic transfers between Lissajous orbits near an artificial libration point. The influence of each solar sail parameter on the impulse maneuver, time and the terminal Lissajous orbital amplitudes was analyzed in detail. We determined that, for different values of the terminal parameters, there are four different transfer strategies, as shown in Figs. 3.8, 3.21, and so on.

3. We conducted an extensive study of heteroclinic transfers using sail impulsive maneuvers for Lissajous orbits. We concluded that, when the initial and final clock angles $\delta_{i,f} = \pi/2$ and the difference in the initial phase angles ϕ_2 of two spacecraft is π, the solar sail spacecraft can transfer to the same terminal Lissajous orbit through an impulse maneuver. This was verified by a large number of numerical simulations. Then we saw that the solar sail parameters can be gradually changed by using multi-impulse maneuvers. Thus, transfers from an initial Lissajous orbit to a terminal orbit can be accomplished via multiple transitional Lissajous orbits. Finally, in case the spacecraft needs to return to its initial Lissajous orbit, we showed the way impulsive maneuvers can realize back-and-forth transfers between two artificial libration point orbits.

4. We researched how the spacecraft can avoid the forbidden zone using sail impulsive maneuvers. The 3D forbidden zone and the enhanced heteroclinic transfer orbits were projected onto a 2D EPP. With this technique it is easy to estimate the time when the spacecraft is going to reach the forbidden zone for different phase angles. First, we devised a strategy for avoiding the forbidden zone based on changing the cone angle. By changing both the cone angle and the initial phase angle, the satellite won't be influenced by the forbidden zone any more after impulsive maneuver. Thus, the forbidden zone can be avoided. Second, we changed the clock angle to avoid the forbidden zone. We solved the problem that the terminal Lissajous orbital amplitude is too narrow. Finally, we also considered the lightness number to avoid the forbidden zone. When cone angle $\alpha = 0$, regardless of the lightness number, the forbidden zone in the EPP cannot be eliminated by an impulse maneuver. However, under the joint action of cone angle and clock angle, the forbidden zone can be avoided. Thus, these different approaches can be of support to diverse missions.

5. We researched station-keeping by a solar sail spacecraft in a Lissajous orbit. By applying the designed station-keeping procedure, periodic maneuvers were identified for a spacecraft that prevent it from escaping from a Lissajous orbit following its unstable manifold. The maneuver was computed so that it cancels out the unstable component of the state. Moreover, it is assumed that there is a random error in the execution of a maneuver. By performing maneuvers every month, the spacecraft can remain near an artificial libration point for at least 5 years, which shows that this strategy is effective for station-keeping.

7.2 Future work

This thesis systematically studied the use of impulse maneuvers and the applications of heteroclinic enhanced orbits for transfers, forbidden zone avoidance, and station-keeping. Thus, there are three areas for follow-up research:

1. Apply the impulse maneuver strategy for solar sail spacecraft to more mission scenarios. The strategy proposed in this thesis can realize enhanced heteroclinic transfers between orbits about the same artificial libration point. It could be applied to more mission scenarios in future research, such as for solar sail spacecraft flying in formation near an artificial libration point and for deep-space exploration missions that rely on multi-impulse maneuvers.

2. Study orbit transfers between families of artificial libration points. In this thesis, our research on the impulse maneuver method was for the same artificial libration point. Future research could consider heteroclinic transfers between different artificial libration points. For example, a spacecraft could use the SL_2 unstable manifold to escape an orbit. After performing multi-impulse maneuvers, it may be able to enter the SL_1 stable manifold.

3. Determine minimal impulse maneuvers. The impulse maneuver method proposed in this thesis realizes heteroclinic transfers, forbidden zone avoidance, and orbit station-keeping. In future research, the optimal control strategy could be combined with minimal impulse maneuvers to complete the task. This would not only avoid large changes to the solar sail parameters but could also extend the life of the spacecraft.

Appendix

Appendix 1: U_{ij}

$$
\begin{aligned}
U_{XX} &= 1 - \frac{1-\mu}{{r_1}^3} - \frac{\mu}{{r_2}^3} + \frac{3(1-\mu)(X+\mu)^2}{{r_1}^5} + \frac{3\mu(X-1+\mu)^2}{{r_2}^5} \\
U_{YY} &= 1 - \frac{1-\mu}{{r_1}^3} - \frac{\mu}{{r_2}^3} + \frac{3(1-\mu)Y^2}{{r_1}^5} + \frac{3\mu Y^2}{{r_2}^5} \\
U_{ZZ} &= -\frac{1-\mu}{{r_1}^3} - \frac{\mu}{{r_2}^3} + \frac{3(1-\mu)Z^2}{{r_1}^5} + \frac{3\mu Z^2}{{r_2}^5} \\
U_{XY} &= \frac{3(1-\mu)(X+\mu)Y}{{r_1}^5} + \frac{3\mu(X-1+\mu)Y}{{r_2}^5} \\
U_{XZ} &= \frac{3(1-\mu)(X+\mu)Z}{{r_1}^5} + \frac{3\mu(X-1+\mu)Z}{{r_2}^5} \\
U_{YZ} &= \frac{3(1-\mu)YZ}{{r_1}^5} + \frac{3\mu YZ}{{r_2}^5} \\
U_{XY} &= U_{YX} \\
U_{XZ} &= U_{ZX} \\
U_{ZY} &= U_{YZ}
\end{aligned}
$$

Appendix 2: a_i, b_i, c_i

Values of the coefficients a_i , b_i, and c_i, for $i = 0, ..., 3$, that appear in the linearized equations of motion (3.3). It must be noted that the values of a_0, b_0 and c_0 are zero at the equilibrium points, so they do not appear in the differential equations.

$$
\begin{aligned}
a_0 &= -A_1 \mp \frac{\mu}{\gamma} + \frac{1-\mu}{\gamma^3}\frac{A_1}{D_1^3} + \frac{\mu}{\gamma^3}\frac{A_2}{D_2^3} - \frac{\beta(1-\mu)\cos^2\alpha}{\gamma^3 D_1^3 D_3}(A_1 D_3 \cos\alpha + C_1 A_1 \sin\alpha\cos\delta \\
&\quad + B_1 D_1 \sin\alpha \sin\delta), \\
a_1 &= 1 + \frac{1-\mu}{\gamma^3}\frac{3A_1^2 - D_1^2}{D_1^5} + \frac{\mu}{\gamma^3}\frac{3A_2^2 - D_2^2}{D_2^5} - \frac{\beta(1-\mu)\cos^2\alpha}{\gamma^3 D_1^3 D_3}\left(\frac{(3A_1^2 - D_1^2)D_3}{D_1^2}\cos\alpha\right. \\
&\quad \left. + C_1(E_3 A_1^2 - 1)\sin\alpha\cos\delta + B_1 E_2 A_1 D_1 \sin\alpha\sin\delta\right), \\
a_2 &= \frac{1-\mu}{\gamma^3}\frac{3A_1 B_1}{D_1^5} + \frac{\mu}{\gamma^3}\frac{3A_2 B_2}{D_2^5} - \frac{\beta(1-\mu)\cos^2\alpha}{\gamma^3 D_1^3 D_3} \\
&\quad \left(\frac{3A_1 B_1 D_3}{D_1^2}\cos\alpha + E_3 B_1 A_1 C_1 \sin\alpha\cos\delta + (E_2 B_1^2 - 1)D_1 \sin\alpha\sin\delta\right), \\
a_3 &= \frac{1-\mu}{\gamma^3}\frac{3A_1 C_1}{D_1^5} + \frac{\mu}{\gamma^3}\frac{3A_2 C_2}{D_2^5} - \frac{\beta(1-\mu)\cos^2\alpha}{\gamma^3 D_1^3 D_3} \\
&\quad \left(\frac{3A_1 C_1 D_3}{D_1^2}\cos\alpha + A_1\left(\frac{3C_1^2}{D_1^2} - 1\right)\sin\alpha\cos\delta + \frac{2B_1 C_1}{D_1}\sin\alpha\sin\delta\right), \\
b_0 &= -B_1 + \frac{1-\mu}{\gamma^3}\frac{B_1}{D_1^3} + \frac{\mu}{\gamma^3}\frac{B_2}{D_2^3} - \frac{\beta(1-\mu)\cos^2\alpha}{\gamma^3 D_1^3 D_3} \\
&\quad (B_1 D_3 \cos\alpha + C_1 B_1 \sin\alpha\cos\delta - A_1 D_1 \sin\alpha\sin\delta), \\
b_1 &= \frac{1-\mu}{\gamma^3}\frac{3A_1 B_1}{D_1^5} + \frac{\mu}{\gamma^3}\frac{3A_2 B_2}{D_2^5} - \frac{\beta(1-\mu)\cos^2\alpha}{\gamma^3 D_1^3 D_3} \\
&\quad \left(\frac{3A_1 B_1 D_3}{D_1^2}\cos\alpha + E_3 B_1 A_1 C_1 \sin\alpha\cos\delta - (E_2 A_1^2 - 1)D_1 \sin\alpha\sin\delta\right), \\
b_2 &= 1 + \frac{1-\mu}{\gamma^3}\frac{3B_1^2 - D_1^2}{D_1^5} + \frac{\mu}{\gamma^3}\frac{3B_2^2 - D_2^2}{D_2^5} - \frac{\beta(1-\mu)\cos^2\alpha}{\gamma^3 D_1^3 D_3} \\
&\quad \left(\frac{(3B_1^2 - D_1^2)D_3}{D_1^2}\cos\alpha + C_1(E_3 B_1^2 - 1)\sin\alpha\cos\delta - B_1 E_2 A_1 D_1 \sin\alpha\sin\delta\right), \\
b_3 &= \frac{1-\mu}{\gamma^3}\frac{3B_1 C_1}{D_1^5} + \frac{\mu}{\gamma^3}\frac{3B_2 C_2}{D_2^5} - \frac{\beta(1-\mu)\cos^2\alpha}{\gamma^3 D_1^3 D_3} \\
&\quad \left(\frac{3B_1 C_1 D_3}{D_1^2}\cos\alpha + B_1\left(\frac{3C_1^2}{D_1^2} - 1\right)\sin\alpha\cos\delta - \frac{2A_1 C_1}{D_1}\sin\alpha\sin\delta\right),
\end{aligned}
$$

$$
\begin{aligned}
c_0 &= \frac{1-\mu}{\gamma^3}\frac{C_1}{D_1^3} + \frac{\mu}{\gamma^3}\frac{C_2}{D_2^3} - \frac{\beta(1-\mu)\cos^2\alpha}{\gamma^3 D_1^3 D_3}(C_1 D_3 \cos\alpha - D_3^2 \sin\alpha\cos\delta),\\
c_1 &= \frac{1-\mu}{\gamma^3}\frac{3A_1C_1}{D_1^5} + \frac{\mu}{\gamma^3}\frac{3A_2C_2}{D_2^5} - \frac{\beta(1-\mu)\cos^2\alpha}{\gamma^3 D_1^3 D_3}\\
&\quad \left(\frac{3A_1C_1D_3}{D_1^2}\cos\alpha - (E_3D_3^2-2)A_1\sin\alpha\cos\delta\right),\\
c_2 &= \frac{1-\mu}{\gamma^3}\frac{3C_1B_1}{D_1^5} + \frac{\mu}{\gamma^3}\frac{3B_2C_2}{D_2^5} - \frac{\beta(1-\mu)\cos^2\alpha}{\gamma^3 D_1^3 D_3}\\
&\quad \left(\frac{3B_1C_1D_3}{D_1^2}\cos\alpha - (E_3D_3^2-2)B_1\sin\alpha\cos\delta\right),\\
c_3 &= \frac{1-\mu}{\gamma^3}\left(\frac{3C_1^2-D_1^2}{D_1^5}\right) + \frac{\mu}{\gamma^3}\left(\frac{3C_2^2-D_2^2}{D_2^5}\right) - \frac{\beta(1-\mu)\cos^2\alpha}{\gamma^3 D_1^3 D_3}\\
&\quad \left(\frac{(3C_1^2-D_1^2)D_3}{D_1^2}\cos\alpha - \frac{3C_1}{D_1^2}D_3^2\sin\alpha\cos\delta\right),
\end{aligned}
$$

where

$$
\begin{aligned}
A_1 &= A_3 = \frac{\gamma_1-\mu}{\gamma}, \qquad A_2 = \frac{\gamma_1-\mu+1}{\gamma},\\
B_1 &= B_2 = B_3 = \frac{\gamma_2}{\gamma},\\
C_1 &= C_2 = -\frac{\gamma_3}{\gamma}, \quad C_3 = 0,\\
D_i^2 &= A_i^2 + B_i^2 + C_i^2, \quad \text{for } i = 1,2,3\\
E_1 &= \frac{D_1^2+D_3^2}{D_1^2D_3^2}, \qquad E_2 = \frac{D_1^2+2D_3^2}{D_1^2D_3^2}, \qquad E_3 = \frac{D_1^2+3D_3^2}{D_1^2D_3^2}.
\end{aligned}
$$

Appendix 3: $k_i, \overline{k}_i$

Values of the coefficients k_i and $\overline{k}_i$, for $i = 1, ..., 6$, that appear in the final form of the solution (3.10).

$$k_i = \frac{\lambda_i^4 - (c_3 + a_1)\lambda_i^2 + a_1 c_3 - a_3 c_1}{2\lambda_i^3 + a_2\lambda_i^2 - 2c_3\lambda_i - a_2 c_3 + a_3 c_2}, \quad \text{for} \quad i = 1, 2,$$

$$\begin{aligned} k_3 &= \frac{AC + BD}{C^2 + D^2}, & k_4 &= \frac{AD - BC}{C^2 + D^2}, \\ k_5 &= \frac{EG + FH}{G^2 + H^2}, & k_6 &= -\frac{FG - EH}{G^2 + H^2}, \end{aligned}$$

$$\overline{k}_i = \frac{c_2\lambda_i^4 + 2c_1\lambda_i^3 + (a_2c_1 - c_2c_3 - a_1c_2)\lambda_i^2 - 2c_1c_3\lambda_i + a_1c_2c_3 - a_2c_1c_3}{2\lambda_i^5 + a_2\lambda_i^4 - 4c_3\lambda_i^3 + (a_3c_2 - 2a_2c_3)\lambda_i^2 + 2c_3^2\lambda_i + a_2c_3^2 - a_3c_2c_3}, \quad \text{for} \quad i = 1, 2,$$

$$\begin{aligned} \overline{k}_3 &= \frac{\overline{A}\,\overline{C} + \overline{B}\,\overline{D}}{\overline{C}^{\,2} + \overline{D}^{\,2}}, & \overline{k}_4 &= \frac{\overline{A}\,\overline{D} - \overline{B}\,\overline{C}}{\overline{C}^{\,2} + \overline{D}^{\,2}}, \\ \overline{k}_5 &= \frac{\overline{H}\,\overline{F} + \overline{E}\,\overline{G}}{\overline{G}^{\,2} + \overline{H}^{\,2}}, & \overline{k}_6 &= \frac{\overline{E}\,\overline{H} - \overline{F}\,\overline{G}}{\overline{G}^{\,2} + \overline{H}^{\,2}}. \end{aligned}$$

where

$$\begin{aligned} A &= 4c_2\eta_1^3\omega_1 + (6c_1 - 4c_2)\eta_1\omega_1^3 - 2c_1\omega_1^3 - (2a_1c_2 - 2a_2c_1 + 2c_2c_3)\eta_1\omega_1 - 2c_1c_3\omega_1, \\ B &= c_2\eta_1^4 - 6c_2\eta_1^2\omega_1^2 + c_2\omega_1^4 + 2c_1\eta_1^3 - 6c_1\eta_1\omega_1^2 - (a_1c_2 - a_2c_1 + c_2c_3)\eta_1^2 \\ &\quad + (a_1c_2 - a_2c_1 + c_2c_3)\omega_1^2 - 2c_1c_3\eta_1 + a_1c_2c_3 - a_2c_1c_3, \\ C &= 10\eta_1^4\omega_1 - 20\eta_1^3\omega_1^2 + 2\omega_1^5 + 4a_2\eta_1^3\omega_1 - 4a_2\eta_1\omega_1^3 - 12c_3\eta_1^2\omega_1 + 4c_3\omega_1^3 \\ &\quad - (4a_2c_3 - 2a_2c_3)\eta_1\omega_1 + 2c_3^2\omega_1, \\ D &= 2\eta_1^5 - 20\eta^3\omega_1^2 + 10\eta_1\omega_1^4 + a_2\eta_1^4 - 6a_2\eta_1^2\omega_1^2 + a_2\omega_1^4 + 12c_3\eta_1\omega_1^2 \\ &\quad - (4c_3 + 2a_2c_3 - a_3c_2)\eta_1^2 + (2a_2c_3 - a_3c_2)\omega_1^2 + 2c_3^2\eta_1 + a_2c_3^2 - a_3c_2c_3, \\ E &= 4\eta_2^3\omega_2 - 4\eta_2\omega_2^3 - (2a_1 + 2c_3)\eta_2\omega_2, \\ F &= \eta_2^4 - 6\eta_2^2\omega_2^2 + \omega_2^4 - (a_1 + c_3)\eta_2^2 + (a_1 + c_3)\omega_2^2 + a_1c_3 - a_3c_1, \\ G &= 2c_2\eta_2\omega_2 + 2c_1\omega_2, \\ H &= c_2\eta_2^2 - c_2\omega_2^2 + 2c_1\eta_2 - a_1c_2 + a_2c_1, \end{aligned}$$

$$
\begin{aligned}
\overline{A} &= -4c_2\eta_1^3\omega_1 + (4c_2 - 6c_1)\eta_1\omega_1^3 - 2c_1\omega_1^3 + (2a_1c_2 - 2a_2c_1 + 2c_2c_3)\eta_1\omega_1 + 2c_1c_3\omega_1, \\
\overline{B} &= c_2\eta_1^4 - 6c_2\eta_1^2\omega_1^2 + c_2\omega_1^4 + 2c_1\eta_1^3 - 6c_1\eta_1\omega_1^2 - (a_1c_2 - a_2c_1 + c_2c_3)\eta_1^2 \\
&\quad +(a_1c_2a_2c_1 + c_2c_3)\omega_1^2 - 2c_1c_3\eta_1 + a_1c_2c_3 - a_2c_1c_3, \\
\overline{C} &= 10\eta_1^4\omega_1 - 20\eta_1^3\omega_1^2 + 2\omega_1^5 + 4a_2\eta_1^3\omega_1 - 4a_2\eta_1\omega_1^3 - 12c_3\eta_1^2\omega_1 + 4c_3\omega_1^3 \\
&\quad -(4a_2c_3 - 2a_2c_3)\eta_1\omega_1 + 2c_3^2\omega_1, \\
\overline{D} &= 2\eta_1^5 - 20\eta_1^3\omega_1^2 + 10\eta_1\omega_1^4 + a_2\eta_1^4 - 6a_2\eta_1^2\omega_1^2 + a_2\omega_1^4 + 12c_3\eta_1\omega_1^2 \\
&\quad -(4c_3 + 2a_2c_3 - a_3c_2)\eta_1^2 + (2a_2c_3 - a_3c_2)\omega_1^2 + 2c_3^2\eta_1 + a_2c_3^2 - a_3c_2c_3, \\
\overline{E} &= 6\eta_2^2\omega_2 - 2\omega_2^3 + 2a_2\eta_2\omega_2 - 2c_3\omega_2, \\
\overline{F} &= 2\eta_2^3 - 6\eta_2\omega_2^2 + a_2\eta_2^2 - a_2\omega_2^2 - 2c_3\eta_2 - a_2c_3 + a_3c_2, \\
\overline{G} &= 2c_2\eta_2\omega_2 + 2c_1\omega_2, \\
\overline{H} &= c_2\eta_2^2 - c_2\omega_2^2 + 2c_1\eta_2 - a_1c_2 + a_2c_1.
\end{aligned}
$$

Appendix 4: $H = (h_{ij})$

Components of the matrix $H = (h_{ij})$ appearing in the transformation (3.11).

$$
\begin{aligned}
h_{11} &= e^{\lambda_1 t},\\
h_{12} &= e^{\lambda_2 t},\\
h_{13} &= e^{\eta_1 t}\cos\omega_1 t,\\
h_{14} &= e^{\eta_1 t}\sin\omega_1 t,\\
h_{15} &= e^{\eta_2 t}(\overline{k}_5\cos\omega_2 t + \overline{k}_6\sin\omega_2 t),\\
h_{16} &= e^{\eta_2 t}(\overline{k}_5\sin\omega_2 t - \overline{k}_6\cos\omega_2 t),\\
h_{21} &= k_1 e^{\lambda_1 t},\\
h_{22} &= k_2 e^{\lambda_2 t},\\
h_{23} &= e^{\eta_1 t}(k_3\cos\omega_1 t + k_4\sin\omega_1 t),\\
h_{24} &= e^{\eta_1 t}(k_3\sin\omega_1 t - k_4\cos\omega_1 t),\\
h_{25} &= e^{\eta_2 t}(k_5\cos\omega_2 t + k_6\sin\omega_2 t),\\
h_{26} &= e^{\eta_2 t}(k_5\sin\omega_2 t - k_6\cos\omega_2 t),\\
h_{31} &= \overline{k}_1 e^{\lambda_1 t},\\
h_{32} &= \overline{k}_2 e^{\lambda_2 t},\\
h_{33} &= e^{\eta_1 t}(\overline{k}_3\cos\omega_1 t + \overline{k}_4\sin\omega_1 t),\\
h_{34} &= e^{\eta_1 t}(\overline{k}_3\sin\omega_1 t - \overline{k}_4\cos\omega_1 t),\\
h_{35} &= e^{\eta_2 t}\cos\omega_2 t,\\
h_{36} &= e^{\eta_2 t}\sin\omega_2 t,\\
h_{41} &= \lambda_1 e^{\lambda_1 t},\\
h_{42} &= \lambda_2 e^{\lambda_2 t},\\
h_{43} &= \eta_1 e^{\eta_1 t}\cos\omega_1 t - \omega_1 e^{\eta_1 t}\sin\omega_1 t,\\
h_{44} &= \eta_1 e^{\eta_1 t}\sin\omega_1 t + \omega_1 e^{\eta_1 t}\cos\omega_1 t,\\
h_{45} &= \eta_2 e^{\eta_2 t}\overline{k}_5\cos\omega_2 t - \omega_2 e^{\eta_2 t}\overline{k}_5\sin\omega_2 t + \eta_2 e^{\eta_2 t}\overline{k}_6\sin\omega_2 t + \omega_2 e^{\eta_2 t}\overline{k}_6\cos\omega_2 t,\\
h_{46} &= \eta_2 e^{\eta_2 t}\overline{k}_5\sin\omega_2 t + \omega_2 e^{\eta_2 t}\overline{k}_5\cos\omega_2 t - \eta_2 e^{\eta_2 t}\overline{k}_6\cos\omega_2 t + \omega_2 e^{\eta_2 t}\overline{k}_6\sin\omega_2 t,\\
h_{51} &= k_1\lambda_1 e^{\lambda_1 t},\\
h_{52} &= \lambda_2 k_2 e^{\lambda_2 t},\\
h_{53} &= \eta_1 e^{\eta_1 t}k_3\cos\omega_1 t - \omega_1 e^{\eta_1 t}k_3\sin\omega_1 t + \eta_1 e^{\eta_1 t}k_4\sin\omega_1 t + \omega_1 e^{\eta_1 t}k_4\cos\omega_1 t,\\
h_{54} &= \eta_1 e^{\eta_1 t}k_3\sin\omega_1 t + \omega_1 e^{\eta_1 t}k_3\cos\omega_1 t - \eta_1 e^{\eta_1 t}k_4\cos\omega_1 t + \omega_1 e^{\eta_1 t}k_4\sin\omega_1 t,\\
h_{55} &= \eta_2 e^{\eta_2 t}k_5\cos\omega_2 t - \omega_2 e^{\eta_2 t}k_5\sin\omega_2 t + \eta_2 e^{\eta_2 t}k_6\sin\omega_2 t + \omega_2 e^{\eta_2 t}k_6\cos\omega_2 t,\\
h_{56} &= \eta_2 e^{\eta_2 t}k_5\sin\omega_2 t + \omega_2 e^{\eta_2 t}k_5\cos\omega_2 t - \eta_2 e^{\eta_2 t}k_6\cos\omega_2 t + \omega_2 e^{\eta_2 t}k_6\sin\omega_2 t,
\end{aligned}
$$

$$
\begin{aligned}
h_{61} &= \overline{k}_1 \lambda_1 e^{\lambda_1 t}, \\
h_{62} &= \overline{k}_2 \lambda_2 e^{\lambda_2 t}, \\
h_{63} &= \eta_1 e^{\eta_1 t} \overline{k}_3 \cos \omega_1 t - \omega_1 e^{\eta_1 t} \overline{k}_3 \sin \omega_1 t + \eta_1 e^{\eta_1 t} \overline{k}_4 \sin \omega_1 t + \omega_1 e^{\eta_1 t} \overline{k}_4 \cos \omega_1 t, \\
h_{64} &= \eta_1 e^{\eta_1 t} \overline{k}_3 \sin \omega_1 t + \omega_1 e^{\eta_1 t} \overline{k}_3 \cos \omega_1 t - \eta_1 e^{\eta_1 t} \overline{k}_4 \cos \omega_1 t + \omega_1 e^{\eta_1 t} \overline{k}_4 \sin \omega_1 t, \\
h_{65} &= \eta_2 e^{\eta_2 t} \cos \omega_2 t - \omega_2 e^{\eta_2 t} \sin \omega_2 t, \\
h_{66} &= \eta_2 e^{\eta_2 t} \sin \omega_2 t + \omega_2 e^{\eta_2 t} \cos \omega_2 t.
\end{aligned}
$$

Note that h_{41}, h_{41},...,h_{66} are the time derivatives of h_{11}, h_{11},...,h_{36}, respectively.

Bibliography

[1] A. R. Pimienta-Penalver, *Attitude Dynamics, Stability, and Control of a Heliogyro Solar Sail*. Ph.D. dissertation, State University of New York at Buffalo, 2017. 1

[2] G. Gómez, W. S. Koon, M. Lo, J. E. Marsden, J. Masdemont, and S. D. Ross, "Connecting orbits and invariant manifolds in the spatial restricted three-body problem," *Nonlinearity*, vol. 17, no. 5, pp. 15–71, 2004. doi:10.1088/0951-7715/17/5/002. 7

[3] M. Romero Gómez, E. Athanassoula, J. J. Masdemont, and G. C. García, "The role of invariant manifolds in the formation of spiral arms and rings in barred galaxies," in *Nonlinear Science and Complexity*, (Barcelona, Spain), pp. 95–98, 2011. doi:10.1007/978-90-481-9884-9-11. 8

[4] C. R. McInnes, *Solar sailing: technology, dynamics and mission applications*. Springer Science and Business Media, 2004. 2, 4, 23

[5] P. Licia, *Dynamic response of a 5PCS square solar sail to torque control*. PhD thesis, University of Pisa, 2022. 1

[6] L. Friedman, K. Pichkhadze, V. Kudryashov, G. Rogovsky, V. Linkin, V. Gotlib, A. Lipatov, J. Cantrell, and J. Garvey, "Cosmos 1: the attempt to fly the first solar sail mission," in *IAF abstracts, 34th COSPAR Scientific Assembly*, (Washington DC, USA), p. 191, 2021. 1

[7] A. Farrés, *Contributions to the dynamics of a solar sail in the Earth-Sun system*. Ph.D. dissertation, Universitat de Barcelona, 2009. 2, 5

[8] L. Johnson, M. Whorton, A. Heaton, R. Pinson, G. Laue, and C. Adams, "Nanosail-d: A solar sail demonstration mission," *Acta astronautica*, vol. 68, no. 5-6, pp. 571–575, 2011. doi:10.1016/J.ACTAASTRO.2010.02.008. 2

[9] O. Mori and H. Sawada, "First solar power sail demonstration by ikaros," *Transactions of the Japan Society for Aeronautical and Space Sciences, Aerospace Technology Japan*, vol. 8, no. 27, pp. 425–431, 2010. doi:10.2322/tastj.8.To425. 2, 15

[10] Y. Tsuda, O. Mori, R. Funase, H. Sawada, T. Yamamoto, T. Saiki, T. Endo, and J. Kawaguchi, "Flight status of ikaros deep space solar sail demonstrator," *Acta astronautica*, vol. 69, no. 9-10, pp. 833–840, 2011. doi:10.1016/j.actaastro.2011.06.005. 2

[11] O. Mori, H. Sawada, F. Hanaoka, J. Kawaguchi, Y. Shirasawa, M. Sugita, Y. Miyazaki, H. Sakamoto, and R. Funase, "Development of deployment system for small size solar sail mission," *Transactions of the Japan Society for Aeronautical and Space Sciences, Space Technology Japan*, vol. 7, no. 26, pp. 87–94, 2009. doi:10.2322/tstj.7.Pd87. 2

[12] C. Katan, "Nasa's next solar sail: lessons learned from nanosail-d2," in *26th Annual AIAA/USU Conference on Small Satellites: Enhancing Global Awareness through Small Satellites*, (Washington DC, USA), pp. 1712–1762, 2012. 2

[13] G. Vulpetti, L. Johnson, and L. Matloff, G, *The NanoSail–D2 NASA mission.* Springer, 2015. 2

[14] A. Farrés and À. Jorba, "Dynamics, geometry and solar sails," *Indagationes Mathematicae*, vol. 27, no. 5, pp. 1245–1264, 2016. doi:10.1016/j.indag.2016.06.005. 2

[15] B. Betts, A. Spencer, D, and B. Nye, "Lightsail–2: Controlled solar sailing using a cubesat," in *4th International Symposium on Solar Sailing*, (Tokyo, Japan), pp. 68–79, 2017. 2

[16] A. Plante, B, A. Spencer, D, and B. Betts, "Lightsail–2 adcs: From simulation to mission readiness," in *4th International Symposium on Solar Sailing*, (Tokyo, Japan), pp. 35–45, 2017. 2, 15

[17] R. H. Frisbee, "Advanced space propulsion for the 21st century," *Journal of propulsion and power*, vol. 19, no. 6, pp. 1129–1154, 2003. doi:10.2514/2.6948. 2

[18] H. Loeb and G. Popov, "Advanced interplanetary mission of the xxi century using electric propulsion," in *IEPC'95- International Electric Propulsion Conference*, vol. 1, (Moscow, Russia), pp. 27–40, 1995. 2

[19] C. Wiley, "Clipper ships of space," *Astounding Science Fiction*, vol. 5, no. 4, pp. 135–142, 1951. 3

[20] R. L. Garwin, "Solar sailing-a practical method of propulsion within the solar system," *Jet Propulsion*, vol. 28, no. 3, pp. 188–190, 1958. 3

[21] J. Van Der Ha and V. Modi, "Long-term evaluation of three-dimensional heliocentric solar sail trajectories with arbitrary fixed sail setting," *Celestial mechanics*, vol. 19, no. 2, pp. 113–138, 1979. doi:10.1007/BF01796085. 3

[22] R. Stevens, I. M. Ross, and S. E. Matousek, "Earth-mars return trajectories using solar sails," in *55th International Astronautical Congress of the International Astronautical Federation*, (Tokyo, Japan), pp. 1–2, 2004. 3

[23] R. L. Forward, "Statite-a spacecraft that does not orbit," *Journal of Spacecraft and Rockets*, vol. 28, no. 5, pp. 606–611, 1991. doi:10.2514/3.26287. 3

[24] M. Macdonald, G. W. Hughes, C. McInnes, A. Lyngvi, P. Falkner, and A. Atzei, "Geosail: an elegant solar sail demonstration mission," *Journal of Spacecraft and Rockets*, vol. 44, no. 4, pp. 784–796, 2007. doi:10.2514/1.22867. 3

[25] J. L. West, "The geostorm warning mission: enhanced opportunities based on new technology," in *Pasadena, CA: Jet Propulsion Laboratory*, (Washington DC, USA), pp. 5–7, 2004. 3, 109

[26] D. Cielaszyk and B. Wie, "New approach to halo orbit determination and control," *Journal of Guidance, Control, and Dynamics*, vol. 19, no. 2, pp. 266–273, 1996. doi:10.2514/3.21614. 4

[27] H. Poynting, J, "Radiation in the solar system: Its effect on temperature and its pressure on small bodies," *Philosophical Transactions of the Royal Society of London. Series A, Containing Papers of a Mathematical or Physical Character*, vol. 202, no. 346-358, pp. 525–552, 1904. doi:10.1098/rsta.1904.0012. 4

[28] I. I. Shapiro and H. M. Jones, "Perturbations of the orbit of the echo balloon," *Science*, vol. 132, no. 3438, pp. 1484–1486, 1960. doi:10.1126/science.132.3438.1484. 4

[29] P. Musen, "The influence of the solar radiation pressure on the motion of an artificial satellite," *Journal of Geophysical Research*, vol. 65, no. 5, pp. 1391–1396, 1960. doi:10.1029/JZ065i005p01391. 4

[30] V. A. Chobotov, *Orbital mechanics*. Washington DC, USA: American Institute of Aeronautics and Astronautics, 2002. 4

[31] C. Colombo and R. McInnes, Colin, "Orbital dynamics of smart–dust devices with solar radiation pressure and drag," *Journal of Guidance, Control, and Dynamics*, vol. 34, no. 6, pp. 1613–1631, 2011. doi:10.2514/1.52140. 4

[32] C. Colombo, C. Lücking, and C. R. McInnes, "Orbital dynamics of high area-to-mass ratio spacecraft with j2 and solar radiation pressure for novel earth observation and communication services," *Acta Astronautica*, vol. 81, no. 1, pp. 137–150, 2012. doi:10.1016/j.actaastro.2012.07.009. 4

[33] G. Aliasi, G. Mengali, and A. A. Quarta, "Artificial equilibrium points for a generalized sail in the circular restricted three-body problem," *Celestial Mechanics and Dynamical Astronomy*, vol. 110, no. 4, pp. 343–368, 2011. doi:10.1007/s10569-011-9366-y. 4

[34] W. E. Wiesel, *Modern astrodynamics*. World Scientific: Aphelion Press Beavercreek, 2010. 4

[35] R. McInnes, Colin and P. Macpherson, K, "Solar sail halo trajectories: Dynamics and applications," in *42nd International Astronautical Congress*, vol. 1, (Montreal, Canada), pp. 5–11, 1991. 4

[36] L. Lei, Han, *Libration, invariant manifold and low energy orbit*. Ph.D. dissertation, Nanjing: Nanjing University, 2015. 4

[37] R. Siyuan, L. Jiafu, and C. Naigang, "A review of solar sail spacecraft research and its key technology," *Aerospace Shanghai*, vol. 2, pp. 53–62, 2011. doi:10.19328/j.cnki.1006-1630.2011.02.012. 4

[38] B. Du, G. Vukovich, and J. Guo, "Analysis of degree of controllability based on gramian for solar sails in artificial lagrangian orbits," in *2018 IEEE CSAA Guidance, Navigation and Control Conference (CGNCC)*, (Washington DC, USA), pp. 1–6, IEEE, 2018. 5

[39] C. R. McInnes, A. J. McDonald, J. F. Simmons, and E. W. MacDonald, "Solar sail parking in restricted three-body systems," *Journal of Guidance, Control, and Dynamics*, vol. 17, no. 2, pp. 399–406, 1994. doi:10.2514/3.21211. 5, 9, 110

[40] C. R. McInnes, "Solar sail mission applications for non-keplerian orbits," *Acta Astronautica*, vol. 45, no. 4–9, pp. 567–575, 1999. doi:10.1016/S0094-5765(99)00177-0. 5

[41] C. R. McInnes, "Artificial lagrange points for a partially reflecting flat solar sail," *Journal of guidance, control, and dynamics*, vol. 22, no. 1, pp. 185–187, 1999. doi:10.2514/2.7627. 5

[42] A. I. McInnes, *Strategies for solar sail mission design in the circular restricted three-body problem*. PhD thesis, West Lafayette: School of Aeronautics and Astronautics, Purdue University, 2000. 5, 15

[43] H. Baoyin and C. R. Mcinnes, "Solar sail halo orbits at the sun–earth artificial L_1 point," *Celestial Mechanics and Dynamical Astronomy*, vol. 94, no. 2, pp. 155–171, 2006. doi:10.1007/s10569-005-4626-3. 5, 6, 33

[44] T. J. Waters and C. R. McInnes, "Periodic orbits above the ecliptic in the solar-sail restricted three-body problem," *Journal of Guidance, Control, and Dynamics*, vol. 30, no. 3, pp. 687–693, 2007. doi:10.2514/1.26232. 5, 110

[45] S. Gong, H. Baoyin, and J. Li, "Solar sail three-body transfer trajectory design," *Journal of Guidance Control and Dynamics*, vol. 33, no. 3, pp. 873–886, 2010. doi:10.2514/1.46077. 5

[46] K. Howell and J. Guzmán, "Spacecraft trajectory design in the context of a coherent restricted four-body problem with application to the map mission(microwave anisotropy probe)," in *IAF, 51 st International Astronautical Congress*, (Rio de Janeiro, Brazil), 2000. 5

[47] G. Gómez, J. J. Masdemont, and J. Mondelo, "Solar system models with a selected set of frequencies," *Astronomy and Astrophysics*, vol. 390, no. 2, pp. 733–749, 2002. doi:10.1051/0004-6361:20020625. 5

[48] M. Andreu, *The quasi-bicircular problem*. Ph.D. dissertation, Britain, Citeseer, 1998. 5

[49] G. Aliasi, G. Mengali, and A. A. Quarta, "Artificial lagrange points for solar sail with electrochromic material panels," *Journal of Guidance, Control, and Dynamics*, vol. 36, no. 5, pp. 1544–1550, 2013. doi:10.2514/1.58167. 5

[50] J. Simo and C. R. McInnes, "Solar sail orbits at the earth–moon libration points," *Communications in Nonlinear Science and Numerical Simulation*, vol. 14, no. 12, pp. 4191–4196, 2009. doi:10.1016/j.cnsns.2009.03.032. 5

[51] X. Pan and M. Xu, "Review on continuous low thrust non kepler suspended orbit," *China Space Science and technology*, vol. 41, no. 4, pp. 1–6, 2021. doi:10.16708/j.cnki.1000-758X.2021.0046. 5

[52] S. Baig and C. R. McInnes, "Artificial three-body equilibria for hybrid low-thrust propulsion," *Journal of Guidance, Control, and Dynamics*, vol. 31, no. 6, pp. 1644–1655, 2008. doi:10.2514/1.36125. 5

[53] K. Ishimura, T. Kawachi, and H. Tanaka, "Artificial lagrange points for spacecraft with a tethered anchor," *Transactions of the Japan Society for Aeronautical and Spaceences Aerospace Technology Japan*, vol. 14, no. 30, pp. 69–73, 2016. doi:10.2322/tastj.14.Pd69. 5

[54] H. Yang, X. Bai, and S. Li, "Artificial equilibrium points near irregular-shaped asteroids with continuous thrust," *Journal of Guidance, Control, and Dynamics*, vol. 41, no. 6, pp. 1308–1319, 2018. doi:10.2514/1.G003295. 5

[55] C. Yao, M. Xu, and T. Luo, "Dynamics and control for nonideal solar sails around artificial lagrangian points," *Journal of Spacecraft and Rockets*, vol. 55, no. 3, pp. 575–585, 2018. doi:10.2514/1.A33990. 5

[56] M. E. Grøtte and M. J. Holzinger, "Solar sail equilibria with albedo radiation pressure in the circular restricted three-body problem," *Advances in Space Research*, vol. 59, no. 4, pp. 1112–1127, 2017. doi:10.1016/j.asr.2016.11.020. 5

[57] A. de Almeida, A. Prado, T. Yokoyama, and D. Sanchez, "Spacecraft motion around artificial equilibrium points," *Nonlinear Dynamics*, vol. 91, no. 3, pp. 1473–1489, 2018. doi:10.1007/s11071-017-3959-2. 5

[58] Y. Gao and J. Wu, "The optimal control for the tethered system formed by an asteroid and a solar sail," *Advances in Space Research*, vol. 57, no. 4, pp. 1002–1014, 2016. doi:10.1016/j.asr.2015.12.018. 6

[59] X. Pan and M. Xu, "Cislunar navigation constellation by displaced solar sails," *The Journal of Navigation*, vol. 70, no. 5, pp. 963–982, 2017. doi:10.1017/S037346331700025X. 6

[60] X. Pan, M. Xu, and R. Santos, "Trajectory optimization for solar sail in cislunar navigation constellation with minimal lightness number," *Aerospace Science and Technology*, vol. 70, pp. 559–567, 2017. doi:10.1016/j.ast.2017.08.042. 6

[61] W. Wang, H. Baoyin, G. Mengali, and A. A. Quarta, "Solar sail cooperative formation flying around l2-type artificial equilibrium points," *Acta Astronautica*, vol. 169, no. 35, pp. 224–239, 2020. doi:10.1016/j.actaastro.2019.10.028. 6

[62] M. A. Lazzara, A. Coletti, and B. L. Diedrich, "The possibilities of polar meteorology, environmental remote sensing, communications and space weather applications from artificial lagrange orbit," *Advances in Space Research*, vol. 48, no. 11, pp. 1880–1889, 2011. doi:10.1016/j.asr.2011.04.026. 6

[63] A. de Almeida Jr, A. F. Prado, D. M. Sanchez, and T. Yokoyama, "Searching for artificial equilibrium points to place satellites "above and below" l_3 in the sun-earth system," *Revista mexicana de astronomía y astrofísica*, vol. 53, no. 2, pp. 293–305, 2017. 6

[64] M. Marchesin and T. Yokoyama, "A family of linear stable equilibria in the sun-earth-sail problem," *Astrophysics and Space Science*, vol. 365, no. 27, pp. 1–13, 2020. doi:10.1007/s10509-020-03802-9. 6

[65] A. Farrés and À. Jorba, "Periodic and quasi-periodic motions of a solar sail close to SL_1 in the earth–sun system," *Celestial Mechanics and Dynamical Astronomy*, vol. 107, no. 1-2, pp. 233–253, 2010. doi:10.1007/s10569-010-9268-4. 6

[66] P. Verrier, T. Waters, and J. Sieber, "Evolution of the halo family in the radial solar sail circular restricted three-body problem," *Celestial Mechanics and Dynamical Astronomy*, vol. 120, no. 4, pp. 373–400, 2014. doi:10.1007/s10569-014-9575-2. 6, 33

[67] Y. Lian, G. Gómez, J. J. Masdemont, and G. Tang, "A note on the dynamics around the Lagrange collinear points of the Earth-Moon system in a complete Solar System model," *Celestial Mechanics and Dynamical Astronomy*, vol. 115, no. 2, pp. 185–211, 2013. doi:10.1007/s10569-012-9459-2. 6, 33

[68] E. M. Alessi, G. Gómez, and J. J. Masdemont, "Further advances on low-energy lunar impact dynamics," *Communications in Nonlinear Science and Numerical Simulation*, vol. 17, no. 2, pp. 854–866, 2012. doi:10.1016/j.cnsns.2011.06.037. 6, 33

[69] E. Canalias, J. Cobos, and J. J. Masdemont, "Impulsive transfers between lissajous libration point orbits," *The Journal of the astronautical sciences*, vol. 51, no. 4, pp. 361–390, 2003. doi:10.1007/BF03546289. 6, 8, 33, 91

[70] E. Perozzi and S. Ferraz-Mello, "Space manifold dynamics," *Space Manifold Dynamics*, vol. 12, no. 3, pp. 513–532, 2010. doi:10.1007/978-1-4419-0348-8. 6

[71] E. Canalias, G. Gómez, and J. J. Masdemont, "Assessment of mission design including utilization of libration points and weak stability boundaries," *ESA Advanced Concept Team*, vol. 23, no. 11, pp. 112–133, 2004. 6

[72] N. Hamilton, D. Folta, and R. Carpenter, "Formation flying satellite control around the l_2 sun-earth libration point," in *Astrodynamics Specialist Conference and Exhibit*, (Houston, the United States), pp. 4528–4529, 2002. doi:10.2514/6.2002-4528. 6

[73] J. P. Gardner, J. C. Mather, M. Clampin, R. Doyon, M. A. Greenhouse, H. B. Hammel, J. B. Hutchings, P. Jakobsen, S. J. Lilly, K. S. Long, *et al.*, "The james webb space telescope," *Space Science Reviews*, vol. 123, no. 4, pp. 485–606, 2006. doi:10.1007/s11214-006-8315-7. 6

[74] R. W. Farquhar, "Halo-orbit and lunar-swingby missions of the 1990's," *Acta Astronautica*, vol. 24, pp. 227–234, 1991. doi:10.1016/0094-5765(91)90170-A. 6

[75] P. H. Scherrer, J. T. Hoeksema, and R. I. Bush, "The solar oscillations investigation michelson doppler imager for soho," *Advances in Space Research*, vol. 11, no. 4, pp. 113–122, 1991. doi:10.1007/978-94-009-0191-95. 6

[76] M. Hechler and J. Cobos, "Herschel, planck and gaia orbit design," in *Libration Point Orbits and Applications*, pp. 231–244, World Scientific, 2003. doi:10.1142/9789812704849-0006. 6

[77] G. D. Racca and P. W. McNamara, "The lisa pathfinder mission," *Space science reviews*, vol. 151, no. 1, pp. 159–181, 2010. doi:10.1007/s11214-009-9602-x. 6

[78] J. Kalirai, "Scientific discovery with the james webb space telescope," *Contemporary Physics*, vol. 59, no. 3, pp. 251–290, 2018. doi:10.1080/00107514.2018.1467648. 6

[79] W. S. Koon, J. E. Marsden, and S. D. Ross, "Constructing a low energy transfer," in *Proceedings of an International Conference on Celestial Mechanics*, (Northwestern University, Evanston, Illinois), pp. 129–131, American Mathematical Soc., 2002. 6, 7

[80] L. Liu, Y. Liu, J. Cao, S. Hu, G. Tang, and J. Xie, "Chang'E-2 lunar escape maneuvers to the Sun-Earth L_2 libration point mission," *Acta Astronautica*, vol. 93, no. 2, pp. 390–399, 2014. doi:10.1016/j.actaastro.2013.07.032. 6

[81] H. Peng, X. Bai, J. J. Masdemont, G. Gómez, and S. Xu, "Libration transfer design using patched elliptic three-body models and graphics processing units," *Journal of Guidance, Control, and Dynamics*, vol. 40, no. 12, pp. 3155–3166, 2017. doi:10.2514/1.G002692. 6

[82] Y. Cheng, G. Gómez, J. J. Masdemont, and J. Yuan, "Study of the transfer between libration point orbits and lunar orbits in Earth-Moon system," *Celestial Mechanics and Dynamical Astronomy*, vol. 128, no. 4, pp. 409–433, 2017. doi:10.1007/s10569-017-9759-7. 6

[83] M. Shirobokov, S. Trofimov, and M. Ovchinnikov, "Survey of station-keeping techniques for libration point orbits," *Journal of Guidance, Control, and Dynamics*, vol. 40, no. 5, pp. 1085–1105, 2017. doi:10.2514/1.G001850. 6

[84] D. L. Richardson, "Halo orbit formulation for the isee–3 mission," *Journal of Guidance and Control*, vol. 3, no. 6, pp. 543–548, 1980. doi:10.2514/3.56033. 7

[85] K. A. Kelly, S. Dickinson, M. J. McPhaden, and G. C. Johnson, "Ocean currents evident in satellite wind data," *Geophysical Research Letters*, vol. 28, no. 12, pp. 2469–2472, 2001. doi:10.1029/2000GL012610. 7

[86] V. Domingo, B. Fleck, and A. I. Poland, "The soho mission: an overview," *Solar Physics*, vol. 162, no. 1-2, pp. 1–37, 1995. doi:10.1007/BF00733425. 7

[87] M. Chiu, U. Von-Mehlem, C. Willey, T. Betenbaugh, J. Maynard, J. Krein, R. Conde, W. Gray, J. Hunt, L. Mosher, *et al.*, "Ace spacecraft," *Space science reviews*, vol. 86, no. 1-4, pp. 257–284, 1998. doi:10.1023/A:1005002013459. 7

[88] C. Bennett, "First year wmap observations," in *Symposium-International Astronomical Union*, vol. 216, (Cambridge University, Britian), pp. 18–27, Cambridge University Press, 2005. doi:10.1017/S0074180900196457. 7

[89] M. W. Lo, B. G. Williams, W. E. Bollman, D. Han, Y. Hahn, J. L. Bell, E. A. Hirst, R. A. Corwin, P. E. Hong, K. C. Howell, *et al.*, "Genesis mission design," *The Journal of the astronautical sciences*, vol. 49, no. 1, pp. 169–184, 2001. doi:10.1007/BF03546342. 7

[90] M. Woodard, D. Folta, and D. Woodfork, "Artemis: The first mission to the lunar libration orbits," in *21st International Symposium on Space Flight Dynamics*, (Toulouse, France), pp. 113–134, 2009. 7

[91] R. Courtin, B. Swinyard, R. Moreno, T. Fulton, E. Lellouch, M. Rengel, and P. Hartogh, "First results of herschel-spire observations of titan," *Astronomy and Astrophysics*, vol. 536, no. 8, pp. 12–36, 2011. doi:10.1051/0004-6361/201118304. 7

[92] J.-M. Reix, T. Passvogel, G. Crone, B. Collaudin, P. Rideau, Y. Roche, and C. Vogel, "The herschel-planck programme, technical challenges for two science missions, successfully launched," *Acta Astronautica*, vol. 66, no. 1-2, pp. 130–148, 2010. doi:10.1016/j.actaastro.2009.05.025. 7

[93] B. Zhao, J. Yang, D. Wen, W. Gao, L. Chang, Z. Song, B. Xue, and W. Zhao, "Overall scheme and on-orbit images of chang'e-2 lunar satellite ccd stereo camera," *Science China Technological Sciences*, vol. 54, no. 9, pp. 22–37, 2011. doi:10.1007/s11431-011-4519-5. 7

[94] P. Li, X. Hu, Y. Huang, G. Wang, D. Jiang, X. Zhang, J. Cao, and N. Xin, "Orbit determination for chang'e-2 lunar probe and evaluation of lunar gravity models," *Science China Physics, Mechanics and Astronomy*, vol. 55, no. 3, pp. 514–522, 2012. doi:10.1007/s11433-011-4596-2. 7

[95] J. De Bruijne, "Science performance of gaia, esa's space-astrometry mission," *Astrophysics and Space Science*, vol. 341, no. 1, pp. 31–41, 2012. doi:10.1007/s10509-012-1019-4. 7

[96] F. Li, M. Ye, J. Yan, W. Hao, and J.-P. Barriot, "A simulation of the four-way lunar lander–orbiter tracking mode for the change-5 mission," *Advances in Space Research*, vol. 57, no. 11, pp. 2376–2384, 2016. doi:10.1016/j.asr.2016.03.007. 7

[97] J. Burt and B. Smith, "Deep space climate observatory: the dscovr mission," in *2012 IEEE Aerospace Conference*, (New York, the United States), pp. 1–13, IEEE, 2012. doi:10.1109/AERO.2012.6187025. 7

[98] P. McNamara, S. Vitale, K. Danzmann, L. P. S. W. Team, *et al.*, "Lisa pathfinder," *Classical and quantum gravity*, vol. 25, no. 11, pp. 034–114, 2008. 7

[99] Y. Gao, Y. Ge, L. Ma, Y. Hu, and Y. Chen, "Correction to: Optimization design of configuration and layout for queqiao relay satellite," *Advances in Astronautics Science and Technology*, vol. 2, no. 1, pp. 39–40, 2019. doi:10.1007/s42423-019-00034-0. 7

[100] S. Shmatov and A. Mordvinkin, "Perturbing effect of solar radiation on the spektr-rg spacecraft in operational orbit," *Solar System Research*, vol. 48, no. 7, pp. 601–605, 2014. doi:10.1134/S0038094614070211. 7

[101] S. Soldini, *Design and control of solar radiation pressure assisted missions in the sun-earth restricted three-body problem.* Ph.D. dissertation, University of Southampton, 2016. 7, 9

[102] G. Gómez, J. J. Masdemont, and J. Mondelo, "Libration point orbits: A survey from the dynamical point of view," in *Libration Point Orbits and Applications*, (Barcelona, Spain), pp. 311–372, 2003. doi:10.1142/9789812704849-0016. 7

[103] A. Deprit, "Canonical transformations depending on a small parameter," *Celestial mechanics*, vol. 1, no. 1, pp. 12–30, 1969. doi:10.1007/BF01230629. 7

[104] À. Jorba and J. J. Masdemont, "Dynamics in the center manifold of the collinear points of the restricted three body problem," *Physica D: Nonlinear Phenomena*, vol. 132, no. 1-2, pp. 189–213, 1999. doi:10.1016/S0167-2789(99)00042-1. 7

[105] C. Conley, C, "Low energy transit orbits in the restricted three-body problems," *SIAM Journal on Applied Mathematics*, vol. 16, no. 4, pp. 732–746, 1968. doi:10.1137/0116060. 7, 33

[106] E. Canalias Vila and J. J. Masdemont, "Homoclinic and heteroclinic transfer trajectories between Lyapunov orbits in the Sun-Earth and Earth-Moon systems," *Discrete Contin. Dyn. Syst*, vol. 14, no. 9, pp. 261–279, 2006. 7

[107] M. Tantardini, E. Fantino, Y. Ren, P. Pergola, G. Gómez, and J. J. Masdemont, "Spacecraft trajectories to the L_3 point of the Sun-Earth three-body problem," *Celestial Mechanics and Dynamical Astronomy*, vol. 108, no. 3, pp. 215–232, 2010. doi:10.1007/s10569-010-9299-x. 7

[108] W. S. Koon, M. W. Lo, J. E. Marsden, and S. D. Ross, "Heteroclinic connections between periodic orbits and resonance transitions in celestial mechanics," *Chaos: An Interdisciplinary Journal of Nonlinear Science*, vol. 10, no. 2, pp. 427–469, 2000. doi:10.1063/1.166509. 7

[109] K. E. Davis, R. L. Anderson, D. J. Scheeres, and G. H. Born, "The use of invariant manifolds for transfers between unstable periodic orbits of different energies," *Celestial Mechanics and Dynamical Astronomy*, vol. 107, no. 4, pp. 471–485, 2010. doi:10.1007/s10569-010-9285-3. 7

[110] E. M. Alessi, G. Gómez, and J. J. Masdemont, "Two-manoeuvres transfers between leos and lissajous orbits in the earth–moon system," *Advances in Space Research*, vol. 45, no. 10, pp. 1276–1291, 2010. doi:10.1016/j.asr.2009.12.010. 7

[111] C. Lücking, C. Colombo, and C. R. McInnes, "Electrochromic orbit control for smart-dust devices," *Journal of Guidance, Control, and Dynamics*, vol. 35, no. 5, pp. 1548–1558, 2012. doi:10.2514/1.55488. 8

[112] C. Colombo, C. Lücking, and C. R. McInnes, "Orbit evolution, maintenance and disposal of spacechip swarms through electro-chromic control," *Acta Astronautica*, vol. 82, no. 1, pp. 25–37, 2013. doi:10.1016/j.actaastro.2012.05.035. 8

[113] A. Farrés and À. Jorba, "Solar sailing with invariant manifolds in the earth-sun system," in *Proceedings of the 66th International Astronautical Congress*, vol. 7, (Jerusalem, Israel), pp. 412–423, 2015. 8

[114] R. Sood and K. Howell, "Solar sail transfers and trajectory design to sun-earth l 4, l 5: Solar observations and potential earth trojan exploration," *The Journal of the Astronautical Sciences*, vol. 66, no. 3, pp. 247–281, 2019. doi:10.1007/s40295-018-00141-4. 9

[115] C. Perera, X. Wu, and H. Dullin, "Solar sailing cubesats co-orbiting around a larger satellite near lagrange point 1," in *43rd COSPAR Scientific Assembly*, (Roma, Italy), pp. 15–19, 2021. 9, 10

[116] J. Heiligers, M. Vergaaij, and M. Ceriotti, "End-to-end trajectory design for a solar-sail-only pole-sitter at venus, earth, and mars," *Advances in Space Research*, vol. 67, no. 9, pp. 2995–3011, 2021. doi:10.1016/j.asr.2020.06.011. 9

[117] J. B. Pezent, R. Sood, and A. Heaton, "Configuration space and stability analysis of solar sail near-vertical earth-trailing orbits," *Advances in Space Research*, vol. 67, no. 9, pp. 2981–2994, 2021. doi:10.1016/j.asr.2020.10.011. 9

[118] A. Fernandez Mora, *Solar–sail invariant objects in the Sun–Earth system and transfers to the L5 region*. Ph.D. dissertation, Netherlands: Delft University, 2019. 9

[119] A. Farrés and À. Jorba, "Artificial equilibria in the RTBP for a solar sail and applications," in *Astrodynamics Network AstroNet-II*, (Bracelona, Spain), pp. 73–89, 2016. doi:10.1007/978-3-319-23986-6-6. 9

[120] S. Soldini, J. J. Masdemont, and G. Gómez, "Dynamics of solar radiation pressure–assisted maneuvers between Lissajous orbits," *Journal of Guidance, Control, and Dynamics*, vol. 42, no. 4, pp. 769–793, 2018. doi:10.2514/1.G003725. 9, 34

[121] J. R. Wertz, *Spacecraft attitude determination and control*. Springer Science and Business Media, 2012. 9

[122] S. W. Evans *et al.*, "Natural environment near the sun earth-moon l_2 libration point," *Next Generation Space Telescope Program*, vol. 5, no. 8, pp. 123–133, 2003. 9

[123] K. C. Howell and H. J. Pernicka, "Station-keeping method for libration point trajectories," *Journal of Guidance, Control, and Dynamics*, vol. 16, no. 1, pp. 151–159, 1993. doi:10.2514/3.11440. 9

[124] K. C. Howell and T. M. Keeter, "Station-keeping strategies for libration point orbits-target point and floquet mode approaches," *Spaceflight mechanics 1995*, pp. 1377–1396, 1995. 9

[125] H. Luo, Jun, *Research on Dynamic Modeling and attitude control of solar sail spacecraft*. Ph.D. dissertation, Harbin: Harbin Institute of Technology, 2007. 9

[126] A. Farrés and À. Jorba, "A dynamical system approach for the station keeping of a solar sail," *The Journal of the Astronautical Sciences*, vol. 56, no. 2, pp. 199–230, 2008. doi:10.1007/BF03256549. 9, 109

[127] A. Farrés and À. Jorba, "Dynamics of a solar sail near a halo orbit," *Acta Astronautica*, vol. 67, no. 7-8, pp. 979–990, 2010. doi:10.1016/j.actaastro.2010.05.022. 9

[128] A. Farrés and À. Jorba, "Station keeping of a solar sail around a halo orbit," *Acta Astronautica*, vol. 94, no. 1, pp. 527–539, 2014. doi:10.1016/j.actaastro.2012.07.002. 9, 110

[129] A. Farrés and À. Jorba, "Station keeping strategies for a solar sail in the solar system," *Recent Advances in Celestial and Space Mechanics*, pp. 83–115, 2016. doi:10.1007/978-3-319-27464-5-3. 9, 110

[130] G. Gerard *et al.*, *Dynamics and mission design near libration points*, vol. 1. World Scientific, 2001. 9

[131] C. Simó, G. Gómez, J. Llibre, R. Martinez, and J. Rodriguez, "On the optimal station keeping control of halo orbits," *Acta Astronautica*, vol. 15, no. 6-7, pp. 391–397, 1987. doi:10.1016/0094-5765(87)90175-5. 9

[132] H. Baoyin and C. R. McInnes, "Solar sail orbits at artificial sun-earth libration points," *Journal of Guidance, control, and dynamics*, vol. 28, no. 6, pp. 1328–1331, 2005. doi:10.2514/1.14598. 9

[133] M. Xu and S. Xu, "Structure-preserving stabilization for hamiltonian system and its applications in solar sail," *Journal of Guidance Control and Dynamics*, vol. 32, no. 3, pp. 997–1004, 2009. doi:10.2514/1.34757. 9

[134] D. J. Scheeres, F.-Y. Hsiao, and N. X. Vinh, "Stabilizing motion relative to an unstable orbit: applications to spacecraft formation flight," *Journal of Guidance, Control, and Dynamics*, vol. 26, no. 1, pp. 62–73, 2003. doi:10.2514/2.5015. 9

[135] S. Soldini, C. Colombo, and S. J. Walker, "Solar radiation pressure Hamiltonian feedback control for unstable libration-point orbits," *Journal of Guidance, Control, and Dynamics*, vol. 40, no. 6, pp. 1374–1389, 2017. doi:10.2514/1.G002090. 10, 110

[136] J. Bookless and R. McInnes, Colin, "Control of lagrange point orbits using solar sail propulsion," *Acta Astronautica*, vol. 62, no. 2-3, pp. 159–176, 2008. doi:10.1016/j.actaastro.2006.12.051. 10, 110

[137] A. Farrés and M. Ceriotti, "Solar sail station keeping of high-amplitude vertical lyapunov orbits in sun-earth system," in *63rd International Astronautical Congress (IAC 2012)*, (Naples, Italy), pp. 1–12, 2012. 10

[138] P. Gong, Sheng, *Research on dynamics and control of solar sail spacecraft.* Ph.D. dissertation, Beijing: Tsinghua University, 2009. 10

[139] M. Zhu, *Research on dynamics and control of solar sail spacecraft.* Ph.D. dissertation, Hefei: University of science and technology of China, 2016. 10

[140] J. Zhang, F. Cao, Xiao, and W. Liu, "Rcd orbit keeping and control of artificial translation point of solar sail spacecraft," *Flight mechanics*, vol. 39, no. 1, pp. 77–81, 2021. doi:10.13645/j.cnki.f.d.20201113.002. 10

[141] D. Tamakoshi and H. Kojima, "Solar sail orbital control using reflectivity variations near the earth–moon l_2 point," *Journal of Guidance, Control, and Dynamics*, vol. 41, no. 2, pp. 417–430, 2018. doi:10.2514/1.G002679. 10

[142] P. Lou, Zhang, *Orbit dynamics and control of translational point of continuous low thrust spacecraft*. Ph.D. dissertation, Hefei: University of science and technology of China, 2019. 10

[143] F. Qin, J and F. Li, J, "Trajectory optimization design of solar sail spacecraft flying to halo orbit," *Journal of Tsinghua University: Natural Science Edition*, vol. 47, no. 8, pp. 1361–1365, 2007. 10

[144] L. Niccolai, G. Mengali, A. A. Quarta, and A. Caruso, "Feedback control law of solar sail with variable surface reflectivity at sun–earth collinear equilibrium points," *Aerospace Science and Technology*, vol. 106, no. 86, pp. 106–144, 2020. doi:10.1016/j.ast.2020.106144. 10

[145] D. Guzzetti, R. Sood, L. Chappaz, and H. Baoyin, "Station keeping analysis for solar sailing the L_4 region of binary asteroid systems," *Journal of Guidance, Control, and Dynamics*, vol. 42, no. 6, pp. 1306–1318, 2019. doi:10.2514/1.G003994. 10

[146] A. Farrés, C. Gao, J. J. Masdemont, G. Gómez, D. C. Folta, and C. Webster, "Geometrical analysis of station-keeping strategies about libration point orbits," *Journal of Guidance, Control, and Dynamics*, vol. 45, no. 6, pp. 1108–1125, 2022. doi:10.2514/1.G006014. 10, 110

[147] J. C. Maxwell, "A discourse on molecules," *The London, Edinburgh, and Dublin Philosophical Magazine and Journal of Science*, vol. 46, no. 308, pp. 453–469, 1873. doi:10.1080/14786447308640975. 15

[148] H. Spencer and K. A. Carroll, "Real solar sails are not ideal, and yes it matters," in *Advances in Solar Sailing*, pp. 921–940, Springer, 2014. doi:10.1007/978-3-642-34907-2-55. 15

[149] M. Macdonald and R. McInnes, Colin, "A near-term roadmap for solar sailing," in *55th International Astronautical Congress of the International Astronautical Federation*, (Brasilia, Brazil), pp. 1–3, 2004. 15

[150] D. Lawrence and S. Piggott, "Solar sailing trajectory control for sub-l_1 station keeping," in *AIAA Guidance, Navigation, and Control Conference and Exhibit, Pittsburgh, the United States*, pp. 155–176, 2004. doi:10.2514/6.2004-5014. 22, 110

[151] L. Rios, Reyes and D. Scheeres, "Robust solar sail trajectory control for large prelaunch modeling errors," in *AIAA Guidance, Navigation, and Control Conference and Exhibit, Atlanta, the United States*, pp. 61–73, 2005. doi:10.2514/6.2005-6173. 22

[152] C. Gordon, S, "Orbit determination error analysis and comparison of station-keeping costs for lissajous and halo-type libration point orbits and sensitivity analysis using experimental design techniques," in *Goddard Space Flight Center, Flight Mechanics*, (Washington, the United States), pp. 245–265, 1993. 33

[153] K. C. Howell and H. J. Pernicka, "Numerical determination of lissajous trajectories in the restricted three-body problem," *Celestial Mechanics*, vol. 41, no. 1, pp. 107–124, 1987. doi:10.1007/BF01238756. 33

[154] G. Gómez, À. Jorba, J. J. Masdemont, and C. Simó, "Study of the transfer from the earth to a halo orbit around the equilibrium point l_1," *Celestial Mechanics and Dynamical Astronomy*, vol. 56, no. 4, pp. 541–562, 1993. doi:10.1007/BF00696185. 33

[155] H. Franz, P. Sharer, K. Ogilvie, and M. Desch, "Wind nominal mission performance and extended mission design," *The Journal of the astronautical sciences*, vol. 49, no. 1, pp. 145–167, 2001. doi:10.1007/BF03546341. 34

[156] W. Farquhar, R, D. Muhonen, and D. Richardson, "Mission design for a halo orbiter of the earth," in *Astrodynamics Conference*, (Beijing, China), pp. 8–10, 1976. doi:10.2514/6.1976-810. 87

[157] A. Delshams, J. J. Masdemont, and P. Roldán, "Computing the scattering map in the spatial hill's problem," *Discrete and Continuous Dynamical Systems-B*, vol. 10, no. 2&3, September, p. 455, 2008. doi:10.3934/dcdsb.2008.10.455. 89

[158] L. Arona and J. J. Masdemont, "Computation of heteroclinic orbits between normally hyperbolic invariant 3-spheres foliated by 2-dimensional invariant tori in hill's problem," in *Conference Publications*, (Barcelona, Spain), p. 64, American Institute of Mathematical Sciences, 2007. 89

[159] O. Mori, H. Sawada, R. Funase, M. Morimoto, T. Endo, T. Yamamoto, Y. Tsuda, Y. Kawakatsu, J. Kawaguchi, and Y. Miyazaki, "First solar power sail demonstration by ikaros," *TRANSACTIONS OF THE JAPAN SOCIETY FOR AERONAUTICAL AND SPACE SCIENCES, AEROSPACE TECHNOLOGY JAPAN*, vol. 8, no. 27, pp. 425–431, 2010. doi:10.2322/tastj.8.To-4-25. 109

[160] C. Gao, J. J. Masdemont, G. Gómez, J. Chen, and J. Yuan, "High order dynamical systems approaches for low-thrust station-keeping of libration point orbits," *Acta Astronautica*, vol. 190, pp. 349–364, 2022. doi:10.1016/j.actaastro.2021.10.015. 109

[161] L. Meireles, A. Prado, C. de Melo, and M. Pereira, "A study on different attitude strategies and mission parameters based on lightsail-2," *Revista Mexicana de Astronomıa y Astrofısica*, vol. 58, pp. 23–35, 2022. doi:10.22201/ia.01851101p.2022.58.01.02. 109

[162] M. Macdonald and R. McInnes, Colin, "Solar sail science mission applications and advancement," *Advances in Space Research*, vol. 48, no. 11, pp. 1702–1716, 2011. doi:10.1016/j.asr.2011.03.018. 109

[163] C. Bianchi, L. Niccolai, G. Mengali, and A. A. Quarta, "Collinear artificial equilibrium point maintenance with a wrinkled solar sail," *Aerospace Science and Technology*, vol. 119, no. 26, pp. 107–150, 2021. doi:10.1016/j.ast.2021.107150. 110

[164] X. Duan, G. Gómez, J. J. Masdemont, and X. Yue, "A picture of solar-sail heteroclinic enhanced connections between lissajous libration point orbits," *Communications in Nonlinear Science and Numerical Simulation*, vol. 85, p. 105252, 2020. doi:10.1016/j.cnsns.2020.105252.